

**Solvatochromic Effects, Photophysical Properties, Fluorescence Quenching, and Molecular Docking of Ferulic and Sinapic Acids: Experimental and Computational Approaches**



**Umer Sherefedin Yasin**

A Dissertation submitted to the Department of Applied Physics  
College of Applied Natural Sciences

Presented in partial fulfillment of the requirements for the degree of Doctor of Philosophy in  
Applied Physics (Specialization in Laser Spectroscopy)

Office of Graduate Studies  
Adama Science and Technology University

April 2025  
Adama, Ethiopia

**Solvatochromic Effects, Photophysical Properties, Fluorescence  
Quenching, and Molecular Docking of Ferulic and Sinapic Acids:  
Experimental and Computational Approaches**

PhD candidate:  
Umer Sherefedin Yasin

Supervisor: Prof. Abebe Belay (PhD)  
Co-supervisor: Kusse Gudishe Goroyo (PhD)

A Dissertation Submitted to the Department of Applied Physics  
College of Applied Natural Sciences

Presented in Partial Fulfillment of the Requirements for the Degree of Doctor of Philosophy  
in Applied Physics (Specialization in Laser Spectroscopy)

Office of Graduate Studies  
Adama Science and Technology University

April 2025  
Adama, Ethiopia

---

## Declaration

---

I declare that this dissertation entitled “**Solvatochromic Effects, Photophysical Properties, Fluorescence Quenching, and Molecular Docking of Ferulic and Sinapic Acids: Experimental and Computational Approaches**” is my work and has not been submitted to any university for a similar purpose. The references used in this dissertation are duly recognized by proper citations.

Umer Sherefedin Yasin

Name of student

\_\_\_\_\_  
Signature

\_\_\_\_\_  
Date

---

## RECOMMENDATION OF SUPERVISORS

---

We, the supervisor and co-supervisor of this research dissertation, hereby certify that we have closely supervised the student while developing this dissertation and read the draft dissertation entitled “ **Solvatochromic Effects, Photophysical Properties, Fluorescence Quenching, and Molecular Docking of Ferulic and Sinapic Acids: Experimental and Computational Approaches**” prepared under our guidance by **Umer Sherefedin Yasin** . Therefore, we recommend the submission of the dissertation to the department for further review and evaluation.

Prof. Abebe Belay (PhD)

Name of supervisor

\_\_\_\_\_

Signature

\_\_\_\_\_

Date

Kusse Gudishe Goroyo (PhD)

Name of co-supervisor

\_\_\_\_\_

Signature

\_\_\_\_\_

Date

---

## Approval Page

---

I/we hereby certify that the recommendation and suggestion given by the dissertation review committee is appropriately incorporated into the dissertation entitled “ **Solvatochromic Effects, Photophysical Properties, Fluorescence Quenching, and Molecular Docking of Ferulic and Sinapic Acids: Experimental and Computational Approaches** ” by Umer Sherefedin Yasin .

Prof. Abebe Belay (PhD)

Name of supervisor

\_\_\_\_\_  
Signature

\_\_\_\_\_  
Date

Kusse Gudishe Goroyo (PhD)

Name of co-supervisor

\_\_\_\_\_  
Signature

\_\_\_\_\_  
Date

---

## Approval of Board of Reviewers

---

We, the undersigned, members of the board of reviewers of the dissertation open defense by **Umer Sherefedin Yasin** have read and evaluated the dissertation proposal entitled “**Solva-tochromic Effects, Photophysical Properties, Fluorescence Quenching, and Molecular Docking of Ferulic and Sinapic Acids: Experimental and Computational Approaches**” and assessed the understanding of the candidate about the dissertation research. This is, therefore, to certify that the dissertation is accepted and we recommend the implementation of the dissertation.

_____	_____	_____
Chairperson	Signature	Date
_____	_____	_____
External Reviewer 1	Signature	Date
_____	_____	_____
External Reviewer 2	Signature	Date
_____	_____	_____
Internal Reviewer 1	Signature	Date
_____	_____	_____
Internal Reviewer 2	Signature	Date

Final approval and acceptance of the dissertation is contingent upon submission of its final copy to the Office of Postgraduate Studies (OPGS) Department Graduate Council (DGC) and School Graduate Committee (SGC).

_____	_____	_____
Department Head	Signature	Date
_____	_____	_____
School Dean	Signature	Date
_____	_____	_____
Office of Postgraduate Studies, Dean	Signature	Date

---

## DEDICATION

---

This work is dedicated to my late father **Sherefedin Yasin**, after whom I am named, and whom I never had the chance to meet. His memory has always inspired me. It is also dedicated to my mother, **Fatum Yasin**, whose love, wisdom, and guidance, despite not having formal education herself, have been a constant source of strength and inspiration in my life. I pray for herself long life, continued health, and happiness, as she remains the foundation of my journey.

---

## ACKNOWLEDGEMENTS

---

First and foremost, I am deeply grateful to **Allah**, the Almighty, for granting me health, knowledge, and perseverance throughout my PhD journey. Alhamdulillah!

I am deeply grateful to **Professor Abebe Belay** for his constant support, mentorship, and insightful guidance, which were vital to the success of this dissertation. I also thank him for providing essential resources, including funding for key materials. My sincere appreciation goes to **Dr. Kusse Gudishe**, my co-supervisor, for his ongoing support and valuable input.

Special thanks to **Dr. Getachew Asmelesh** for providing valuable information about my supervisor, **Professor Abebe Belay**, and **Dr. Demissie Jobir** for his guidance and support, especially in helping me overcome the challenges I faced due to curriculum during the 2019 G.C. Thanks to **Dr. Demissie** and **Professor Abebe**, I was able to begin my studies in 2020 G.C.

I wish to extend my heartfelt thanks to the esteemed members of **ASTU Dr. Fikadu Tolosa, Mr. Fitsum Ayalew, Dr. Alemu Kebede, Dr. Kumneger Tadele**, and **Dr. T. Gurumurthi**, for their academic support. My gratitude extends to the PhD students **Mr. Semahegn Asemare, Mr. Adem Beriso, Mr. Tadesse Lemma, Mr. Dereje Gelanu, Mr. Jebel Haji, Mrs. Urge Debele, Mr. Tesfaye Feyisa, Mr. Bayisa Batu, and Mr. Gemischis Matiwos** for their valuable feedback and support. I appreciate the friendship and shared experiences with **Dr. Alemayehu Getahun** and **Dr. Kinfu W/Giorges Bachare**. I am equally grateful to the Department of Physics at **Madda Walabu University**, particularly **Mr. Ibrahim Kedir, Mr. Jeilain Husien, and Mr. Abdulkedir Gemachu**, for their guidance. My sincere appreciation goes to the **Ethiopian Ministry of Education** for providing me with this valuable chance.

I would like to extend special thanks to **Mr. Awol Eda'o, Mr. Ibrahim Abdulrahman, Mr. Jemal Koji, Mr. Teha Reshad, Mr. Wayema Gamedo, Mr. Danebo Dekebo, Mr. Bahmud Gelato, Mr. Mustafa Abdulkedir, and Mr. Jemal sado** for their generous assistance with my housing and settling in Adama city. Their support provided me with the stability needed to focus fully on my academic work.

Last, I owe my deepest gratitude to my family, my mother, **Mrs. Fatum Yasin**, my brother, **Mr. Husein Sherefedin**, and my wife, **Mrs. Dureti Husein**, whose patience and strength allowed me to focus on my research. The love, encouragement, and support of my children, **Sumeya, Amir, and Amar**, motivated me to succeed.

---

# Contents

---

List of Figures . . . . .	xii
List of Tables . . . . .	xiv
List of Acronyms and Abbreviations . . . . .	xv
List of Abstract . . . . .	xv
<b>1 INTRODUCTION</b>	<b>1</b>
1.1 Background of the Study . . . . .	1
1.2 Statement of the Problem . . . . .	3
1.3 Objectives of the Study . . . . .	4
1.3.1 General Objective . . . . .	4
1.3.2 Specific Objectives . . . . .	4
1.4 Significance of the Study . . . . .	4
1.5 Scope of the Study . . . . .	5
1.6 Organization of the Document . . . . .	5
<b>2 LITERATURE REVIEW</b>	<b>7</b>
2.1 Molecular Structure of FA and SA . . . . .	7
2.2 Biological Activities of FA and SA . . . . .	8
2.3 Interactions of FA and SA with Other Drugs . . . . .	10
2.4 Pharmacokinetics of Caffeine and Its Interaction with Other Drugs . . . . .	11
2.4.1 Pharmacokinetics of Caffeine in the Human Body . . . . .	11
2.4.2 Binding of Caffeine with Other Drugs . . . . .	12
2.5 Basic Spectroscopic Theory . . . . .	13
2.5.1 Maxwell's Equations and Wave Equations . . . . .	13
2.5.2 Light Propagation in Isotropic Dielectrics . . . . .	15
2.5.3 Time-Dependent Schrodinger Equation . . . . .	18
2.5.4 Interaction of EMR with Molecular System . . . . .	19
2.5.5 Phenomenon of Absorption . . . . .	21
2.5.6 Phenomenon of Fluorescence . . . . .	25
2.6 Solvatochromic Effects . . . . .	29
2.7 Quantum Mechanical Methods . . . . .	32
2.7.1 Semi-empirical Theory . . . . .	32
2.7.2 Hartree–Fock Method . . . . .	33

2.7.3	Density Functional Theory . . . . .	34
2.7.4	Time-Dependent Density-Functional Theory . . . . .	38
2.8	Molecular Docking . . . . .	40
<b>3</b>	<b>MATERIALS AND METHODS</b>	<b>42</b>
3.1	Chemicals and Solvents . . . . .	42
3.2	Software and Data Bases . . . . .	42
3.3	Apparatus and Instruments . . . . .	42
3.3.1	Working Principles of UV-Vis Spectrophotometer . . . . .	43
3.3.2	Working Principles of Fluorescence Spectrophotometer . . . . .	43
3.3.3	Working Principles of FTIR Spectrophotometer . . . . .	44
3.4	Experimental Methods . . . . .	44
3.4.1	Effects of the Solvent Polarity . . . . .	44
3.4.2	Optical Transition and Photophysical Properties . . . . .	45
3.4.3	Fluorescence Quenching . . . . .	46
3.5	Computational Methods . . . . .	46
3.5.1	Density Functional Theory . . . . .	46
3.5.2	Molecular Docking Methods . . . . .	47
<b>4</b>	<b>RESULTS AND DISCUSSION</b>	<b>49</b>
4.1	Solvatochromic Effects . . . . .	49
4.1.1	Absorption and Emission Spectra . . . . .	49
4.1.2	Estimation of Dipole Moments . . . . .	50
4.1.3	Optical Transition and Photophysical Properties . . . . .	55
4.1.4	Effect of Concentration on Photophysical Properties . . . . .	60
4.1.5	Fluorescence Quenching of FA and SA by Caffeine . . . . .	61
4.1.6	Binding Sites and Binding Constants . . . . .	67
4.1.7	Thermodynamic Parameters and Interaction Forces . . . . .	67
4.1.8	UV–Vis Absorption Spectra . . . . .	69
4.1.9	Fourier Transform Infrared Spectra . . . . .	71
4.2	Molecular Quantum Calculations . . . . .	71
4.2.1	Geometry Optimization . . . . .	71
4.2.2	Effects of Solvent Polarity and Temperature on the Thermodynamic Properties . . . . .	80
4.2.3	Molecular Orbital Analysis . . . . .	87
4.2.4	Dipole Moment . . . . .	88
4.2.5	Chemical Reactivity Descriptor . . . . .	90
4.2.6	Molecular Electrostatic Potential . . . . .	91
4.2.7	UV–Vis Absorption Spectral Analysis . . . . .	92
4.2.8	Emission Spectral Analysis . . . . .	92
4.2.9	Fourier Transform Infrared Spectra . . . . .	94

4.3	Molecular Docking Analysis . . . . .	95
4.3.1	Ligand-Protein Interaction . . . . .	95
4.3.2	Binding Mode . . . . .	99
4.3.3	Multiligand-Protein Interactions . . . . .	100
<b>5</b>	<b>CONCLUSIONS AND RECOMMENDATIONS</b>	<b>104</b>
5.1	Conclusions . . . . .	104
5.2	Future Research and Recommendations . . . . .	105

---

## List of Figures

---

2.1	Structures of (a) ferulic and (b) sinapic acids. . . . .	8
2.2	Molecular structure of caffeine. . . . .	11
2.3	Energy level diagrams with electronic transitions. . . . .	22
2.4	Jablonski diagram. . . . .	25
3.1	Schematic representation of UV-Vis spectrophotometer. . . . .	43
3.2	Schematic representation of a fluorescence spectrophotometer. . . . .	44
3.3	Schematic representation of an FTIR spectrophotometer setup. . . . .	45
4.1	UV-vis absorption spectra of (a) ferulic acid and (b) sinapic acid in various solvents. . . . .	51
4.2	Emission spectra of (a) ferulic acid and (b) sinapic acid in various solvents. . . . .	52
4.3	Plot of $\tilde{\nu}_a - \tilde{\nu}_f$ versus the Lippert-Mataga solvent polarity function for (a) ferulic acid and (b) sinapic acid in various solvents: acetonitrile (1), dimethyl sulfoxide (2), ethanol (3), isopropanol (4), methanol(5), distilled water (6), chloroform (7), and dichloromethane (8). . . . .	55
4.4	Plot of $\tilde{\nu}_a - \tilde{\nu}_f$ versus Bakhshiev's solvent polarity function for (a) ferulic acid and (b) sinapic acid in various solvents: acetonitrile (1), dimethyl sulfoxide (2), ethanol (3), isopropanol (4), methanol(5), distilled water (6), chloroform (7), and dichloromethane (8). . . . .	56
4.5	Plot of $\tilde{\nu}_a + \tilde{\nu}_f$ versus the Kawski-Chamma-Violet solvent polarity function for (a) ferulic acid and (b) sinapic acid in various solvents:acetonitrile (1), dimethyl sulfoxide (2), ethanol (3), isopropanol (4), methanol(5), distilled water (6), chloroform (7), and dichloromethane (8). . . . .	57
4.6	Plot of $\tilde{\nu}_a - \tilde{\nu}_f$ , ( $\text{cm}^{-1}$ ) versus the $E_T^N$ microscopic solvent polarity function for (a) ferulic acid and (b) sinapic acid in various solvents: acetonitrile (1), dimethyl sulfoxide (2), ethanol (3), isopropanol (4), methanol(5), distilled water (6), chloroform (7), and dichloromethane (8). . . . .	58
4.7	Variations in the quantum yield and fluorescence lifetime with concentration for (a) ferulic acid and (b) sinapic acid. . . . .	62

4.8	Fluorescence emission spectra of ferulic acid at various concentrations: (a) 1.72 mM, (b) 1.82 mM, (c) 1.93 mM, (d) 2.06 mM, (e) 2.21 mM, (f) 2.38 mM, (g) 2.58 mM, (h) 2.81 mM, (i) 3.09 mM, (j) 3.43 mM, (k) 3.86 mM, and (l) 4.41 mM. The inset shows the variation in fluorescence intensity with concentration. . . . .	63
4.9	Fluorescence intensity spectra of sinapic acid at various concentrations: (a) 2.10 mM, (b) 2.23 mM, (c) 2.38 mM, (d) 2.55 mM, (e) 2.75 mM, (f) 2.98 mM, (g) 3.25 mM, (h) 3.57 mM, (i) 3.97 mM, (j) 4.46 mM, (k) 5.10 mM, and (l) 5.95 mM. The inset shows the variation in fluorescence intensity with concentration. . . . .	64
4.10	Fluorescence intensity spectra of (a) ferulic acid and (b) sinapic acid, in the presence and absence of different caffeine concentrations. . . . .	65
4.11	$F/F_0$ versus caffeine concentration for (a) ferulic acid and (b) sinapic acid at 298 K, 303 K, and 310 K. . . . .	66
4.12	Modified Stern–Volmer plot of fluorescence quenching of (a) ferulic acid and (b) sinapic acid by caffeine at 298 K, 303 K, and 310 K. . . . .	68
4.13	UV-Vis absorption spectra of (a) ferulic acid and (b) sinapic acid in the absence and presence of different caffeine. . . . .	70
4.14	FTIR spectra of (a) ferulic acid (FA), caffeine (CF), and ferulic acid-caffeine (FA-CF) and (b) sinapic acid (SA), caffeine (CF), and sinapic acid-caffeine (SA-CF) interactions. . . . .	72
4.15	Optimization of the molecular structure of ferulic acid using semiempirical (MP6) in the (a) gas phase and (b) water. . . . .	74
4.16	Molecular structure of ferulic acid optimized using the Hartree-Fock method with B3LYP and the 6-311++G (d, p) basis set: (a) gas and (b) water phases. . . . .	77
4.17	Molecular structure of ferulic acid optimized using DFT/B3LYPP with 6-311++G (d, p) (a) gas and (b) water phases. . . . .	80
4.18	Optimization of the molecular structure of sinapic acid using semiempirical (MP6) in the (a) gas phase and (b) water . . . . .	81
4.19	Molecular structure of sinapic acid optimized using the Hartree-Fock method with B3LYP and the 6-311++G (d, p) basis set: (a) gas and (b) water phases. . . . .	82
4.20	Molecular structure of sinapic acid optimized using DFT/B3LYPP with 6-311++G (d, p) (a) gas and (b) water phases. . . . .	83
4.21	Changes in the enthalpy, entropy, and heat capacity of (a) FA and (b) SA molecules in the gas phase from 100 K to 1000 K using DFT (B3LYP)/6-311++G (d, p). . . . .	85
4.22	Changes in the enthalpy, entropy, and heat capacity of (a) FA and (b) SA molecules in the water from 100 K to 1000 K using DFT (B3LYP)/6-311++G (d, p). . . . .	86

4.23	Energy levels of the HOMO, LUMO, and band gaps for (a) ferulic acid and (b) sinapic acid in gas, computed via DFT (B3LYP)/6-311++G (d, p). . . . .	89
4.24	Energy levels of the HOMO, LUMO, and band gaps for (a) ferulic acid and (b) sinapic acid in water, computed via DFT (B3LYP)/6-311++G (d, p). . . . .	90
4.25	Total density matrix with electrostatic potential map (TDM-ESP) of ferulic acid (a) and sinapic acid (b) via DFT (B3LYP)/6-311++G (d, p). . . . .	93
4.26	Absorption spectra of ferulic acid (a) and sinapic acid (b) in gas and various solvents, computed using TD-DFT/B3LYP with the 6-311++G (d, p) basis set. . . . .	94
4.27	Emission spectra of ferulic acid (a) and sinapic acid (b) in in the gas phase and solvents, computed using TD-DFT (B3LYP)/6-311++G (d, p). . . . .	96
4.28	FTIR absorption spectra of ferulic acid (a) and sinapic acid (b) in gas phase, computed using TD-DFT (B3LYP)/6-311++G (d, p). . . . .	97
4.29	FTIR absorption spectra of ferulic acid (a) and sinapic acid (b) in water, computed using TD-DFT (B3LYP)/6-311++G (d, p). . . . .	98
4.30	3D (a) and 2D (b) representations of nonbonding interactions between ferulic acid and 3m18 protein. . . . .	101
4.31	3D (a) and 2D (b) representations of nonbonding interactions between sinapic acid and 3m18 protein. . . . .	102

---

## List of Tables

---

4.1	Peak absorption and fluorescence spectra of FA and SA in solvents of various polarities. . . . .	50
4.2	Solvent polarity functions of different solvents using the refractive index and dielectric constant. . . . .	53
4.3	Slopes, intercepts, and correlation coefficients of spectral shifts for ferulic acid and sinapic acid. . . . .	54
4.4	Ground and excited state dipole moments (Debye) and Onsager cavity radius ( $\text{\AA}$ ) for ferulic acid and sinapic acid. . . . .	54
4.5	Optical transition probabilities of ferulic acid and sinapic acid in polar and nonpolar solvents. . . . .	59
4.6	Solvent-dependent photophysical properties of ferulic acid and sinapic acid.	60
4.7	Stern–Volmer constants ( $\kappa_{SV}$ ) and quenching rates ( $k_q$ ) for FA-CF and SA-CF interactions at different temperatures (T). . . . .	67
4.8	Modified binding constant ( $K_a$ ), number of binding sites (n), and correlation coefficient (R) of caffeine with FA and SA interactions at different temperatures (K) . . . . .	67
4.9	Thermodynamic analysis: entropy ( $\Delta S^\circ$ ), enthalpy ( $\Delta H^\circ$ ), and Gibbs free energy ( $\Delta G^\circ$ ) for FA-CF and SA-CF interactions at temperature (T). . . . .	69
4.10	Dipole moment ( $\mu$ ), polarizability ( $\alpha$ ), thermal energy (E), heat capacity ( $C_p$ ), entropy (S), and HOMO–LUMO gap ( $\Delta E$ ) for FA and SA in the gas phase via DFT (B3LYP). . . . .	73
4.11	Bond lengths, angles, and dihedrals of ferulic acid in the gas phase via HF and DFT (B3LYP) with 6-311++G (d,p). . . . .	75
4.12	Calculated bond lengths, bond angles, and dihedral angles of the sinapic acid molecule in the gas phase computed by the HF and DFT (B3LYP) methods and with basis set of 6-311++G (d, p). . . . .	76
4.13	Bond lengths, angles, and dihedrals of ferulic acid in the water via HF and DFT (B3LYP) with 6-311++G(d, p). . . . .	78
4.14	Calculated bond lengths, bond angles, and dihedral angles of the sinapic acid molecule in water computed by the HF and DFT (B3LYP) methods with a basis set of 6-311++G (d, p). . . . .	79

4.15	Heat capacity ( $C_p$ ), entropy (S), and enthalpy (E) of SA via DFT (B3LYP)/6-311++G(d,p). . . . .	82
4.16	Thermodynamic properties of FA and SA in gas and water from 100–1000 K.	84
4.17	HOMO, LUMO, and energy gap ( $\Delta E$ ) (eV) of FA and SA via B3LYP/6-311++G(d,p) with IEFPCM in solvents. . . . .	88
4.18	Ground ( $\mu_g$ ) and excited ( $\mu_e$ ) state dipole moments (Debye) of ferulic acid and sinapic acid in various solvents with different dielectric constants ( $\epsilon_r$ ). . . . .	91
4.19	Global softness (S), electrophilicity index ( $\omega$ ), electronegativity ( $\chi$ ), global hardness ( $\eta$ ), and chemical potential ( $\mu$ ) of FA and SA in solvents. . . . .	92
4.20	Wavelengths ( $\lambda$ ), excitation energies (E, eV), and oscillator strengths (f, nm) of FA and SA in various solvent polarity. . . . .	95
4.21	Binding affinity and RMSD (bounds) for FA and SA with potential anticancer proteins. . . . .	99
4.22	Ferulic acid and sinapic acid interaction modes with amino acids in protein complexes. . . . .	100
4.23	Predicted binding affinities of ligands docked with selected anticancer proteins.	103

---

## List of Acronyms and Abbreviations

---

AMX	Amoxicillin
B3LYP	Becke 3-parameter Lee-Yang-Parr
BSA	Bovine Serum Albumin
CF	Caffeine
CA	Caffeic Acid
CGA	Chlorogenic Acid
DFT	Density Functional Theory
EA	Electron Affinity
EMR	Electromagnetic Radiation
FA	Ferulic Acid
HF	Hartree-Fock
HCAs	Hydroxycinnamic Acids
HOMO	Higher Occupied Molecular Orbital
HSA	Human Serum Albumin
ICT	Internal Charge Transfer
KCV	Kawski-Chamma-Viallet
LUMO	Lower Unoccupied Molecular Orbital
ROS	Reactive Oxygen Species
SA	Sinapic Acid
SCF	Self-Consistent Field
TDDFT	Time Dependent Density Functional Theory
UV-Vis	Ultraviolet Visible

---

## ABSTRACT

---

*Ferulic and sinapic acids are common hydroxycinnamic acids known for their strong antioxidant properties and potential health benefits. This study investigated the Solvatochromic effects, photophysical properties, fluorescence quenching, and molecular docking of FA and SA. The Solvatochromic effect analysis revealed that the solvent polarity significantly affected the emission spectra compared with the absorption spectra of FA and SA. The change in the ground and excited dipole moments was calculated using various models, with the Lippert–Mataga method showing the largest change due to the exclusion of solute–solvent interactions and solute polarizability. Analysis of UV–Vis and fluorescence spectra demonstrated that solvent polarity and concentration significantly affected the optical transition properties, including the integrated absorption cross-section, oscillator strength, integrated absorption coefficient, Einstein coefficients (A and B), and transition dipole moment. Furthermore, the interaction between solvent and FA or SA influenced key photophysical parameters, such as fluorescence quantum yield, radiative and nonradiative decay rates, and fluorescence lifetime. The fluorescence quenching experiments revealed that CF induced static quenching of FA and SA fluorescence, resulting in the formation of nonfluorescent complexes. The van't Hoff equation showed that the FA–CF interactions were primarily governed by electrostatic forces, while the SA–CF interactions were influenced by van der Waals forces and hydrogen bonding. The negative Gibbs free energy further confirmed the spontaneity of these interactions. Conformational changes in the FTIR spectra of FA and SA detected upon binding to CF. Quantum chemical calculations revealed that increasing the temperature increased the enthalpy, entropy, and heat capacity, suggesting potential molecular instability. The solvent polarity affected the thermodynamic parameters, dipole moments, HOMO–LUMO energy gaps, and chemical reactivity descriptors. The excited-state dipole moments were larger than those of the ground state using computational method, confirming the experimental results. TDDFT analysis revealed redshifts in both the absorption and emission spectra, which align with the experimental findings. Molecular docking revealed FA–CF and SA–CF interactions, validating the fluorescence quenching and linking these interactions to anticancer properties by binding to anticancer proteins.*

**Keywords:** *Ferulic acid, Sinapic acid, Caffeine, Solvatochromic effect, Dipole moments, Photophysical properties, Thermodynamics properties, Anticancer properties, Density functional theory, Molecular docking.*

---

## INTRODUCTION

---

### 1.1 Background of the Study

Ferulic and sinapic acids are a class of hydroxycinnamic acids (Hădărugă and Hădărugă, 2023). These molecules are abundantly found in coffee, fresh fruits, and vegetables, either in their free form or bound to polysaccharides (El-Seedi et al., 2018, 2012). Chemically, FA molecules are characterized by a benzene ring and functional groups such as hydroxyl, methoxyl, and side-chain carboxyl groups (Wang et al., 2021). SA also features hydroxyl, methoxy, carboxyl, and conjugated double bonds (Yang et al., 2021). These functional groups enable FA and SA to exhibit a range of biological activities, such as anticancer, anti-inflammatory, antimicrobial, and antioxidant effects (Gao et al., 2018; Taştumur et al., 2023; Gurbuzer, 2021; Yang et al., 2021). However, these biological activities are affected by factors such as solvent, temperature, pH, concentration, quenchers, and excitation wavelength (Mota et al., 2009; Campolongo et al., 2014). The interactions between these functional groups and solvents influence the photophysical properties of drugs (Mabesoone et al., 2020). Therefore, studying solvent–drug, drug–drug, drug–food, or drug–protein interactions is crucial for optimizing the therapeutic potential of FA and SA and gaining insights into their electronic properties upon excitation.

Investigating the Solvatochromic effects on the photophysical properties of biologically active compounds is essential for understanding how solvent polarity influences the molecular behavior of drugs. The solvent polarity significantly affects the absorption and emission spectra of these compounds by affecting their excited-state dipole moments (Belay et al., 2016b). Calculating the dipole moments in both ground and excited states through solvatochromic effects and computational methods is crucial for analyzing the electronic structure and charge distribution of drug molecules (Woldegiorges et al., 2021). A small change in dipole moment or molecular structure can cause significant alterations in a drug's biological activity. These dipole moments offer valuable insights into how a drug interacts with its environment. This interaction influences key properties such as stability, solubility, and binding affinity (Shivaleela et al., 2023).

Previous studies have shown that solvent polarity significantly influences the photophysical properties and dipole moments of bioactive compounds, such as zoledronic acid (Liu et al., 2016), folic acid, folinic acid (Sadigh et al., 2016), caffeic acid, and chlorogenic acid (Belay et al., 2016b). Solvent polarity can significantly influence the fluorescence emission of compounds, thereby affecting their interactions with biological targets and potentially their therapeutic efficacy (Liu et al., 2016). For instance, in the case of folic acid and folinic acid, solvent polarity alters their fluorescence behavior and solubility, which in turn affects their pharmacological activity and effectiveness (Sadigh et al., 2016). Likewise, compounds like chlorogenic acid, caffeic acid, ferulic acid, and sinapic acid exhibit solvent polarity-dependent shifts in their absorption and fluorescence spectra, which in turn influence their electronic properties and biological activities (Belay et al., 2016b). These solvent-induced modifications in molecular characteristics can impact drug–receptor interactions and bioavailability, resulting in variations in biological activity (Sadigh et al., 2016; Belay et al., 2016b).

Similarly, interactions between drugs or between drugs and proteins can affect their biological activity and therapeutic outcomes. The simultaneous use of multiple medications has become increasingly common in clinical practice, making it essential to study drug–drug, drug–food, and drug–protein interactions at the molecular level to optimize drug efficacy. Recent studies have shown that drug–drug or drug–protein interactions can be studied using fluorescence quenching, which provides insights into binding constants, interaction mechanisms, and stability. For example, (Li et al., 2010) reported that caffeic acid, chlorogenic acid, and ferulic acid interact differently with bovine serum albumin (BSA). Among these, ferulic acid showed the strongest binding affinity. Similarly, chlorogenic acid and ferulic acid enhance drug transport by stabilizing human serum albumin (HSA), whereas ferulic acid induces structural changes in zein, optimizing drug delivery (Wang et al., 2022). Sinapic acid has been shown to stabilize protein structures during interactions with BSA and egg albumin, improving drug efficacy (Smyk, 2003). Also, the binding of caffeic and chlorogenic acids to caffeine has been shown to alter their fluorescence spectra and thermodynamic properties, potentially influencing the bioavailability and pharmacokinetics of these compounds (Belay et al., 2016a).

Drug–drug interactions and drug–protein interactions have also been studied using molecular docking. This approach provides critical insights into the binding modes, affinities, and stabilities of HCA-protein complexes, enhancing our understanding of the molecular forces that govern these interactions. For example, (Precupas et al., 2017) demonstrated that caffeic acid binds efficiently to human serum albumin, increasing its solubility and bioavailability, which in turn improves drug delivery. Similarly, (Tamayose et al., 2019) reported that chlorogenic acid inhibits the HIV-1 protease, emphasizing its antiviral properties. Additionally, (Nile et al., 2016) reported that ferulic acid derivatives inhibit xanthine oxidase and cyclooxygenase-2, reinforcing their anti-inflammatory potential.

## 1.2 Statement of the Problem

Despite numerous studies investigating the biological activities, such as anticancer, anti-inflammatory, antimicrobial, and antioxidant effects (Gao et al., 2018; Taştemur et al., 2023; Gurbuzer, 2021; Yang et al., 2021) and related molecules, there have been no specific reports on their solvent polarity and temperature effects on dipole moments, optical transition probabilities, photophysical and thermodynamic properties, and FA–protein, SA–protein, FA–CF, and SA–CF interactions using spectroscopic, DFT, TDDFT, and molecular docking. Solvatochromic investigations have yielded essential information on the structural transformations of these compounds, the reorganization of drug molecules in the presence of solvent molecules, variations in dipole moments between ground and excited states, and the associated electronic transition energies of these states (Melavanki et al., 2021). The photophysical properties provide extensive information regarding the electronic properties and potential phototoxicity of these drugs (Viola et al., 2004). The thermodynamic properties provide vital data about stability, Gibbs free energy, heat capacity, and entropy (Van Speybroeck et al., 2010).

The interaction between caffeine and various drugs represents an important area within pharmacology that requires further exploration. Investigating these interactions elucidated the pharmacological effectiveness, distribution, and metabolic activities of drugs, particularly in clinical settings where patients commonly take multiple medications simultaneously. Interactions between drugs and transporters play a crucial role in determining therapeutic safety and effectiveness, frequently resulting in diminished drug efficacy, heightened side effects, and uncertain therapeutic results. Understanding these dynamics through techniques such as fluorescence quenching and molecular docking is crucial for clarifying the binding affinities and interactions that are essential for optimizing drug (Carrillo and Benitez, 2000).

Therefore, this study aimed to investigate Solvatochromic effects, ground and excited state dipole moments, and optical transition probabilities, including oscillator strength, integrated absorption coefficients, and Einstein coefficients (A and B). The research also explored photophysical characteristics, such as fluorescence lifetimes, quantum yields, and the rates of radiative and nonradiative transitions. Fluorescence quenching methods were employed to determine thermodynamic parameters, including binding constants and quenching rate constants, across varying temperatures. FTIR provided insights into structural changes upon interaction with caffeine. To further elucidate the molecular characteristics, DFT was employed to optimize the structures and evaluate the geometric parameters, infrared spectra, thermodynamic properties, and electronic characteristics, such as the HOMO and LUMO energy levels. TDDFT predicted absorption and fluorescence spectra based on optimized geometries. Molecular docking were used to examine the interactions among FA-protein, SA-protein, FA-CF-protein, and SA-CF-protein to evaluate their potential anticancer activity.

## 1.3 Objectives of the Study

### 1.3.1 General Objective

The main aim of this study was to examine the solvatochromic effects, photophysical properties, fluorescence quenching, and molecular docking of FA and SA through both experimental and computational approaches.

### 1.3.2 Specific Objectives

The specific objectives of this research were

- + to calculate the dipole moments in both the ground and excited states of ferulic and sinapic acids through the analysis of absorption and emission spectra.
- + to determine the photophysical characteristics of ferulic and sinapic acids and their fluorescence quenching behavior in the presence of caffeine.
- + to investigate the effects of temperature and solvent polarity on the molecular, photophysical, thermodynamic, and chemical descriptors of ferulic and sinapic acid using DFT and TDDFT.
- + to predict the binding affinity and binding mode of FA-protein, SA-protein, FA-CF-protein, and SA-CF-protein using molecular docking.

## 1.4 Significance of the Study

Ferulic and sinapic acids are a class of HCAs found in common natural sources such as coffee, fruits, and vegetables. These compounds exhibit fluorescence, with emission wavelengths between 400 and 500 nm. FA and SA have various biological activities, such as anticancer, anti-inflammatory, and antimicrobial properties, which can be affected by solvent polarity, pH, temperature, drug concentration, and quenchers. These factors influence the photophysical and thermodynamic properties, including fluorescence behavior, solubility, and stability. Understanding the chemical reactivity and the effect of the environment factors on FA and SA is essential for optimizing their therapeutic potential and improving drug efficacy.

Fluorescence quenching studies are important in exploring the interactions between FA, SA, and drugs, providing insights into binding constants and the formation of complexes. These interactions can significantly affect the bioavailability and pharmacokinetics of drugs. Additionally, molecular docking simulations help further to understand the binding mechanisms at the molecular level, enabling the identification of the most stable interactions and potential side effects. In general, this study will:

- + provide a detailed understanding of the influence of solvent polarity on the electronic properties and structure of FA and SA, potentially affecting their biological activities.

- + contribute to the design of more effective drugs by revealing how these compounds interact with various drugs, such as caffeine and amoxicillin.
- + offer valuable insights into how FA and SA might be used in drug development and therapy by identifying potential drug interactions and improving their pharmacokinetic properties.
- + establish a basis for future exploration of other biologically active compounds, contributing to the pharmaceutical and medical fields by advancing drug design and improving therapeutic delivery systems.

## 1.5 Scope of the Study

This work investigated the Solvatochromic effects, photophysical properties, thermodynamic parameters, fluorescence quenching mechanisms, and molecular docking interactions of FA and SA using experimental, DFT/TDDFT, and molecular docking methods. The research centered on examining how solvent polarity affects the absorption and emission spectra, assessing the dipole moments in both ground and excited states, and evaluating optical transition probabilities across various solvents. The photophysical properties, including fluorescence intensity and quantum yield, were studied at various solvent polarities and sample concentrations. In addition, fluorescence quenching parameters, such as binding constants, quenching mechanisms, and energy transfer efficiencies, were analyzed to understand the interaction dynamics between FA, SA, and quenchers such as caffeine. The study also examined the thermodynamic parameters, focusing on the types of binding forces and how solvent polarity influences the binding affinity.

DFT and TDDFT were employed to complement the experimental findings to calculate the optimized molecular structures, transition dipole moments, oscillator strengths, and HOMO-LUMO energy gaps. These computational analyses provided insights into the electronic properties and charge distributions of FA and SA, helping to predict their molecular interactions. Molecular docking was also performed to evaluate the binding affinities, identify the binding sites, and analyze the forces involved in drug–protein interactions, offering a computational viewpoint to complement the experimental findings.

## 1.6 Organization of the Document

This dissertation is organized into five chapters. Chapter 1 provides an introduction to the study. Chapter 2 presents a literature review covering various FA and SA aspects. The molecular structures of these compounds, their biological activities, and their significance in medical applications are discussed. This review also examines how FA and SA interact with other drugs, potentially influencing their therapeutic effects. Additionally, the pharmacokinetics of caffeine, including its absorption in the human body and its interactions with other medications, have been explored. Fundamental theories, including Maxwell's equations and the time-dependent Schrödinger equation, are presented to provide a foundational

understanding of light–matter interactions. Phenomena such as absorption and fluorescence are also addressed, along with the Beer–Lambert law and optical transition probability. Solvatochromic effects are discussed, and quantum mechanical theories, including DFT and TDDFT, are covered to explain molecular properties and optical behavior. Furthermore, this chapter reviews the molecular docking techniques used to predict molecular interactions.

Chapter 3 outlines the materials and methods used in the study, beginning with the chemicals, solvents, and data analysis tools. It details the equipment, including UV–Vis, fluorescence, and FTIR spectroscopy, and describes the experimental procedures focusing on solvent polarity’s effect on FA and SA fluorescence behavior, optical transitions, and fluorescence quenching. The chapter concludes with an overview of the computational methods, including DFT and molecular docking, and the preparation of proteins and ligands for docking.

In Chapter 4, the results begin with the analysis of solvatochromic effects, including absorption and emission spectra, dipole moment estimation, and photophysical properties of FA and SA. The impact of concentration on these properties and fluorescence spectra is discussed. The chapter also examines the fluorescence quenching of FA and SA by caffeine using the Stern–Volmer equation, thermodynamic parameters, and UV–Vis and FTIR spectra. Quantum chemical calculations cover molecular structure optimization, thermodynamic analysis, and spectral analyses. The discussion concludes with molecular docking and affinity prediction, focusing on ligand–protein binding and amino acid interactions.

Finally, Chapter 5 presents the conclusion, recommendations, and suggestions for future research.

---

## LITERATURE REVIEW

---

This chapter provides a literature review related to FA and SA. Section 2.1 describes the molecular structures of FA and SA. In section 2.2, the biological activities of these compounds are discussed, showing their importance in medicine. Section 2.3 explores how FA and SA interact with other drugs, which may impact their therapeutic effects. Section 2.4 cover the pharmacokinetics of caffeine, including its absorption in the human body and its interactions with HCAs and other drugs. Section 2.5 introduces basic theories, including Maxwell's equations (2.5.1) and the time-dependent Schrödinger equation (2.5.3), providing a foundation for understanding light-matter interactions. The section also discusses phenomena like absorption (2.5.5) and fluorescence (2.5.6), as well as key concepts such as the Beer-Lambert law (2.5.5.1) and optical transition probability (2.5.5.2). Section 2.6 examines solvatochromic effects, whereas Section 2.7 focuses on quantum mechanical theories, including DFT and TDDFT (2.7.4), which are crucial for understanding molecular properties and optical behavior. Section 2.8 covers molecular docking methods used to predict binding affinities and interactions in drug-protein and drug-drug complexes.

### 2.1 Molecular Structure of FA and SA

Ferulic and sinapic acids ( Fig. 2.1) are a class of hydroxycinnamic acids derived from cinnamic acid. They are characterized by hydroxyl (-OH) groups attached to a benzene ring (Lorigooini et al., 2020). FA contains a hydroxyl group, a methoxyl group (-OCH<sub>3</sub>), and a trans-double bond, enhancing its antioxidant properties (Vinholes et al., 2015). The trans-double bond increases FA's ability to donate electrons, facilitating free radical scavenging and contributing to its anti-inflammatory and anticancer activities (Yang et al., 2021). SA , with an additional methoxyl group, has a more complex structure, improving its interactions with biological targets, including enzymes and receptors. This structural difference amplifies SA's antioxidant and anticancer properties compared to FA (Yang et al., 2021). The molecular structures of FA and SA are crucial in their biological activities, positioning them as promising compounds for different biological activities.

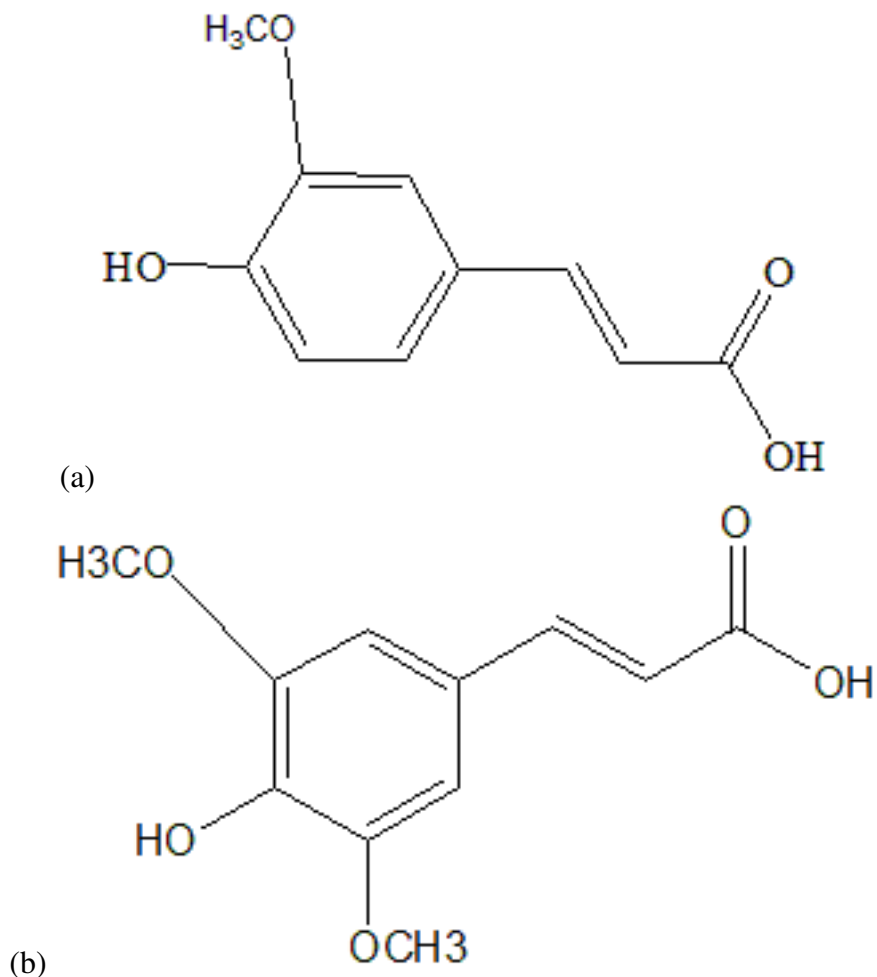


Figure 2.1: Structures of (a) ferulic and (b) sinapic acids.

## 2.2 Biological Activities of FA and SA

Ferulic and sinapic acids exhibit antioxidant (Yang et al., 2021), antimicrobial (Borges et al., 2013; Mandal et al., 2024), anticancer (Taştemur et al., 2023), anti-inflammatory (Papagiouvannis et al., 2024), and neuroprotective effects (Yin et al., 2019; Zare et al., 2015). Their actions are driven by hydroxyl and methoxy functional groups, which donate electrons to neutralize free radicals and interact with biological targets (Yang et al., 2021).

FA and SA exhibit antioxidant properties mainly by scavenging reactive oxygen species (ROS) and neutralizing free radicals, thereby safeguarding cells from oxidative harm (Yang et al., 2021). Ferulic acid, which is characterized by its phenolic structure with multiple hydroxyl groups, donates hydrogen atoms to free radicals, stabilizing them and preventing further oxidative chain reactions. This ability mitigates oxidative stress and enhances the effectiveness of other antioxidants, such as vitamins C and E, by restoring their reduced forms, which are crucial for maintaining cellular health (Zheng et al., 2024). Sinapic acid has similar antioxidant properties due to its phenolic structure, enabling it to effectively inhibit lipid peroxidation and reduce oxidative stress (Jalaludeen and Pari, 2011). (Shahid et al., 2022) previously demonstrated that sinapic acid effectively scavenges reactive oxygen

species (ROS) and neutralizes free radicals, thereby shielding cells from oxidative damage. This action alleviated symptoms of acetic acid-induced ulcerative colitis in rats, reducing inflammation, oxidative stress, and apoptosis in colonic tissue.

The antimicrobial activity of ferulic acid (Borges et al., 2013) and sinapic acid (Mandal et al., 2024) arises from their ability to inhibit the growth of various pathogenic microorganisms, including bacteria and fungi. Ferulic acid exhibits antimicrobial properties by disrupting microbial cell membranes and interfering with cellular functions due to its phenolic structure, which can disrupt enzymatic processes and lead to increased permeability of the cell wall. (Borges et al., 2013) reported that ferulic and gallic acids have strong antibacterial effects on pathogenic bacteria. They disrupt bacterial cell membranes, causing cell damage and lysis. (Mandal et al., 2024) reported that a guar gum nanoformulation infused with sinapic acid enhances wound care by providing strong antimicrobial and anti-inflammatory effects. Sinapic acid effectively combats pathogenic bacteria and reduces inflammation, promoting faster healing and lowering infection risk.

The anticancer activities of ferulic acid (Li et al., 2012) and sinapic acid (Taştemur et al., 2023) are attributed to their ability to modulate various cellular signaling pathways, induce apoptosis, and inhibit tumor growth through multiple mechanisms. (Li et al., 2012) reported that ferulic acid derivatives have strong anticancer effects by inducing apoptosis and inhibiting cancer cell growth. These compounds work by disrupting key signaling pathways involved in cell survival. These results indicate that ferulic acid derivatives are promising candidates for the development of new cancer therapies. Similarly, (Othman et al., 2023) reported that sinapic acid enhances the antitumor activity of cyclophosphamide by inducing apoptosis and inhibiting metastasis in cancer cells. Othman's work result revealed that sinapic acid works by activating apoptotic pathways and suppressing mechanisms that promote cancer spread. These findings suggest that combining sinapic acid with cyclophosphamide could improve cancer treatment outcomes.

The anti-inflammatory activity of ferulic acid and sinapic acid is associated primarily with their ability to inhibit proinflammatory mediators and pathways thereby mitigating inflammation in various biological systems (Papagiouvannis et al., 2024). Ferulic acid has been shown to suppress the expression of inflammatory cytokines such as TNF- $\alpha$  and IL-6, effectively reducing the inflammatory response in conditions such as arthritis and other inflammatory diseases. It achieves this through the inhibition of nuclear factor-kappa B (NF- $\kappa$ B), a key transcription factor involved in the inflammatory process, which reduces the transcription of target genes associated with inflammation (Adeyi et al., 2023). (Shahid et al., 2022) also reported that sinapic acid helps reduce ulcerative colitis in rats by lowering inflammation and oxidative stress. It works by neutralizing free radicals and decreasing the levels of proinflammatory markers. These findings suggest that sinapic acid could be a promising treatment for ulcerative colitis.

Neuroprotective activity of FA and SA is linked to their capacity to mitigate oxidative stress and inflammation, both of which play key roles in the progression of neurodegenerative

diseases (Yin et al., 2019; Zare et al., 2015). (Di Giacomo et al., 2022) reported that ferulic acid has neuroprotective effects on Alzheimer's disease by reducing oxidative stress and inflammation in neuronal cells. Ferulic acid works by scavenging free radicals and inhibiting neuroinflammatory pathways, ultimately promoting neuronal survival. Additionally, (Dong and Huang, 2022) reported that ferulic acid possesses significant neuroprotective and anti-depressive properties by reducing oxidative stress and inflammation in neuronal cells. Ferulic acid works by scavenging free radicals and modulating neurotransmitter levels, which improves mood and cognitive function. On the other hand, (Zare et al., 2015) reported that sinapic acid has neuroprotective effects on a 6-hydroxydopamine-induced hemi-parkinsonian rat model by reducing oxidative stress and inflammation.

## 2.3 Interactions of FA and SA with Other Drugs

Ferulic and sinapic acids can interact with several common drugs and vitamins, including aspirin (Thakkar et al., 2014), clopidogrel (Li et al., 2011), metformin (Paul et al., 2022), vitamin C, and vitamin E (Lin et al., 2005). These interactions occur due to the overlapping pharmacological effects of FA and SA and these drugs, which are related primarily to their antioxidant, anti-inflammatory, and anticoagulant properties.

Aspirin (Thakkar et al., 2014) and clopidogrel (Li et al., 2011) are antiplatelet medications that inhibit platelet aggregation and reduce the risk of thrombus formation. When used in conjunction with ferulic acid, which also has mild anticoagulant effects, these drugs may enhance overall antiplatelet activity, providing additional cardiovascular protection. However, this synergy raises the risk of bleeding, necessitating close monitoring during coadministration. Additionally, metformin, an antidiabetic drug, may enhance the beneficial effects of ferulic acid. With ferulic acid showing promise in improving insulin sensitivity and glucose metabolism, its combined use could synergistically improve glycemic control, although monitoring glucose levels is essential to avoid potential hypoglycemia (Paul et al., 2022). Ferulic acid interacts with antioxidants such as vitamin C and vitamin E owing to their shared antioxidant properties. This interaction can increase the efficacy of these vitamins through increased free radical scavenging capabilities, leading to improved overall antioxidant protection. However, excessive consumption of vitamin C or vitamin E could mask the pharmacological effects of ferulic acid and alter its bioavailability (Lin et al., 2005).

Sinapic acid interacts with several common drugs, particularly those used in oncology and psychiatry, including poziotinib (Zargar et al., 2020), ibrutinib (Iqbal et al., 2022), and doxorubicin (Bin Jardan et al., 2020), owing to its biochemical properties and pharmacological effects. Poziotinib, a targeted therapy for specific cancer types, may experience altered efficacy when used in conjunction with sinapic acid. Given the antioxidant properties of SA, it could enhance the therapeutic effects of poziotinib while potentially protecting normal cells from oxidative damage, which is a common concern with cancer treatments (Zargar et al., 2020). Similarly, ibrutinib, a Bruton's tyrosine kinase inhibitor for B-cell malignancies, may benefit from the anti-inflammatory of SA, potentially improving its therapeutic

outcomes while reducing associated side effects (Iqbal et al., 2022). The interaction with doxorubicin, a well-known chemotherapeutic agent, is particularly important, as sinapic acid might mitigate some of its cardiotoxic effects by offering protection against oxidative stress, thus enhancing the safety profile of doxorubicin during treatment (Bin Jordan et al., 2020).

## 2.4 Pharmacokinetics of Caffeine and Its Interaction with Other Drugs

Caffeine is a widely recognized pharmacologically active substance found in commonly consumed beverages such as coffee (Burdan, 2015) and tea (Ghosh et al., 2013). The molecular structure of caffeine, shown in Fig. 2.2, contains three methyl groups (-CH<sub>3</sub>) and a carbonyl groups (=O) attached to nitrogen atoms within the xanthine backbone. These functional groups contribute to caffeine's stimulant effects on the body. Upon consumption, caffeine increases heart rate, promotes vasodilation, and raises the levels of free fatty acids and glucose. Caffeine stimulates the nervous system, enhancing brain blood and promoting alertness (Krishna Sri and Padmavathy, 2018). According to recent research, a daily intake of up to 400 mg of caffeine is considered safe for most healthy adults (Roberts, 2021).

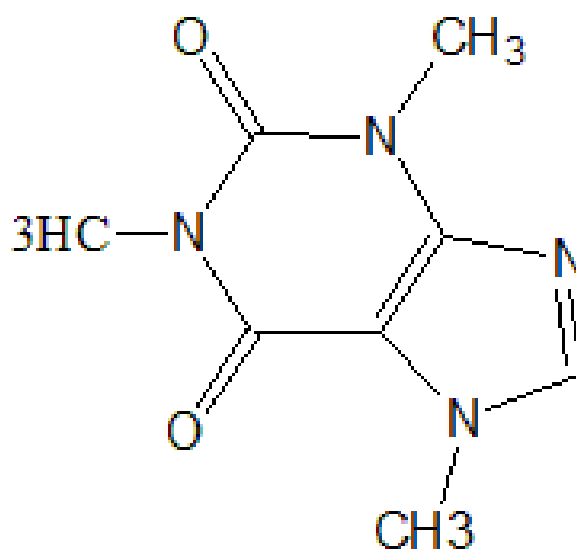


Figure 2.2: Molecular structure of caffeine.

### 2.4.1 Pharmacokinetics of Caffeine in the Human Body

Caffeine exhibits a pharmacokinetic pathway involving four key processes: absorption into the bloodstream, distribution to organs and tissues, metabolism primarily in the liver, and elimination through the kidneys.

Absorption of caffeine occurs rapidly in the gastrointestinal tract, with peak plasma concentrations typically reached within 15 to 120 minutes after ingestion. The timing of this absorption can be influenced by various factors, such as the source of caffeine—whether it comes from coffee (Burdan, 2015), tea (Ghosh et al., 2013), or energy drinks (Mihaiescu et al., 2024) and individual physiological factors like metabolic rate and gut health. Caffeine's solubility in both aqueous and lipid environments ensures its efficient absorption through the stomach and intestinal walls. This quick bioavailability allows caffeine to enter the bloodstream rapidly, setting the stage for its physiological effects (Reddy et al., 2024).

Caffeine is widely distributed throughout the body and can cross the blood-brain barrier due to its lipophilic nature (Saraiva et al., 2023). This allows caffeine to reach various tissues, with particularly high concentrations in the central nervous system, where it exerts stimulant effects. The volume of distribution for caffeine typically ranges from 0.5 to 0.7 L/kg, indicating its effective accumulation in target tissues. This extensive distribution contributes to its effects on physical performance (Panyam and Patil, 2008).

Caffeine is mainly metabolized in the liver by cytochrome P450 enzymes. This process generates three primary metabolites: paraxanthine, theobromine, and theophylline, each contributing to caffeine's overall effects on the body (Acheson et al., 2004). The speed of caffeine metabolism is affected by age, genetics, and lifestyle choices like smoking or diet. These variables can either speed up or slow down metabolism, making it important to consider individual characteristics when assessing caffeine consumption (dePaula and Farah, 2019).

The elimination half-life of caffeine typically ranges from 3 to 7 hours in healthy adults, though it can be longer in pregnant women, neonates, and individuals with certain liver conditions (Reddy et al., 2024). Caffeine and its metabolites are mainly excreted through the kidneys, making renal function crucial for caffeine clearance. The rate of elimination is affected by hydration status, kidney health, and medications. A clear understanding of these factors helps optimize caffeine consumption, reduce adverse effects, and identify populations more sensitive to caffeine's effects (de Carvalho et al., 2024).

### **2.4.2 Binding of Caffeine with Other Drugs**

Caffeine forms stable complexes with hydroxycinnamic acids such as caffeic acid (CA) and chlorogenic acid (CGA) through non-covalent interactions, significantly influencing their photophysical and thermodynamic properties. Fluorescence quenching experiments reveal a static quenching mechanism, indicating ground-state complex formation between caffeine and both CA and CGA. This interaction alters the fluorescence spectra, with decreased intensity and red-shifted peaks, suggesting electronic energy transfer. UV-Vis spectrometry further corroborates this binding, displaying bathochromic shifts in the absorption maxima of CA and CGA in the presence of caffeine, indicative of molecular interactions. Thermodynamic analysis shows negative Gibbs free energy, suggesting that the binding process is spontaneous, with hydrogen bonding and hydrophobic forces playing dominant

roles. FTIR spectroscopy supports this by revealing shifts in the vibrational frequencies of functional groups, confirming the involvement of these groups in hydrogen bonding. These interactions may modulate the antioxidant properties, stability, and bioavailability of CA and CGA, potentially impacting their therapeutic efficacy (Belay et al., 2016a).

Caffeine also exhibits strong binding interactions with nicotinamide, levofloxacin, and norfloxacin, influencing their fluorescence properties, thermodynamic parameters, and binding forces. For nicotinamide, caffeine induces static fluorescence quenching, demonstrating the formation of a stable complex driven by hydrogen bonding and van der Waals interactions. UV-Vis spectrometer reveals spectral shifts, confirming electronic perturbation caused by caffeine. The negative Gibbs free energy values obtained highlight the spontaneity of this binding, which may affect nicotinamide's solubility and pharmacokinetic profile (Abraha and Belay, 2023). Similarly, for levofloxacin and norfloxacin, caffeine also acts as a static quencher of fluorescence, with  $\pi$ - $\pi$  stacking interactions and hydrogen bonding providing stability to the formed complexes. Changes in absorption spectra further validate these interactions, revealing notable disruptions in the electronic environments of the drugs. Thermodynamic analyses show that these bindings are enthalpically driven, emphasizing the role of hydrogen bonding and hydrophobic forces. Such molecular interactions could significantly modify the photophysical properties, antibacterial efficacy, and pharmacological profiles of these drugs (Woldegiorges et al., 2022).

## 2.5 Basic Spectroscopic Theory

Basic spectroscopic theory explores the interaction between light and matter, offering valuable insights into molecular structures. It is grounded in Maxwell's equations, governing the behavior of electromagnetic fields, and the time-dependent Schrödinger equation, modeling molecular responses to light. The theory also examines key phenomena like absorption and fluorescence, essential for understanding molecular energy transitions and enabling advanced spectroscopic analysis.

### 2.5.1 Maxwell's Equations and Wave Equations

Maxwell's equations are a set of four fundamental equations that describe the behavior of electric and magnetic fields and their interactions with matter. They form the foundation of classical electromagnetism and electromagnetic wave theory (Becker and Sauter, 1982). The differential form of Maxwell's equations are given by (Frankel, 1974; Langer et al., 2019).

$$\vec{\nabla} \times \vec{E} = -\frac{\partial \vec{B}}{\partial t}, \quad (2.1)$$

$$\vec{\nabla} \times \vec{H} = \frac{\partial \vec{D}}{\partial t} + \vec{J} \quad (2.2)$$

$$\vec{\nabla} \cdot \vec{D} = \rho, \quad (2.3)$$

$$\vec{r} \cdot \vec{B} = 0, \quad (2.4)$$

The response of the material medium to an external field is described by

$$\vec{D} = \epsilon_0 \vec{E} + \vec{P}, \quad (2.5)$$

and

$$\vec{B} = \mu_0(\vec{H} + \vec{M}), \quad (2.6)$$

where  $\vec{E}$  is the electric field strength,  $\vec{D}$  is the electric displacement field, and  $\vec{B}$  is the magnetic induction.  $\rho$  represents the electric charge density (charge per unit volume),  $\vec{P}$  is the electric dipole moment per unit volume, or polarization,  $\vec{M}$  is the magnetic dipole moment per unit volume, or magnetization, and  $\vec{J}$  is the current density (electric current per unit area).  $\epsilon_0$  and  $\mu_0$  are the permittivity and permeability of vacuum, respectively.

In non-magnetic and non-conducting media, there are no free charges, currents, or magnetic dipoles. Thus, the volume densities of electric charge ( $\rho$ ), electric current density ( $\vec{J}$ ), and magnetization ( $\vec{M}$ ) are zero (Schwab, 2012). By substituting Eqs. (5) and (6) into Eqs. (1) through (4), Maxwell's equations are reformulated as follows

$$\vec{r} \cdot \vec{E} = -\mu_0 \frac{\partial \vec{H}}{\partial t}, \quad (2.7)$$

$$\vec{r} \cdot \vec{H} = \epsilon_0 \frac{\partial \vec{E}}{\partial t} + \frac{\partial \vec{P}}{\partial t}, \quad (2.8)$$

$$\vec{r} \cdot \vec{E} = 0, \quad (2.9)$$

$$\vec{r} \cdot \vec{H} = 0 \quad (2.10)$$

The general wave equation for the electric field can be derived from Maxwell's equations by taking the curl of Eq. (2.7) and substituting the time derivative of Eq. (2.8), resulting in the following

$$\vec{r} \cdot (\vec{r} \cdot \vec{E}) + \frac{1}{c^2} \frac{\partial^2 \vec{E}}{\partial t^2} = \mu_0 \frac{\partial^2 \vec{P}}{\partial t^2} \quad (2.11)$$

By using a general vector calculus identity, the first term on the left-hand side of Eq. (2.11) can be expressed

$$\vec{r} \cdot (\vec{r} \cdot \vec{E}) = \vec{r} \cdot (\vec{r} \cdot \vec{E}) - \vec{r}^2 \vec{E} \quad (2.12)$$

Substituting Eq. (2.12) into Eq. (2.11) yields the general wave equation for the electric field

$$\nabla^2 \vec{E} - \nabla(\nabla \cdot \vec{E}) = \frac{1}{c^2} \frac{\partial^2 \vec{E}}{\partial t^2} = \frac{1}{\epsilon_0 c^2} \frac{\partial^2 \vec{P}}{\partial t^2}, \quad (2.13)$$

and

$$\epsilon_0 \mu_0 = \frac{1}{c^2}, \quad (2.14)$$

where  $c$  represents the velocity of light in vacuum ( $2.99792458 \times 10^8$  m/s). In non-conducting media, such as a neutral isotropic dielectric, the polarization term plays a significant role. This term helps explain various optical phenomena, including dispersion and absorption. Our focus will specifically be on transverse fields, also known as solenoidal fields

$$\nabla \cdot \vec{E} = 0 \quad (2.15)$$

For solenoidal fields, Eq. (2.13) fulfills the wave equation

$$\nabla^2 \vec{E} = \frac{1}{c^2} \frac{\partial^2 \vec{E}}{\partial t^2} = \frac{\partial^2 \vec{p}}{\epsilon_0 \epsilon^2 \partial t^2} \quad (2.16)$$

In the absence of a medium ( $\vec{p} = 0$ ), the right-hand side of Eq. (2.16) becomes zero, leading to the "homogeneous" wave equation.

$$\nabla^2 \vec{E} = \frac{1}{c^2} \frac{\partial^2 \vec{E}}{\partial t^2} = 0 \quad (2.17)$$

For a wave propagating in the  $z$ -direction in free space, the solution to the wave equation is given by

$$\vec{E}(z, t) = E_0 \cos(\omega t - kz), \quad (2.18)$$

where  $k$  is wave vector velocity given by

$$k = \frac{\omega}{c} \quad (2.19)$$

and phase velocity ( $v_p$ )

$$v_p = \frac{\omega}{k} = c \quad (2.20)$$

## 2.5.2 Light Propagation in Isotropic Dielectrics

Isotropic dielectrics are materials that have the same dielectric properties (such as permittivity) in all directions. In isotropic dielectrics, the polarization induced by light can be described using the Lorentz model. This model describes the interaction between light and matter, incorporating solenoidal effects. When an atom or molecule absorbs light, the electron oscillates around its equilibrium position (Vanzo et al., 2015). Mathematically, it is expressed using Newton's equation as follows

$$m \frac{d^2 \vec{x}}{dt^2} = -e \vec{E}(R, t) - K \vec{x}, \quad (2.21)$$

for electron,  $e$  is charge,  $\vec{E}(R, t)$  represents the electric field at position  $R$  and time  $t$ ,  $K$  is the spring constant, and  $\vec{x}$  is the displacement of the electron from its equilibrium. Applying an electric field to a dielectric material displaces each electron by a distance  $\vec{x}$  from its equilibrium position, creating a dipole moment  $\vec{P}$  for each atom. With an atomic density of  $N$ , the total polarization density in the material is the product of  $N$  and the individual dipole moment  $\vec{P}$  (Patsidis and Psarras, 2024). Mathematically it expressed as

$$\vec{P} = N\vec{P} = Ne\vec{x} \quad (2.22)$$

The electron oscillator model ties Maxwell's equations with Newton's law of motion. Solving these equations reveals the interaction between light and matter. Additionally, if atoms or molecules absorb radiation as it passes through the material, the strength of the electromagnetic radiation is reduced (Parker, 2000). This absorption can be explained by the Lorentz electron oscillator model (Dutta et al., 2022) as in Eq (2.21).

The classical damped harmonic oscillators, caused by the bound electron, modify Newton's force Eq. (2.21) as follows (Bocko and Onofrio, 1996)

$$m \frac{d^2 \vec{x}}{dt^2} = e\vec{E}(R, t) - K\vec{x} + \vec{F}_{\text{fric}} \quad (2.23)$$

The frictional damping force is proportional to the velocity  $\vec{F}_{\text{fric}} = -\gamma\vec{v}$ , and  $\gamma$  is the proportionality constant.  $\vec{v} = \frac{d\vec{x}}{dt}$  represents the velocity. From Newton's second law, force is related to mass and acceleration. Rewrite the damping force as  $\vec{F}_{\text{fric}} = -m\gamma\frac{d\vec{x}}{dt}$  and substituting into Eq. (2.23)

$$m \frac{d^2 \vec{x}}{dt^2} + m\gamma \frac{d\vec{x}}{dt} + K\vec{x} = e\vec{E}(R, t) \quad (2.24)$$

In Eq. (2.24),  $m\gamma$  is the proportionality constant that relates the frictional damping force to the velocity of the electron. To find the trial solution of Eq. (2.24), we assume that the electric field varies harmonically with time and that the electron's motion also follows a similar harmonic time dependence,  $\vec{x} = e^{i\omega t}$ . Substituting  $\vec{x} = e^{i\omega t}$  into Eq. (2.24) gives

$$(m\omega^2 + i\omega m\gamma + K)\vec{x} = e\vec{E}(R, t) \quad (2.25)$$

Substitute Eq. (2.25) into Eq. (2.22)

$$\vec{P} = \frac{Ne^2}{m\omega^2 + i\omega m\gamma + K} \vec{E}(R, t) \quad (2.26)$$

Using  $K = m\omega_0^2$  and factor out the  $m$  from the denominator, Eq. (2.26) can be rewritten

$$\vec{P} = \frac{Ne^2/m}{\omega^2 - \omega_0^2 + i\omega\gamma} \vec{E}(R, t) \quad (2.27)$$

Polarization can also be expressed in terms of the dielectric constant or susceptibility

$$\vec{P} = \epsilon_0(\epsilon_r - 1)\vec{E}(R, t) = \epsilon_0(\epsilon_r - 1)\vec{E}(R, t), \quad (2.28)$$

where  $\epsilon_0$  is the permittivity of free space.  $\epsilon_r$  is the relative permittivity (dielectric constant) of the material.  $\chi$  is the electric susceptibility. The relative dielectric constant ( $\epsilon_r$ ) is related to the refractive index  $n$  by

$$n = \sqrt{\epsilon_r} \quad (2.29)$$

By substituting Eq. (2.29) into Eq. (2.28) and comparing it with Eq. (2.27), we get

$$n^2 - 1 = \frac{Ne^2}{\epsilon_0 m(\omega^2 - \omega_0^2 - i\gamma\omega)} \quad (2.30)$$

Using the approximation  $n^2 - 1 \approx 2(n - 1)$ , Eq. (2.30) simplifies to

$$n = 1 + \frac{Ne^2}{2\epsilon_0 m(\omega^2 - \omega_0^2 - i\gamma\omega)} \quad (2.31)$$

Eq. (2.31) can be expressed in terms of its real and imaginary components as follows.

$$n = n' - i\kappa' \quad (2.32)$$

For an electromagnetic wave traveling in the  $z$ -direction

$$\vec{E} = E_0 \exp[i(\omega t - kz)] \quad (2.33)$$

The complete expression for the electric field then becomes

$$E = E_0 e^{-k_0 \kappa z} e^{i(\omega t - k_0 n z)} \quad (2.34)$$

In Eq. (2.34), the imaginary part  $\kappa$  of the complex refractive index  $n$  represents the absorption of the electromagnetic wave. At the penetration depth, the amplitude of  $E_0 e^{-k_0 \kappa z}$  reduces to  $\frac{1}{e}$  of its initial value at  $z = 0$ . The real part  $n_0(\omega)$  corresponds to the dispersion of wave. It describes how the phase velocity  $v(\omega) = \frac{c}{n(\omega)}$  depends on the frequency. The intensity  $I$ , proportional to  $E^2$ , decreases as

$$I = I_0 e^{-2\kappa k_0 z} = I_0 e^{-\alpha z} \quad (2.35)$$

The wave number  $k_0$  in vacuum is given by  $k_0 = \frac{2\pi}{\lambda_0}$  where  $\lambda_0$  is the wavelength in vacuum. The absorption coefficient  $\alpha = 2k_0 \kappa = \frac{4\pi\kappa}{\lambda_0}$  is proportional to the imaginary part of the complex refractive index. The terms  $\alpha$  and  $n'$ , as the real and imaginary parts, are given by

$$\alpha = \frac{Ne^2 \omega_0 \gamma \omega}{c \epsilon_0 m [(\omega_0^2 - \omega^2)^2 + \gamma^2 \omega^2]} \quad (2.36)$$

$$n^{\theta} = 1 + \frac{Ne^2(\omega_0^2 - \omega^2)}{2\epsilon_0 m [(\omega_0^2 - \omega^2)^2 + \gamma^2 \omega^2]} \quad (2.37)$$

Eqs. (2.36) and (2.37) represent the Kramers-Kronig dispersion relations, which describe the absorption and dispersion of the complex refractive index.

### 2.5.3 Time-Dependent Schrodinger Equation

This section derives the transition dipole moment of a molecule from the time-dependent Schrödinger equation using a semiclassical approach. In semiclassical approach, the atom is treated quantum mechanically, while the incident radiation is modeled as a classical electromagnetic plane wave (Belay, 2011). To simplify the analysis, we limit the system to two states,  $|jK\rangle$  and  $|jm\rangle$ , with energies  $E_k$  and  $E_m$ , respectively. When a system initially in a stationary state with a definite energy is exposed to electromagnetic radiation for a finite duration, it transitions to another stationary state (Zel'Dovich, 1975). If  $\hat{H}^0$  represents the Hamiltonian of the molecular system without the radiation field, the time-independent equation is given by (Carlström et al., 2022)

$$\hat{H}^0 \psi_k^{(0)}(x) = E_k^{(0)} \psi_k^{(0)}(x) \quad (2.38)$$

Where  $E_k(0)$  and  $\psi_k(0)(x)$  are the energy and wave function for the unperturbed system, respectively. On the other hand, if  $\hat{H}^{\theta}(t)$  represents the Hamiltonian describing the interaction between the system and radiation, the time-dependent Schrödinger equation can be written to show how the system's state evolves over time (Kunstatter et al., 2020)

$$i\hbar \frac{\partial}{\partial t} \psi(x, t) = \hat{H}^{\theta} \psi(x, t) \quad (2.39)$$

During the time interval, the total Hamiltonian is the sum of the unperturbed Hamiltonian of the isolated atom and the perturbation operator (Durand and Malrieu, 1987).

$$i\hbar \frac{\partial}{\partial t} \psi(x, t) = \left( \hat{H}^0 + \hat{H}^{\theta} \right) \psi(x, t) \quad (2.40)$$

where the general state function is represented as a linear combination of

$$\psi(x, t) = \sum c_k \exp(-iE_k^{(0)}t/\hbar) \psi_k^{(0)}(x) \quad (2.41)$$

For two-level systems, Eq. (2.41) simplifies to

$$\psi(x, t) = c_k(t) \psi_k^{(0)} e^{-iE_k t/\hbar} + c_m(t) \psi_m^{(0)} e^{-iE_m t/\hbar} \quad (2.42)$$

The coefficients  $c_k(t)$  and  $c_m(t)$  represent the time-dependent probability amplitudes for the two atomic states  $k$  and  $m$ . This indicates that the term  $|c_k(t)|^2$  provides the likelihood of locating the system in the state  $|jK\rangle$  at time  $t$ . Additionally, the equation  $|c_k(t)|^2 + |c_m(t)|^2 = 1$  remains valid at all times  $t$ , assuming that transitions to other levels are disregarded. By

substituting Eq (2.41) into Eq (2.40), we obtain

$$i\hbar \frac{d}{dt} \left( \sum c_k(t) \exp\left( i \frac{E_k^{(0)} t}{\hbar} \right) \psi_k^{(0)} \right) = \left( \hat{H}^0 + \hat{H}^{\theta} \right) \sum c_k \exp\left( i \frac{E_k^{(0)} t}{\hbar} \right) \psi_k^{(0)} \quad (2.43)$$

where the relation in Eq. (2.38) has been used to cancel equal terms on both sides. Further multiplication by the conjugate with  $\psi_n$  (where  $n = k, m$ ) and spatial integration results in the following two equations

$$\frac{dc_k(t)}{dt} = \frac{i}{\hbar} \left\{ c_k(t) \hat{H}_{kk} + c_m(t) \hat{H}_{km}^{\theta} e^{i \frac{(E_k - E_m)t}{\hbar}} \right\} \quad (2.44)$$

and

$$\frac{dc_m(t)}{dt} = \frac{i}{\hbar} \left\{ c_m(t) \hat{H}_{mm}^{\theta} + c_k(t) \hat{H}_{km}^{\theta} e^{i \frac{(E_k - E_m)t}{\hbar}} \right\} \quad (2.45)$$

with the spatial integral

$$\hat{H}_{km}^{\theta} = \int \psi_k \hat{H}_0 \psi_m d\tau = e \vec{E} \int \psi_k \vec{r} \psi_m d\tau = \vec{E} \cdot \vec{\mu}_{km} \quad (2.46)$$

$$\vec{\mu}_{km} = \vec{\mu}_{mk} = e \int \psi_k \vec{r} \psi_m d\tau \quad (2.47)$$

## 2.5.4 Interaction of EMR with Molecular System

When electromagnetic radiation interacts with a molecule, the oscillating electric field can disturb the molecule's energy (Salam, 2015). The  $\vec{x}$  component of the radiation at the molecule's position is described by Eq (2.48)

$$\vec{E}_x = \vec{E}_x^{(0)} \frac{(e^{i\omega t} + e^{-i\omega t})}{2} \quad (2.48)$$

This field can interact with the dipole moment, causing a change in energy. It is responsible for the change in the Hamiltonian when radiation is applied to the system. Therefore, the change in the Hamiltonian is given by:

$$\hat{H}^{\theta} = \vec{E}_x \cdot \vec{\mu}_x \quad (2.49)$$

Substituting Eq. (2.48) into Eq. (2.49), the perturbed Hamiltonian is expressed as

$$\hat{H}^{\theta} = \vec{E}_x^{(0)} \frac{(e^{i\omega t} + e^{-i\omega t})}{2} \mu_x \quad (2.50)$$

Before substituting into Eq. (2.44) and Eq. (2.45), a weak-field approximation is applied. In this approximation, at  $t = 0$ , the atoms are assumed to be in the lower state, so  $c_k(t) = 1$  and  $c_m(t) = 0$ . Additionally, it is assumed that the field amplitude is small for  $t < T$ , and the population of the excited state  $E_m$  remains much smaller than that of the ground state

$E_k$ . With these assumptions, the first approximation of Eq. (2.44) and (2.45) becomes

$$\frac{dc_k(t)}{dt} = 0 \quad (2.51)$$

$$\frac{dc_m}{dt} = \frac{i}{2} E_x^{(0)} \hbar \psi_m^0 j \mu_x j \psi_k^0 i [e^{it(\omega + \omega_{mk})} + e^{it(\omega_{mk} - \omega)}] \quad (2.52)$$

where,

$$j \mu_{xkm} j = \int \hbar \psi_m^0 j \mu_x j \psi_k^0 i > dx \quad (2.53)$$

With the initial condition of  $c_k(0) = 1$  and  $c_m(0) = 0$ , the integration over the time interval from 0 to  $t$  will give

$$c_k(t) = 0 \quad (2.54)$$

$$c_m(t) = \frac{E_x^{(0)} j \mu_{xkm} j^2}{2} \left[ \frac{e^{it(E_m - E_k - \hbar \nu)}}{E_m - E_k - \hbar \nu} + \frac{e^{it(E_m - E_k + \hbar \nu)}}{E_m - E_k + \hbar \nu} \right] \quad (2.55)$$

The process of interest is the transition of the system from the lower energy level  $k$  to the higher energy level  $m$ . In this case, the denominator of the first term in Eq. (2.55) becomes zero when the radiation frequency satisfies the condition

$$\hbar \nu = E_m - E_k \quad (2.56)$$

For the emission process, the second term becomes significant since the energy of state  $m$  is higher than that of state  $k$ . Thus, with the assumed energy level structure, Eq. (2.55) simplifies to

$$c_m(t) = \frac{E_x^{(0)} j \mu_{xkm} j^2}{2} \left[ \frac{e^{it(E_m - E_k - \hbar \nu)}}{E_m - E_k - \hbar \nu} \right] \quad (2.57)$$

The transition probability for absorption from the  $k$ -state to the  $m$ -state is given by

$$c_m(t)c_k(t) = E_0^2 j \mu_{xkm} j^2 \left( \frac{\sin^2 \left( \frac{(E_m - E_k - \hbar \nu)t}{2\hbar \nu} \right)}{(E_m - E_k - \hbar \nu)^2} \right) \quad (2.58)$$

The transition probabilities are proportional to this energy density. When considering incoming radiation with multiple frequencies, we replace  $u$  with the energy density in the frequency range  $d\omega$ , meaning  $u = \rho(\omega) d\omega$ , and then integrate over the frequency spectrum. Since the term in the bracket is sharply peaked at  $\omega = \omega_{mk}$  while  $\rho(\omega)$  changes slowly, we can take  $\rho(\omega)$  outside the integral.

$$c_m(t)c_k(t) = \frac{1}{2\rho(\omega)} E_0^2 j \mu_{xkm} j^2 \int \frac{\sin^2 \left( \frac{(\omega_{mk} - \omega)t}{2} \right)}{(\omega_{mk} - \omega)^2} d\omega \quad (2.59)$$

After integration, Eq. (2.59) becomes

$$c_m(t)c_k(t) = \frac{\pi \rho(\omega)}{\epsilon_0^2} j \mu_{xkm} j^2 t \quad (2.60)$$

Eq.(2.60) gives the probability that a molecule will have a transition to state  $m$  after being illuminated for a time  $t$ . To integrate Eq. (2.59), we apply the following integration technique:

$$\int \frac{\sin^2(ax)}{x^2} dx = a \quad (2.61)$$

The number of transitions to state  $m$  per second, or the rate of transition probability, becomes

$$\frac{d(c_m c_m)}{dt} = \frac{\pi \rho(\omega)}{\epsilon_0^{-2}} j\mu_{xkm} j^2 \quad (2.62)$$

For isotropic radiation, the three components of the radiation dipole interaction are identical, allowing us to express it as follows:

$$\frac{d(c_m c_m)}{dt} = \frac{\pi \rho(\omega)}{3\epsilon_0^{-2}} j\mu_{km} j^2 \quad (2.63)$$

This represents the rate at which the system changes due to absorption under the perturbation caused by the electric field of the radiation. It is commonly expressed using Einstein's coefficient of induced absorption and Eq.(2.63) becomes (Salam, 2011)

$$\frac{d(c_m c_m)}{dt} = B_{km} \quad (2.64)$$

## 2.5.5 Phenomenon of Absorption

Absorption is when a substance captures or takes in energy, matter, or light. This can occur through various processes, such as a material soaking up light or absorbing heat. This occurs when waves, such as electromagnetic radiation (light, sound, etc.), or particles, interact with a medium and are retained, rather than reflected or transmitted. Absorption is the process in which molecules capture light energy, causing electrons to move from the ground state to an excited state. This transition happens when a photon with energy matching the gap between these states is absorbed. The Beer–Lambert law and transition probability are applied to quantify the likelihood of these electronic transitions following photon absorption (Douglas et al., 2013).

### 2.5.5.1 Electronic Transition

Electron transition occurs when an electron absorbs energy, typically from UV or visible light, and moves from a lower energy molecular orbital to a higher one (Wu and Zhu, 2013). Fig. 2.3 shows energy level diagrams with electronic transitions.  $\sigma \rightarrow \sigma^*$  transition occurs when an electron is excited from a bonding  $\sigma$  orbital to an anti-bonding  $\sigma^*$  orbital (Maity, 2002). This type of transition typically happens in organic molecules like alkanes or molecules with single bonds, where the electrons are relatively tightly bound in the bonding orbitals. This transition requires high-energy photons, typically in the far UV range (with wavelengths shorter than 200 nm), because the energy gap between the bonding and anti-bonding  $\sigma$ -orbitals is large. This transition weakens the molecular bonds, making the

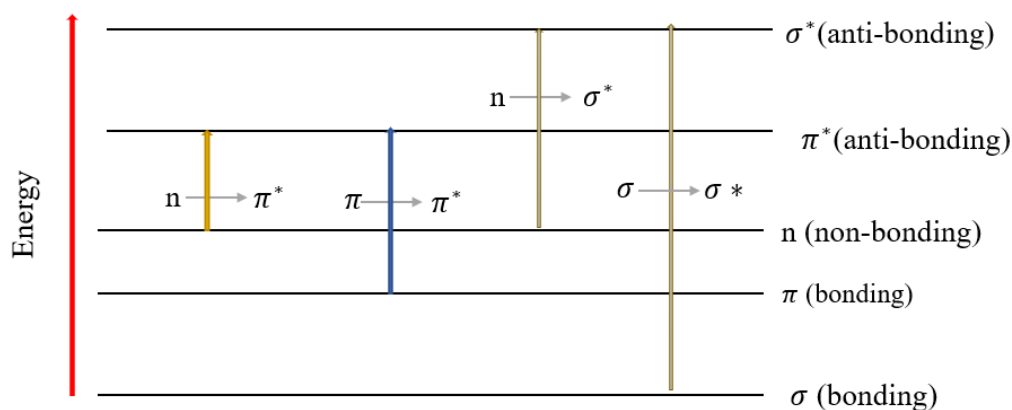


Figure 2.3: Energy level diagrams with electronic transitions.

molecule more reactive. Peak shifts are observed when electron-withdrawing groups (such as halogens or nitro groups) are attached to the molecule. These groups increase the energy gap between the  $\sigma$  and  $\sigma^*$  orbitals, requiring absorption of higher-energy photons (blue shift). In contrast, electron-donating groups (such as alkyl groups) decrease the energy gap, resulting in a red shift (longer wavelengths) as the transition becomes easier with less energy (Pathak et al., 2005).

$\pi \rightarrow \pi^*$  transition involves the promotion of an electron from a bonding  $\pi$ -orbital (which occurs in conjugated systems, such as double bonds or aromatic rings) to an anti-bonding  $\pi^*$ -orbital. This transition is common in organic molecules such as alkenes, dienes, and aromatic compounds like benzene. The energy gap between the  $\pi$  and  $\pi^*$  orbitals is smaller than the gap for  $\sigma \rightarrow \sigma^*$  transitions, which makes this transition accessible to photons in the UV-visible region (between 200-400 nm). The  $\pi \rightarrow \pi^*$  transition is responsible for the colored nature of many organic compounds, as they absorb light in the visible spectrum. Peak shifts occur due to the electronic environment around the conjugated system. When electron-withdrawing groups (like nitro groups) are attached to the molecule, the energy gap between the  $\pi$  and  $\pi^*$  orbitals increases, resulting in a blue shift (absorption at shorter wavelengths). On the other hand, electron-donating groups (such as alkyl or methoxy groups) lower the energy gap, leading to a red shift (absorption at longer wavelengths) (Yoon et al., 1999).

$n \rightarrow \pi^*$  transition involves the promotion of an electron from a non-bonding orbital (often a lone pair on a heteroatom like oxygen or nitrogen) to an anti-bonding  $\pi^*$ -orbital. This type of transition is observed in organic molecules such as carbonyl compounds (e.g., aldehydes and ketones), amines, and ethers, where heteroatoms like oxygen or nitrogen possess lone pairs that can interact with the conjugated  $\pi$ -system. The energy gap between the non-bonding orbital and the anti-bonding  $\pi^*$  orbital is smaller than that of a  $\sigma \rightarrow \sigma^*$  transition, which means this transition occurs with moderate-energy photons in the UV-visible range (200-350 nm). The  $n \rightarrow \pi^*$  transition often appears as a weak absorption band in the spectrum. Peak shifts occur when the molecular environment around the heteroatom

changes electron-withdrawing groups attached to the molecule raise the energy gap between the non-bonding and  $\pi$  orbitals, resulting in a blue shift (shorter wavelengths). Electron-donating groups, such as alkyl groups, lower the energy gap, leading to a red shift (longer wavelengths) (Goodman, 1961).

Charge transfer transitions occur when an electron moves from a donor group, such as a lone pair on a donor atom or a site rich in electrons, to an acceptor group, which is typically a metal ion or an electron-deficient site. This type of transition is commonly seen in systems where there is a significant difference in electron density between the donor and acceptor, allowing for the transfer of electrons under the right conditions. The energy required for these transitions falls within the UV-Vis region of the electromagnetic spectrum, and they are often characterized by broad absorption bands. These transitions are particularly common in transition metal complexes, where electrons are transferred between the metal center and ligands. Charge transfer transitions can lead to intense absorption peaks, making them important in the study of metal-ligand complexes and some organic molecules with electron-deficient sites (Pacchioni, 2013).

### 2.5.5.2 Beer–Lambert Law

In optics, the Beer-Lambert's law relates the absorption of light to the properties of the materials through which the light travels. According to this law, the intensity of light decreases exponentially as it passes in a medium (Mayerhöfer et al., 2020).

$$\frac{I}{I_0} = e^{-\epsilon cl}, \quad (2.65)$$

Where  $I_0$  is the incident light intensity,  $I$  is the transmitted light intensity,  $\epsilon$  is the molar absorptivity (molar absorption coefficient),  $c$  is the concentration of the absorbing substance,  $l$  is the path length (cm). Take the natural logarithm of both sides of the equation:

$$\ln\left(\frac{I}{I_0}\right) = -\epsilon cl \quad (2.66)$$

The absorbance  $A$  is given by

$$A = -\log_{10}\left(\frac{I}{I_0}\right) \quad (2.67)$$

By converting the natural logarithm to a base-10 logarithm ( $\log_b(x) = \frac{\ln(x)}{\ln(b)}$ )

$$\log_{10}\left(\frac{I}{I_0}\right) = \frac{\ln\left(\frac{I}{I_0}\right)}{\ln 10} \quad (2.68)$$

Thus

$$A = \frac{\epsilon cl}{\ln 10} \quad (2.69)$$

The constant  $\ln 10$  is often omitted using base-10 logarithms and simplified

$$A = \epsilon cl \quad (2.70)$$

where,  $A$  is the absorbance,  $\epsilon$  is the molar absorptivity or extinction coefficient (in  $\text{L mol}^{-1} \text{cm}^{-1}$ ),  $c$  is the concentration of the absorbing species (in  $\text{mol L}^{-1}$ ),  $l$  is the path length of light through the sample (in cm).

### 2.5.5.3 Optical Transition Probability

The optical transition probability quantifies the likelihood that a quantum system, such as an atom or molecule, transition between different energy states when exposed to electromagnetic radiation, especially light (Nicholls, 1977). Oscillator strength ( $f$ ) is a dimensionless quantity that measures the probability of an electronic transition in an atom or molecule when it interacts with light. It indicates the strength of light absorption or emission, with higher values representing stronger transitions. It is calculated from experimental data and can be expressed in terms of the integrated molar extinction coefficient  $\epsilon(\nu)$  (Forsman and Clark, 1973)

$$f = 4.32 \cdot 10^{-9} \int \epsilon(\nu) d\nu \quad (2.71)$$

The integrated absorption coefficient ( $\alpha_t$ ) is the total amount of light absorbed by a material over a specific wavelength range. A high value of  $\alpha_t$  indicates that the material absorbs a larger amount of light, suggesting stronger interaction with the radiation and higher absorption efficiency. It is calculated as in Eq. (2.68) (Belay, 2010)

$$\alpha_t = \int \alpha_\lambda d\nu, \quad (2.72)$$

where  $\alpha$  absorption coefficient of the molecules.

The integrated absorption cross-section ( $\sigma_t$ ) measures the probability of photon absorption by a molecule. It quantifies the effective area that determines how likely a photon will be absorbed by a molecule per incident photon. A higher  $\sigma_t$  indicates a greater chance of absorption at a given molecular concentration (Belay, 2011). Mathematically, it is expressed as

$$\sigma_t = \frac{1}{N} \int a_\lambda d\nu, \quad (2.73)$$

where  $N$  is the number density of the absorbing molecules.

Einstein coefficients ( $A$  and  $B$ ) describe the rates of photon interactions through spontaneous and stimulated processes. The spontaneous emission coefficient ( $A$ ) measures the probability per unit time of a photon being emitted. This coefficient is crucial in determining how molecules release energy without external influence. The stimulated emission and absorption coefficients ( $B$ ) describe how light affects the emission and absorption rates of molecules (Abraha et al., 2016b). Specifically,  $B_{mk}$  and  $B_{km}$  represent the rates for

stimulated emission and absorption, respectively. The relationship between  $A$  and  $B$  is given by the equation:

$$B_{mk} = B_{km} = \frac{A_{km}}{8\pi h c \nu^3}, \quad (2.74)$$

where  $h$  is Planck's constant and  $\nu$  is the frequency of the radiation. Coefficients  $B_{km}$  and  $B_{mki}$  represent the rates of stimulated emission and absorption processes, respectively. For  $B_{km}$

$$B_{km} = \frac{\ln 10}{h N_0} \int \frac{\varepsilon(\nu)}{\nu} d\nu, \quad (2.75)$$

where  $N_0$  is the number density of absorbers. The  $B$  coefficients show how the presence of light influences the rates at which molecules transition between energy states (Abebe, 2011).

The transition dipole moment ( $\mu_{km}$ ) determine the strength and direction of the interaction between an electronic transition in a molecule and the electric field of light. It reflects how effectively a molecule absorbs or emits light. The relationship between the transition dipole moment and light absorption is expressed as (Abebe, 2011)

$$j\mu_{km}f^2 = \frac{3}{S} \int \frac{\varepsilon(\nu)}{\nu} d\nu, \quad (2.76)$$

where  $S = 2.9352 \times 10^{60} C^2 mol^{-1}$ .

## 2.5.6 Phenomenon of Fluorescence

Fluorescence is a photophysical process where a molecule absorbs light and then re-emits it at a longer wavelength. The Jablonski diagram (Fig. 2.4) illustrates this process, with a downward arrow indicating the transition from the excited state ( $S_1$ ) to the ground state ( $S_0$ ). The emission will only occur as long as the stimulating radiation is present, and the

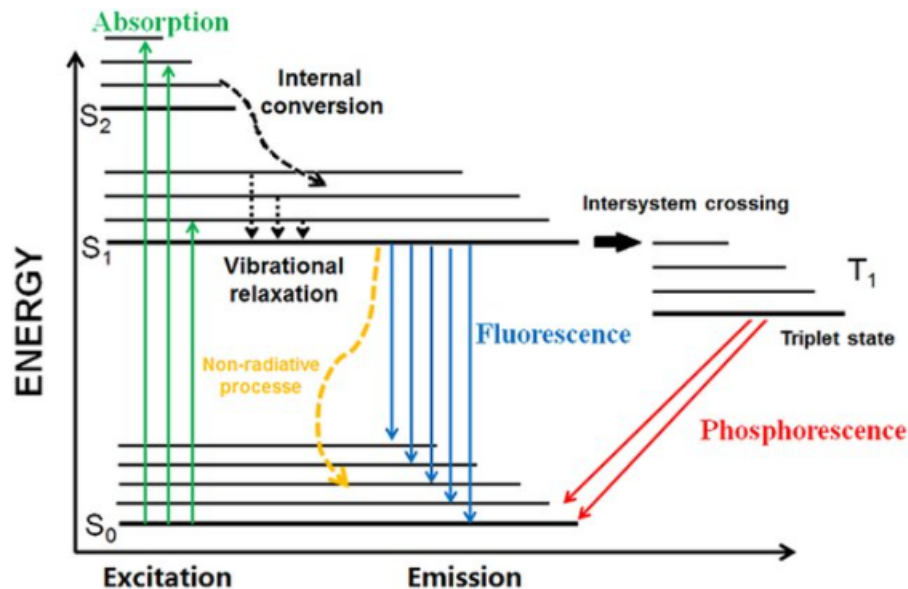


Figure 2.4: Jablonski diagram.

fluorescence typically lasts a very short time, from less than  $10^{-10}$  to  $10^{-7}$  seconds. Upon absorbing a photon, a molecule transitions from its ground state ( $S_0$ ) to an excited state, such as  $S_1$  or  $S_2$ . The energy of the absorbed photon can be described by the equation (Povrozin and Barbieri, 2016)

$$h\nu_{\text{abs}} = E_{\text{excited}} - E_{\text{ground}} \quad (2.77)$$

After absorbing the photon, the molecule may not immediately reach the lowest vibrational level of the excited state. It undergoes vibrational relaxation, losing excess energy as heat through nonradiative collisions, which ultimately brings the molecule to the lowest vibrational state of the excited singlet ( $S_1$ ). This relaxation occurs on the picosecond timescale. Once relaxed, the molecule returns to the ground state ( $S_0$ ) by emitting a photon, which is the process known as fluorescence. The emitted photon has lower energy than the absorbed photon due to energy loss during relaxation, leading to a longer wavelength. This difference in energy is called the Stokes shift, and it can be calculated using the equation

$$\Delta E = h(\nu_{\text{abs}} - \nu_{\text{em}}) = h\Delta\nu, \quad (2.78)$$

where  $\nu_{\text{em}}$  is the frequency of the emitted photon, and  $\Delta\nu = \nu_{\text{abs}} - \nu_{\text{em}}$  is the Stokes shift (Kable, 2019). Fluorescence also encompasses various photophysical properties, including quantum yield, fluorescence lifetime, and both radiative and non-radiative transitions. These properties are discussed in detail in the next section.

### 2.5.6.1 Photophysical Properties

Photophysical properties refer to the behaviors of molecules when they absorb and emit light, particularly focusing on their interactions at the molecular level (Arbogast and Foote, 1991). The fluorescent quantum yield measures how efficiently a fluorescent molecule transforms absorbed light into emitted light. It is defined as the ratio of emitted photons to absorbed photons (Thomasson, 2016)

$$\Phi_f = \frac{\text{Number of photons emitted}}{\text{Number of photons absorbed}} \quad (2.79)$$

The fluorescence quantum yield was calculated comparing it to a reference compound with a known sample (Demasa and Crosby, 1968). It was calculated using Eq. (2.80).

$$\Phi_{\text{drug}} = \Phi_r \frac{I_{\text{drug}} A_r n_{\text{water}}^2}{I_r A_{\text{drug}} n_r^2} = \frac{\kappa_r}{\kappa_r + \kappa_{nr}}, \quad (2.80)$$

where  $\Phi_{\text{drug}}$  represents the fluorescence quantum yield of the drug being tested.  $\Phi_r$  indicates the known quantum yield of a reference compound (methylene blue), such as methylene blue. The term  $I_{\text{drug}}$  refers to the fluorescence intensity emitted by the drug when it is excited by light. In contrast,  $I_r$  refers to the fluorescence intensity emitted by the reference compound.  $A_{\text{drug}}$  reflects the absorbance of the drug, showing how much light it

absorbs.  $A_r$  represents the absorbance of the methylene blue. The refractive index of the water solvent used for the drug is denoted as  $n_{water}$ .  $n_r$  is the refractive index of the solvent for the ethanol.

The radiative decay rate ( $\kappa_r$ ) quantifies how quickly an excited electron returns to its ground state by emitting a photon (Strickler and Berg, 1962)

$$\kappa_r = \frac{1}{\tau_0} = 2.88 \times 10^9 n^2 \frac{\int I(\nu) d\nu}{\int I(\nu) \nu^3 d\nu} \int \epsilon(\nu) d\nu, \quad (2.81)$$

where  $\kappa_r$  is the radiative decay rate.  $\tau_0$  is the radiative decay rate.  $I(\nu)$  is the emission intensity as a function of frequency  $\nu$ .  $\epsilon(\nu)$  is the absorption coefficient as a function of frequency. When the absorption and emission spectra are perfectly mirrored and the Stokes shift is zero, Eq. (2.81) simplifies to Eq. (2.82)."

Let me know if you need any (Bolton and Archer, 1991).

$$\kappa_r = 2.88 \times 10^9 n^2 (\nu^2)_{av} \int \epsilon(\nu) d\nu \quad (2.82)$$

The fluorescence lifetime ( $\tau_f$ ) represents the average duration for which a molecule remains in its excited state before returning to the ground state (Buterbaugh et al., 1997)

$$\tau_f = \tau_0 \Phi_f = \frac{1}{\kappa_r + \kappa_{nr}} \quad (2.83)$$

The nonradiative decay rate ( $\kappa_{nr}$ ) indicates how quickly an excited state dissipates energy through processes that do not involve photon emission

$$\kappa_{nr} = \frac{1}{\tau_f} - \kappa_r \quad (2.84)$$

### 2.5.6.2 Fluorescence Quenching

Fluorescence quenching reduces the emitted light intensity from a fluorophore (Lakowicz and Lakowicz, 1983). It occurs via three main pathways such as collisional, static, and combined quenching (Callis, 2014). Collisional quenching occurs when an excited-state fluorophore interacts with a quencher molecule, transferring its energy to the quencher and inhibiting light emission. It is described by the Stern-Volmer equation (Gehlen, 2020)

$$\frac{F_0}{F} = 1 + K_{SV}[Q] = 1 + k_q \tau_0 [Q], \quad (2.85)$$

where  $F_0$  and  $F$  are the fluorescence intensities in the absence and presence of the quencher,  $K_{SV}$  is Stern-Volmer quenching constant,  $k_q$  is the quenching rate constant,  $\tau_0$  is the lifetime of the fluorophore without quenching, and  $[Q]$  is the quencher concentration. In contrast, static quenching refers to the formation of a nonfluorescent ground-state complex that includes both a fluorophore and a quencher before the fluorophore is excited. Upon light absorption, this complex returns to the ground state without emitting a photon. Static quench-

ing reduces the number of fluorophores capable of emitting light while leaving the remaining uncomplexed fluorophores unaffected. As a result, the lifetime of the fluorophore remains unchanged  $\tau = \tau$  where  $\tau$  is the effective lifetime in the presence of static quenching and  $\tau$  is the original lifetime of the fluorophore. The dependence of the fluorescence intensity on the concentration of the quencher can be derived by considering the association constant  $k_a$  (Matos et al., 2008)

$$K_a = \frac{[FQ]}{[F][Q]}, \quad (2.86)$$

where  $[FQ]$  is defined as the concentration of the fluorophore-quencher complex,  $[F]$  is the concentration of uncomplexed fluorophore, and  $[Q]$  is the concentration of uncomplexed quencher. The total concentration of fluorophore  $[F]_0$  is given by

$$[F]_0 = [F] + [FQ] \quad (2.87)$$

Rearranging Eq. (2.86) and substituting it into Eq. (2.87) gives

$$[F]_0 = [F] + K_a[F][Q] \quad (2.88)$$

Dividing both sides of Eq. (2.88) by  $[F]$  yields the Stern-Volmer equation for static quenching

$$\frac{[F]_0}{[F]} = 1 + K_a[Q] \quad (2.89)$$

In pharmacodynamics and pharmacokinetics, the binding constant ( $K_a$ ) and the number of binding sites ( $n$ ) are crucial factors that affect the distribution profile of a drug. These parameters can be precisely determined through modified double logarithmic regression, as described by (Bi et al., 2004)

$$\log\left(\frac{F}{F_0}\right) = \log(k_a) + n \log\left([Q] + n[D]\left(\frac{F_0}{F_0} - \frac{F}{F_0}\right)\right), \quad (2.90)$$

where  $k_a$  is the binding constant and  $n$  is the number of binding sites, while  $[Q]$  and  $[D]$  represent the total concentrations of quencher (CF) and drugs (FA, SA), respectively.

### 2.5.6.3 Thermodynamic Parameters and Forces

Thermodynamic parameters such as the Gibbs free energy ( $\Delta G$ ), enthalpy ( $\Delta H$ ), and entropy ( $\Delta S$ ) are fundamental for understanding the spontaneity and equilibrium of chemical reactions (Perez, 2024b). The Gibbs free energy change is particularly important, as it determines the spontaneity and direction of a reaction. A negative  $\Delta G$  indicates a spontaneous reaction, whereas a positive  $\Delta G$  suggests non-spontaneity. The enthalpy change represents the heat absorbed or released during the reaction, indicating whether the reaction is exothermic or endothermic. The entropy change measures the disorder or randomness of the system, with a positive value suggesting an increase in disorder and a negative value

indicating a decrease (Alberty, 1969).

The intermolecular forces, such as van der Waals interactions, electrostatic forces, and hydrogen bonds, play a crucial role in determining both enthalpy and entropy changes. Van der Waals forces, although weak, stabilize molecular interactions and influence the internal energy of the system, affecting enthalpy. Electrostatic interactions between charged species impact both enthalpy and entropy, especially when ions or polar molecules are involved. Hydrogen bonds, being relatively strong, can significantly alter the stability of molecular complexes and influence the overall thermodynamic parameters (Van Oss et al., 1986). These forces are also related to the van't Hoff equation, which connects the equilibrium constant ( $K_a$ ) of a reaction to enthalpy and entropy changes (Lima et al., 2020)

$$\ln K_a = \frac{\Delta H}{RT} + \frac{\Delta S}{R} \quad (2.91)$$

Where  $K_a$  represents the equilibrium constant for the reaction,  $\Delta H$  denotes the standard enthalpy change for the reaction (expressed in joules per mole, J/mol),  $R$  is the universal gas constant, approximately 8.314 J/(mol·K),  $T$  indicates the temperature in Kelvin (K), and  $\Delta S$  refers to the standard entropy change for the reaction (measured in joules per mole per Kelvin, J/(mol·K)). The free energy change is estimated obtained by related to the equilibrium constant and the temperature of the reaction

$$\Delta G = RT \ln K_a = \Delta H - T\Delta S \quad (2.92)$$

At equilibrium,  $\Delta G = 0$ , meaning that no net change occurs between the reactants and products and becomes

$$0 = \Delta H - T\Delta S \quad (2.93)$$

At equilibrium, the heat absorbed or released is perfectly balanced by the entropy change, indicating a state of maximum stability for the system.

## 2.6 Solvatochromic Effects

Solvatochromic effects occur due to changes in the absorption and fluorescence spectra of molecules when dissolved in solvents with different polarities (Prachalith et al., 2024). General solvent properties, such as polarity and dielectric constant, play a significant role in these effects. Polar solvents stabilize the excited state more than the ground state, often leading to a redshift in the spectra. Non-polar solvents, on the other hand, result in less stabilization and can cause a blueshift. The dielectric constant affects the solvent's ability to reduce electrostatic interactions, influencing the molecular behavior in different environments (Gorbatsevich and Smirnova, 2004).

Specific interactions between solute and solvent molecules, such as hydrogen bonding, dipole-dipole interactions, and van der Waals forces, further modify solvatochromic effects. For example, hydrogen bonding can either stabilize the ground or excited state depending on

the functional groups present in the solute, which results in noticeable shifts in the spectra. Dipole-dipole interactions between the solute and solvent molecules can alter the electronic structure of the solute, while van der Waals interactions provide additional stabilization. These specific interactions are system-dependent and often act synergistically with the general solvent properties, leading to more complex solvatochromic behaviors and shifts in the absorption and fluorescence spectra (Sıdır et al., 2016).

Dipole moments in the ground and excited states can be estimated by analyzing shifts in absorption ( $\bar{\nu}_a$ ) and fluorescence ( $\bar{\nu}_f$ ) wavenumbers in relation to solvent polarity. These shifts can be quantitatively related to the solvent effects using Lippard-Mataga, Bakhshiev, Kaski-Chamma-Viallet, and Reichardt Theory. The Lippard-Mataga equation (Lippert, 1955; Mataga et al., 1956)

$$\tilde{\nu}_a - \tilde{\nu}_f = m f_{LM}(\varepsilon, n) + \text{const} \quad (2.94)$$

Bakhshiev's equation (Bakhshiev et al., 1969)

$$\tilde{\nu}_a - \tilde{\nu}_f = m_1 f_{BK}(\varepsilon_r, n) + \text{const} \quad (2.95)$$

Kaski-Chamma-Viallet equation (Kawski et al., 2002; Bilot and Kawski, 1962):

$$\frac{\tilde{\nu}_a + \tilde{\nu}_f}{2} = m_2 f_{KCV}(\varepsilon_r, n) + \text{const} = m_2 [f_{BK}(\varepsilon_r, n) + 2g(n)] + \text{const} \quad (2.96)$$

Reichardt Theory (Reichardt, 1994):

$$\tilde{\nu}_a = m_3 f_{Rei}(\varepsilon_r, n) + \text{const} \quad (2.97)$$

where  $f_{LM}(\varepsilon_r, n)$ ,  $f_{BK}(\varepsilon_r, n)$ ,  $f_{KCV}(\varepsilon_r, n)$ , and  $f_{Rei}$  are solvent polarity functions for Lippard-Mataga, Bakhshiev, Kaski-Chamma-Viallet, and Reichardt, respectively. Lippard-Mataga solvent polarity function (Lippert, 1955; Mataga et al., 1956) :

$$f_{LM}(\varepsilon_r, n) = \frac{\varepsilon_r - 1}{2\varepsilon_r + 1} - \frac{n^2 - 1}{2n^2 + 1} \quad (2.98)$$

Bakhshiev solvent polarity function (Bakhshiev et al., 1969):

$$f_{BK}(\varepsilon_r, n) = \frac{2n^2 + 1}{n^2 + 2} \left[ \frac{\varepsilon_r - 1}{\varepsilon_r + 2} - \frac{n^2 - 1}{n^2 + 2} \right] \quad (2.99)$$

Kaski-Chamma-Viallet solvent polarity function (Kawski et al., 2002; Bilot and Kawski, 1962)

$$f_{KCV}(\varepsilon_r, n) = f_{BK}(\varepsilon_r, n) + 2g(n), \quad (2.100)$$

where

$$g(n) = \frac{3}{2} \left[ \frac{n^4 - 1}{(n^2 + 2)^2} \right] \quad (2.101)$$

Reichardt solvent polarity function (Reichardt, 1994)

$$f_{Rei}(\varepsilon_r, n) = \frac{\varepsilon_r - 1}{\varepsilon_r + 2} \frac{n^2 - 1}{n^2 + 2} \quad (2.102)$$

The slopes  $m$  (Eq. (2.94)),  $m_1$  (Eq. (2.95)),  $m_2$  (Eq. (2.96)), and  $m_3$  (Eq. (2.97)) are linked to the ground and excited-state dipole moments as follows

$$m = \frac{2(\mu_e - \mu_g)^2}{hca^3} \quad (2.103)$$

$$m_1 = \frac{2(\mu_e - \mu_g)^2}{hca^3} \quad (2.104)$$

$$m_2 = \frac{2(\mu_e^2 - \mu_g^2)}{hca^3} \quad (2.105)$$

$$m_3 = \frac{2(\mu_e - \mu_g)}{hca^3}, \quad (2.106)$$

where  $h$  is Planck's constant,  $c$  is the speed of light, and  $a$  is the Onsager radius of the solute molecule. The Onsager radius is the distance around a solute molecule where the solvent starts to respond to an electric field and affects the solute's behavior. It is approximated using Suppan's equation (Suppan, 1983)

$$a = \left( \frac{3M}{4\pi\delta N} \right)^{1/3}, \quad (2.107)$$

where  $M$  is the relative molecular mass.  $\delta$  is the density of the solute molecules.  $N$  is Avogadro's number. The dipole moments of molecules in both their ground and excited states provide valuable information about how molecules interact with light, particularly in fluorescence studies. The ground state dipole moment ( $\mu_g$ ) can be calculated :

$$\mu_g = \frac{m_2 - m_1}{2} \left( \frac{hca^3}{2m_1} \right)^{1/2} \quad (2.108)$$

and the excited state dipole moment ( $\mu_e$ ) is given by

$$\mu_e = \frac{m_2 + m_1}{2} \left( \frac{hca^3}{2m_1} \right)^{1/2} \quad (2.109)$$

The change in the dipole moment ( $\Delta\mu$ ) between the excited and ground states is given as

$$\Delta\mu = \mu_e - \mu_g = \frac{m_2 + m_1}{m_2 - m_1} \mu_g \quad \text{for } m_2 > m_1 \quad (2.110)$$

The relationship between spectral shifts and solvent polarity is given by

$$\tilde{\nu}_a - \tilde{\nu}_f = 11307.6 \left[ \left( \frac{\Delta\mu}{\Delta\mu_B} \right)^2 \left( \frac{a_B}{a} \right)^3 \right] E_T^N + \text{const} \quad (2.111)$$

Eq. (2.111) was first suggested by Reichardt (Reichardt, 1994) and later refined by Ravi (Ravi et al., 1995). It describes how the shifts in absorption and fluorescence wavenumbers ( $\tilde{\nu}_a - \tilde{\nu}_f$ ) correspond to changes in the dipole moment  $\Delta\mu$  relative to a known value ( $\Delta\mu_B$ ). The terms account for solvent interactions affecting the energy of the excited state. The slope from a linear plot of shifts versus microscopic solvent polarity  $mE_T^N$  is represented by:

$$mE_T^N = 11307.6 \left[ \left( \frac{\Delta\mu}{\Delta\mu_B} \right)^2 \left( \frac{a_B}{a} \right)^3 \right] \quad (2.112)$$

Eq. (2.112) relates the slope obtained from experimental data to the changes in dipole moments and the influence of solvent polarity. The solvent polarity function  $E_T^N$  can be defined as

$$E_T^N = \frac{E_T(\text{solvent}) - E_T(\text{TMS})}{E_T(\text{water}) - E_T(\text{TMS})} \quad (2.113)$$

## 2.7 Quantum Mechanical Methods

Quantum mechanics methods are mathematical techniques used to analyze particle behavior at the atomic and subatomic levels, including the Schrödinger equation, perturbation theory, and density functional theory. They are categorized into four main types: semiempirical, ab initio, density functional, and molecular Perez (2024a).

### 2.7.1 Semi-empirical Theory

Semi-empirical methods use a certain number of experimental data throughout the calculation. Usually, semi-empirical methods are used for very big systems, since they can handle large amounts of calculation. Examples of semiempirical methods are ZINDO and AM1. ZINDO method was parametrized to reproduce electronic spectra. It is most often used to compute UV transitions. Austin Model 1 (AM1) is a method that is most often used to model organic molecules.

In semi-empirical methods such as PM3 or AM1, electrons are treated within an average potential  $V(r)$  created by all other electrons, which is parameterized using empirical data rather than calculated from direct interactions. These methods simplify the complexity of the full Schrödinger equation by fitting constants to experimental data, resulting in an effective potential that approximates some interactions without direct computation, as shown below.

$$-\frac{\hbar^2}{2m} \nabla^2 \psi(r) + V_{eff}(r) \psi(r) = E \psi(r), \quad (2.114)$$

where  $V_{eff}(r)$  is an effective potential that includes both the empirical adjustments and the contributions from the average fields of other electrons. In more advanced semiempirical

methods, one may see formulations that rely on the Hartree–Fock equation, which considers exchange terms and is expressed as follows:

$$\sum_j \left( \frac{\hbar^2}{2m} r^2 + V_{eff}(r) + \int \frac{j\psi_j(r^\theta)^2}{r_{ij}} dr^\theta \right) \psi_i(r) = E_i \psi_i(r), \quad (2.115)$$

where  $r_{ij}$  represents the distance between different electrons  $i$  and  $j$ .

The effective potential  $V_{eff}$  is determined based on empirical fitting, which can include terms such as

$$V_{eff} = \sum_n \frac{Z_n}{r_{in}} + V_{corr} \quad (2.116)$$

where  $Z_n$  is the charge of the nucleus,  $V_{corr}$  is a correction term often derived from empirical data, capturing additional electron–electron repulsion effects.

## 2.7.2 Hartree–Fock Method

Hartree-Fock (HF) is an ab initio quantum chemical method for approximating the solution to the many-electron Schrodinger equation. It simplifies the complex interactions between electrons by averaging the Coulombic electron-electron repulsion rather than considering explicit repulsive interactions, which is referred to as the central field approximation. The method involves calculating molecular orbitals using two main approaches. UHF assigns separate orbitals to each electron, even if they are paired, making it useful for systems like ions, excited states, and radicals. RHF assigns the same orbital function to paired electrons, making it suitable for species with paired electrons and preventing spin contamination (Dovesi et al., 2000).

Hartree Fock method enforcing the asymmetry requirement for indistinguishable fermions, such as electrons, and employs the mean-field approximation to include electron exchange interactions. Each electron is treated as moving in an effective potential created by the nucleus and the average field of other electrons, with the wavefunction represented as a Slater determinant to ensure antisymmetry, adhering to the Pauli exclusion principle (Blinder, 2019). For a system of  $N$  electrons, the wavefunction  $\Psi$  is given by

$$\Psi(\mathbf{r}_1, r_2, \dots, r_N) = \frac{1}{N!} \sum_{\sigma} \text{sgn}(\sigma) \phi_1(r_{\sigma(1)}) \phi_2(r_{\sigma(2)}) \dots \phi_N(r_{\sigma(N)}), \quad (2.117)$$

where  $\phi_i(r)$  are the single-electron wavefunctions (molecular orbitals), and  $\sigma$  denotes a permutation of indices. The Hartree–Fock method centers on the Fock operator, which combines kinetic energy with the effective potential from external nuclei and average electron–electron interactions, including exchange effects (Tsuneda and Tsuneda, 2014). For each electron  $i$ , the Fock operator  $F_i$  is defined as:

$$F_i = -\frac{\hbar^2}{2m} \nabla^2 + V_{ne} + V_{ee}, \quad (2.118)$$

here,  $V_{ne}$  represents the potential from the nuclei and average field of other electrons, while  $V_{ee}$  accounts for the exchange potential due to electron indistinguishability. For the wavefunctions  $\phi_i$ , these equations take the form

$$F_j \phi_j(\mathbf{r}) = \epsilon_j \phi_j(\mathbf{r}), \quad (2.119)$$

where  $\epsilon_j$  are the energies associated with each molecular orbital.

The Hartree–Fock method employs an iterative self-consistent field (SCF) procedure. It begins with an initial guess for the molecular orbitals  $\phi_i$  and uses these orbitals to calculate the Fock operator  $F_j$ . The Hartree–Fock equations are then solved to obtain new orbitals. This process is repeated until the orbitals converge, meaning that changes in their shapes and energies become negligible. The total electronic energy  $E$  in Hartree Fock (Mazziotti, 2012) given by

$$E_{HF} = \sum_i (h\phi_i | F_j | \phi_i) + \frac{1}{2} \sum_{i,j} h\phi_i \phi_j | \frac{1}{r_{ij}} | \phi_i \phi_j \quad (2.120)$$

### 2.7.3 Density Functional Theory

DFT is a widely used method for studying the electronic structure of many-body systems. It focuses on the electron density, which simplifies the problem by reducing the complexity of many-body interactions. The electron density represents the probability of finding an electron at a particular point in space. For a single electron with wave function  $\psi(r, s)$ , the electron density  $\rho(r)$  is defined as proportional to the square of the wave function's amplitude (Kohn et al., 1996)

$$\rho(r) = \int |\psi(r, s)|^2 ds \quad (2.121)$$

#### 2.7.3.1 Hohenberg–Kohn Theorem

First Hohenberg-Kohn theorem: The ground state properties of a many-electron system depend only on the electronic density  $n(\mathbf{r})$ . The  $n(\mathbf{r})$  allows one to reconstruct the potential  $V(\mathbf{r})$  and is given by (Kristyan, 2008)

$$V_{ext} = V_{ext}[\mathbf{r}] \quad (2.122)$$

Second Hohenberg-Kohn theorem: The correct ground state density for a system is the one that minimizes the total energy through the functional  $E[n(\mathbf{r})]$ . For a given external potential  $V(\mathbf{r})$ , there exists a unique ground state electron density  $n(\mathbf{r})$ . The total energy  $E_n$  is a functional of the electron density, and the true ground state can be obtained by minimizing this energy functional (Sahni and Sahni, 2004)

$$E_n = T_n + V_n + E_{ee_n}, \quad (2.123)$$

where  $T_n$  is kinetic energy functional.  $V_n$  is external potential energy functional and  $E_{ee_n}$  is electron–electron interaction energy functional.

### 2.7.3.2 Kohn-Sham Method

The Kohn–Sham method reformulates the many-body problem in terms of noninteracting particles, allowing calculations to be manageable while still accounting for electron interactions (Bartolotti, 1982). For a system of  $N$  noninteracting particles moving in an effective potential  $V_{eff}(r)$ . The Kohn–Sham equations are then given by

$$\left( \frac{\hbar^2}{2m} \nabla^2 + V_{eff}(r) \right) \psi_i(r) = \epsilon_i \psi_i(r) \quad (2.124)$$

The effective potential  $V_{eff}(r)$  can be expressed as

$$V_{eff}(r) = V_{ext}(r) + V_{Hartree}(r) + V_{xc}(r) \quad (2.125)$$

where  $V_{ext}(r)$  is external potential from nuclei.  $V_{Hartree}(r)$  is classical electron–electron interaction described using the Hartree potential

$$V_{Hartree}(r) = e^2 \int \frac{n(\mathbf{r}^j)}{|\mathbf{r} - \mathbf{r}^j|} d\mathbf{r}^j \quad (2.126)$$

where  $V_{xc}(r)$  is exchange-correlation potential accounting for quantum effects and electron correlation. Start with an arbitrary density  $n(r)$ . Solve for and calculate the density  $\psi$  and calculate the density

$$n(r) = \sum_{i=1}^N |\psi_i(r)|^2 \quad (2.127)$$

The process is repeated until the density  $n$  converges, i.e., the changes between iterations are below a set threshold. Once self-consistency is achieved, the total energy can be computed

$$E_n = \sum_{i=1}^N \epsilon_i + V_{xc}(n) + V(n) \quad (2.128)$$

where  $\epsilon_i$  are the energy eigenvalues,  $V_{xc}(n)$  is the exchange-correlation potential, and  $V(n)$  represents the external potential.

### 2.7.3.3 Functional Models

Functional models in DFT are used to approximate the exchange-correlation energy, which describes the interactions among electrons. The accuracy of DFT can vary depending on the specific model used and the application domain. Several functional models have been developed, each with different levels of complexity and accuracy (Neese, 2009). Local density approximation (LDA) assumes that the exchange-correlation energy at a point in

space depends only on the electron density at that point. It is particularly effective for systems with slowly varying electron densities, such as dense metals. For example, LDA is often used in calculations involving crystalline solids where electron density is uniform (Sahni et al., 1988).

The Generalized Gradient Approximation (GGA) enhances the Local Density Approximation (LDA) by including the gradient of electron density, which allows for a more accurate representation of non-uniform density. A widely used GGA functional is the Perdew-Burke-Ernzerhof (PBE) functional. GGA is useful for systems such as molecular complexes and surfaces, where electronic structure varies significantly (Hua et al., 1997). Hybrid functionals mix traditional DFT methods with Hartree-Fock theory to improve the description of electronic interactions, particularly for systems where electron-electron interactions are significant (Eichinger et al., 1999). The B3LYP functional is a popular hybrid functional widely used in organic and inorganic chemistry for its accuracy in predicting molecular geometries and energy levels. BLYP functional is effective for modeling metals but less accurate for organic compounds (Szekeres et al., 2005).

#### 2.7.3.4 Orbitals and Basis Sets

Orbitals are mathematical functions used to describe the probability distribution of an electron within an atom or molecule. They represent regions in space where there is a high probability of finding an electron, and their shapes are determined by quantum numbers. The most commonly known types of orbitals include s, p, d, and f orbitals, each with distinct shapes and angular momentum. S orbitals are spherical, p orbitals have a dumbbell shape, d orbitals are more complex with a cloverleaf shape, and f orbitals are even more intricate. These orbitals form the foundation for the electron configurations of atoms and molecules, playing a central role in quantum physics and molecular modeling (Tsaparlis, 1997).

Types of orbitals, such as Slater-type orbitals (STOs) and Gaussian-type orbitals (GTOs), are used to model atomic orbitals (AOs). STOs closely resemble real atomic orbitals, providing accurate descriptions of electron distributions with exponential decay and precise asymptotic behavior. However, they are computationally expensive (Majumdar et al., 2021). In contrast, GTOs are based on simpler Gaussian functions, making them faster to compute. Although GTOs provide less precise representation of the shape of atomic orbitals, combining multiple GTOs can effectively approximate STOs, achieving a balance between accuracy and computational efficiency (Magalhaes, 2014).

A basis set consists of a group of wave functions. These wave functions describe the shape of atomic orbitals (AOs). AOs are the building blocks used to create molecular orbitals (MOs). The molecular orbitals are determined by linearly combining the atomic orbitals using the linear combination of atomic orbitals (LCAO) method (Nagy and Jensen, 2017). Theoretical models, such as the semiempirical models PM<sub>n</sub> (where n=3,...,6), use an internal basis set, methods like ab initio and DFT require the user to select an appropriate basis set. The choice of basis set plays a crucial role in determining the level of approximation in the

calculation, directly influencing both the accuracy of the results and the computational time required. Selecting a basis set involves a trade-off, where larger, more accurate basis sets provide better results but at the cost of increased computational effort (Sarangi et al., 2020; Mosapour Kotena et al., 2021).

There are several types of basis sets, each varying in complexity, accuracy, and computational cost. Minimal basis sets, such as STO-3G, use only a single function to represent each atomic orbital (Kapusta et al., 2018). In the STO-nG notation (where  $n=2,\dots,6$ ),  $n$  Gaussian-type orbitals (GTOs) are employed to approximate one Slater-type orbital (STO). These basis sets are typically limited to single Zeta, where only one STO is used per AO (Lu et al., 2004).

Split valence basis sets, also known as Pople basis sets, offer greater flexibility by allowing separate specifications for the number of GTOs used for core and valence electrons. These sets can be configured as double Zeta (two functions per AO) or triple Zeta. The notation for these sets is typically K-LMG, where K indicates the number of sp-type inner shell GTOs, L refers to the inner valence s- and p-type GTOs, M represents the outer valence s- and p-type GTOs, and G signifies the use of GTOs. Pople basis sets, such as 3-21G, 6-31G, and 6-311G, are commonly used for organic molecules, with different numbers of GTOs applied to the core, inner valence, and outer valence shells. Polarized Pople basis sets introduce additional flexibility by allowing atomic orbitals (AOs) to distort under the influence of the environment, with polarization indicated by \* or (d). Diffuse Pople basis sets, indicated by + or ++, extend electron distributions and are particularly useful for anions, excited states, and molecules with lone pairs. Furthermore, correlation-consistent basis sets, optimized for correlated wavefunctions (e.g., CISD), are denoted as cc-pVXZ, where X represents the zeta number (e.g., D for double, T for triple), and aug- can be added to include diffuse functions, such as in aug-cc-pVTZ (Echenique and Alonso, 2008).

### 2.7.3.5 DFT Predicted Parameters

DFT enables the calculation of a wide range of parameters essential for understanding the electronic structure, reactivity, and stability of molecules and materials. Molecular orbitals ( $\psi_i$ ) describe electron behavior, with the HOMO and LUMO being crucial for predicting reactivity, ionization, and electron affinity (Choudhary et al., 2019). The ionization potential (IP) refers to the energy needed to eject an electron from a molecule. It is calculated as (Zhan et al., 2003)

$$IP = -E_{\text{HOMO}} \quad (2.129)$$

On the other hand, electron affinity (EA) is the energy released when an electron is added to a molecule. It is related to the energy of the LUMO (Zhan et al., 2003)

$$EA = E_{\text{LUMO}} \quad (2.130)$$

The chemical potential ( $\mu$ ), calculated as the average of the IP and EA, measures a

molecule's tendency to either gain or lose electrons. It reflects the energy change associated with the addition or removal of an electron from the molecular system (Pearson, 1992):

$$\mu = \frac{IP + EA}{2} \quad (2.131)$$

A higher chemical potential implies a greater likelihood of the molecule participating in redox reactions, whether donating or accepting electrons. The electronegativity ( $\chi$ ) is another important parameter for quantifying a molecule's ability to attract and retain electrons during chemical bonding. It is defined as the difference between the IP and EA (Komorowski, 1987)

$$\chi = \frac{IP + EA}{2} \quad (2.132)$$

A higher electronegativity indicates that a molecule can more strongly attract electrons in a bond, which is critical for predicting bond polarity and understanding how the molecule interacts in chemical reactions. Chemical Hardness ( $\eta$ ) represents a molecule's resistance to changes in its electron density, offering a measure of its stability. A higher chemical hardness value suggests that the molecule is less likely to undergo reactions that cause large fluctuations in electron density (Pearson, 1992)

$$\eta = \frac{IP - EA}{2} \quad (2.133)$$

A molecule with greater hardness is more stable and less reactive, which means that it resists changes in its electron configuration. Global softness ( $S$ ), which is inversely related to chemical hardness, quantifies a molecule's ability to donate electrons. Therefore, molecules are more reactive and capable of easily donating electrons during chemical reactions (Cohen et al., 1995)

$$S = \frac{1}{2\eta} \quad (2.134)$$

The global electrophilicity index ( $\omega$ ) measures a molecule's ability to accept electrons, providing insight into its potential to act as an electrophile in chemical reactions. It is given by (Pérez et al., 2007)

$$\omega = \frac{\mu^2}{2\eta} \quad (2.135)$$

A higher electrophilicity index indicates a stronger tendency for the molecule to accept electrons, making it more reactive toward nucleophiles.

## 2.7.4 Time-Dependent Density-Functional Theory

Time-dependent density functional theory (TDDFT) is a computational method that extends DFT to study electronic excited states in response to time-varying external fields, such as light. It allows for the calculation of optical spectra and electronic transitions and is widely used in fields such as photovoltaics and biosensing to analyze light absorption and emission,

aiding in the design of materials with enhanced optical and electronic properties (Liu et al., 2010).

### 2.7.4.1 Kohn–Sham Equations

The Kohn–Sham equations in TDDFT extend ground-state DFT to analyze the dynamic behavior of electron systems in time-dependent external fields (Baer and Kronik, 2018). TDDFT models interacting systems as noninteracting electrons within an effective time-dependent potential, allowing for calculations of excited states and optical properties. The time-dependent Kohn–Sham equations describe the evolution of the orbitals  $\psi_i(r, t)$

$$i\frac{\partial}{\partial t}\psi_i(r, t) = \left( \frac{1}{2}r^2 + v_{KS}(r, t) \right) \psi_i(r, t), \quad (2.136)$$

with the total electron density given by  $\rho(r, t) = \sum_i |\psi_i(r, t)|^2$ . The effective potential  $v_{KS}(r, t)$  comprises the external potential  $v_{ext}(r, t)$ , the Hartree potential  $v_H(r, t)$ , and the exchange-correlation potential  $v_{XC}(r, t)$

$$v_{KS}(r, t) = v_{ext}(r, t) + v_H(r, t) + v_{XC}(r, t), \quad (2.137)$$

with  $v_H(r, t)$  accounting for Coulomb repulsion and  $v_{XC}(r, t)$  capturing many-body effects (Elliott et al., 2007).

### 2.7.4.2 TDDFT Predicted Optical Properties

In TDDFT, optical properties are calculated by analyzing the response of an electron system to an external time-dependent perturbation, typically an electromagnetic field. The main optical properties that can be computed include absorption spectra, emission spectra, excitation energies, optical transition dipoles, polarizability, and the dielectric function (Chen et al., 2010). In TDDFT, absorption is linked to the transitions between occupied and unoccupied states, with the transition dipole moment playing a crucial role (Jabed et al., 2021). The absorption spectrum  $A(\omega)$  is given by

$$A(\omega) \propto \sum_{i,j} |\langle \psi_i | \mathbf{r} | \psi_j \rangle|^2 \delta(\omega - \Omega_{ij}), \quad (2.138)$$

where  $\langle \psi_i | \mathbf{r} | \psi_j \rangle$  is the dipole matrix element between the  $i$ -th occupied and  $j$ -th unoccupied orbitals.  $\Omega_{ij}$  is the excitation energy between these states (i.e., the energy difference).  $\delta(\omega - \Omega_{ij})$  represents the Dirac delta function that selects the resonance frequency.

The emission spectrum describes the light emitted when the system relaxes from an excited state to a lower-energy state. The emission spectra are related to the difference in energy between the excited state and the ground state, with a corresponding transition dipole moment. The emission intensity  $I_{em}(\omega)$  is given by

$$I_{em}(\omega) \propto \sum_{i,j} |\langle \psi_i | \mathbf{r} | \psi_j \rangle|^2 \delta(\omega - (\Omega_{ij} - E_0)), \quad (2.139)$$

where  $\Omega_{ij}$  is the excitation energy,  $E_0$  is the energy of the ground state.

Excitation energies are the energy differences between the ground state and the excited state. These are derived from solving the Casida equations in TDDFT, which describe the linear response of the electron density to an external time-dependent perturbation. The Casida equations are as follows:

$$\sum_j (\delta_{ij}\omega_i^2 + 2\omega_i\omega_j K_{ij}) F_j = \Omega F_i, \quad (2.140)$$

where  $\omega_i$  and  $\omega_j$  are the energy levels of the occupied and unoccupied orbitals,  $K_{ij}$  represents the interaction terms due to exchange-correlation effects,  $\Omega$  is the set of excitation energies, and  $F_i$  are the eigenvectors corresponding to each excitation (Baerends et al., 2002).

The optical transition dipole moment quantifies the strength of the transition between an occupied state and an unoccupied state under the influence of an electromagnetic field. It is computed as the matrix element of the position operator  $r$  between the initial and final states:

$$d_{ij} = \langle \psi_i | r | \psi_j \rangle, \quad (2.141)$$

where  $\psi_i$  and  $\psi_j$  are the Kohn–Sham orbitals of the occupied and unoccupied states, respectively.  $r$  is the position operator (Sarkar et al., 2021).

Polarizability describes the system’s response to an external electric field, i.e., how much the electron cloud distorts in response to the field. In TDDFT, the polarizability  $\alpha(\omega)$  is related to the susceptibility  $\chi(\omega)$  by

$$\alpha(\omega) = \frac{1}{\omega} \chi(\omega), \quad (2.142)$$

where  $\chi(\omega)$  is the linear response function, which can be obtained from the Casida equations or through the perturbative expansion of the electron density in response to an external field (Pluta and Skrzyński, 2021). The dielectric function  $\epsilon(\omega)$  describes how the material’s electron density responds to an external field, affecting the ability of the material to transmit or reflect light. In TDDFT, the dielectric function is related to the polarizability and is given by (Kootstra et al., 2000)

$$\epsilon(\omega) = 1 + \frac{4\pi}{\omega^2} \alpha(\omega). \quad (2.143)$$

## 2.8 Molecular Docking

Molecular docking is a computational method used to predict how a ligand (a small molecule) binds to a receptor (typically a protein or nucleic acid) (Guedes et al., 2014). It helps in determining the optimal binding mode of the ligand, including its orientation and conformation. This technique is crucial in drug discovery, as it allows researchers to evaluate the binding mechanisms, efficacy, and selectivity of potential drug candidates (Ferreira et al., 2015).

There are two main types of molecular docking: rigid and flexible (Sahu et al., 2024). Rigid docking assumes that both the ligand and receptor remain fixed in structure during the process, making it computationally less expensive but less accurate. The energy function for rigid docking includes the internal and external energies of the system:

$$E_{rigid} = E_{int} + E_{ext} \quad (2.144)$$

where  $E_{int}$  is the internal energy of the ligand and receptor (including bond stretch, angle bending, torsion, and nonbonded interactions) and  $E_{ext}$  accounts for the external forces such as electrostatic and van der Waals interactions between the ligand and receptor (Matsuzaki et al., 2017).

In flexible docking, both the ligand and the receptor can change conformation, making it more realistic but computationally demanding. The energy function here includes the flexibility of both molecules and is given as follows:

$$E_{flexible} = E_{int}(R, L) + E_{ext}(R, L) + E_{flex}(R, L) \quad (2.145)$$

where  $E_{flex}$  refers to the energy change due to the flexibility of the ligand and/or receptor. Accurate prediction of how the ligand fits into the receptor's binding site is crucial for drug design. Binding affinity quantifies the strength of the interaction between the ligand and its receptor. It can be quantified by the free energy of binding ( $\Delta G_{bind}$ )

$$\Delta G_{bind} = RT \ln K_d \quad (2.146)$$

where  $K_d$  is the dissociation constant,  $R$  is the gas constant, and  $T$  is the temperature. A lower  $K_d$  indicates stronger binding. Scoring functions, which evaluate various molecular interactions like van der Waals, electrostatic forces, and hydrogen bonds, are used in docking simulations to estimate  $\Delta G_{bind}$  and predict binding affinity (Gohlke and Klebe, 2002).

# 3

---

## MATERIALS AND METHODS

---

This chapter provides an overview of the materials and methods used in the study. Section 3.1 describes the chemicals and solvents employed. Section 3.2 discusses the software and databases used for data analysis. Section 3.3 details the apparatus and instruments, including the principles of UV–Vis spectrophotometer (section 3.3.1), fluorescence spectrophotometer (section 3.3.2), and FTIR spectrophotometer (section 3.3.3). Section 3.4 explains the experimental methods, covering solvent polarity effects on FA and SA (section 3.4.1), optical transition probabilities and photophysical properties (section 3.4.2), and fluorescence quenching (section 3.4.3). Section 3.5 presents the computational methods, including density functional theory (section 3.5.1) and molecular docking techniques (section 3.5.2), with a focus on protein and ligand preparation and docking.

### 3.1 Chemicals and Solvents

Ferulic acid, caffeine, and sinapic acid were obtained from Sigma Aldrich (India) and used as received, without any alterations. Methylene blue (molecular weight: 285.14 g/mol, 95% purity) to calculate fluorescence quantum yield of FA or SA. Trisodium citrate buffer solution was used to keep the pH value at 7.4. Protein structures (3ML8, 5EKN, and 6YKY). Polar solvents such as water, isopropanol, acetonitrile, ethanol, methanol, and dimethyl sulfoxide and nonpolar solvents such as dichloromethane, benzene, chloroform, and acetone.

### 3.2 Software and Data Bases

Software such as ChemDraw Ultra 08 (Mendelsohn, 2004), Gaussian 09 W (Frisch et al., 2009), GaussView 6.0 (Kumar et al., 2022), Chemcraft (Han, 2021), BIOVIA Discovery Studio 2021 (Pawar and Rohane, 2021), AutoDock Vina (Trott and Olson, 2010), and PyRx (Dallakyan and Olson, 2015) were used in the study. Data and resources such as the Research Collaboratory for Structural Bioinformatics Protein Data Bank (RCSB PDB) and PubChem were used to download protein structures 3ML8, 5EKN and 6YKY.

### 3.3 Apparatus and Instruments

Laboratory apparatuses such as digital balances, ovens, volumetric flasks, measuring cylinders, pipettes, magnetic stirers with hot plates, spatulas, thermometers, beakers, alu-

minum foils, cuvettes, and water baths were used in this study. Instruments such as a UV–Vis (JASCO-V-770, Japan), an Eclipse fluorescence spectrophotometer (Agilent, country: Malaysia), and an FTIR spectrophotometer (Nicolet ISO50) were used in this study.

### 3.3.1 Working Principles of UV-Vis Spectrophotometer

A UV–Vis spectrophotometer analyzes the absorption of light by a sample via several basic components. Fig. 3.1 shows a UV–Vis absorption spectrophotometer schematic diagram. In this method, a sample is exposed to light in the UV (200–400 nm) and visible (400–700 nm) regions of the electromagnetic spectrum. The deuterium lamp (D<sub>2</sub> lamp) provides light in the UV range, whereas the tungsten lamp covers the visible and IR regions. Mirrors guide the light through the system, ensuring precise alignment. A filter or monochromator selects specific wavelengths from the light source, allowing only the desired range to pass through. The beam splitter divides the light into two paths: the reference cell and the sample cell. The reference measures baseline readings, whereas the sample measures absorption. After passing through the sample, the remaining light reaches a photomultiplier tube, which converts the light signal into an electrical signal. This signal is processed by a data processing unit, which calculates absorbance values. Finally, the results are displayed on the data readout as an absorption spectrum, indicating the sample's molecular and concentration information (Förster, 2004).

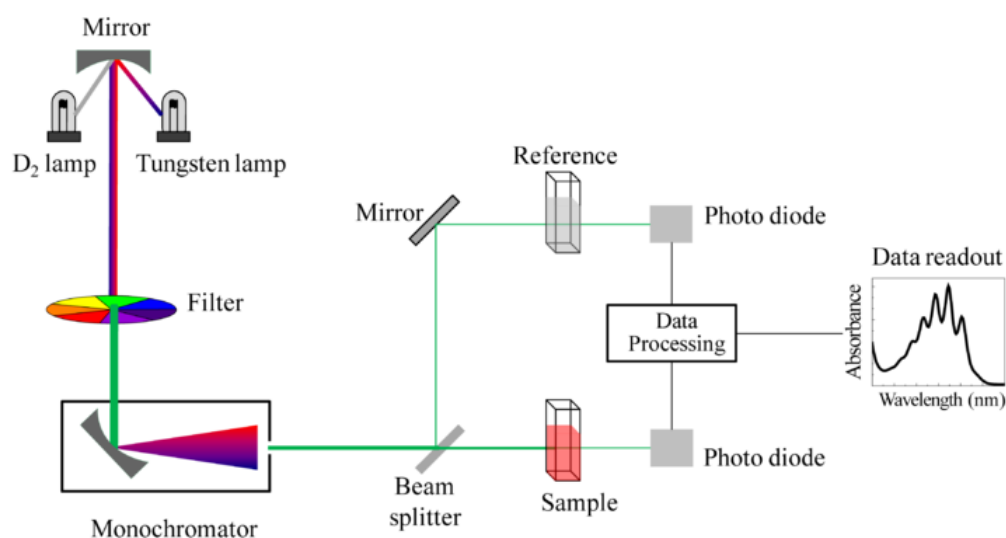


Figure 3.1: Schematic representation of UV-Vis spectrophotometer.

### 3.3.2 Working Principles of Fluorescence Spectrophotometer

Fluorescence spectrophotometer detects light emitted by a sample after excitation via basic components. Fig. 3.2 shows schematic illustration of fluorescence spectrophotometer. The xenon (Xe) lamp generates intense light to excite the sample. The mirror directs this light to the entrance slit, which limits the beam width for precision. The excitation monochromator selects the specific wavelength needed to excite the sample, and the exit slit ensures that

only this wavelength reaches the sample cuvette containing the analyte. The sample absorbs light and emits fluorescence, which is directed by another mirror to the entrance slit of the emission monochromator. This monochromator isolates the emitted wavelength of interest, and the exit slit focuses it onto the detector. The photomultiplier amplifies the weak fluorescent signal, which is then processed by a data processing unit (Singh et al., 2021).

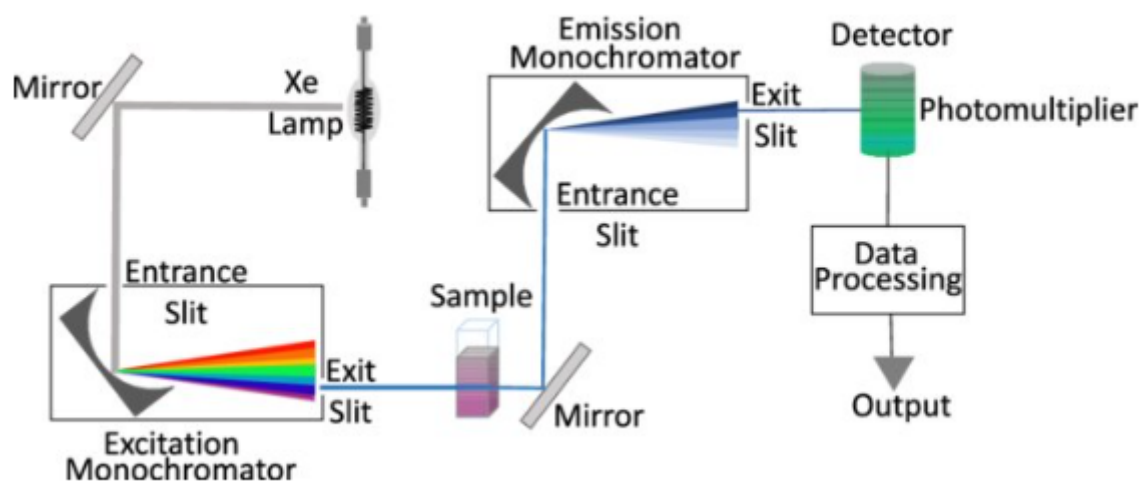


Figure 3.2: Schematic representation of a fluorescence spectrophotometer.

### 3.3.3 Working Principles of FTIR Spectrophotometer

An FTIR spectrophotometer identifies molecular structures by analyzing how infrared light interacts with a sample. Fig. 3.3 shows schematic illustration of FTIR spectrophotometer. The IR source generates infrared radiation, which is directed to a beam splitter. The beam splitter divides the light into two beams: one travels to the fixed mirror, and the other travels to the moving mirror. These mirrors reflect the light back to the beam splitter, where the beams recombine and create an interference pattern. This combined beam passes through the sample, where molecules absorb specific wavelengths, and the remaining light reaches the detector. The detector captures the light and generates an interferogram signal, which is converted into a readable spectrum via Fourier transformation (Jaggi and Vij, 2006).

## 3.4 Experimental Methods

### 3.4.1 Effects of the Solvent Polarity

To estimate the effect of solvent polarity on the absorption and emission spectra, stock solutions of FA and SA were prepared in various solvents at a concentration of  $2 \times 10^{-4}$  M. These solutions were stored in a dark section of the refrigerator to minimize light exposure. Low concentrations were used to avoid self-quenching during steady-state fluorescence and ultraviolet-visible absorbance experiments. UV-Vis absorption spectra were recorded from

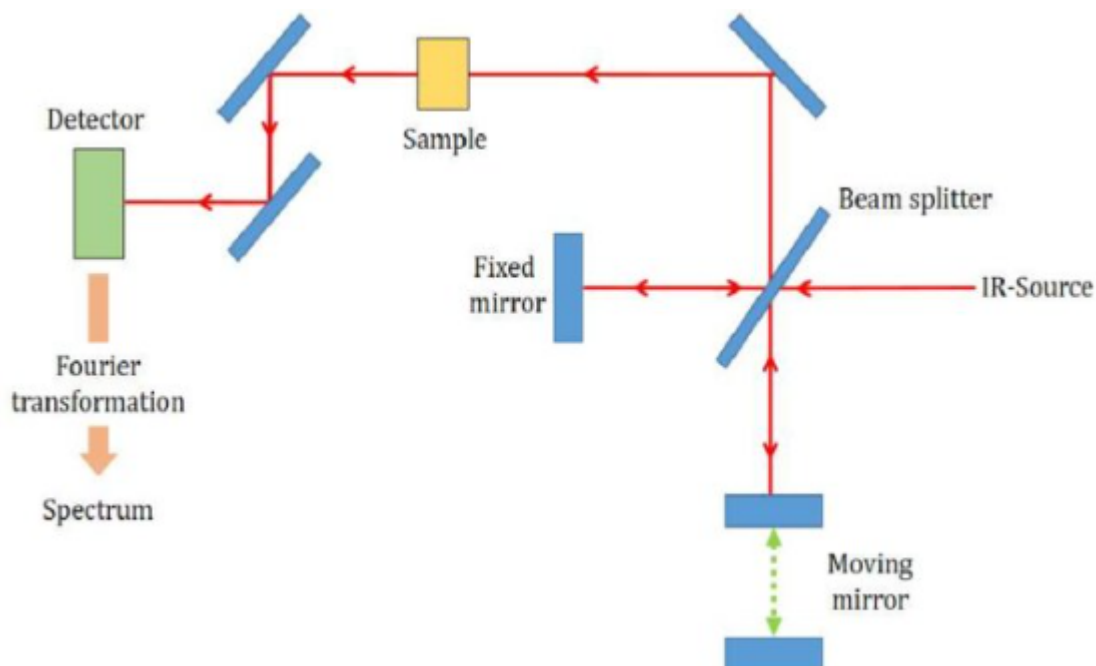


Figure 3.3: Schematic representation of an FTIR spectrophotometer setup.

200 to 500 nm using a 1 cm cuvette, with a spectral bandwidth of 0.1 nm. Fluorescence measurements were conducted using an excitation wavelength of 320 nm and emission between 350 and 600 nm. Excitation and emission slit widths, and scan speed were set at 10 nm and 240 nm/min, respectively. The scanning rate was set to 600 nm/min with a scanning range of 200–1000 nm, and Photomultiplier tube voltage was adjusted for optimal detector sensitivity.

Solvent polarity was evaluated using various methods, such as Lippert–Mataga (Eq. (2.94)), Bakhshiev (Eq. (2.95)), Kawski–Chamma–Viallet (Eq. (2.96)), Reichardt (Eq. (2.97)), and molecular–microscopic solvent functions (Eq. (2.112)) using the relative permittivity, refractive index, and empirical polarity values. In addition, the ground-state dipole moment (Eq. (2.108)), excited-state dipole moment (Eq. (2.109)), and change in dipole moment (Eq. (2.110)) were also calculated.

### 3.4.2 Optical Transition and Photophysical Properties

To investigate the optical transition probabilities and photophysical properties, stock solutions of FA ( $6.18 \times 10^{-3}$  M) and SA ( $5.35 \times 10^{-3}$  M) were prepared in chloroform, dichloromethane, dimethyl sulfoxide, methanol, water, acetonitrile, and isopropanol. The concentrations were kept low to minimize self-quenching. UV–Vis absorption spectra and fluorescence measurements followed a protocol similar to those used for studying the effect of solvent polarity on absorption and emission spectra, respectively.

Optical transition probabilities, such as the oscillator strength (Eq. (2.71)), integrated absorption coefficient (Eq. (2.72)), integrated absorption cross-section (Eq. (2.73)), Einstein coefficients (A and B) (Eq. (2.74)), and transition dipole moment (Eq. (2.76)), were

calculated from the UV–Vis absorption spectra. From the fluorescence data, the fluorescence quantum yield (Eq. (2.80)), radiative decay rate (Eq. (2.81)), fluorescence lifetime (Eq. (2.83)), and nonradiative decay rate (Eq. (2.84)) were determined.

### 3.4.3 Fluorescence Quenching

To study the effects of concentration on the fluorescence spectra, solutions of FA and SA were prepared in water at concentration of  $1.72 \times 10^{-3}$  M for FA and  $2.10 \times 10^{-3}$  M for SA. These solutions were kept at room temperature and stored in the dark to prevent light exposure. Fluorescence measurements followed a similar protocol to those used for studying the effect of solvent polarity on emission spectra. Concentration-dependent fluorescence emission was plotted using OriginPro 18 to analyze variations in fluorescence intensity, spectral shifts, and quenching effects across different concentrations.

To investigate the fluorescence quenching of FA and SA by caffeine, stock solutions of FA ( $6.18 \times 10^{-4}$  M) and SA ( $5.35 \times 10^{-4}$  M) were prepared in trisodium citrate buffer at pH 7.4 ( $2.0 \times 10^{-5}$  M), and a caffeine stock solution ( $2.06 \times 10^{-3}$  M) was prepared with deionized water. UV-Vis measurements were performed by successively adding CF solutions ( $4.12$ – $11.8 \times 10^{-4}$  M) to the FA solution ( $0.088 \times 10^{-4}$  M) and CF solutions ( $4.12$ – $9.16 \times 10^{-4}$  M) to the SA solution ( $0.076 \times 10^{-4}$  M). Fluorescence measurements were performed by progressively adding caffeine solutions to both FA and SA solutions at temperatures of 310 K, 298 K, and 303 K.

To interpret the quenching mechanism of FA and SA by CF, the Stern–Volmer equation (Eq. (2.85)) was applied to calculate the bimolecular quenching rate constants. The modified binding constant and the number of binding sites were determined using Eq. (2.90). Molecular interactions and thermodynamic parameters, such as enthalpy and entropy, were obtained using the van't Hoff equation (Eq. (2.91)) and Gibbs free energy (Eq. (2.92)).

FTIR analysis was performed to investigate the structural interactions between FA, SA, and CF. The samples were prepared as solutions and then converted to powders by evaporating the solvent. The resulting powders were analyzed using FTIR, and spectra were recorded over the range of  $400$ – $4000$   $\text{cm}^{-1}$  at a resolution of  $4$   $\text{cm}^{-1}$ .

## 3.5 Computational Methods

### 3.5.1 Density Functional Theory

Geometric optimizations of FA and SA were performed using semiempirical MP6 and Hartree-Fock methods with the B3LYP functional and the 6-311++G (d,p) basis set. Further refinements were carried out using DFT with the B3LYP functional and various basis sets such as STO-3G\*, SDD, 3-21+G\*, Aug-CC-pVDZ, 6-31++G(d,p), LANL2DZ, and 6-311++G(d,p) to understand effect of methods and basis sets on optimizations of structure. Calculations were performed in gas and various solvents, including chloroform, benzene, dichloromethane, ethanol, acetone, methanol, dimethyl sulfoxide, and acetonitrile. Solvent

effects were incorporated using the polarizable continuum model (IEFPCM). The optimized geometries were validated via vibrational frequency analysis to confirm the absence of imaginary frequencies. Convergence criteria, including the maximum force, RMS force, maximum displacement, RMS displacement, and energy change, were checked to ensure reliability of the results. A temperature range of 100 K to 1000 K was used to evaluate the thermodynamic properties of the selected molecules. From the DFT-optimized structures, optimized molecular structural parameters, such as bond lengths, bond angles, dihedral angles, FTIR, thermodynamic properties, HOMOs, LUMOs, and chemical reactivity descriptors, such as chemical potential (Eq. (2.131)), electronegativity (Eq. (2.132)), chemical hardness (Eq. (2.133)), global softness (Eq. (2.134)), and electrophilicity index (Eq. (2.135)), were analyzed. Furthermore, absorption and fluorescence emission spectra were simulated via TDDFT based on the optimized geometries of the compounds in both their ground-state and excited-state configurations, to provide comprehensive insights into their optical properties.

### 3.5.2 Molecular Docking Methods

**Protein preparation:** The three-dimensional structures of the anticancer proteins (3M18, 5EKN, and 6YKY) were downloaded from the Research Collaboratory for Structural Bioinformatics (RCSB) Protein Data Bank. In Discovery Studio 2021 (Pawar and Rohane, 2021), nonessential water molecules were removed, and sphere-based docking (SBD) spheres were generated to define binding sites, with coordinates (x, y, z) and radii saved in a cofi.txt file. Polar hydrogen atoms were added to ensure proper protonation and complete valence states. Ligands were removed, and the cleaned protein structures were saved in .pdb format for further analysis and docking simulations.

**Ligand Preparation:** The two-dimensional chemical structures of ferulic acid, sinapic acid, caffeine, and amoxillin were sketched using ChemDraw Ultra 8.0 (Mendelsohn, 2004). These ligands were optimized using DFT with the B3LYP functional and the 6-311++G (d,p) basis set in Gaussian 09 (Frisch et al., 2009). Stability was confirmed by verifying the absence of imaginary frequencies, indicating a local minimum on the potential energy surface. The ligands were then saved in pdb format for further analysis and docking simulations.

**Protein–ligand docking:** For protein–ligand docking, the protein structures (3M18, 5EKN, and 6YKY) were imported into AutoDock Vina version 1.5.7 (Trott and Olson, 2010). Kollman charges, Gasteiger charges, and AD4 atom types were assigned to the proteins, and the modified structures were saved in .pdbqt format. The ligands (ferulic acid and sinapic acid) were also imported into AutoDock Vina version 1.5.7, where torsion trees were generated to identify rotatable bonds. Their configurations were then saved in .pdbqt format. A grid box was created around the protein to define the docking space, and specific ligand mapping was applied. Docking simulations were executed via the command prompt, and protein–ligand interactions were analyzed and visualized in both two-dimensional and three-dimensional formats via Discovery Studio 2021.

**Multiple ligand docking:** For multiple ligand docking, the proteins (3M18, 5EKN, and

6YKY) were imported into PyRx (Dallakyan and Olson, 2015) and subsequently converted to pdbqt. Ligands (ferulic acid, sinapic acid, caffeine, and amoxicillin) were prepared via Open Babel, energy-minimized, and saved in pdbqt. Docking simulations were performed for ligand complexes, including ferulic acid-caffeine (FA-CF), sinapic acid-caffeine (SA-CF), FA-CF-amoxicillin (FA-CF-AMX), and SA-CF-amoxicillin (SA-CF-AMX). Using PyRx's Wizard functionality, a grid box was centered over the active site of each protein to ensure biologically relevant docking. The simulations analyzed the binding affinities and interaction patterns of each complex, providing insights into protein–ligand interactions.

# 4

---

## RESULTS AND DISCUSSION

---

This chapter presents the results and analysis of the study. Section 4.1 covers Solvatochromic effects, including the absorption and emission spectra, optical transition probabilities, dipole moments, and photophysical properties of FA and SA. Section 4.2 explores how concentration affects the fluorescence spectra of FA and SA. Section 4.3 discusses quenching of FA and SA by caffeine, focusing on the Stern-Volmer equation, thermodynamic parameters, UV-Vis absorption, and FTIR spectra. Section 4.4 presents quantum chemical calculations, including molecular structure optimization, thermodynamic analysis, molecular orbitals, dipole moments, chemical reactivity, electrostatic potential, and spectral analysis. Furthermore, Section 4.5 examines molecular docking, ligand-protein binding, amino acid interactions, and multiligand binding with proteins.

### 4.1 Solvatochromic Effects

#### 4.1.1 Absorption and Emission Spectra

Solvent effects on absorption and emission provide valuable insights into photophysical properties, such as changes in dipole moment and molecular polarizability, leading to spectral shifts. These shifts result from solvation, where solvent molecules influence the electronic structure and geometry of solute molecules, affecting their absorption and emission spectra. Thus, variations in solvent polarity can significantly impact drug stability and behavior in biological environments (Lalasanghi et al., 2024). The UV-Vis absorption and fluorescence spectra of FA and SA were measured in eight different solvents, including acetonitrile, dimethyl sulfoxide, ethanol, isopropanol, methanol, distilled water, chloroform, and dichloromethane, as shown in Figs. 4.1 and 4.2, respectively. The corresponding shifts in absorption and emission maxima, depending on the solvent polarity, are summarized in Table 4.1. Both compounds showed a bathochromic shift (longer wavelength) in their absorption maxima as the solvent polarity increased, indicating a  $\pi \rightarrow \pi^*$  transition. For FA, the primary absorption band occurred between 275–325 nm, with a weaker absorption band from 325–350 nm (Fig. 4.1 (a)). In the case of SA, the strongest absorption was observed between 275–300 nm, and another band appeared between 300–350 nm (Fig. 4.1 (b)). The absorption maxima shifted by 10.9 nm for FA and 23.0 nm for SA, which was relatively

small compared to the shifts observed in their fluorescence spectra. This minimal shift in absorption maxima suggests that there is no significant charge transfer in the ground state of the compounds (Mannekutla et al., 2008). The results are consistent with previous reports on similar compounds (Belay et al., 2016b) and other studies on dyes (Shivaleela et al., 2022).

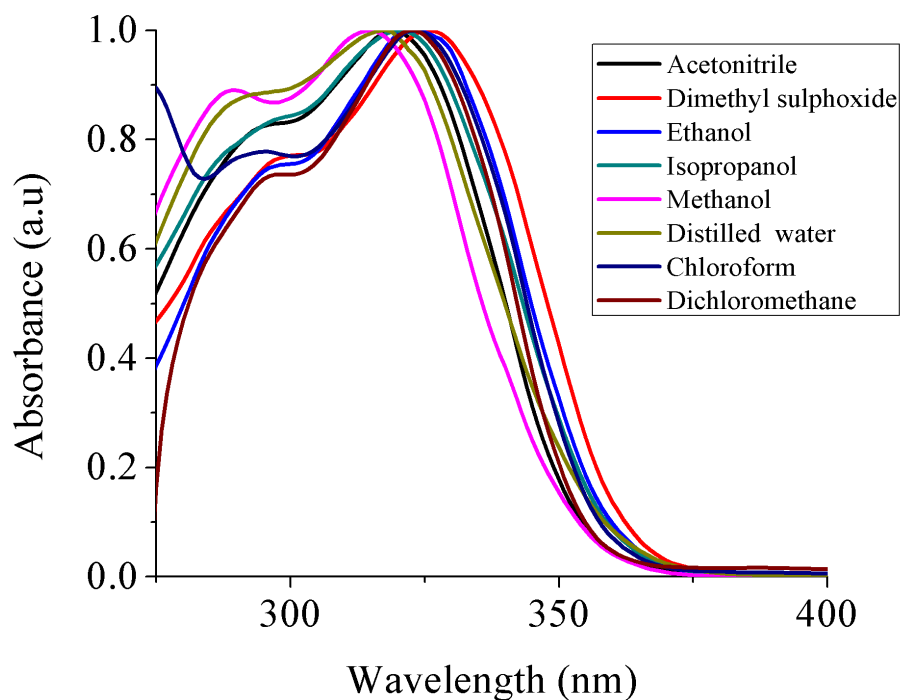
Table 4.1: Peak absorption and fluorescence spectra of FA and SA in solvents of various polarities.

Solvents	Ferulic acid		Sinapic acid	
	$\tilde{\nu}_a(cm^{-1})$	$\tilde{\nu}_f(cm^{-1})$	$\tilde{\nu}_a(cm^{-1})$	$\tilde{\nu}_f(cm^{-1})$
Acetonitrile	31347.96	24630.54	32679.74	24271.84
Dimetyly sulphoxide	30674.85	24509.80	30395.14	23696.68
Ethanol	31055.90	24271.84	30959.75	23809.52
Isopropanol	31250.00	24937.66	30581.04	23923.44
Methanol	31746.03	24038.46	32362.46	23041.47
Distilled water	31545.74	21739.13	31152.65	21978.02
Chloroform	30959.75	25252.53	30674.85	25125.63
Dichloromethane	30959.75	24813.90	30674.85	24390.24

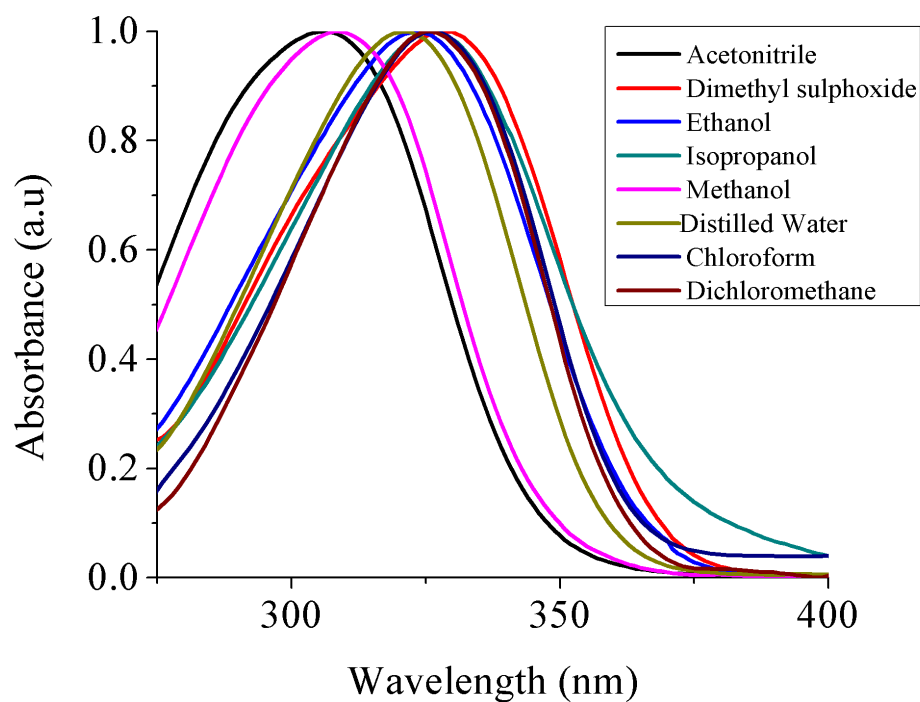
The normalized fluorescence spectra of FA and SA are presented in Fig. 4.2 (a) and (b), respectively. A significant observation is that the redshifts in the fluorescence maxima were much larger than the shifts observed in the absorption maxima. FA exhibited a redshift of 64.0 nm, and SA showed a redshift of 56.9 nm, as indicated in Fig. 4.2 (a) and (b), respectively. This difference in shift suggests that the solvent has a more considerable effect on the excited-state energy levels than on the ground-state levels. The smaller shift in the absorption spectra suggests that the ground-state energy distribution is less sensitive to solvent polarity. This is likely due to the relatively low polarity of FA and SA in the ground state and the reorientation of the solute with the solvent being very small. The more significant shift in fluorescence maxima in chloroform compared to distilled water suggests that specific interactions between the solute and the solvent in polar environments, particularly in alcoholic solvents, influence the excited-state properties of both compounds. Furthermore, the differences between shifts in fluorescence and absorption maxima (Table 4.1) suggest that the excited-state energy levels of the compounds are more sensitive to changes in solvent polarity. The observed red shift in fluorescence maxima indicates the presence of  $\pi / \pi$  transitions, which point to significant differences in charge distributions between the ground and excited states (Thanikachalam et al., 2014). These differences arise from stronger intermolecular interactions in the excited state, especially in polar solvents, further confirming that the excited-state properties of FA and SA are highly influenced by solvent polarity (Woldegiorges et al., 2021).

#### 4.1.2 Estimation of Dipole Moments

The dipole moments of FA and SA in both the ground and excited states were estimated by correlating absorption and fluorescence spectral data with the Lippert-Mataga (Eq. (2.94)),



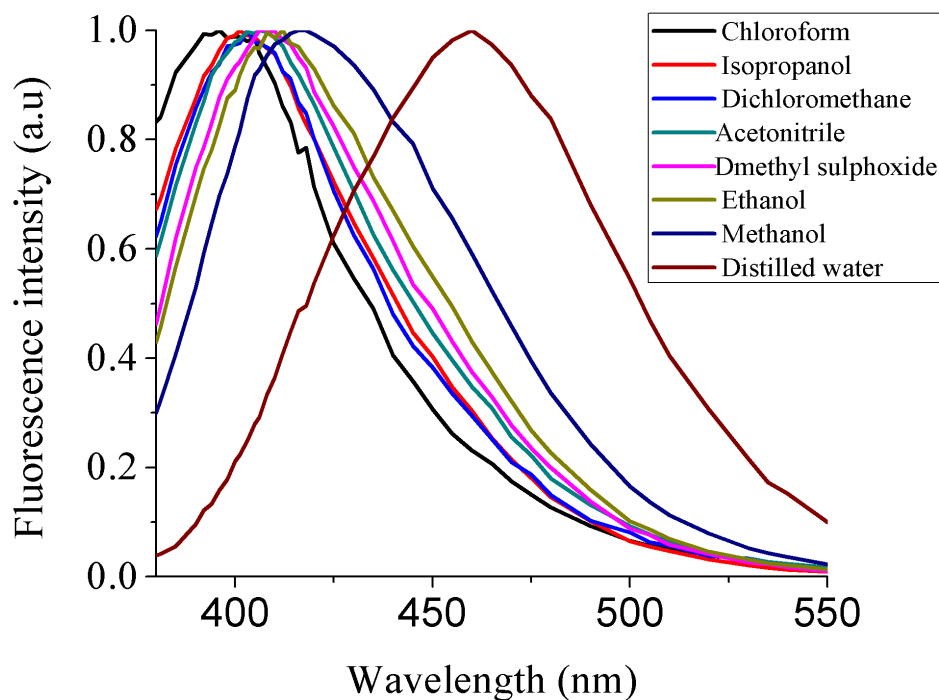
(a)



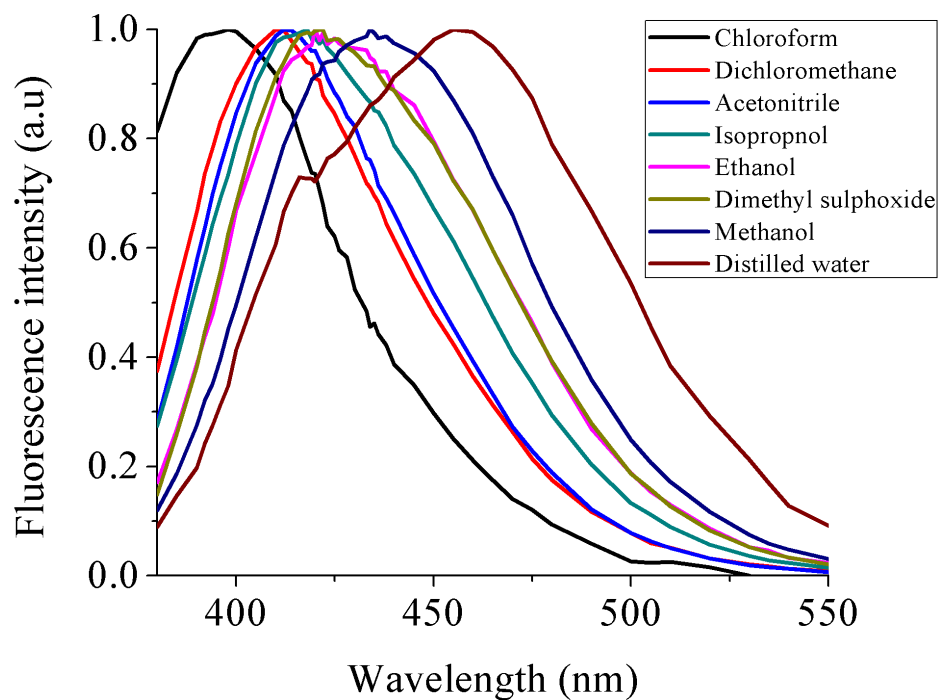
(b)

Figure 4.1: UV-vis absorption spectra of (a) ferulic acid and (b) sinapic acid in various solvents.

Bakhshiev (Eq. (2.95)), and Kawski-Chamma-Viallet (Eq. (2.96)). Table 4.2 provides the solvent polarity functions  $f_{LM}$  (Eq. (2.98)),  $f_{Back}$  (Eq. (2.99)), and  $f_{KCV}$  (Eq. (2.100)) for various solvents. Figs. 4.3 to 4.6 illustrate the relationship between solvent polarity and spectral shifts as calculated by each model. Table 4.3 summarizes the slopes, intercepts,



(a)



(b)

Figure 4.2: Emission spectra of (a) ferulic acid and (b) sinapic acid in various solvents.

and correlation coefficients for the spectral shifts observed in FA and SA. The Lippert-Mataga model (Fig. 4.3) shows moderate linearity, with correlation coefficients of 0.54 for FA and 0.74 for SA, indicating a better fit for SA. The Bakhshiev model (Fig. 4.4) also shows moderate linearity, with correlation coefficients of 0.50 for FA and 0.58 for SA. The Kawski-Chamma-Viallet model (Fig. 4.5), however, shows poor linearity, with correlation

coefficients of 0.32 for FA and 0.41 for SA, suggesting that this model is less effective in describing the solvent effects on these molecules. In contrast, the ENT model (Fig. 4.6) provides the best fit, with correlation coefficients of 0.81 for FA and 0.76 for SA, indicating that it most accurately describes the relationship between solvent polarity and spectral shifts.

The deviations in linearity, particularly with the Kawski-Chamma-Viallet model, can be attributed to the way each model accounts for solvent polarity. The Lippert-Mataga (Lippert, 1955; Mataga et al., 1956) and Bakhshiev models (Bakhshiev et al., 1969) use empirical relationships that account for changes in dipole moments in various solvents, but they may not fully capture all the factors influencing solvent-solute interactions. The Kawski-Chamma-Viallet model (Kawski et al., 2002; Bilot and Kawski, 1962) employs a more complex function, which may not be suitable for these molecules if their solvent interactions are not properly represented. On the other hand, the  $E_T^N$  model considers both electrostatic and specific interactions between the solute and solvent at the molecular level, leading to better linearity and more accurate results (Reichardt, 1979). The higher correlation coefficients for the  $E_T^N$  model suggest that it is more effective in capturing the complex solvent effects on ferulic acid and sinapic acid.

Table 4.2: Solvent polarity functions of different solvents using the refractive index and dielectric constant.

Solvents	$^a n$	$^b \epsilon_r$	$^c f_{LM}$	$^d f_{Bakh}$	$^e f_{KCV}$	$^f f_{Rai}$	$^g E_T^N$
Acetonitrile	1.344	36.640	0.305	0.861	1.330	0.711	0.472
Dimethyl sulphoxide	1.479	47.240	0.263	0.841	1.489	0.656	0.441
Ethanol	1.361	24.300	0.289	0.812	1.303	0.665	0.654
Isopropanol	1.377	19.900	0.276	0.779	1.292	0.633	0.546
Methanol	1.330	32.700	0.308	0.854	1.304	0.710	0.762
Distilled water	1.333	80.100	0.320	0.914	1.367	0.758	1.000
Chloroform	1.442	4.810	0.150	0.373	0.972	0.295	0.259
Dichloromethane	1.424	8.930	0.217	0.590	1.166	0.470	0.320

<sup>a</sup> refractive index of the solvents, <sup>b</sup> dielectric constant, <sup>c</sup> Lippert-Mataga solvent polarity function using Eq. (2.98), <sup>d</sup> Bakhshiev solvent polarity function using Eq. (2.99), <sup>e</sup> Kawski-Chamma-Viallet solvent polarity function using Eq. (2.100), <sup>f</sup> Reichardt solvent polarity function using Eq. (2.102), and <sup>g</sup> Empirical molecular-microscopic solvent polarity function.

Table 4.4 displays the dipole moments of FA and SA in both the ground and excited states. The variation of the dipole moment of the excited state obtained by different Solvatochromic methods is due to the different assumptions of the methods. The ground state dipole moments were calculated using Eq. (2.108) from the slopes ( $m_1$ ) of the Bilot-Kawski method, giving values of 0.86 D for FA and 1.51 D for SA. The excited state dipole moments were determined using Eq. (2.109) from the slopes of the same method, resulting in values of 4.21 D for FA and 4.86 D for SA. The excited state dipole moments are larger than the ground state ones, indicating that the solvent polarity affects the excited state more than the

Table 4.3: Slopes, intercepts, and correlation coefficients of spectral shifts for ferulic acid and sinapic acid.

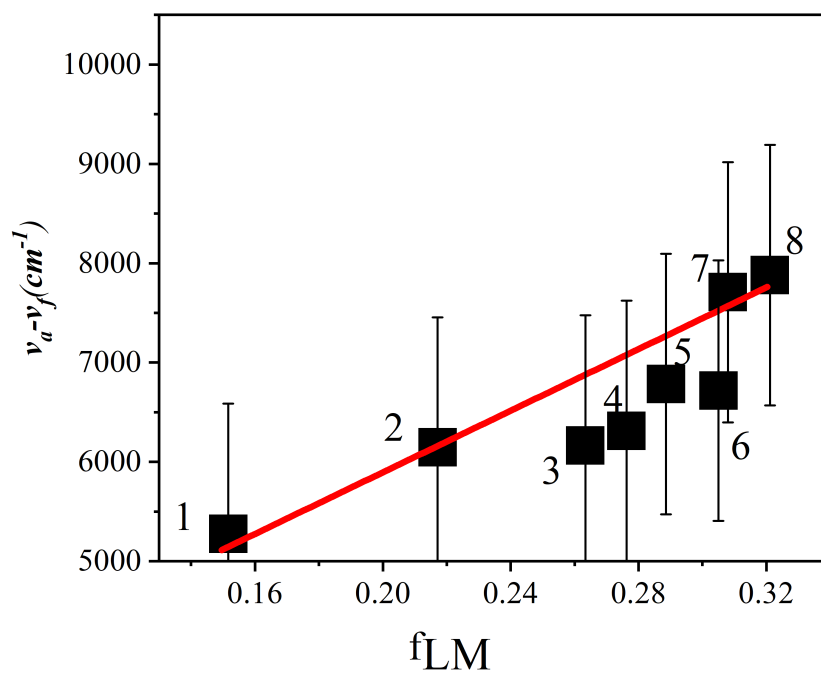
Correlations	Molecule	Slope	Intercept	Correlation coefficient
Lippert-Mataga	FA	14772.7	2592.50	0.54
	SA	23340.5	809.5395	0.74
Bakhshiev	FA	4312.7	3363.581	0.5
	SA	7436.5	1589.194	0.58
Kawaski-Chamma-Viallet	FA	2186.7	58429.79	0.32
	SA	4681	60768.94	0.41
$E_T^N$ correlation	FA	4276.1	4411.274	0.81
	SA	4528.2	4718.758	0.76

ground state. The ratio of  $\mu_e$  to  $\mu_g$  was calculated using Eq. (2.110), and obtained 4.90 for FA and 3.22 for SA. The excited state dipole moments from the Lippert-Mataga method (Eq. (2.94)) were 9.49 D for FA and 11.90 D for SA, while the Kawaski-Chamma-Viallet method (Eq. (2.95)) gave values of 5.07 D for FA and 6.38 D for SA, based on slopes  $m_3$  and  $m_4$ . The differences in  $\mu_e$  values depend on the method used. The Lippert-Mataga method give higher dipole moments than other methods because it does not consider polarizability, gives the highest value of  $\mu_e$ , and the solvent polarity parameter method, which takes into account certain solvent-solvent interactions (Lippert, 1955; Mataga et al., 1956). The increase in the excited state dipole moment may arise from charge density redistribution in excited electronic states, intramolecular bonding between solute and solvent, intermolecular charge transfer (ICT), and geometrical variations between electronic states (Grabowski et al., 2003). These findings are consistent with previous work (Belay et al., 2016b).

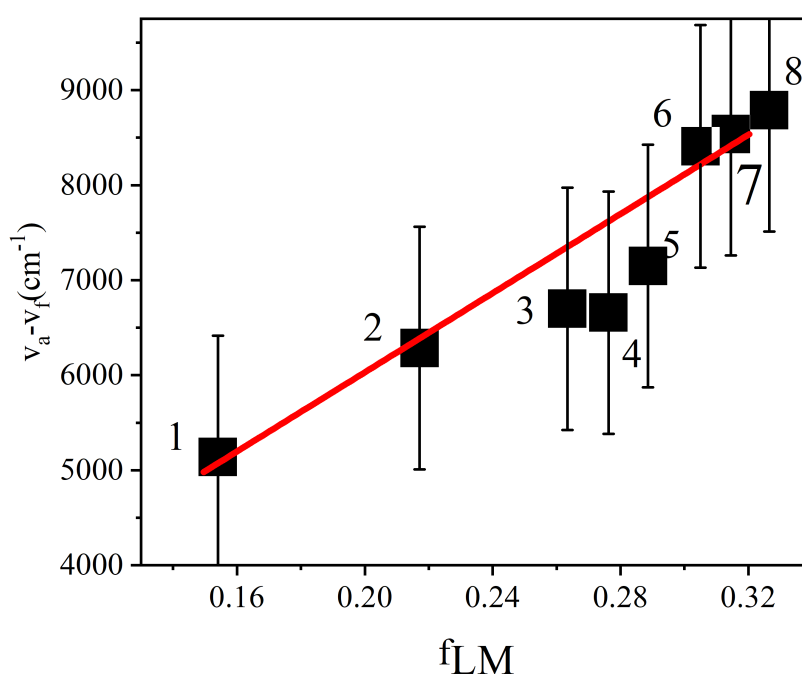
Table 4.4: Ground and excited state dipole moments (Debye) and Onsager cavity radius (Å) for ferulic acid and sinapic acid.

Drug	<sup>a</sup> $a$	<sup>b</sup> $\mu_g$	<sup>c</sup> $\mu_e$	<sup>d</sup> $\Delta\mu$	<sup>e</sup> $\Delta\mu$	<sup>f</sup> $\Delta\mu$	<sup>g</sup> $\Delta\mu$	<sup>h</sup> $\Delta\mu$
FA	3.88	0.86	4.21	9.49	5.07	5.67	5.41	4.90
SA	4.09	1.51	4.86	11.90	6.38	7.10	5.52	3.22

<sup>a</sup> Onsager cavity radius calculated from Eq.(2.107). <sup>b</sup> ground state dipole moments calculated from Eq. (2.108). <sup>c</sup> excited state dipole moments calculated from Eq. (2.109). <sup>d</sup> $\Delta\mu$  calculated from Lippert–Mataga. <sup>e</sup>  $\Delta\mu$  calculated from Bakhshiev. <sup>f</sup>  $\Delta\mu$  calculated from McRaechardt. <sup>g</sup>  $\Delta\mu$  calculated from molecular–microscopic solvent function ( $E_T^N$ ). <sup>h</sup>  $\frac{\mu_e}{\mu_g}$  is the ratio of excited state to ground state dipole moments calculated from Eq. (2.110).



(a)

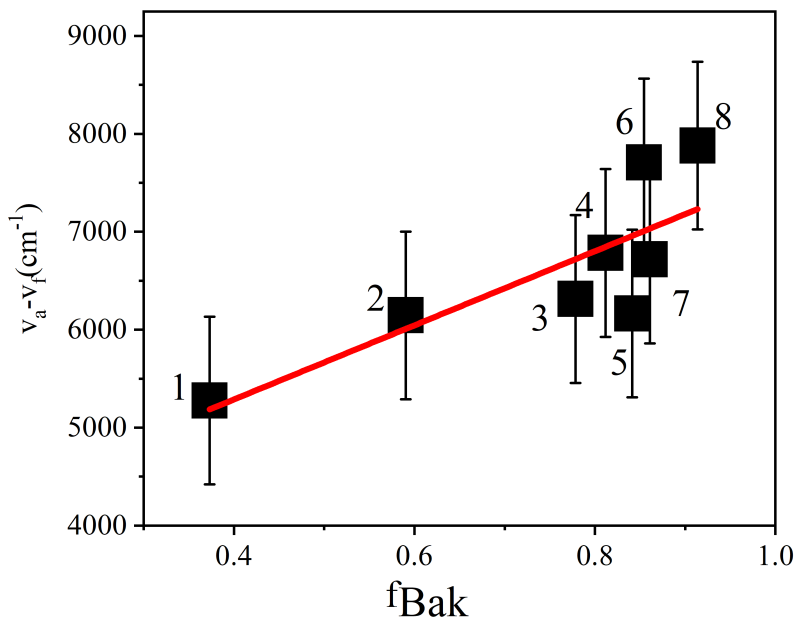


(b)

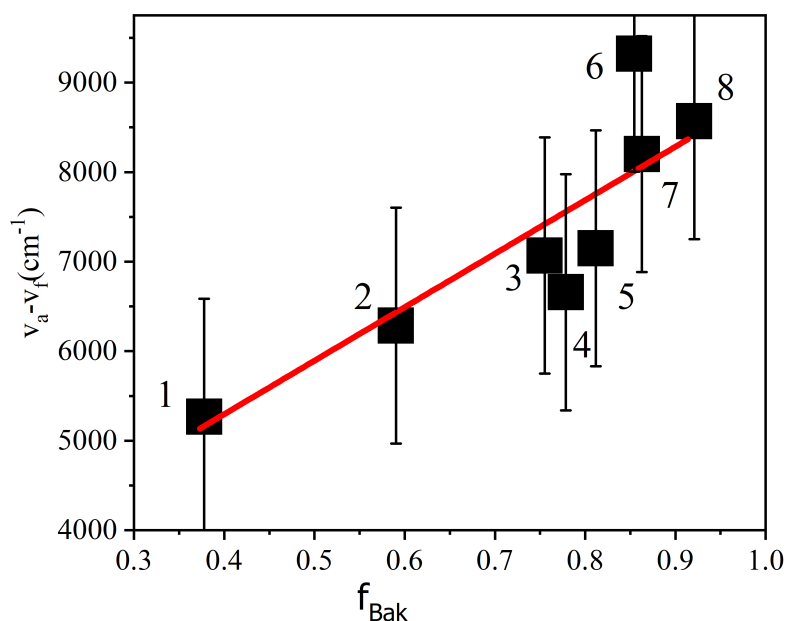
Figure 4.3: Plot of  $\tilde{\nu}_a - \tilde{\nu}_f$  versus the Lippert-Mataga solvent polarity function for (a) ferulic acid and (b) sinapic acid in various solvents: acetonitrile (1), dimethyl sulfoxide (2), ethanol (3), isopropanol (4), methanol(5), distilled water (6), chloroform (7), and dichloromethane (8).

### 4.1.3 Optical Transition and Photophysical Properties

The optical transition probability measures the likelihood that a molecule makes transition between different energy states upon absorbing or emitting light (Belay, 2012; Abraha



(a)

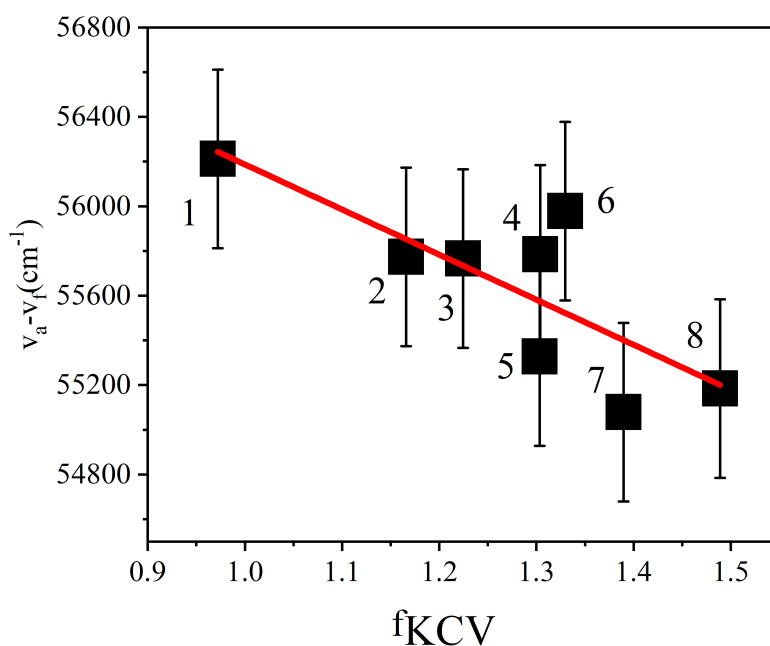


(b)

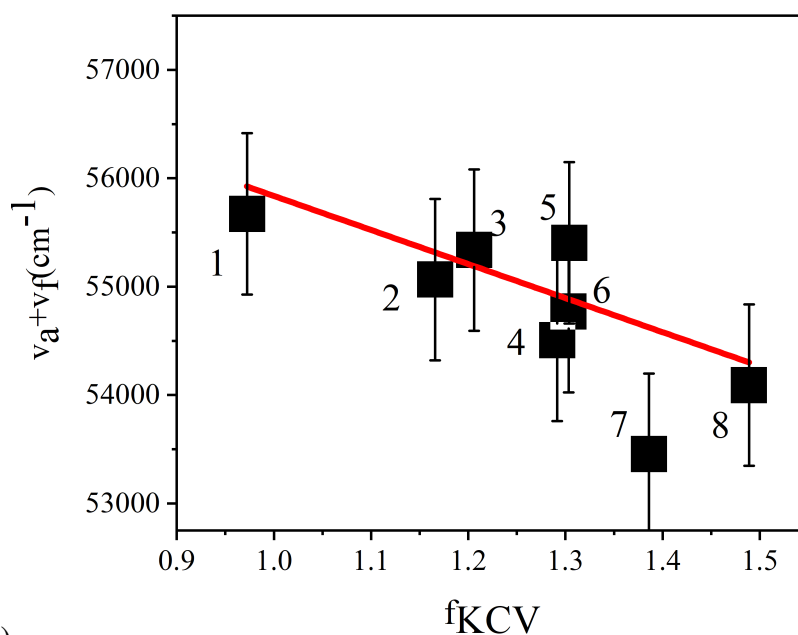
Figure 4.4: Plot of  $\tilde{\nu}_a - \tilde{\nu}_f$  versus Bakhshiev's solvent polarity function for (a) ferulic acid and (b) sinapic acid in various solvents: acetonitrile (1), dimethyl sulfoxide (2), ethanol (3), isopropanol (4), methanol(5), distilled water (6), chloroform (7), and dichloromethane (8).

et al., 2016a). Table 4.5 presents oscillator strength, molar extinction coefficient, integrated absorption cross-section, Einstein coefficients, and transition dipole moments.

Oscillator strength ( $f$ ) measures the likelihood of an electronic transition when a molecule absorbs light and is calculated using Eq. (2.71) (Belay, 2010). In Table 4.5, the  $f$  values for FA and SA differ across solvents. For FA, the highest  $f$  values (0.425) are



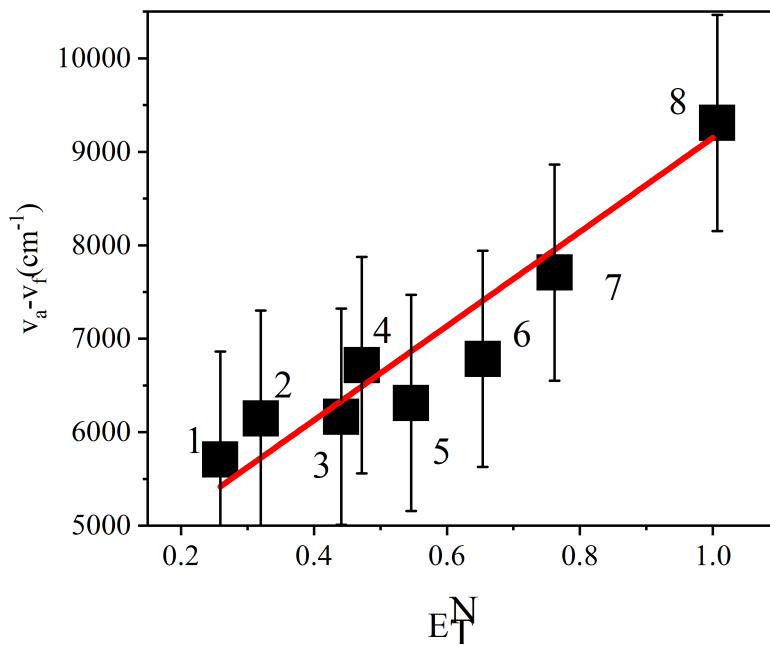
(a)



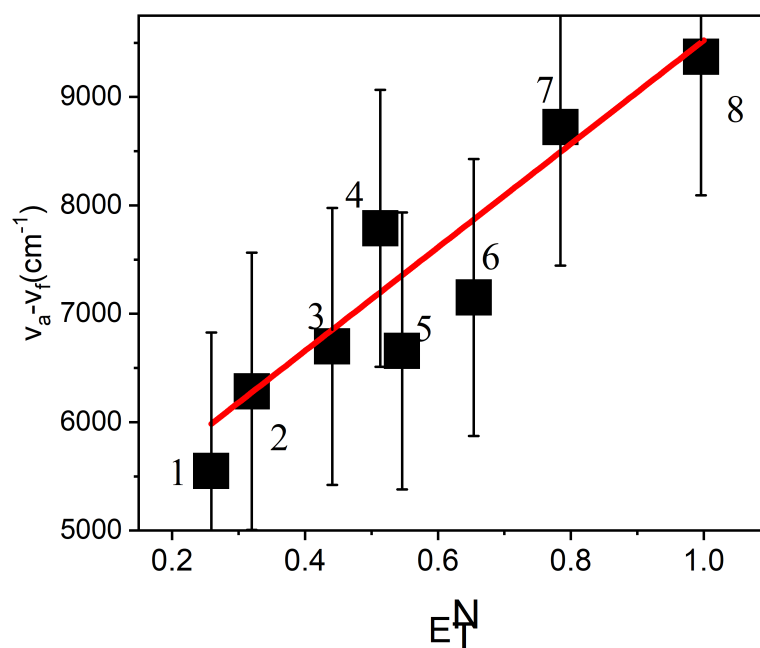
(b)

Figure 4.5: Plot of  $\tilde{\nu}_a + \tilde{\nu}_f$  versus the Kawski-Chamma-Violet solvent polarity function for (a) ferulic acid and (b) sinapic acid in various solvents: acetonitrile (1), dimethyl sulfoxide (2), ethanol (3), isopropanol (4), methanol (5), distilled water (6), chloroform (7), and dichloromethane (8).

found in DCM and water, indicating stronger transitions in these environments. For SA, the highest  $f$  (0.186) occurs in MeOH, with a significant value of 0.163 in water. These results highlight the influence of solvent polarity on electronic transitions. A similar trends were observed on recent study of levofloxacin and norfloxacin in various solvents (Woldegiorges



(a)



(b)

Figure 4.6: Plot of  $\tilde{\nu}_a - \tilde{\nu}_f$ , (cm $^{-1}$ ) versus the  $E_T^N$  microscopic solvent polarity function for (a) ferulic acid and (b) sinapic acid in various solvents: acetonitrile (1), dimethyl sulfoxide (2), ethanol (3), isopropanol (4), methanol(5), distilled water (6), chloroform (7), and dichloromethane (8).

et al., 2022).

The absorption cross-section ( $\delta_t$ ) measures how likely a molecule is to absorb light and is calculated using Eq. (2.73). For both FA and SA,  $\delta_t$  values increase in polar solvents like water and methanol. For example, the  $\delta_t$  value for FA in water ( $1.30 \cdot 10^{21}$  cm $^2$ ) is

Table 4.5: Optical transition probabilities of ferulic acid and sinapic acid in polar and nonpolar solvents.

Drug	Media	A	f	$\int \frac{\varepsilon(\nu)d\nu}{10^8}$	$\int \alpha(\nu)d\nu$	$\delta_t$ 10 <sup>-21</sup>	$B_{km}$ 10 <sup>21</sup>	$A_{km}$ 10 <sup>10</sup>	$\mu_{km}$ 10 <sup>-29</sup>
FA	Chl	0.142	0.162	0.374	2155.65	0.496	4.40	1.76	0.14
	DCM	0.297	0.425	3.460	19925.09	0.458	0.926	37.0	8.81
	DMSO	0.214	0.127	0.295	1698.12	0.390	3.04	12.2	2.79
	MeOH	0.189	0.221	0.511	2940.30	0.676	7.79	31.1	3.99
	W	0.344	0.425	0.985	5669.84	1.30	6.65	26.6	5.50
SA	Chl	0.147	0.155	0.358	2000.06	0.473	7.13	6.95	3.39
	DCM	0.122	0.116	0.268	1000.54	0.354	4.88	4.76	2.93
	DMSO	0.119	0.119	0.275	1000.59	0.364	5.00	4.88	3.01
	MeOH	0.173	0.186	0.430	2000.48	0.569	8.25	8.05	3.62
	W	0.993	0.163	0.377	2000.17	0.499	6.88	6.71	3.53

much higher than in chloroform ( $0.496 \times 10^{-21} \text{ cm}^2$ ). A higher  $\delta_t$  indicates that the molecule absorbs more light, leading to greater excitation (Pernas and Cantelar, 2005). This suggests that polar solvents enhance solute-solvent interactions, making absorption more efficient. These findings align with previous reports (Fahmy et al., 2018). The molar extinction coefficient ( $\epsilon$ ) reflects a molecule's ability to absorb light per unit concentration. The higher the extinction coefficient is, the stronger the absorption at a given concentration. Table 4.5 shows that FA and SA in polar solvents such as methanol and water exhibit relatively high extinction coefficients. For example, the extinction coefficient for FA in water (0.985) is significantly greater than in chloroform (0.374), further reinforcing the influence of solvent polarity on absorption strength.

Einstein coefficients ( $B_{km}$  and  $A_{km}$ ) measure the transition probabilities for the absorption and emission processes and is calculated using Eq. (2.74). A higher value for these coefficients indicates a faster transition between energy states (Renk and Renk, 2012). In Table 4.5, FA in dichloromethane has a particularly high absorption transition rate, with  $A_{km}$  reaching  $37.0 \times 10^{10} \text{ s}^{-1}$ . Similarly, both FA and SA show relatively higher transition rates in methanol and dichloromethane, suggesting that these solvents facilitate quicker transitions. The transition dipole moment ( $\mu_{km}$ ), which represents the spatial separation between the charge distributions in the ground and excited states, is critical in determining the strength of optical transitions and is calculated using Eq. (2.76). From Table 4.5, it is clear that FA in methanol has the largest transition dipole moment ( $31.1 \times 10^{-29} \text{ C cm}$ ), whereas SA also has the highest dipole moment in methanol ( $8.05 \times 10^{-29} \text{ C cm}$ ). Larger transition dipole moments typically indicate stronger transitions (Grechko and Zanni, 2012).

Photophysical properties describe how molecules interact with light, including absorption and emission (Grabowski and Gantt, 1978). The Solvatochromic effect modifies these properties by changing a molecule's electronic structure in response to solvent polarity, resulting in shifts in absorption and emission wavelengths, fluorescence intensity, and quantum yield (Melavanki et al., 2012). The photophysical properties of FA and SA were

Table 4.6: Solvent-dependent photophysical properties of ferulic acid and sinapic acid.

Solvents	Ferulic acid					Sinapic acid				
	$\phi_f$	$\kappa_r$ 10 <sup>8</sup>	$\kappa_{nr}$ 10 <sup>8</sup>	$\tau_0(ns)$	$\tau_f(ns)$	$\phi_f$	$\kappa_r$ 10 <sup>6</sup>	$\kappa_{nr}$ 10 <sup>8</sup>	$\tau_0(ns)$	$\tau_f(ns)$
Chl	0.562	0.147	1.15	6.80	3.82	0.163	9.35	0.480	0.011	0.174
DCM	0.080	0.629	7.23	0.159	1.27	0.151	6.22	0.35	0.016	0.243
DMSO	0.122	0.583	41.9	0.0172	0.210	0.087	6.30	0.661	0.016	0.138
MeOH	0.112	0.104	8.23	0.964	0.108	0.061	7.86	1.21	0.013	7.76
W	0.026	0.232	8.68	0.420	1.120	0.032	6.68	2.02	0.150	4.79

measured at room temperature and calculated using Eqs. (2.80–2.84). The results are presented in Table 4.6.

The fluorescence quantum yield ( $\phi_f$ ) measures the efficiency of fluorescence emission, reflecting how effectively a molecule converts absorbed energy into emitted light (Grabowski and Gantt, 1978). It is calculated using Eq. (2.80). Table 4.6 reveals that FA has the highest fluorescence quantum yield in chloroform (0.562), compared to lower values in dichloromethane (0.080) and water (0.026). Similarly, SA exhibits the highest yield in chloroform (0.163), with a lower value in water (0.032). This trend suggests that nonpolar solvents, like chloroform, enhance fluorescence efficiency for both FA and SA, likely due to reduced solvation and minimized excited state quenching (Tamaki, 1982).

The radiative decay rate ( $\kappa_r$ ) represents the rate at which a molecule relaxes to its ground state via photon emission (Addison, 2015). In chloroform FA results in the highest radiative decay rate (0.147  $\times 10^8$  s<sup>-1</sup>), and in methanol and water, the rates are considerably lower. This suggests that FA in chloroform undergoes faster radiative transitions, which is consistent with the higher fluorescence quantum yield in this solvent. For SA, a similar trend was observed, with chloroform showing the highest radiative decay rate (9.35  $\times 10^8$  s<sup>-1</sup>).

The nonradiative decay rate ( $\kappa_{nr}$ ) is a critical parameter for understanding the loss of energy through nonradiative processes such as internal conversion or vibrational relaxation (Addison, 2015). From the Table 4.6, it is clear that FA and SA exhibit lower nonradiative decay rates in chloroform and dichloromethane than in more polar solvents such as water and methanol. For example, the nonradiative decay rate for FA in water is 8.68  $\times 10^8$  s<sup>-1</sup>, which is significantly higher than that in chloroform (1.15  $\times 10^8$  s<sup>-1</sup>), indicating that polar solvents favor nonradiative decay processes.

The fluorescence lifetime ( $\tau_f$ ) provides additional insight into the dynamics of fluorescence (Krystkowiak et al., 2006). For FA, the longest fluorescence lifetime was observed in chloroform (3.82 ns), and SA had a slightly longer fluorescence lifetime in dichloromethane (1.27 ns) than the other solvents. As the solvent polarity increases, the fluorescence lifetime decreases due to enhanced nonradiative decay (Vollmer and Rettig, 1996).

#### 4.1.4 Effect of Concentration on Photophysical Properties

Concentration can affect photophysical properties, such as fluorescence quantum yields, fluorescence lifetime, and fluorescence intensity spectra (Grabowski and Gantt, 1978). Fig.

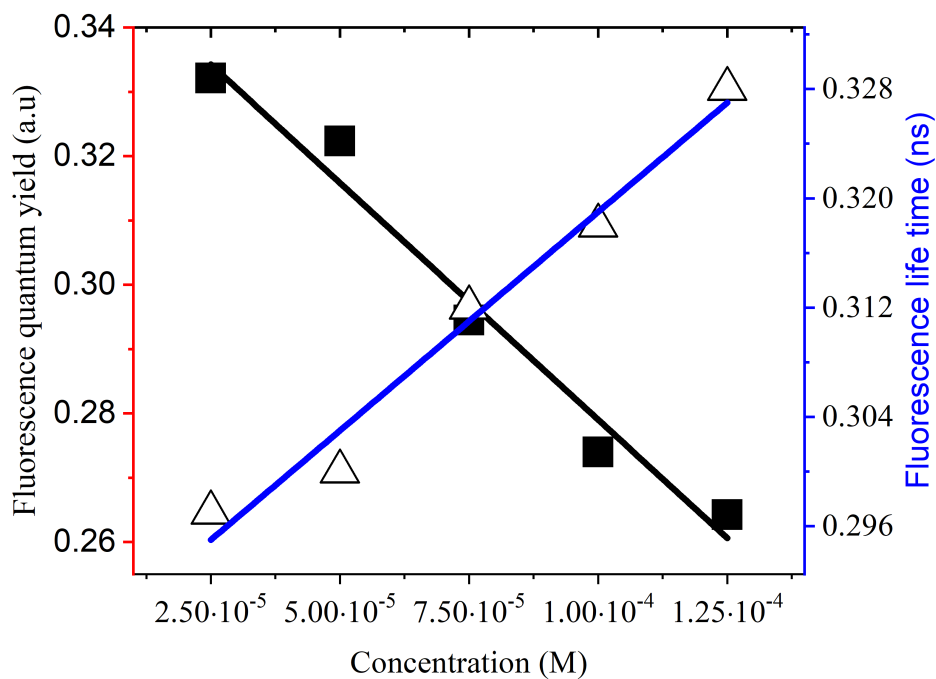
4.7 (a) and (b) show the fluorescence quantum yields of FA and SA at different concentrations. As concentration increases, the fluorescence quantum yield decreases. This reduction is may due to self-quenching and concentration quenching, where molecules become closely packed at higher concentrations. It promotes nonradiative processes such as fluorescence resonance energy transfer (FRET) and excimer formation. Excimers, which form when excited molecules interact, emit less efficiently than individual monomers, resulting in a significant drop in fluorescence efficiency (Barzykin et al., 1991). The increased molecular interactions at higher concentrations, such as energy transfer between molecules or excimer formation, lead to a loss of fluorescence energy as heat instead of light, reducing the overall fluorescence intensity (Taneja et al., 1995). A similar trend has been observed in phenylalanine solutions, where increased concentration leads to more self-quenching and excimer formation, ultimately decreasing the fluorescence quantum yield (Melhuish, 1961).

Fig. 4.7 (a) and (b) also show that fluorescence lifetime increases with concentration. This effect can be attributed to restricted molecular motion at higher concentrations, which slows the radiative decay process. As molecules come closer together, the transition from the excited state to the ground state becomes slower, leading to a longer fluorescence lifetime. The efficiency of radiative decay decreases because intermolecular interactions become more significant, and internal conversion processes also contribute to this extended lifetime. Despite the reduction in fluorescence intensity due to quenching effects, the fluorescence lifetime is prolonged as concentration increases (Johnson, 1980).

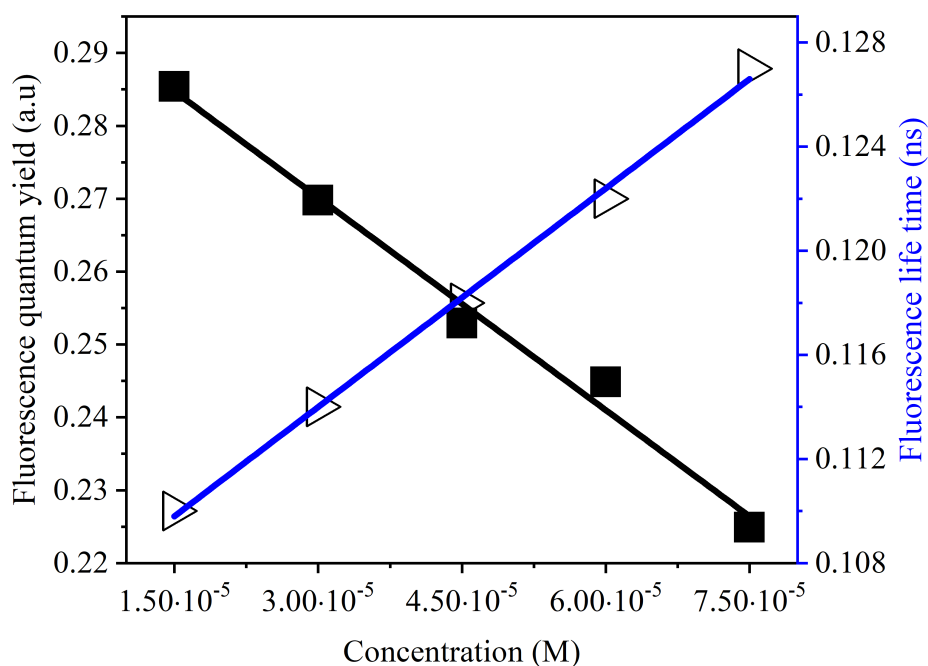
Concentration also influences fluorescence intensity spectra, as shown in Fig. 4.8 and Fig. 4.9. For FA, the concentration ranges from 1.72 mM to 4.41 mM, while for SA, it ranges from 2.10 mM to 5.95 mM. A blueshift in emission wavelength is observed as concentration increases. This is clearly observed in inset Fig. 4.8 and Fig. 4.9. This blueshift results from molecular interactions like aggregation and  $\pi$  -  $\pi$  stacking, which intensify at higher concentrations. These interactions strain the fluorophore molecules, altering their photophysical properties. Additionally, higher concentrations promote excimer formation, where excited-state dimers exhibit different properties from individual molecules. Changes in the solvent environment, such as variations in viscosity and polarity, also contribute to these spectral shifts. Similar trends have been reported in other systems, such as humic substances, where concentration-induced molecular aggregation leads to a decrease in fluorescence intensity and changes in spectral characteristics (Yang and Zhang, 1995).

#### 4.1.5 Fluorescence Quenching of FA and SA by Caffeine

Fig. 4.10 (a) and (b) display the emission spectra of FA and SA in the presence and absence of caffeine. In the absence of caffeine, FA and SA show emission maxima around 430 nm and 450 nm, respectively. Upon the addition of caffeine, a gradual decrease in fluorescence intensity is observed, which could result from static or dynamic quenching, or the inner filter effect (Ojha et al., 2012). A slight shift in the emission spectra is observed, likely due to the concentration dependence of the fluorophores. The observed quenching is



(a)



(b)

Figure 4.7: Variations in the quantum yield and fluorescence lifetime with concentration for (a) ferulic acid and (b) sinapic acid.

attributed to interactions between caffeine's nitrogen and oxygen atoms and the hydroxyl and carboxyl groups in FA and SA, involving hydrogen bonding, electron transfer, or  $\pi / \pi$  stacking. Hydrogen bonding can influence the electronic properties of a molecule, potentially affecting its excited-state stability and leading to non-radiative relaxation that

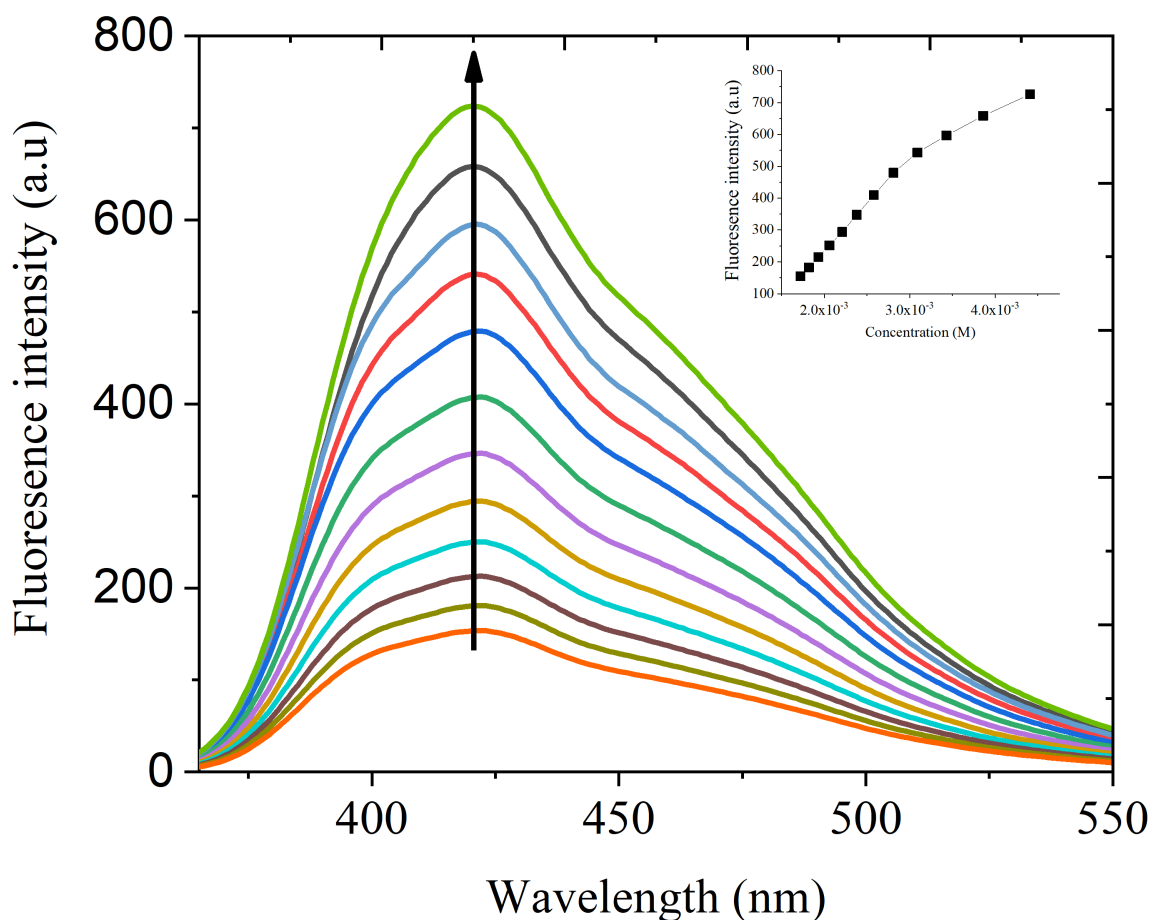


Figure 4.8: Fluorescence emission spectra of ferulic acid at various concentrations: (a) 1.72 mM, (b) 1.82 mM, (c) 1.93 mM, (d) 2.06 mM, (e) 2.21 mM, (f) 2.38 mM, (g) 2.58 mM, (h) 2.81 mM, (i) 3.09 mM, (j) 3.43 mM, (k) 3.86 mM, and (l) 4.41 mM. The inset shows the variation in fluorescence intensity with concentration.

reduces fluorescence intensity. This occurs because hydrogen bonds may facilitate energy transfer to the surrounding environment, thereby dissipating energy instead of emitting it as light Zhao and Han (2012).  $\pi / \pi$  stacking interactions occurring between aromatic rings can also influence quenching by stabilizing the excited state of the molecule Shirai et al. (1999). This interaction facilitates electron transfer or energy transfer to other parts of the molecule or surrounding environment, leading to fluorescence quenching. These results are consistent with previous studies on caffeic acid and chlorogenic acid (Belay et al., 2016a), demonstrating similar fluorescence quenching by caffeine. Moreover, caffeine has been shown to reduce fluorescence in other compounds, such as levofloxacin and norfloxacin (Woldegiorges et al., 2022), further supporting the conclusion that caffeine quenches fluorescence through molecular interactions.

To investigate the quenching mechanism, the interaction of caffeine with FA and SA was analyzed using the Stern-Volmer equation (Eq. (2.85)). The Stern-Volmer plots for FA-CF and SA-CF (Fig. 4.11 (a) and (b)) show linear relationships. The Stern-Volmer

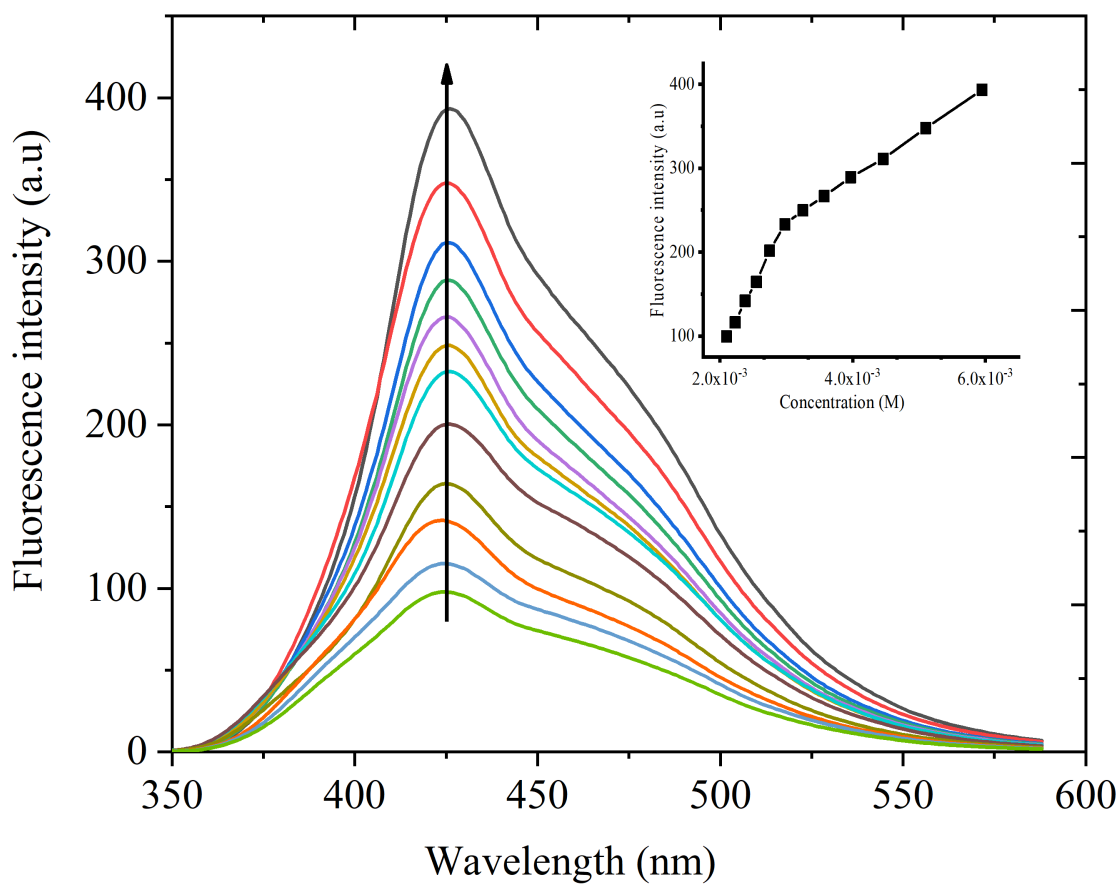
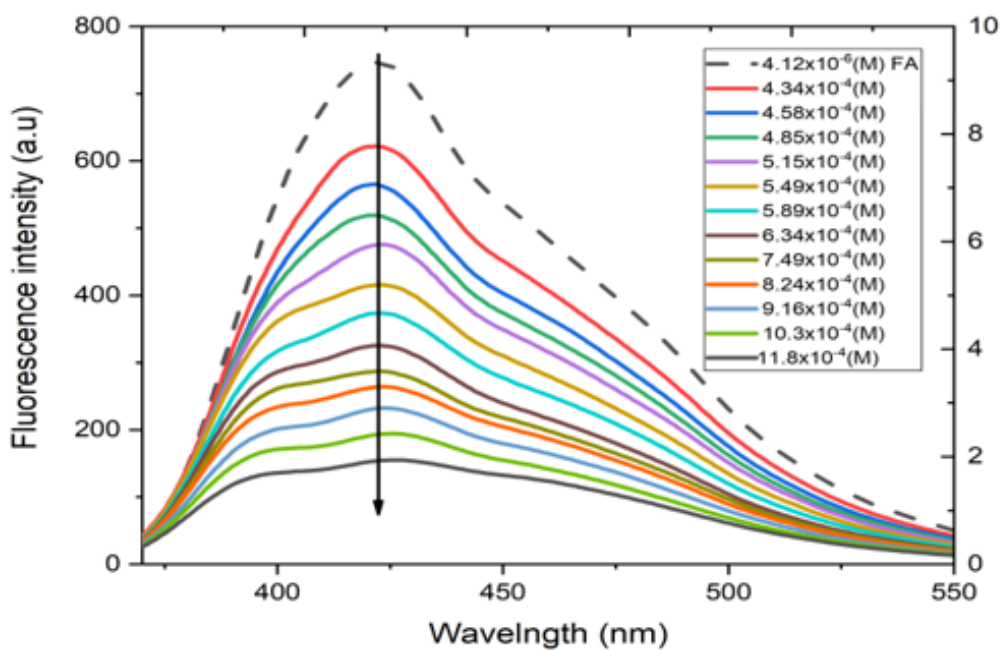


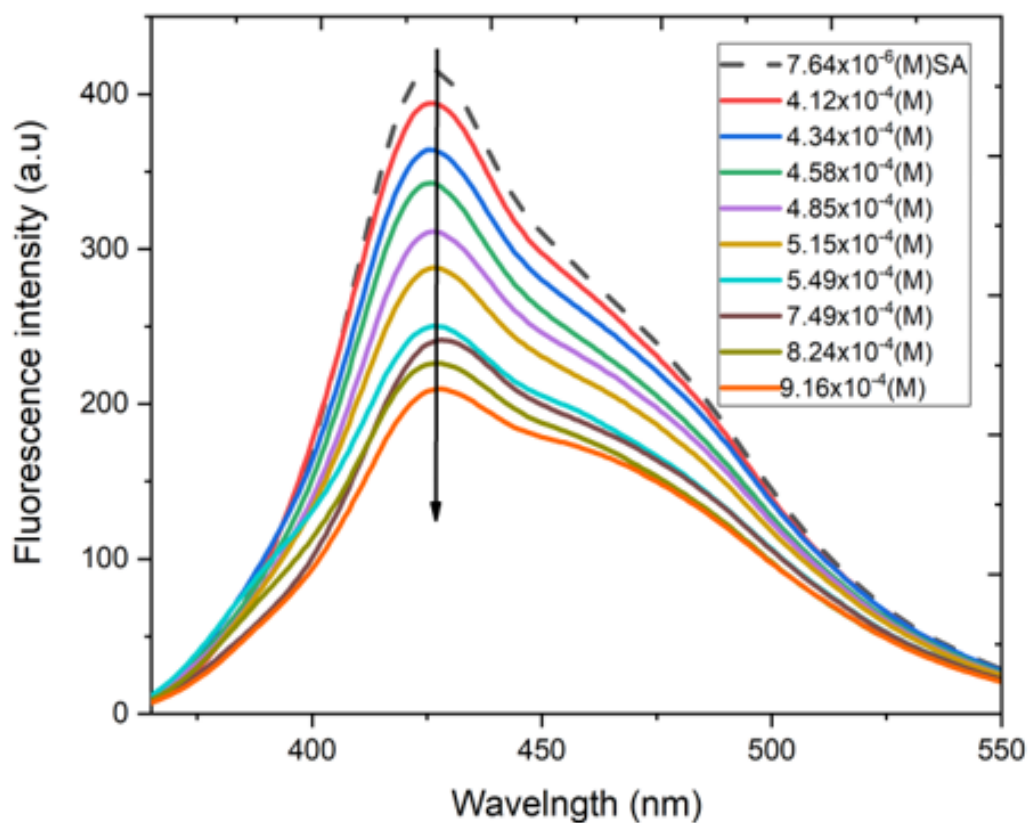
Figure 4.9: Fluorescence intensity spectra of sinapic acid at various concentrations: (a) 2.10 mM, (b) 2.23 mM, (c) 2.38 mM, (d) 2.55 mM, (e) 2.75 mM, (f) 2.98 mM, (g) 3.25 mM, (h) 3.57 mM, (i) 3.97 mM, (j) 4.46 mM, (k) 5.10 mM, and (l) 5.95 mM. The inset shows the variation in fluorescence intensity with concentration.

quenching constant, derived from the fluorescence intensity ratio ( $F_0/F$ ) against caffeine concentration, indicates a decrease in  $F_0/F$  values with increasing temperature from 298 K to 310 K. This reduction leads to a smaller slope in the plots, suggesting a static quenching mechanism. In this process, FA and SA form stable, nonfluorescent complexes with caffeine before being excited by light. These findings align with previous studies, which show that static quenching involves noncovalent interactions like hydrogen bonding, van der Waals forces, or electrostatic interactions, resulting in a non-emissive complex (Hu et al., 2005). Similar static quenching effects have been reported for caffeine's interactions with caffeic acid, chlorogenic acid (Belay et al., 2016a), levofloxacin, and norfloxacin (Woldegiorges et al., 2022), supporting the conclusion that caffeine quenches fluorescence through stable complex formation.

The bimolecular quenching rate constants ( $K_q$ ) for FA-CF and SA-CF interactions are calculated (Eq.(2.85)) from the slopes of the Stern–Volmer plots in Fig. 11 (a) and (b), respectively. The values of  $K_q$  are provided in Table 4.7. For FA, the  $K_q$  values are



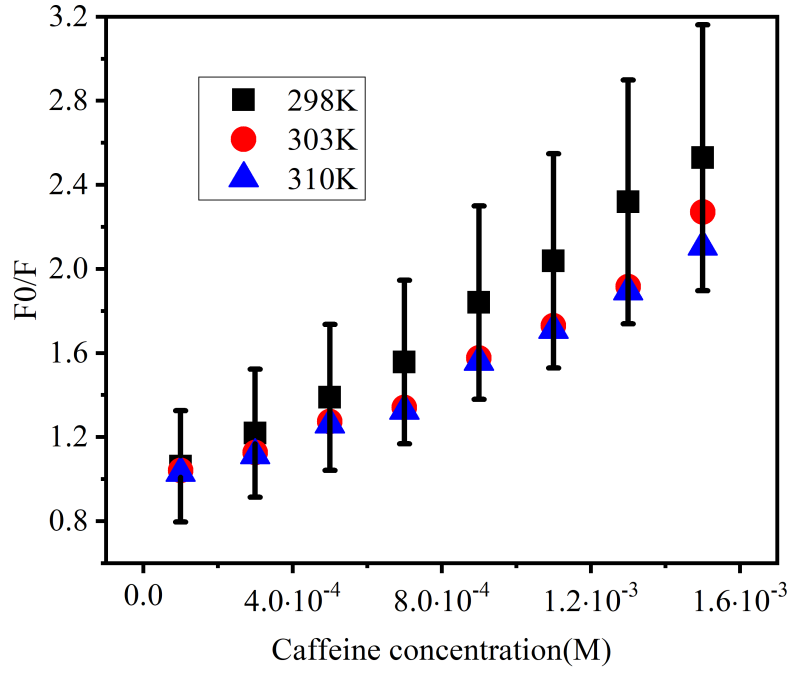
(a)



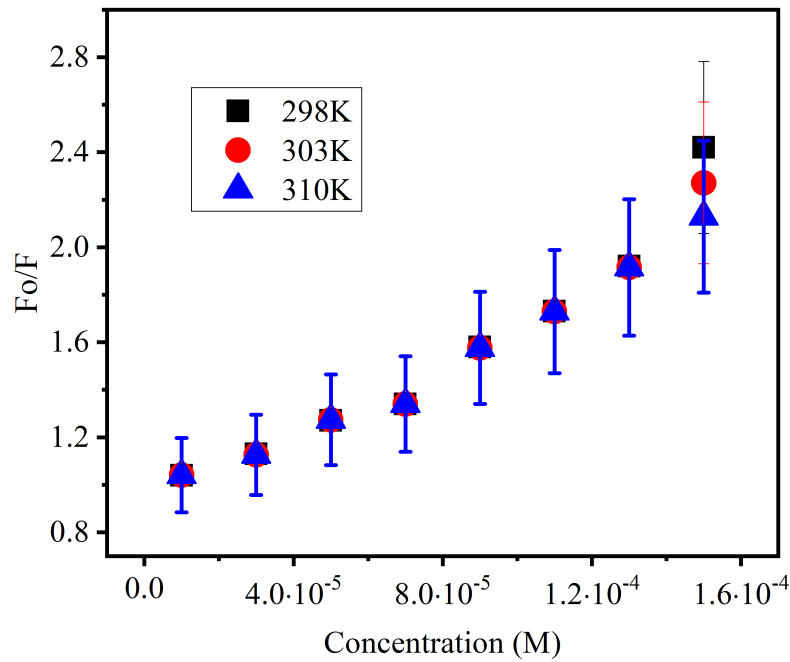
(b)

Figure 4.10: Fluorescence intensity spectra of (a) ferulic acid and (b) sinapic acid, in the presence and absence of different caffeine concentrations.

$1.13 \times 10^{11} \text{ M}^{-1} \text{ s}^{-1}$  at 298 K,  $0.88 \times 10^{11} \text{ M}^{-1} \text{ s}^{-1}$  at 303 K, and  $0.82 \times 10^{11} \text{ M}^{-1} \text{ s}^{-1}$  at 310 K. For SA, the values are  $1.29 \times 10^{11} \text{ M}^{-1} \text{ s}^{-1}$  at 298 K,  $1.21 \times 10^{11} \text{ M}^{-1} \text{ s}^{-1}$  at



(a)



(b)

Figure 4.11:  $F/F_0$  versus caffeine concentration for (a) ferulic acid and (b) sinapic acid at 298 K, 303 K, and 310 K.

303 K, and  $1.16 \cdot 10^{11} \text{ M}^{-1} \text{ s}^{-1}$  at 310 K. This decrease suggests static quenching as the main mechanism. The  $R$  values, approximately 1, show strong correlations for FA-CF and SA-CF, supporting static quenching. These findings are consistent with previous research on caffeine's interactions with nicotinamide (Abraha and Belay, 2023) and bovine serum

Table 4.7: Stern–Volmer constants ( $\kappa_{SV}$ ) and quenching rates ( $k_q$ ) for FA-CF and SA-CF interactions at different temperatures (T).

Drug	T (K)	$\kappa_{SV} (M^{-1})$	$k_q \cdot 10^{11} (M^{-1}s^{-1})$	R
FA	298	1081.13±0.75	1.13±0.0008	0.99±0.005
	303	845.25±1.90	0.88±0.0020	0.96±0.007
	310	789.88±1.84	0.82±0.0019	0.98±0.570
SA	298	9114.77±0.79	1.29±0.0011	0.99±0.0011
	303	8542.61±0.28	1.21±0.00039	0.96±0.013
	310	8237.62±0.36	1.16±0.00051	0.98±0.001

M: molarity; s: second

Table 4.8: Modified binding constant ( $K_a$ ), number of binding sites (n), and correlation coefficient (R) of caffeine with FA and SA interactions at different temperatures (K)

Drugs	T(K)	Log $K_a$	$\kappa_a (M^{-1}) \cdot 10^5$	n
Ferulic acid	298	3.634 0.081	4.387 0.858	1.207 0.026
	303	3.575 0.042	3.774 0.373	1.237 0.016
	310	3.432 0.063	2.73 0.374	1.140 0.026
Sinapic acid	298	4.93 0.01	0.85 0.023	1.3 0.001
	303	4.84 0.002	0.69 0.005	1.3 0.004
	310	4.75 0.03	0.57 0.03	1.2 0.008

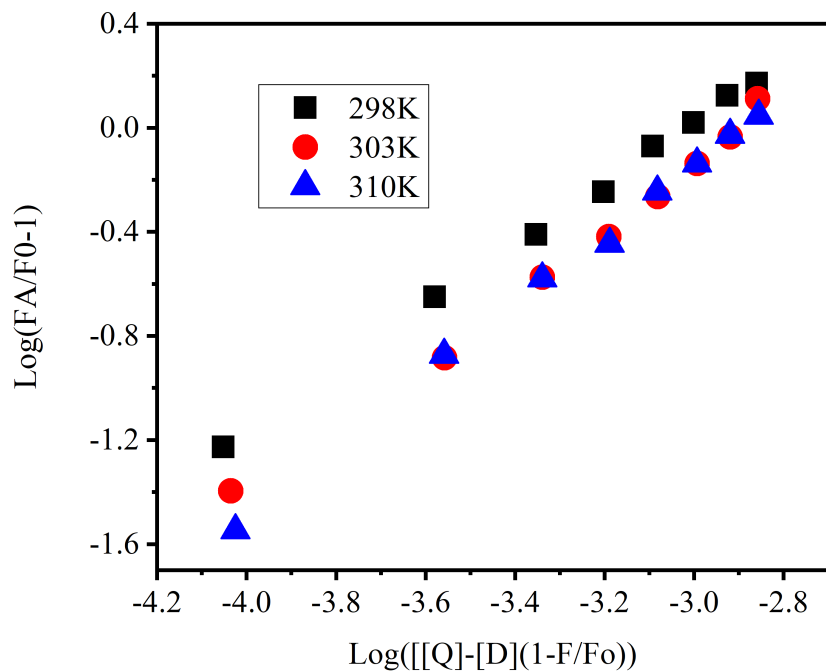
albumin (Wu et al., 2011). Therefore, the temperature dependence of  $K_q$  confirms static quenching in FA-CF and SA-CF systems.

#### 4.1.6 Binding Sites and Binding Constants

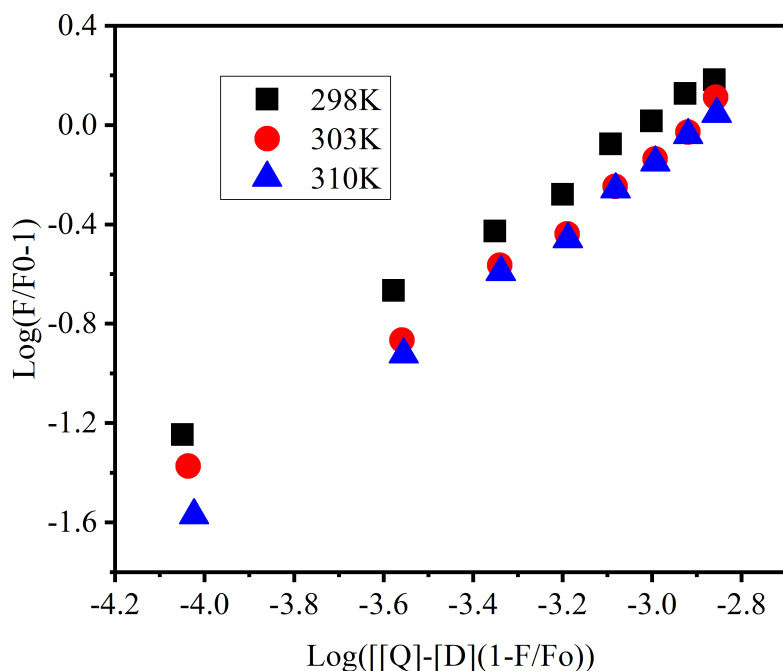
The binding constants and the number of binding sites for FA and SA were determined by plotting  $\log\left(\frac{F-F_0}{F_0}\right)$  versus  $\log\left([Q] + n[D]\left(\frac{F_0-F}{F_0}\right)\right)$ , as described in Eq. (2.90). The results, shown in Fig. 4.12 (a) and (b), with detailed values provided in Table 4.8. For the FA-caffeine (FA-CF) interaction, the binding constant decreased with increasing temperature, from  $4.89 \cdot 10^3 M^{-1}$  at 298 K to  $3.04 \cdot 10^3 M^{-1}$  at 310 K, indicating a weakened interaction at higher temperatures. The number of binding sites ( $n$ ) remained constant at approximately 1.2, suggesting that caffeine binds to a single site on FA. Similarly, for the SA-caffeine (SA-CF) interaction,  $K_a$  decreased from  $55.0 \cdot 10^3 M^{-1}$  at 298 K to  $4.90 \cdot 10^3 M^{-1}$  at 310 K, and the number of binding sites ( $n$ ) was approximately 1, indicating single-site binding for caffeine on SA.

#### 4.1.7 Thermodynamic Parameters and Interaction Forces

To better understand the FA-CF and SA-CF interactions, thermodynamic parameters were calculated using Van't Hoff Eqs. (2.91) and (2.92) and the results presented in Table 4.9. The results in Table 4.9 show that both FA-CF and SA-CF interactions are exothermic, as evidenced by negative enthalpy values. This indicates that energy is released during



(a)



(b)

Figure 4.12: Modified Stern–Volmer plot of fluorescence quenching of (a) ferulic acid and (b) sinapic acid by caffeine at 298 K, 303 K, and 310 K.

binding. For FA, the Gibbs free energy remains around  $-20.80$  kJ/mol from 298 K to 310 K. The positive entropy value of  $11.33$  J/mol·K at 298 K suggests that the FA-caffeine interaction is mainly driven by entropy, likely due to increased disorder from solvent molecule rearrangement. On the other hand, SA shows a stronger thermodynamic drive,

Table 4.9: Thermodynamic analysis: entropy ( $\Delta S^\circ$ ), enthalpy ( $\Delta H^\circ$ ), and Gibbs free energy ( $\Delta G^\circ$ ) for FA-CF and SA-CF interactions at temperature (T).

Drug	T(K)	$\ln k_a$	$\Delta H^\circ$ (Jmol <sup>-1</sup> )	$\Delta S^\circ$ (JK <sup>-1</sup> mol <sup>-1</sup> )	$\Delta G^\circ$ (kJ/mol)
FA	298	8.40±0.44	-17393.29	11.33	-20.80
	303	8.24±0.13			-20.76
	310	8.02±0.08			-20.66
SA	298	10.9±0.15	-152907.12	-423.31	-27.01
	303	9.60±1.49			-24.20
	310	8.49±0.13			-21.88

with Gibbs free energy values ranging from -27.01 kJ/mol at 298 K to -21.88 kJ/mol at 310 K. The negative entropy value of -423.31 J/mol·K at 298 K suggests that the SA-caffeine interaction reduces disorder, indicating a more ordered binding process.

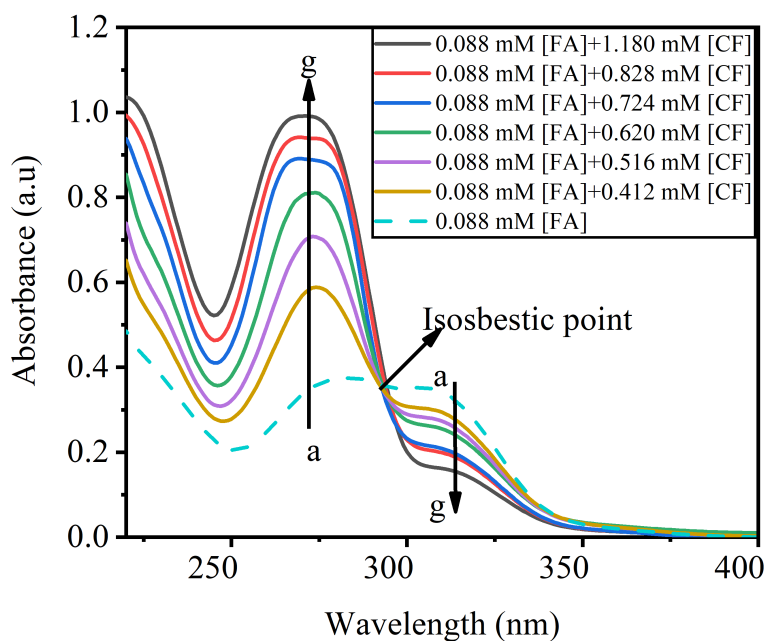
According to the Ross and Subramanian theory (Ross and Subramanian, 1981) and the signs of enthalpy and entropy changes, the forces responsible for the interaction between the drug and the biomolecule are determined as follows (1) If  $\Delta H > 0$  and  $\Delta S < 0$ , hydrophobic forces are present. (2) If  $\Delta H < 0$  and  $\Delta S > 0$ , van der Waals forces and hydrogen bonds are present. (3) If  $\Delta H < 0$  and  $\Delta S < 0$ , electrostatic forces are present. As shown in Table 4.9,  $\Delta H < 0$  and  $\Delta S > 0$  for FA indicate that van der Waals forces and hydrogen bonds promote the interaction with CF.  $\Delta H < 0$  and  $\Delta S < 0$  for SA suggest that electrostatic forces are responsible for the interaction. Furthermore, the  $\Delta G$  of both compounds was negative, indicating a spontaneous binding process (Cooper, 2005).

#### 4.1.8 UV–Vis Absorption Spectra

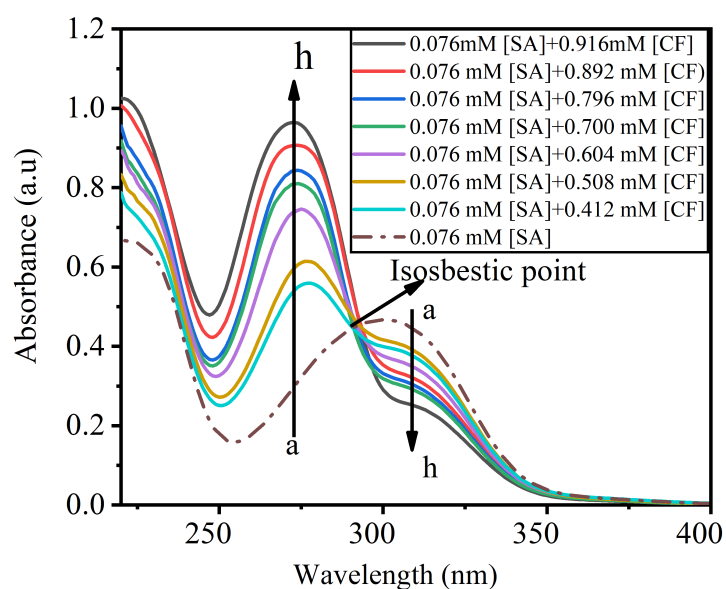
Figures 4.13 (a) and (b) clearly show the interaction between caffeine and both ferulic acid and sinapic acid. In the absence of CF, FA has a maximum absorption wavelength around 280 nm, while SA peaks near 300 nm. As the concentration of CF increases, both FA and SA undergo a noticeable blue shift in their absorption spectra, moving to shorter wavelengths. This shift, observed in curves (a-g) for FA and (a-h) for SA, indicates that CF interacts with both acids, altering their electronic transitions. The blue shift is likely a result of changes in the electronic environment of FA and SA upon complex formation with CF. This interaction can be explained by the  $n \rightarrow \pi$  electronic transition, where the lone pair of electrons from the heteroatoms (such as oxygen in the hydroxyl groups) in FA and SA interact with the  $\pi$  orbitals of CF. The increase in CF concentration enhances this interaction, leading to a stronger perturbation of the electronic structure and the resulting blue shift. This is consistent with previous research on similar phenolic acids, such as caffeic and chlorogenic acids, which also exhibit interactions with CF (Belay et al., 2016a).

Moreover, the presence of isosbestic points at 293 nm for FA and 292 nm for SA indicates the formation of a stable 1:1 complex between CF and each of these acids. An isosbestic point suggests a dynamic equilibrium between two chemical species the free acid (FA or

SA) and the acid-CF complex. The clear isosbestic points observed in this study reinforce the idea of a well-defined and specific interaction. These changes in absorbance, along with the isosbestic points, point to a static quenching mechanism. This mechanism occurs when the formation of a ground-state complex between CF and FA or SA alters their absorption properties. The observed static quenching is similar to previous studies on CF interactions with other compounds, such as fluoroquinolone antibiotics like levofloxacin and norfloxacin (Woldegiorges et al., 2022).



(a)



(b)

Figure 4.13: UV-Vis absorption spectra of (a) ferulic acid and (b) sinapic acid in the absence and presence of different caffeine.

## 4.1.9 Fourier Transform Infrared Spectra

FTIR can be used to identify the functional groups present in a sample by analyzing the characteristic vibrations of bonds in those groups (Khan et al., 2018). Fig. 4.14 (a) and (b) FTIR absorption spectra of FA and SA in the presence and absence of caffeine. Upon the addition of caffeine, significant shifts occur in several spectral bands, indicating strong molecular interactions. Specifically, the O-H stretching band for SA shifts from 3373-3297  $\text{cm}^{-1}$  to 3485  $\text{cm}^{-1}$ . In FA, the shift is from 3429  $\text{cm}^{-1}$  to 3422  $\text{cm}^{-1}$  were bserved. These shifts suggest that caffeine interacts with the hydroxyl groups of both acids, likely altering their hydrogen bonding environment. The larger shift observed in SA compared to FA may be due to the additional functional group present in SA. The shifts in the O-H stretching band reflect changes in the electronic environment around these bonds, which is a clear sign of molecular reorganization upon caffeine interaction.

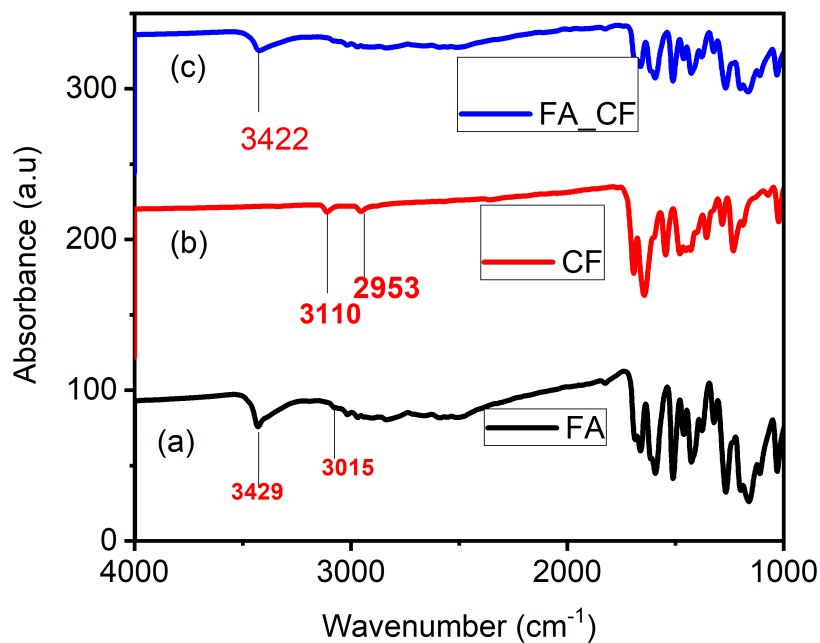
The disappearance of the C-H stretching bands at 3297  $\text{cm}^{-1}$  for SA and 3015  $\text{cm}^{-1}$  for FA further suggests that caffeine interacts with the C-H functional groups, inducing conformational changes in both acids. The disappearance of these bands suggests that caffeine may affect the vibrational modes of the C-H bonds, potentially through steric effects or noncovalent interactions like  $\pi$ - $\pi$  stacking, which could alter the usual stretching frequencies of the C-H groups. Such interactions can cause conformational changes in the molecular structure, altering the spatial arrangement of atoms and their bonding characteristics. The observed spectral changes are thus indicative of a reorganization in the molecular structure and the electronic environment around the functional groups, reinforcing the idea that caffeine can significantly modify the properties of FA and SA.

## 4.2 Molecular Quantum Calculations

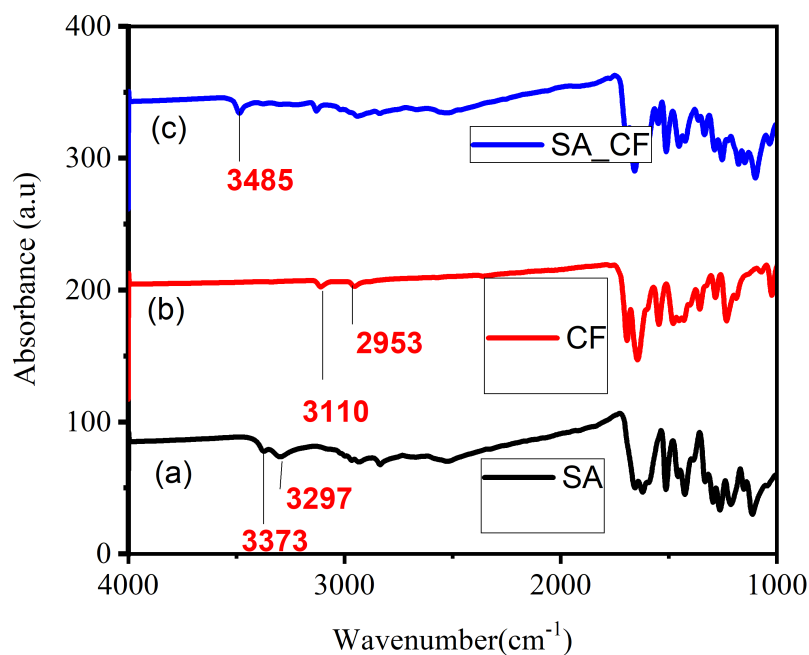
### 4.2.1 Geometry Optimization

The molecular structures of FA and SA were optimized via density functional theory with various basis sets to evaluate their impact on molecular properties. Table 4.10 shows the values of dipole moment, polarizability, thermal energy, heat capacity, entropy, and HOMO-LUMO gap using diffrent basis sets. For example, the dipole moment of ferulic acid ranged from 3.646 Debye (STO-3G\*) to 5.583 Debye (LanL2DZ), and for sinapic acid, it ranged from 3.949 Debye (STO-3G\*) to 5.351 Debye (LanL2DZ). Similarly, the polarizability of ferulic acid increased from 92.362 atomic units (STO-3G\*) to 135.895 atomic units (LanL2DZ), and the thermal energy varied from 130.025 kilocalories per mole (STO-3G\*) to 124.346 kilocalories per mole (6-311++G (d,p)).

The HOMO-LUMO gap, which reflects the electronic stability and reactivity, also showed substantial variation across basis sets. For ferulic acid, the gap ranged from 44.308 electron volts (STO-3G\*) to 3.951 electron volts (SDD), whereas for sinapic acid, it varied from 4.145 electron volts (STO-3G\*) to 3.905 electron volts (SDD). These differences indicate that smaller basis sets, such as STO-3G\* or 3-21G+, may not accurately predict



(a)



(b)

Figure 4.14: FTIR spectra of (a) ferulic acid (FA), caffeine (CF), and ferulic acid-caffeine (FA-CF) and (b) sinapic acid (SA), caffeine (CF), and sinapic acid-caffeine (SA-CF) interactions.

electronic properties, whereas larger basis sets, such as 6-311++G (d,p) and LanL2DZ may yield more reliable results. previously Wiberg report basis set effects on calculated geometries using 6-311++G\*\* and aug-cc-pVDZ. The result show The aug-cc-pVDZ basis set generally gives less satisfactory geometries than 6-311++G\*\*. This is probably a result of the latter being of triple-zeta quality for the valence electrons, whereas the former is of

Table 4.10: Dipole moment ( $\mu$ ), polarizability ( $\alpha$ ), thermal energy ( $E$ ), heat capacity ( $C_p$ ), entropy ( $S$ ), and HOMO–LUMO gap ( $\Delta E$ ) for FA and SA in the gas phase via DFT (B3LYP).

		Basis sets					
Drug	parameters	3TO-3G*	3-21G+*	6-311++G (d, p)	DGDZVP	LanL2DZ	SDD
FA	$\mu$ (D)	3.646	4.229	4.84	5.487	5.583	5.582
	$\alpha$ (a.u)	92.362	138.173	130.220	140.543	135.895	136.077
	$E$ ( kcal/mol)	130.025	118.124	132.689	124.638	124.351	124.346
	$C_p$ ( cal/mol-K)	48.543	46.29	46.436	49.609	49.628	49.634
	$S$ ( cal/mol-K)	119.15	106.514	114.85	117.112	116.784	116.805
	$\Delta E$ (eV)	44.308	0.000	9.239	4.079	3.950	3.951
SA	$\mu$ (D)	3.949	5.297	4.918	4.916	5.351	5.349
	$\alpha$ (a.u)	107.788	169.221	171.809	159.537	154.973	155.145
	$E$ ( kcal/mol)	153.421	146.319	146.376	147.036	146.642	146.628
	$C_p$ ( cal/mol-K)	57.318	57.616	58.566	58.390	58.617	58.629
	$S$ ( cal/mol-K)	132.141	125.847	130.026	129.576	129.761	129.792
	$\Delta E$ (eV)	4.145	3.889	4.042	4.042	3.905	3.905

double-zeta quality (Wiberg, 2004). Consequently, the 6-311++G(d,p) basis set was selected for further calculations, as it provided a balance between accuracy and computational efficiency Mosapour Kotena et al. (2021).

Figures 4.15- 4.17 and 4.18-4.20 display the optimized molecular structures of FA and SA in the gas and water phases using semiempirical, Hartree-Fock, and density functional theory methods. In the gas phase, the semiempirical method (Figs. 4.15 and 4.18) provides a quick approximation of the structures, but it lacks accuracy in capturing detailed electron interactions. The Hartree-Fock method (Figs. 4.16 and 4.19) improves upon this by considering electron-electron interactions more precisely, yet it still has limitations in describing the molecule's true geometry. DFT (Figs. 4.17 and 4.20) provides the most accurate results by accounting for both electronic interactions and overall molecular energy, giving the best representation of the optimized structures for FA and SA in the gas phase (Gill and von Rague Schleyer, 1994).

In the water phase, solvation effects become crucial, influencing the molecular structures and dipole moments. Semiempirical methods (Pariser and Parr, 1953) struggle to accurately capture these interactions, leading to less reliable results (Fig. 4.18). The Hartree-Fock method (Gill and von Rague Schleyer, 1994) captures some solvation effects but still lacks precision in modeling solute-solvent interactions (Fig. 4.19). However, DFT with a solvation model provides the most accurate optimized geometries for FA and SA in water, reflecting how water molecules affect their structures. These results also show that DFT can more accurately predict the dipole moments, which are influenced by the electronic distribution and interactions with the surrounding environment.

Furthermore, FA and SA were optimized in both the gas and water phases using DFT with the 6-311++G (d,p) basis set to understand the effect of solvent polarity on the optimized geometry. Tables 4.11 and 4.12 present the optimized geometric parameters of FA and SA in

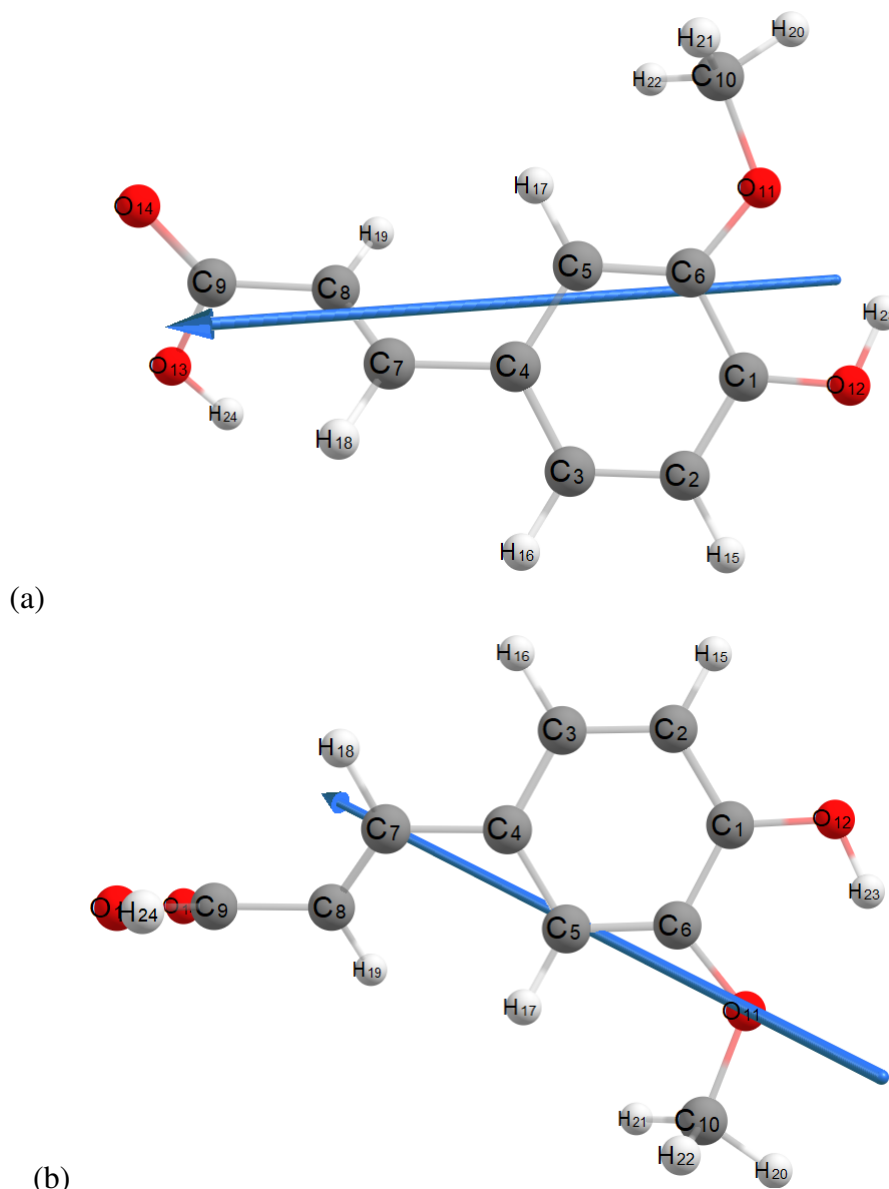


Figure 4.15: Optimization of the molecular structure of ferulic acid using semiempirical (MP6) in the (a) gas phase and (b) water.

the gas phase using the HF and DFT methods. In the gas phase, the HF method reveals that FA's bond lengths range from 1.072 Å (C-H) to 1.476 Å (C-C), indicating a stable aromatic structure. Sinapic acid (SA), on the other hand, shows bond lengths from 0.941 Å (O-H) to 1.476 Å (C-C). The shorter O-H bond in SA suggests enhanced hydrogen bonding potential due to the presence of hydroxyl groups. Bond angles in FA vary from 115.52° (C(10)-H(20)) to 127.75° (C(4)-C(7)-C(8)), indicating structural stability. In SA, bond angles range from 106.44° (O(16)-C(15)-H(26)) to 127.82° (C(5)-C(7)-C(8)), with some angles showing lower values, indicating steric strain introduced by the additional hydroxyl groups. This suggests that functional groups play a significant role in influencing molecular strain and flexibility in the gas phase (Isbell and Brodbelt, 1996).

Tables 4.13 and 4.14 show the optimized geometric parameters of FA and SA in aqueous

Table 4.11: Bond lengths, angles, and dihedrals of ferulic acid in the gas phase via HF and DFT (B3LYP) with 6-311++G (d,p).

No	Bond	Bond length (Å)			Bond angles (°)	
		HF	DFT	Bonds	HF	DFT
1	C(1)-C(2)	1.387	1.398	C(2)-C(1)-C(6)	119.442	119.455
2	C(1)-C(6)	1.391	1.406	C(2)-C(1)-O(12)	122.519	122.541
3	C(1)-O(12)	1.346	1.365	C(6)-C(1)-O(12)	118.039	118.001
4	C(2)-C(3)	1.381	1.385	C(1)-C(2)-C(3)	120.752	120.958
5	C(2)-H(15)	1.077	1.087	C(1)-C(2)-H(15)	119.405	119.086
6	C(3)-C(4)	1.391	1.405	C(3)-C(2)-H(15)	119.841	119.951
7	C(3)-H(16)	1.074	1.083	C(2)-C(3)-C(4)	120.643	120.565
8	C(4)-C(5)	1.393	1.405	C(2)-C(3)-H(16)	118.707	118.998
9	C(4)-C(7)	1.47	1.458	C(4)-C(3)-H(16)	120.649	120.436
10	C(5)-C(6)	1.381	1.389	C(3)-C(4)-C(5)	117.897	117.819
11	C(5)-H(17)	1.076	1.084	C(3)-C(4)-C(7)	123.528	123.499
12	C(6)-O(11)	1.354	1.37	C(5)-C(4)-C(7)	118.575	118.681
13	C(7)-C(8)	1.327	1.345	C(4)-C(5)-C(6)	122.058	122.205
14	C(7)-H(18)	1.077	1.087	C(4)-C(5)-H(17)	120.307	120.267
15	C(8)-C(9)	1.475	1.47	C(6)-C(5)-H(17)	117.630	117.524
16	C(8)-H(19)	1.072	1.083	C(1)-C(6)-C(5)	119.205	118.988
17	C(9)-O(13)	1.331	1.364	C(1)-C(6)-O(11)	121.109	122.05
18	C(9)-O(14)	1.187	1.212	C(5)-C(6)-O(11)	119.620	118.83
19	C(10)-O(11)	1.41	1.435	C(4)-C(7)-C(8)	127.750	127.807
19	C(10)-H(20)	1.081	1.089	C(4)-C(7)-H(18)	115.520	115.884
20	C(10)-H(21)	1.083	1.092	C(8)-C(7)-H(18)	116.730	116.309
21	C(10)-H(22)	1.086	1.095	C(7)-C(8)-C(9)	119.838	120.288
22	O(12)-H(23)	0.941	0.963	C(7)-C(8)-H(19)	123.725	123.181
23	O(13)-H(24)	0.945	0.968	C(9)-C(8)-H(19)	116.437	116.531
24	C(1)-C(2)	1.387	1.398	C(8)-C(9)-O(13)	111.711	111.27
25				C(8)-C(9)-O(14)	126.264	126.889
26				O(13)-C(9)-O(14)	122.025	121.84
27				O(11)-C(10)-H(20)	106.498	105.822
28				O(11)-C(10)-H(21)	111.096	111.366
29				O(11)-C(10)-H(22)	110.571	110.418
30				H(20)-C(10)-H(21)	109.465	109.698
31				H(20)-C(10)-H(22)	109.451	109.445
32				H(21)-C(10)-H(22)	109.697	109.998
33				C(6)-O(11)-C(10)	116.432	116.62
34				C(1)-O(12)-H(23)	111.074	109.726
35				C(9)-O(13)-H(24)	108.497	106.694
36				C(2)-C(1)-C(6)	119.442	119.455

Table 4.12: Calculated bond lengths, bond angles, and dihedral angles of the sinapic acid molecule in the gas phase computed by the HF and DFT (B3LYP) methods and with basis set of 6-311++G (d, p).

Bonds	Bond length (Å)		Bonds	Bond angles (°)		Bonds	Dihedral angle (°)	
	HF	DFT		HF	DFT		HF	DFT
C(1)-C(2)	1.379	1.397	C(2)-C(1)-C(6)	119.638	119.218	C(6)-C(1)-C(2)-C(3)	0.535	1.042
C(1)-C(6)	1.389	1.395	C(2)-C(1)-O(16)	121.04	122.069	C(6)-C(1)-C(2)-O(14)	-179.31	-178.106
C(1)-O(16)	1.353	1.369	C(6)-C(1)-O(16)	119.263	118.595	O(16)-C(1)-C(2)-C(3)	177.699	177.039
C(2)-C(3)	1.401	1.411	C(1)-C(2)-C(3)	119.375	119.36	O(16)-C(1)-C(2)-O(14)	-2.143	-2.109
C(2)-O(14)	1.342	1.358	C(1)-C(2)-O(14)	120.163	120.664	C(2)-C(1)-C(6)-C(5)	-0.321	-0.43
C(3)-C(4)	1.373	1.383	C(3)-C(2)-O(14)	120.463	119.97	C(2)-C(1)-C(6)-H(18)	179.009	179.126
C(3)-O(12)	1.353	1.372	C(2)-C(3)-C(4)	120.867	121.185	O(16)-C(1)-C(6)-C(5)	-177.54	-176.566
C(4)-C(5)	1.4	1.41	C(2)-C(3)-O(12)	113.554	112.881	O(16)-C(1)-C(6)-H(18)	1.794	2.989
C(4)-H(17)	1.071	1.081	C(4)-C(3)-O(12)	125.578	125.929	C(2)-C(1)-O(16)-C(15)	74.823	63.326
C(5)-C(6)	1.382	1.4	C(3)-C(4)-C(5)	119.875	119.727	C(6)-C(1)-O(16)-C(15)	-108	-120.654
C(5)-C(7)	1.47	1.457	C(3)-C(4)-H(17)	120.018	120.165	C(1)-C(2)-C(3)-C(4)	-0.407	-0.947
C(6)-H(18)	1.075	1.084	C(5)-C(4)-H(17)	120.106	120.107	C(1)-C(2)-C(3)-O(12)	-179.99	179.869
C(7)-C(8)	1.328	1.346	C(4)-C(5)-C(6)	118.964	118.777	O(14)-C(2)-C(3)-C(4)	179.434	178.208
C(7)-H(19)	1.077	1.087	C(4)-C(5)-C(7)	122.69	122.712	O(14)-C(2)-C(3)-O(12)	-0.148	-0.977
C(8)-C(9)	1.476	1.469	C(6)-C(5)-C(7)	118.346	118.511	C(1)-C(2)-O(14)-H(25)	178.336	178.909
C(8)-H(20)	1.073	1.083	C(1)-C(6)-C(5)	121.28	121.725	C(3)-C(2)-O(14)-H(25)	-1.504	-0.234
C(9)-O(10)	1.331	1.364	C(1)-C(6)-H(18)	117.892	117.757	C(2)-C(3)-C(4)-C(5)	0.053	0.208
C(9)-O(11)	1.187	1.212	C(5)-C(6)-H(18)	120.824	120.517	C(2)-C(3)-C(4)-H(17)	-179.7	-179.472
O(10)-H(21)	0.946	0.968	C(5)-C(7)-C(8)	127.816	127.902	O(12)-C(3)-C(4)-C(5)	179.582	179.28
O(12)-C(13)	1.403	1.425	C(5)-C(7)-H(19)	115.406	115.713	O(12)-C(3)-C(4)-H(17)	-0.173	-0.4
C(13)-H(22)	1.08	1.088	C(8)-C(7)-H(19)	116.779	116.385	C(2)-C(3)-O(12)-C(13)	178.194	177.797
C(13)-H(23)	1.085	1.094	C(7)-C(8)-C(9)	119.902	120.429	C(4)-C(3)-O(12)-C(13)	-1.366	-1.342
C(13)-H(24)	1.085	1.094	C(7)-C(8)-H(20)	123.763	123.163	C(3)-C(4)-C(5)-C(6)	0.167	0.414
O(14)-H(25)	0.944	0.968	C(9)-C(8)-H(20)	116.335	116.408	C(3)-C(4)-C(5)-C(7)	-179.8	-179.963
C(15)-O(16)	1.411	1.435	C(8)-C(9)-O(10)	111.665	111.254	H(17)-C(4)-C(5)-C(6)	179.922	-179.905
C(15)-H(26)	1.081	1.089	C(8)-C(9)-O(11)	126.304	126.966	H(17)-C(4)-C(5)-C(7)	-0.041	-0.282
C(15)-H(27)	1.087	1.095	O(10)-C(9)-O(11)	122.031	121.78	C(4)-C(5)-C(6)-C(1)	-0.034	-0.305
C(15)-H(28)	1.083	1.091	C(9)-O(10)-H(21)	108.468	106.643	C(4)-C(5)-C(6)-H(18)	-179.34	-179.849
			C(3)-O(12)-C(13)	120.048	118.734	C(7)-C(5)-C(6)-C(1)	179.931	-179.944
			O(12)-C(13)-H(22)	106.289	105.946	C(7)-C(5)-C(6)-H(18)	0.621	0.512
			O(12)-C(13)-H(23)	111.05	110.976	C(4)-C(5)-C(7)-C(8)	-1.12	-0.818
			O(12)-C(13)-H(24)	111.036	110.944	C(4)-C(5)-C(7)-H(19)	178.973	179.268
			H(22)-C(13)-H(23)	109.294	109.514	C(6)-C(5)-C(7)-C(8)	178.916	178.806
			H(22)-C(13)-H(24)	109.346	109.591	C(6)-C(5)-C(7)-H(19)	-0.99	-1.108
			H(23)-C(13)-H(24)	109.745	109.791	C(5)-C(7)-C(8)-C(9)	-179.94	-179.949
			C(2)-O(14)-H(25)	109.331	107.531	C(5)-C(7)-C(8)-H(20)	0.025	-0.014
			O(16)-C(15)-H(26)	106.443	105.74	H(19)-C(7)-C(8)-C(9)	-0.038	-0.035
			O(16)-C(15)-H(27)	110.5	110.298	H(19)-C(7)-C(8)-H(20)	179.93	179.9
			O(16)-C(15)-H(28)	111.116	111.426	C(7)-C(8)-C(9)-O(10)	-179.81	-179.952
			H(26)-C(15)-H(27)	109.391	109.445	C(7)-C(8)-C(9)-O(11)	0.213	0.084
			H(26)-C(15)-H(28)	109.526	109.814	H(20)-C(8)-C(9)-O(10)	0.224	0.109
			H(27)-C(15)-H(28)	109.796	110.022	H(20)-C(8)-C(9)-O(11)	-179.76	-179.855
			C(1)-O(16)-C(15)	116.583	116.86	C(8)-C(9)-O(10)-H(21)	179.976	-179.99
						O(11)-C(9)-O(10)-H(21)	-0.043	-0.024
						C(3)-O(12)-C(13)-H(22)	-179.25	-179.237
						C(3)-O(12)-C(13)-H(23)	61.975	61.972
						C(3)-O(12)-C(13)-H(24)	-60.427	-60.372
						H(26)-C(15)-O(16)-C(1)	178.929	176.951
						H(27)-C(15)-O(16)-C(1)	60.248	58.72
						H(28)-C(15)-O(16)-C(1)	-61.892	-63.78

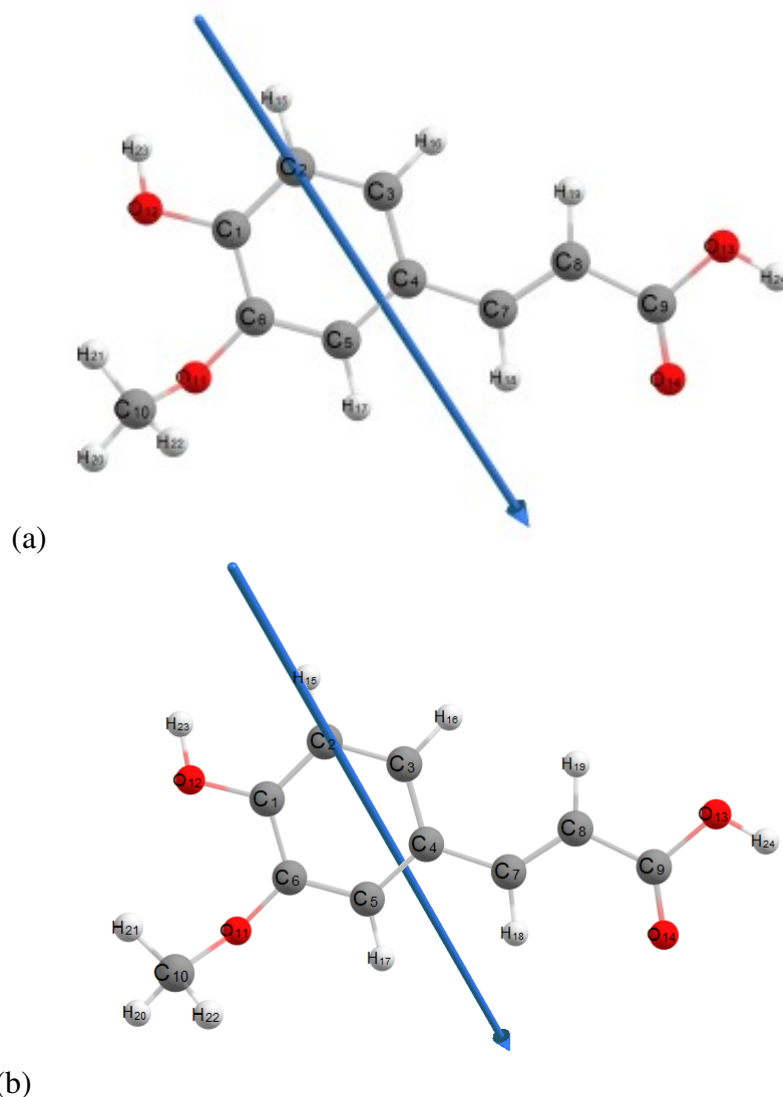


Figure 4.16: Molecular structure of ferulic acid optimized using the Hartree-Fock method with B3LYP and the 6-311++G (d, p) basis set: (a) gas and (b) water phases.

solutions, revealing notable differences in their conformation compared to the gas phase. For FA, the bond lengths range from 1.072 Å (C-H) to 1.476 Å (C-C), similar to the gas phase, indicating stable covalent bonding. The bond angles in FA vary from 115.52° (C(10)-H(20)-C(9)) to 127.75° (C(4)-C(7)-C(8)), reflecting consistent structural stability observed in the gas phase. On the other hand, for SA in aqueous solutions, the bond lengths range from 0.941 Å (O-H) to 1.476 Å (C-C), which are similar to the gas phase values, but hydrogen bonding is likely enhanced due to solvation. The bond angles in SA, ranging from 106.44° (O(16)-C(15)-H(26)) to 127.82° (C(5)-C(7)-C(8)), exhibit greater variation compared to FA, indicating increased steric strain due to the presence of additional hydroxyl groups. This suggests that solvation in water influences the molecular geometry, making it more flexible and altering interactions between functional groups, in contrast to the more rigid conformation observed in the gas phase (Tiwari et al., 2008).

Table 4.13: Bond lengths, angles, and dihedrals of ferulic acid in the water via HF and DFT (B3LYP) with 6-311++G(d, p).

No	Bonds	Bond length(Å)		Bonds	Bond angles(°)	
		HF	DFT		HF	DFT
1	C(1)-C(2)	1.39	1.388	C(2)-C(1)-C(6)	119.424	119.374
2	C(1)-C(6)	1.391	1.391	C(2)-C(1)-O(12)	122.552	122.547
3	C(1)-O(12)	1.344	1.346	C(6)-C(1)-O(12)	118.023	118.079
4	C(2)-C(3)	1.38	1.38	C(1)-C(2)-C(3)	120.567	120.769
5	C(2)-H(15)	1.075	1.077	C(1)-C(2)-H(15)	119.459	119.325
6	C(3)-C(4)	1.393	1.39	C(3)-C(2)-H(15)	119.973	119.904
7	C(3)-H(16)	1.073	1.074	C(2)-C(3)-C(4)	120.699	120.668
8	C(4)-C(5)	1.393	1.394	C(2)-C(3)-H(16)	118.535	118.696
9	C(4)-C(7)	1.469	1.47	C(4)-C(3)-H(16)	120.765	120.636
10	C(5)-C(6)	1.38	1.38	C(3)-C(4)-C(5)	118.062	117.917
11	C(5)-H(17)	1.076	1.076	C(3)-C(4)-C(7)	123.473	123.583
12	C(6)-O(11)	1.359	1.354	C(5)-C(4)-C(7)	118.465	118.5
13	C(7)-C(8)	1.33	1.327	C(4)-C(5)-C(6)	121.734	122.014
14	C(7)-H(18)	1.077	1.077	C(4)-C(5)-H(17)	120.297	120.341
15	C(8)-C(9)	1.472	1.475	C(6)-C(5)-H(17)	117.969	117.641
16	C(8)-H(19)	1.073	1.072	C(1)-C(6)-C(5)	119.512	119.256
17	C(9)-O(13)	1.324	1.331	C(1)-C(6)-O(11)	120.337	121.069
18	C(9)-O(14)	1.194	1.187	C(5)-C(6)-O(11)	120.105	119.609
19	C(10)-O(11)	1.415	1.41	C(4)-C(7)-C(8)	127.59	127.707
19	C(10)-H(20)	1.08	1.081	C(4)-C(7)-H(18)	115.27	115.563
20	C(10)-H(21)	1.084	1.083	C(8)-C(7)-H(18)	117.14	116.73
21	C(10)-H(22)	1.085	1.086	C(7)-C(8)-C(9)	120.236	119.838
22	O(12)-H(23)	0.943	0.941	C(7)-C(8)-H(19)	123.444	123.725
23	O(13)-H(24)	0.948	0.945	C(9)-C(8)-H(19)	116.32	116.437
24	C(1)-C(2)	1.39	1.388	C(8)-C(9)-O(13)	111.879	111.708
25				C(8)-C(9)-O(14)	126.16	126.264
26				O(13)-C(9)-O(14)	121.961	122.028
27				O(11)-C(10)-H(20)	106.754	106.519
28				O(11)-C(10)-H(21)	110.82	111.11
29				O(11)-C(10)-H(22)	110.466	110.545
30				H(20)-C(10)-H(21)	109.603	109.465
31				H(20)-C(10)-H(22)	109.516	109.404
32				H(21)-C(10)-H(22)	109.634	109.732
33				C(6)-O(11)-C(10)	115.692	116.453
34				C(1)-O(12)-H(23)	111.324	111.074
35				C(9)-O(13)-H(24)	109.629	108.485

Table 4.14: Calculated bond lengths, bond angles, and dihedral angles of the sinapic acid molecule in water computed by the HF and DFT (B3LYP) methods with a basis set of 6-311++G (d, p).

Bonds	Bond length (Å)		Bonds	Bond angles (°)		Bonds	Dihedral angle (°)	
	HF	DFT		HF	DFT		HF	DFT
C(1)-C(2)	1.378	1.397	C(2)-C(1)-C(6)	119.887	119.582	C(6)-C(1)-C(2)-C(3)	0.336	0.648
C(1)-C(6)	1.389	1.393	C(2)-C(1)-O(16)	120.125	120.685	C(6)-C(1)-C(2)-O(14)	-179.4	-178.705
C(1)-O(16)	1.357	1.375	C(6)-C(1)-O(16)	119.947	119.641	O(16)-C(1)-C(2)-C(3)	178.029	177.164
C(2)-C(3)	1.403	1.413	C(1)-C(2)-C(3)	119.518	119.507	O(16)-C(1)-C(2)-O(14)	-1.708	-2.189
C(2)-O(14)	1.343	1.356	C(1)-C(2)-O(14)	120.014	120.295	C(2)-C(1)-C(6)-C(5)	-0.272	-0.219
C(3)-C(4)	1.374	1.384	C(3)-C(2)-O(14)	120.468	120.195	C(2)-C(1)-C(6)-H(18)	179.419	179.5
C(3)-O(12)	1.347	1.364	C(2)-C(3)-C(4)	120.557	120.771	O(16)-C(1)-C(6)-C(5)	-177.97	-176.772
C(4)-C(5)	1.402	1.411	C(2)-C(3)-O(12)	113.666	113.028	O(16)-C(1)-C(6)-H(18)	1.722	2.947
C(4)-H(17)	1.071	1.08	C(4)-C(3)-O(12)	125.777	126.198	C(2)-C(1)-O(16)-C(15)	85.414	74.051
C(5)-C(6)	1.383	1.402	C(3)-C(4)-C(5)	119.944	119.879	C(6)-C(1)-O(16)-C(15)	-96.894	-109.435
C(5)-C(7)	1.47	1.455	C(3)-C(4)-H(17)	119.799	119.853	C(1)-C(2)-C(3)-C(4)	-0.189	-0.624
C(6)-H(18)	1.075	1.084	C(5)-C(4)-H(17)	120.256	120.268	C(1)-C(2)-C(3)-O(12)	-179.98	179.95
C(7)-C(8)	1.329	1.348	C(4)-C(5)-C(6)	119.188	118.985	O(14)-C(2)-C(3)-C(4)	179.547	178.729
C(7)-H(19)	1.076	1.087	C(4)-C(5)-C(7)	122.672	122.754	O(14)-C(2)-C(3)-O(12)	-0.242	-0.697
C(8)-C(9)	1.474	1.465	C(6)-C(5)-C(7)	118.14	118.261	C(1)-C(2)-O(14)-H(25)	-179.73	179.967
C(8)-H(20)	1.073	1.082	C(1)-C(6)-C(5)	120.905	121.272	C(3)-C(2)-O(14)-H(25)	0.538	0.619
C(9)-O(10)	1.324	1.358	C(1)-C(6)-H(18)	118.314	118.264	C(2)-C(3)-C(4)-C(5)	-0.028	0.159
C(9)-O(11)	1.194	1.219	C(5)-C(6)-H(18)	120.78	120.463	C(2)-C(3)-C(4)-H(17)	-179.78	-179.538
O(10)-H(21)	0.947	0.97	C(5)-C(7)-C(8)	127.674	127.879	O(12)-C(3)-C(4)-C(5)	179.734	179.505
O(12)-C(13)	1.411	1.433	C(5)-C(7)-H(19)	115.055	115.322	O(12)-C(3)-C(4)-H(17)	-0.02	-0.193
C(13)-H(22)	1.079	1.087	C(8)-C(7)-H(19)	117.271	116.798	C(2)-C(3)-O(12)-C(13)	179.612	178.651
C(13)-H(23)	1.084	1.093	C(7)-C(8)-C(9)	120.161	120.682	C(4)-C(3)-O(12)-C(13)	-0.164	-0.738
C(13)-H(24)	1.084	1.093	C(7)-C(8)-H(20)	123.599	122.93	C(3)-C(4)-C(5)-C(6)	0.096	0.272
O(14)-H(25)	0.945	0.97	C(9)-C(8)-H(20)	116.239	116.389	C(3)-C(4)-C(5)-C(7)	-179.79	-179.92
C(15)-O(16)	1.416	1.441	C(8)-C(9)-O(10)	111.829	111.502	H(17)-C(4)-C(5)-C(6)	179.848	179.968
C(15)-H(26)	1.08	1.089	C(8)-C(9)-O(11)	126.165	126.896	H(17)-C(4)-C(5)-C(7)	-0.032	-0.224
C(15)-H(27)	1.378	1.094	O(10)-C(9)-O(11)	122.006	121.602	C(4)-C(5)-C(6)-C(1)	0.054	-0.244
C(15)-H(28)	1.389	1.092	C(9)-O(10)-H(21)	109.664	107.894	C(4)-C(5)-C(6)-H(18)	-179.63	-179.957
			C(3)-O(12)-C(13)	120.144	118.921	C(7)-C(5)-C(6)-C(1)	179.939	179.939
			O(12)-C(13)-H(22)	106.091	105.731	C(7)-C(5)-C(6)-H(18)	0.256	0.226
			O(12)-C(13)-H(23)	110.828	110.747	C(4)-C(5)-C(7)-C(8)	-1.219	-0.897
			O(12)-C(13)-H(24)	110.821	110.709	C(4)-C(5)-C(7)-H(19)	178.891	179.181
			H(22)-C(13)-H(23)	109.541	109.741	C(6)-C(5)-C(7)-C(8)	178.9	178.913
			H(22)-C(13)-H(24)	109.541	109.766	C(6)-C(5)-C(7)-H(19)	-0.99	-1.009
			H(23)-C(13)-H(24)	109.939	110.059	C(5)-C(7)-C(8)-C(9)	-179.98	179.989
			C(2)-O(14)-H(25)	109.511	107.91	C(5)-C(7)-C(8)-H(20)	-0.052	-0.087
			O(16)-C(15)-H(26)	106.707	106.123	H(19)-C(7)-C(8)-C(9)	-0.093	-0.089
			O(16)-C(15)-H(27)	110.48	110.244	H(19)-C(7)-C(8)-H(20)	179.836	179.835
			O(16)-C(15)-H(28)	110.787	111.04	C(7)-C(8)-C(9)-O(10)	179.852	179.82
			H(26)-C(15)-H(27)	109.538	109.629	C(7)-C(8)-C(9)-O(11)	-0.142	-0.168
			H(26)-C(15)-H(28)	109.584	109.719	H(20)-C(8)-C(9)-O(10)	-0.082	-0.109
			H(27)-C(15)-H(28)	109.693	110.01	H(20)-C(8)-C(9)-O(11)	179.925	179.903
			C(1)-O(16)-C(15)	115.688	115.39	C(8)-C(9)-O(10)-H(21)	-179.96	-179.933
						O(11)-C(9)-O(10)-H(21)	0.035	0.056
						C(3)-O(12)-C(13)-H(22)	-179.96	-179.76
						C(3)-O(12)-C(13)-H(23)	61.215	61.427
						C(3)-O(12)-C(13)-H(24)	-61.13	-60.938
						H(26)-C(15)-O(16)-C(1)	-179.42	-179.815
						H(27)-C(15)-O(16)-C(1)	61.583	61.544
						H(28)-C(15)-O(16)-C(1)	-60.188	-60.639

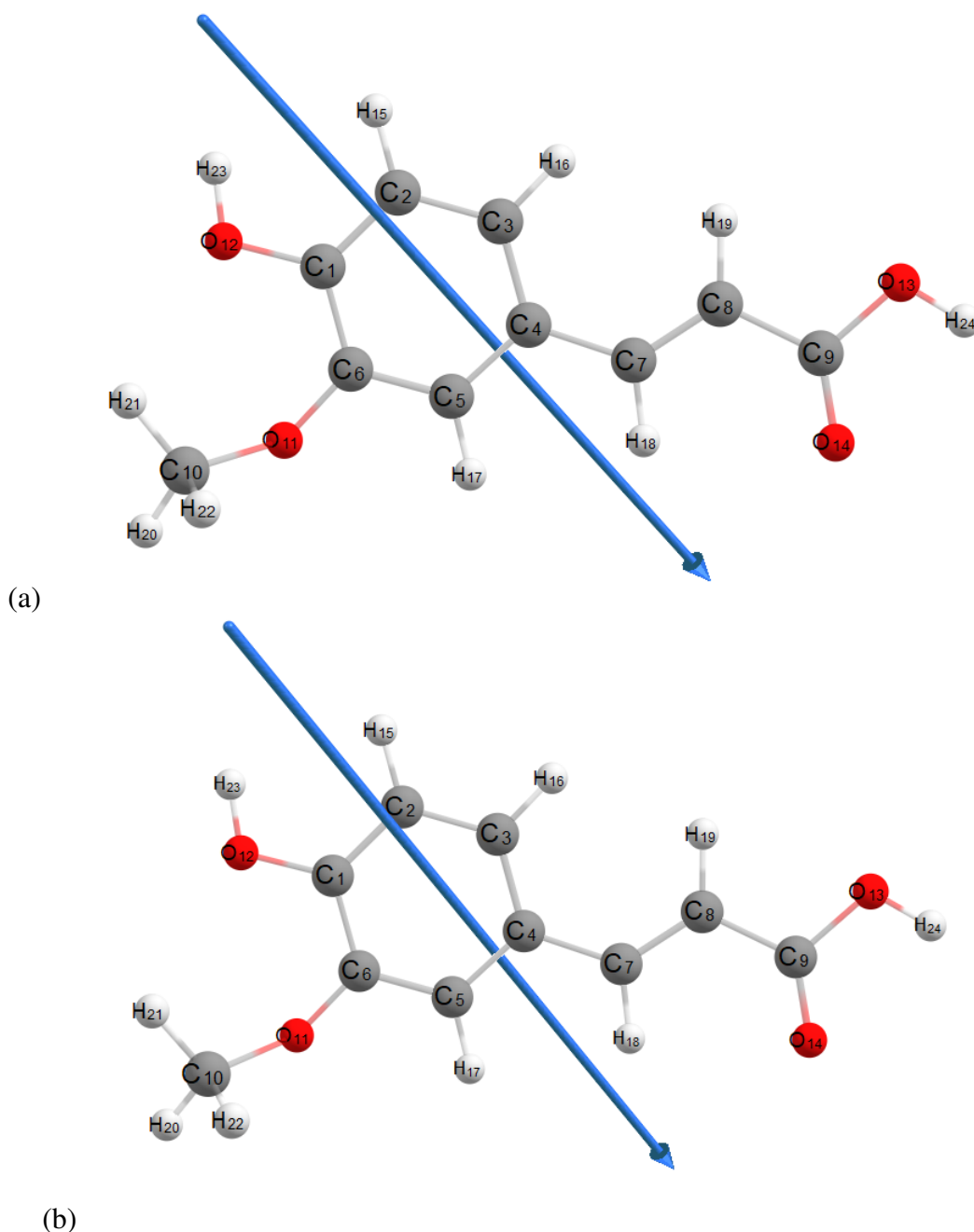


Figure 4.17: Molecular structure of ferulic acid optimized using DFT/B3LYPP with 6-311++G (d, p) (a) gas and (b) water phases.

#### 4.2.2 Effects of Solvent Polarity and Temperature on the Thermodynamic Properties

Table 4.15 illustrates the effect of solvent polarity on the thermodynamic properties of FA and SA. For FA, the enthalpy maintains a stable level of approximately 124 Cal/mol-K in nonpolar solvents like benzene, chloroform, and DCM, indicating minimal interaction with the solvent. In polar solvents such as ethanol and water, the enthalpy slightly decreases to 123.966 Cal/mol-K, suggesting that FA is relatively unaffected by changes in solvent polarity. Conversely, SA exhibits a significant response to solvent conditions; its enthalpy decreases

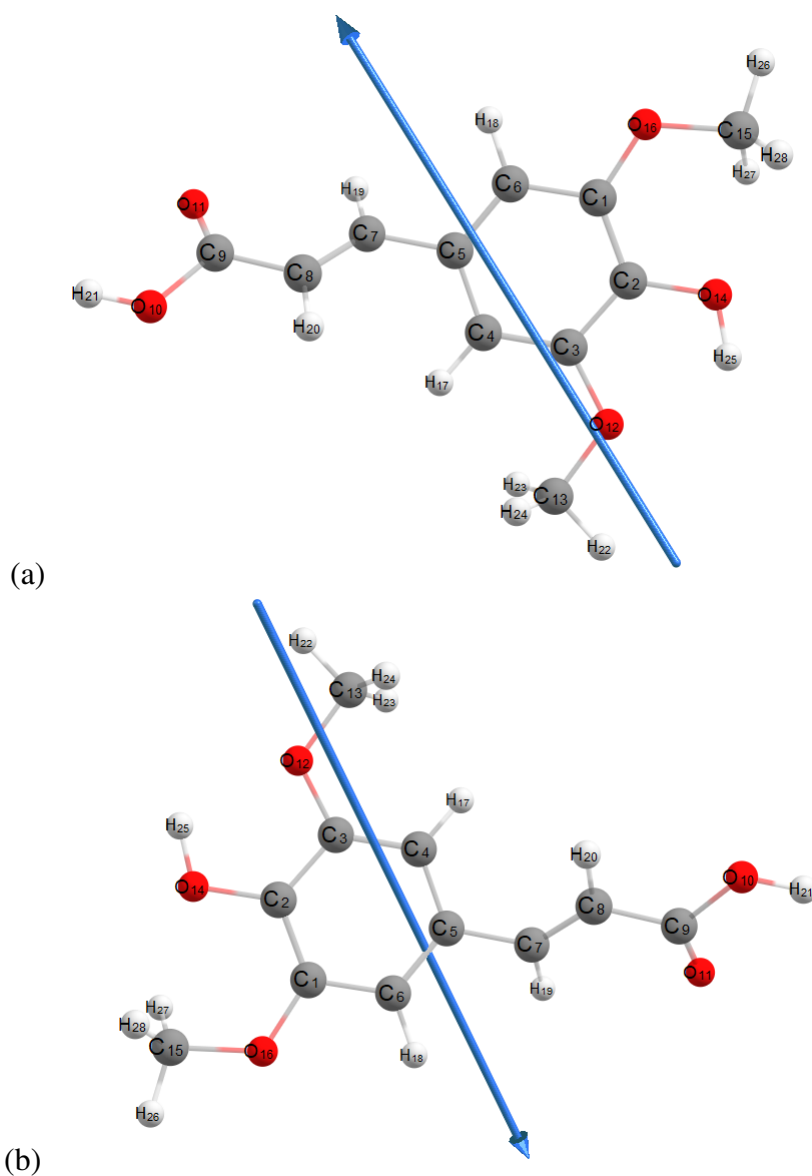


Figure 4.18: Optimization of the molecular structure of sinapic acid using semiempirical (MP6) in the (a) gas phase and (b) water

from 146.231 Cal/mol-K in nonpolar solvents to 146.007 Cal/mol-K in water, indicating that polar solvents help stabilize the molecule by lowering its energy. The heat capacity of SA also increases from 58.640 Cal/mol-K to 58.771 Cal/mol-K in water, reflecting more substantial solvation effects. These findings align with prior research on dibenzothiophene metal complexes (Srivastava et al., 2020) and tetrathiafulvalene (Srivastava et al., 2020).

Temperature also plays a crucial role in determining the thermodynamic properties of drugs. Table 4.16 presents the thermodynamic properties of FA and SA in both the gas phase and water at temperature range of 100 to 1000 K. In the gas phase, as temperature increases, enthalpy, heat capacity, and entropy for both FA and SA steadily rise. This indicates that higher temperatures require more energy for molecular vibration and rotation, leading to increased disorder and a higher heat absorption capacity. These trends align with the findings

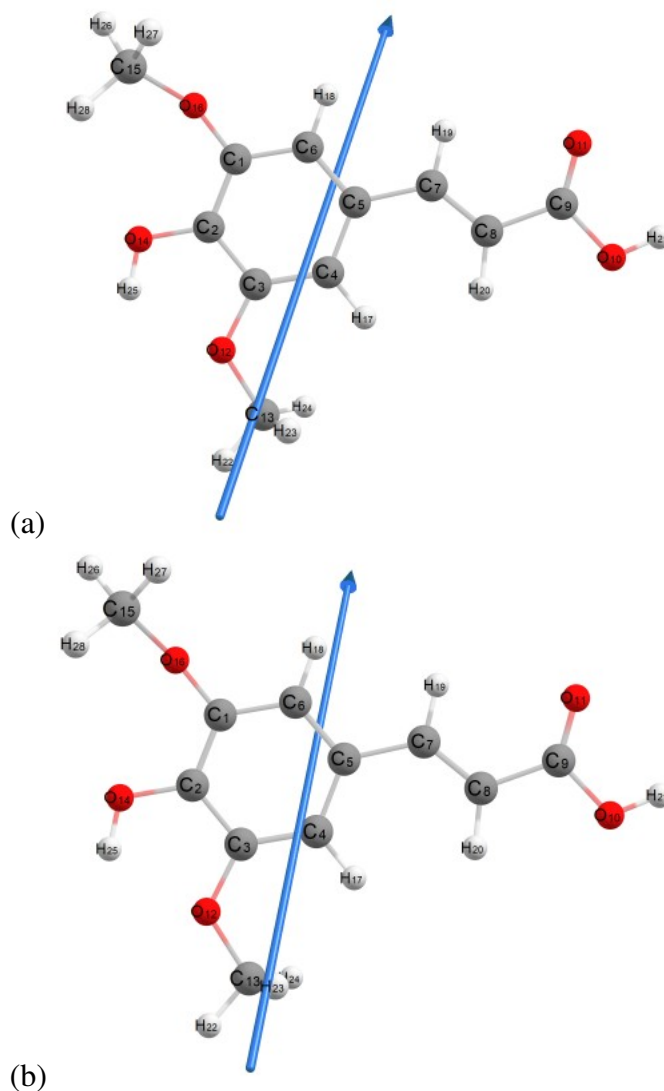


Figure 4.19: Molecular structure of sinapic acid optimized using the Hartree-Fock method with B3LYP and the 6-311++G (d, p) basis set: (a) gas and (b) water phases.

Table 4.15: Heat capacity ( $C_p$ ), entropy (S), and enthalpy (E) of SA via DFT (B3LYP)/6-311++G(d,p).

Drug	Non-polar			Polar				
	Bz	Chl	DCM	EtoH	MeOH	DMSO	W	
FA	E	124.116	124.055	124.023	123.978	123.974	123.970	123.966
	$C_p$	49.611	49.612	49.614	49.650	49.651	49.653	49.654
	S	117.301	117.668	117.838	118.189	118.218	118.240	118.264
SA	E	146.231	146.131	146.071	146.025	146.019	146.013	146.007
	$C_p$	58.640	58.698	58.737	58.760	58.764	58.768	58.771
	S	129.906	130.112	130.435	130.318	130.296	130.295	130.280

of (Politzer and Murray, 2021), who observed similar increases in thermodynamic properties with temperature, reflecting enhanced molecular energy and interactions.

In the water phase, temperature changes exert a more significant influence on thermody-

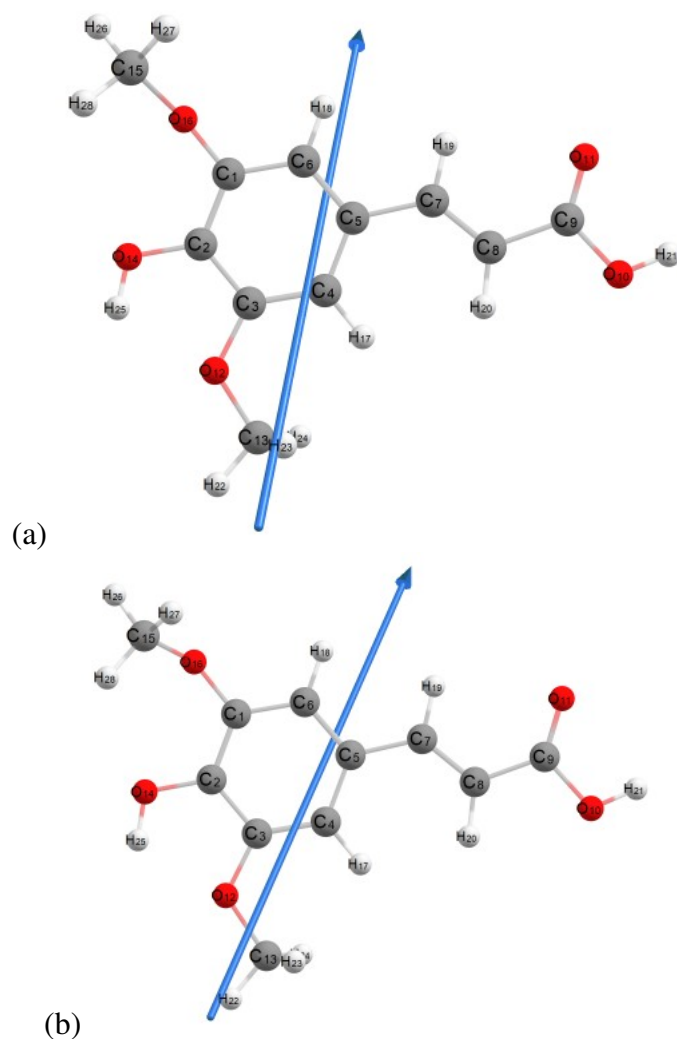


Figure 4.20: Molecular structure of sinapic acid optimized using DFT/B3LYPP with 6-311++G (d, p) (a) gas and (b) water phases.

dynamic properties. Both enthalpy and heat capacity rise more sharply compared to the gas phase, indicating stronger molecular interactions between FA, SA, and water molecules. As temperature increases, the solvation effect becomes more pronounced, enhancing molecular motion and leading to larger entropy changes. These results are consistent with FTIR studies on compounds like 1,1-difluoro-2-vinylcyclopropane, where solvation in water intensifies the temperature dependence of thermodynamic properties. This behavior is also observed in the vibrational analysis of formaldehyde, where water substantially alters molecular interactions, resulting in more significant thermodynamic variations compared to the gas phase (Limbu et al., 2024).

Table 4.16: Thermodynamic properties of FA and SA in gas and water from 100–1000 K.

Drug	Temp (K)	Gas phase			Water		
		E	$C_p$	S	E	$C_p$	S
FA	100	117.086	21.891	78.835	116.876	21.901	79.709
	200	119.985	35.969	99.747	119.768	35.883	100.573
	300	124.189	49.665	117.460	124.058	49.910	118.584
	400	129.938	62.952	134.537	129.938	62.952	134.537
	500	136.804	74.011	150.256	136.594	74.118	151.087
	600	144.671	82.991	164.935	144.471	83.114	165.788
	700	153.345	90.254	178.599	153.159	90.378	179.471
	800	162.678	96.201	191.317	162.503	96.319	192.205
	900	172.552	101.147	203.176	172.389	101.255	204.078
	1000	182.881	105.313	214.264	182.728	105.410	215.176
SA	100	137.880	26.520	84.127	137.476	26.664	84.196
	200	141.382	43.145	109.121	140.995	43.316	109.302
	300	146.376	58.566	130.026	146.007	58.771	130.280
	400	153.122	73.627	149.966	152.776	73.877	150.287
	500	161.141	86.357	168.249	160.821	86.624	168.628
	600	170.317	96.821	185.314	170.024	97.079	185.741
	700	180.441	105.359	201.208	180.172	105.594	201.674
	800	191.339	112.394	216.016	191.093	112.603	216.511
	900	202.881	118.266	229.837	202.654	118.450	230.356
	1000	214.962	123.224	242.771	214.752	123.384	243.307

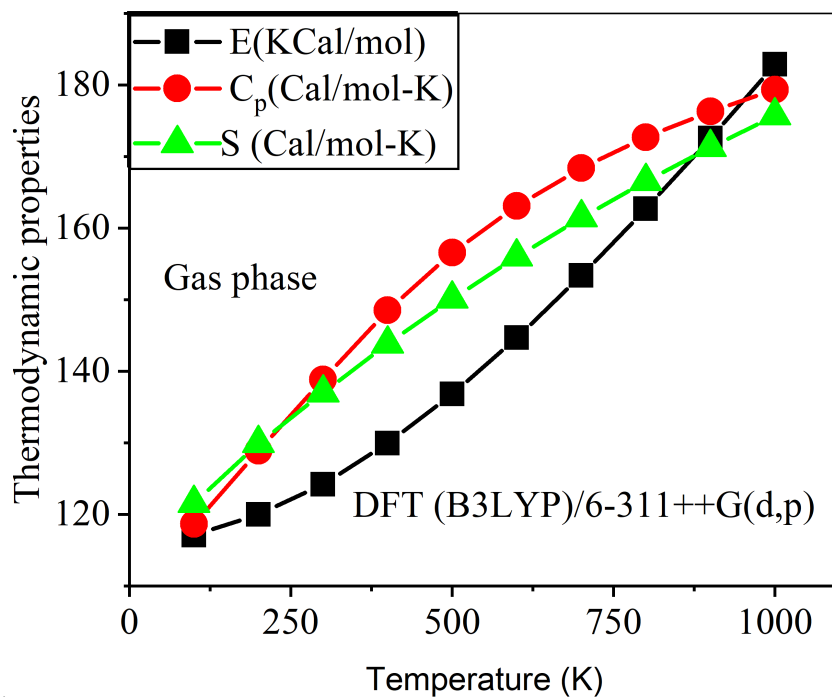
Furthermore, Fig.4.21 and Fig. 4.22 illustrate the variations in the thermodynamic properties of FA and SA in both the gas and solvents. Furthermore, Fig. 4.21 and Fig. 4.22 illustrate the variations in the thermodynamic properties of FA and SA in the gas and solvent phases. In the gas phase, the relationship between temperature and these thermodynamic properties is accurately modeled using quadratic equations, demonstrating high precision. For FA, the following equations describe the behavior of enthalpy ( $E$ ), heat capacity ( $C_p$ ), and entropy ( $S$ ), all with a perfect correlation coefficient of  $R^2 = 1.000$ :

$$E = 113.5793 + 0.0236T + 4.6311 \cdot 10^{-5}T^2 \quad (R^2 = 1.000)$$

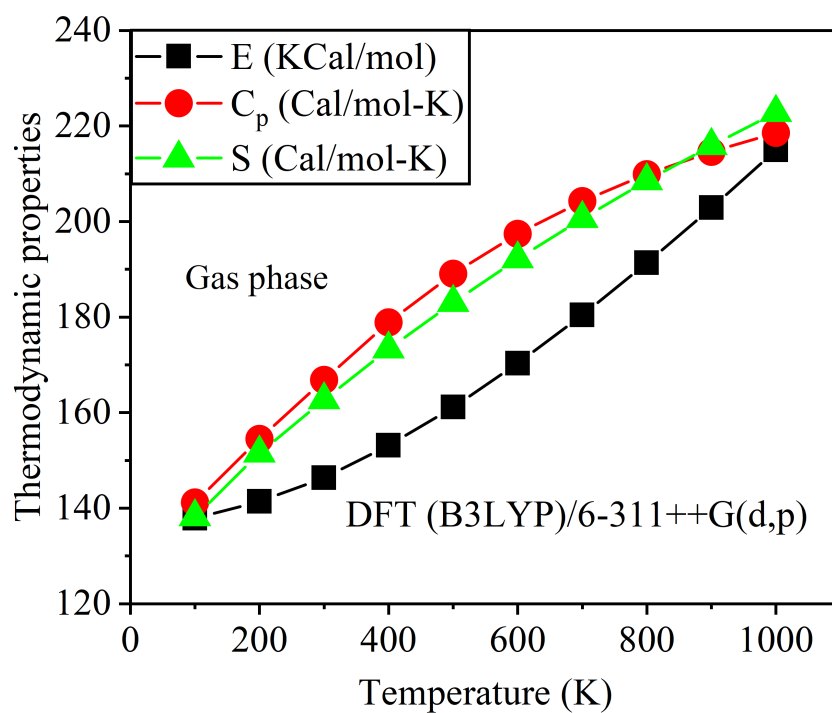
$$C_p = 4.6827 + 0.1745T - 7.4256 \cdot 10^{-5}T^2 \quad (R^2 = 1.000)$$

$$S = 59.3030 + 0.2092T - 5.4738 \cdot 10^{-5}T^2 \quad (R^2 = 1.000)$$

Similarly, for SA, the thermodynamic properties are modeled with quadratic equations, yielding the following relationships, all showing excellent correlation with  $R^2$  values greater than 0.99944:



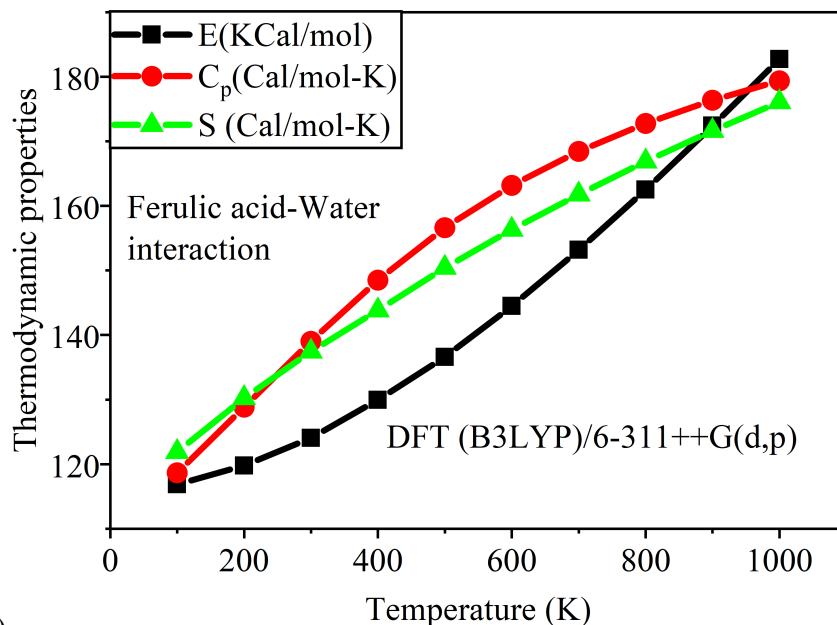
(a)



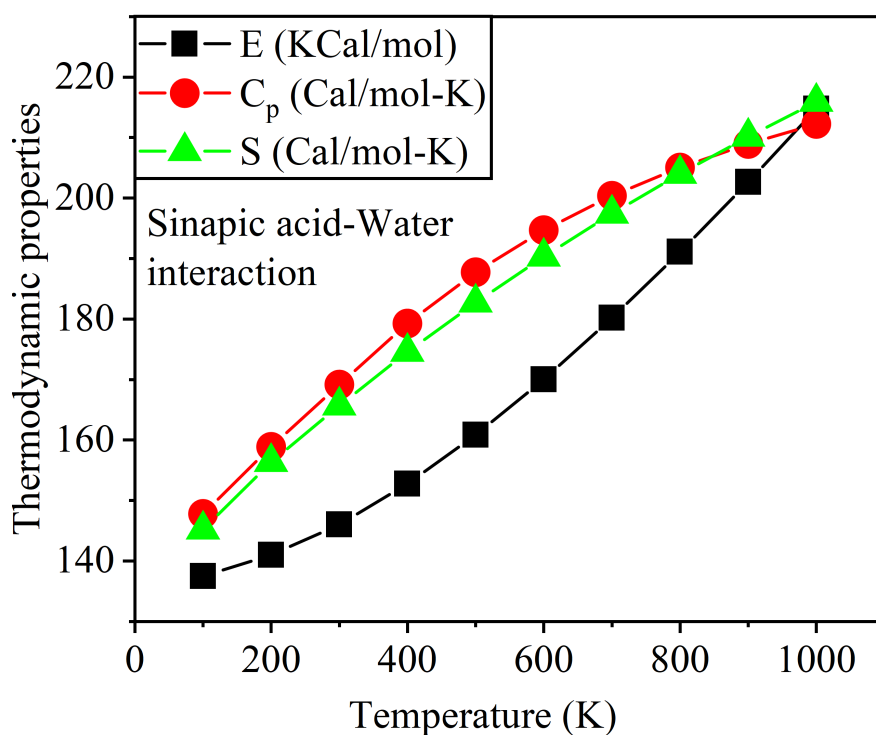
(b)

Figure 4.21: Changes in the enthalpy, entropy, and heat capacity of (a) FA and (b) SA molecules in the gas phase from 100 K to 1000 K using DFT (B3LYP)/6-311++G (d, p).

$$E = 133.7566 + 0.0284T + 5.3539 \cdot 10^{-5}T^2 \quad (R^2 = 0.99944)$$



(a)



(b)

Figure 4.22: Changes in the enthalpy, entropy, and heat capacity of (a) FA and (b) SA molecules in the water from 100 K to 1000 K using DFT (B3LYP)/6-311++G (d, p).

$$C_p = 7.1165 + 0.1987T - 8.3085 \cdot 10^{-5}T^2 \quad (R^2 = 0.99973)$$

$$S = 61.3359 + 0.2469T - 6.6103 \times 10^{-5}T^2 \quad (R^2 = 0.99978)$$

These highly accurate models reflect the robust relationship between temperature and the thermodynamic properties of both FA and SA solvent phases. In the gas phase, the relationship between these thermodynamic properties and temperature is modeled via quadratic equations, yielding the following relationships for FA, all with a correlation coefficient of  $R^2 = 1.000$ :

In the water phase, Figure 4.22 shows similar trends, with the temperature dependence of enthalpy, heat capacity, and entropy again following quadratic relationships. These relationships exhibit high correlation coefficients ( $R^2 = 0.9995$ ), reflecting the robust nature of the temperature dependence in this phase. For FA, the quadratic equations describing the thermodynamic properties are:

$$E = 113.3746 + 0.0238T + 4.6146 \times 10^{-5}T^2 \quad (R^2 = 0.9995)$$

$$C_p = 4.6235 + 0.1750T - 7.4623 \times 10^{-5}T^2 \quad (R^2 = 1.000)$$

$$S = 60.2675 + 0.2082T - 5.3675 \times 10^{-5}T^2 \quad (R^2 = 1.000)$$

Similarly, for SA, the temperature dependence is also modeled by quadratic equations with strong correlation coefficients ( $R^2 = 0.99944$ ):

$$E = 133.3249 + 0.0286T + 5.3539 \times 10^{-5}T^2 \quad (R^2 = 0.99944)$$

$$C_p = 7.1985 + 0.1993T - 8.3628 \times 10^{-5}T^2 \quad (R^2 = 0.99971)$$

$$S = 61.3167 + 0.2479T - 6.6597 \times 10^{-5}T^2 \quad (R^2 = 0.99978)$$

### 4.2.3 Molecular Orbital Analysis

Molecular orbitals (MOs) provide crucial insights into the electronic behavior of molecules by illustrating the distribution of electrons within their structure (Umar and Abdalla, 2017; Miar et al., 2021). Table 4.17 presents the HOMO, LUMO, and energy gap ( $\Delta E$ ) values for FA and SA, calculated using B3LYP/6-311++G (d, p) with IEFPCM across various solvents at room temperature. Both FA and SA show a decrease in energy gap as solvent polarity increases, with FA consistently displaying higher energy gaps than SA. Specifically, FA's energy gap ranges from 4.154 eV in non-polar solvents (hp) to 4.086 eV in polar solvents (W), while SA's gap ranges from 4.042 eV to 3.931 eV in the same solvents. These results suggest that FA may have a more stable electronic configuration, potentially influencing its

reactivity and photophysical behavior. These observations align with the findings of (Fatima et al., 2022).

Furthermore, the HOMO-LUMO gap is closely related to the chemical reactivity of molecules. A smaller HOMO-LUMO gap generally indicates higher reactivity (Miar et al., 2021; Janani et al., 2021). For both FA and SA, the energy gap decreases slightly in polar solvents (e.g., DMSO and water), suggesting that these compounds may exhibit higher reactivity in such environments. The electronic structure of FA and SA indicates that they can interact more readily with biological targets, particularly in polar environments where their electronic flexibility is enhanced. In contrast, non-polar solvents result in larger energy gaps, indicating lower reactivity. This suggests that FA and SA may have stronger biological interactions in polar environments systems.

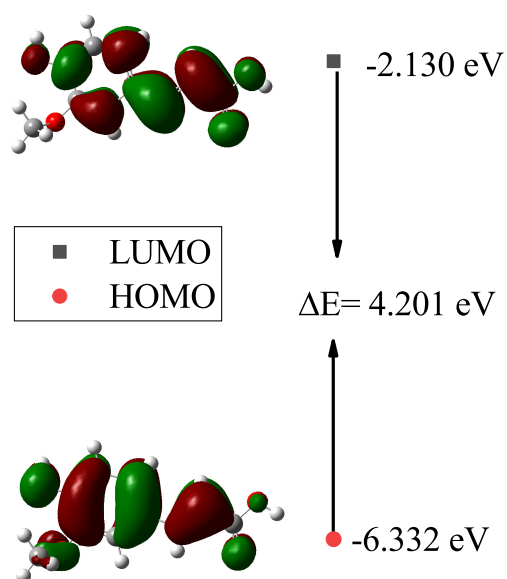
Table 4.17: HOMO, LUMO, and energy gap ( $\Delta E$ ) (eV) of FA and SA via B3LYP/6-311++G(d,p) with IEFPCM in solvents.

Drug		Non-polar				Polar				
		hp	Bz	Chl	DCM	Ace	EtoH	MeOH	DMSO	W
FA	LUMO	-2.165	-2.174	-2.210	-2.230	-2.245	-2.247	-2.250	-2.252	-2.254
	HOMO	-6.319	-6.319	-6.324	-6.331	-6.336	-6.338	-6.339	-6.339	-6.341
	$\Delta E$	4.154	4.144	4.114	4.101	4.092	4.090	4.089	4.089	4.086
SA	LUMO	-2.096	-2.160	-2.204	-2.228	-2.244	-2.247	-2.249	-2.252	-2.254
	HOMO	-6.138	-6.145	-6.160	-6.170	-6.179	-6.180	-6.181	-6.182	-6.184
	$\Delta E$	4.042	3.985	3.956	3.943	3.935	3.933	3.932	3.932	3.931

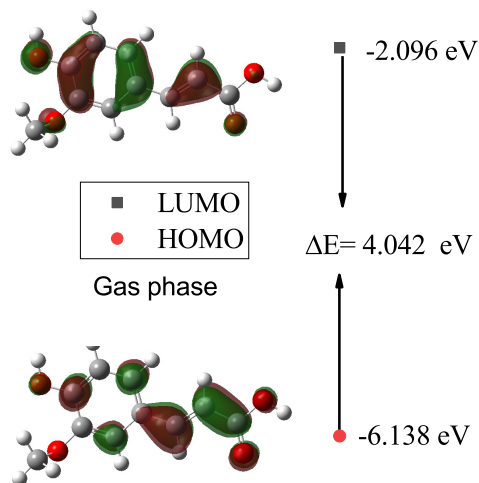
To understand the effect of solvents on electronic distribution, FA and SA were optimized in gas and water using DFT/6-311++G (d, p). Figures 4.23 and 4.24 provide visual representations of the spatial distributions of the HOMO and LUMO orbitals for FA and SA in the gas and water phases. These plots help identify the regions where electrons are most likely to be found in each orbital, with darker areas indicating higher electron density. For both FA and SA, the HOMO is concentrated mainly over the aromatic ring and functional groups such as the methoxy group in FA and the carboxyl group in SA suggesting that both molecules exhibit nucleophilic characteristics and are capable of electron donation. On the other hand, the LUMO is generally localized around the aromatic ring and the carboxyl group, which are regions typical for molecules susceptible to electrophilic attack. The slight shifts in the HOMO and LUMO distributions between the gas and water phases indicate the influence of solvent interactions on the electron density (Pilli et al., 2015).

#### 4.2.4 Dipole Moment

Table 4.18 shows the calculated dipole moments ( $\mu_g$  and  $\mu_e$ ) of FA and SA in various solvents using DFT/B3LYP/6-311++G (d, p). The dipole moments increase with solvent polarity, from the lowest in gas phase to the highest in water. This behavior indicates that both the ground and excited states of FA and SA are significantly influenced by the dielectric constant of the solvent. In non-polar solvents, the dipole moments are smaller, but as the



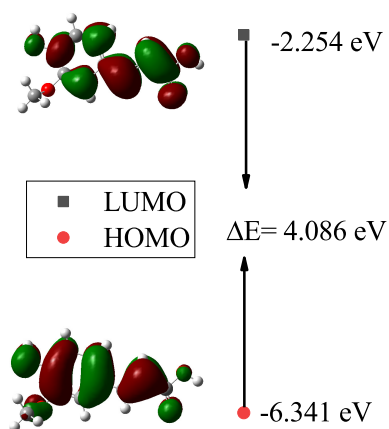
(a)



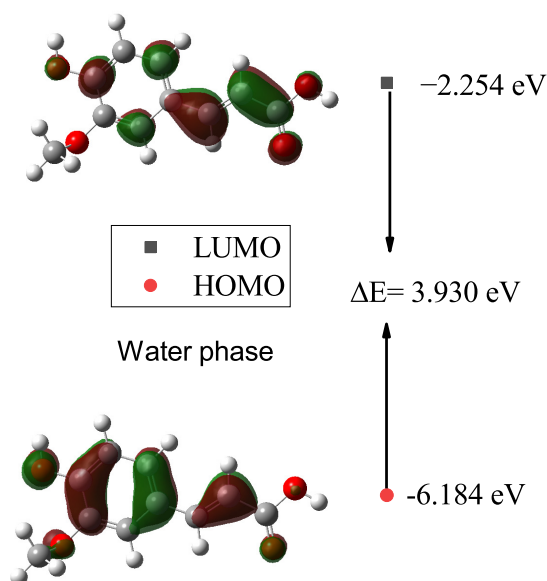
(b)

Figure 4.23: Energy levels of the HOMO, LUMO, and band gaps for (a) ferulic acid and (b) sinapic acid in gas, computed via DFT (B3LYP)/6-311++G (d, p).

solvent's polarity increases, the dipole moments of both compounds grow, especially in water, which has the highest dielectric constant. These results align with experimental data reported by (Sherefedin et al., 2023). Similarly, (Choudhary and Sekar, 2015) confirmed



(a)



(b)

Figure 4.24: Energy levels of the HOMO, LUMO, and band gaps for (a) ferulic acid and (b) sinapic acid in water, computed via DFT (B3LYP)/6-311++G (d, p).

that solvent polarity also affects the dipole moment in phenazine-fused benzo-coumarins.

#### 4.2.5 Chemical Reactivity Descriptor

Chemical reactivity descriptors, such as global softness, the electrophilicity index, electronegativity, global hardness, and chemical potential, are invaluable tools for understanding drug interactions at the molecular level. These descriptors help predict how drugs interact

Table 4.18: Ground ( $\mu_g$ ) and excited ( $\mu_e$ ) state dipole moments (Debye) of ferulic acid and sinapic acid in various solvents with different dielectric constants ( $\epsilon_r$ ).

Media	$\epsilon_r$	ferulic acid		sinapic acid	
		$\mu_g$	$\mu_e$	$\mu_g$	$\mu_e$
Gas	1	4.498	9.398	4.918	9.449
Benzene	2.28	5.145	11.308	5.579	10.927
Chloroform	4.81	5.524	11.999	5.968	11.836
Dichloromethane	8.93	5.715	12.356	6.171	12.313
Acetone	20.7	5.852	12.620	6.303	12.625
Ethanol	24.55	5.871	12.658	6.323	12.672
Methanol	32.7	5.893	12.703	6.345	12.725
Acetonitrile	37.5	5.899	12.715	6.352	12.739
DMSO	46.68	5.915	12.746	6.367	12.776
water	78.39	5.935	12.787	6.389	12.826

with biological molecules, providing insights into their binding affinities, reaction mechanisms, and potential biological activity (Venkatesh et al., 2024). Table 4.19 presents the chemical reactivity parameters calculated using Eqs. (2.129–2.135). For FA, the chemical potential increases slightly from 4.247 to 4.298 as the solvent polarity increases, indicating that FA becomes more electron-accepting in polar solvents. Similarly, the electrophilicity index rises from 4.287 to 4.480, suggesting that FA is more electrophilic in polar solvents. The global softness and electronegativity remain fairly constant, indicating stable reactivity across solvents. In contrast, for SA, the  $\mu$  increases from 4.153 to 4.219, while  $\omega$  rises from 4.333 to 4.559, exhibiting a similar trend; however, the values are slightly higher than those for FA, implying greater electrophilic behavior in polar solvents. These findings align with previous studies, indicating that solvent polarity plays a crucial role in the reactivity and solubility of drugs, affecting their pharmacokinetic behavior (Chattaraj et al., 2003; Khan et al., 2017).

## 4.2.6 Molecular Electrostatic Potential

Molecular Electrostatic Potential (MEP) analysis serves as a powerful tool for interpreting and predicting chemical reactivity (Suresh et al., 2022). Figures 4.25 (a) and (b) present the electrostatic potential maps for FA and SA, respectively, calculated using TD-DFT with the 6-311G basis set. These maps show the distributions of positive and negative charges within the molecules. For FA, the map highlights electron-rich areas around the hydroxyl (-OH) and carboxyl (-COOH) groups, whereas regions with electron deficiency are observed around the hydrogen atoms and oxygen atoms of the functional groups. Similarly, the electrostatic potential map of SA shows electron rich areas near the phenolic and carboxyl groups and electron-deficient regions around the hydrogen atoms. These electrostatic potential maps suggest that both FA and SA could form hydrogen bonds or other intermolecular interactions with electron-deficient species, which is crucial for understanding their behavior in various

Table 4.19: Global softness ( $S$ ), electrophilicity index ( $\omega$ ), electronegativity ( $\chi$ ), global hardness ( $\eta$ ), and chemical potential ( $\mu$ ) of FA and SA in solvents.

Drug		Non-polar		Polar					
		Bz	Chl	DCM	Ace	EtoH	MeOH	DMSO	W
FA	EA	-2.174	-2.21	-2.23	-2.245	-2.247	-2.25	-2.252	-2.254
	IP	-6.319	-6.324	-6.331	-6.336	-6.338	-6.339	-6.339	-6.341
	$\mu$	4.247	4.267	4.281	4.291	4.293	4.295	4.296	4.298
	$\eta$	2.073	2.057	2.051	2.046	2.046	2.045	2.044	2.044
	$S$	0.4824	0.4861	0.4876	0.4888	0.4888	0.4890	0.4892	0.4892
	$\chi$	-4.247	-4.267	-4.281	-4.291	-4.293	-4.295	-4.296	-4.298
	$\omega$	4.287	4.375	4.423	4.459	4.463	4.471	4.474	4.480
SA	EA	-2.160	-2.204	-2.228	-2.244	-2.247	-2.249	-2.252	-2.254
	IP	-6.145	-6.160	-6.170	-6.179	-6.180	-6.181	-6.182	-6.184
	$\mu$	4.153	4.182	4.199	4.212	4.214	4.216	4.217	4.219
	$\eta$	1.993	1.978	1.971	1.968	1.967	1.966	1.965	1.965
	$S$	0.5018	0.5056	0.5074	0.5081	0.5084	0.5086	0.5089	0.5089
	$\chi$	-4.153	-4.182	-4.199	-4.212	-4.214	-4.215	-4.216	-4.219
	$\omega$	4.333	4.439	4.497	4.535	4.543	4.547	4.550	4.559

environments.

## 4.2.7 UV-Vis Absorption Spectral Analysis

Figure 4.26 (a) and (b) show the UV-Vis absorption spectra of FA and SA in the gas phase and various solvents, computed using TD-DFT/B3LYP with the 6-311++G (d,p) basis set. For FA (Fig. 4.26 (a)), the absorption maximum in the gas phase is at 396 nm, which shifts to longer wavelengths (e.g., 429 nm in water and DMSO) as the solvent polarity increases. This shift is attributed to the stabilization of the excited state by polar solvents. The oscillator strength, which reflects the absorption intensity, also increases with solvent polarity, peaking at 0.4161 in water (Table 4.20). Similar behavior is observed for SA (Fig. 4.26 (b)), where the absorption peak shifts from 320 nm in the gas phase to 356 nm in polar solvents, with the oscillator strength reaching 0.8651 in water. These results align with experimental data, including those by (Sherfedin et al., 2023), confirming that solvent polarity significantly influences the absorption properties of FA and SA. The observed shifts and enhanced oscillator strengths in polar solvents support the idea that solvation effects play a key role in modulating the UV-Vis spectra of these compounds. These finding consistent with (Aravindhan et al., 2023; Rauf et al., 2015).

## 4.2.8 Emission Spectral Analysis

Figures 4.27 (a) and (b) show the emission spectra of FA and SA computed using TDDFT with the B3LYP/6-311++G (d, p), respectively. For FA (Fig.4.27 (a)), the emission spectra reveal a peak at approximately 400 nm in the gas phase, which is consistent with the emission characteristics expected for a molecule conjugated  $\pi$ -systems, such as FA. Upon

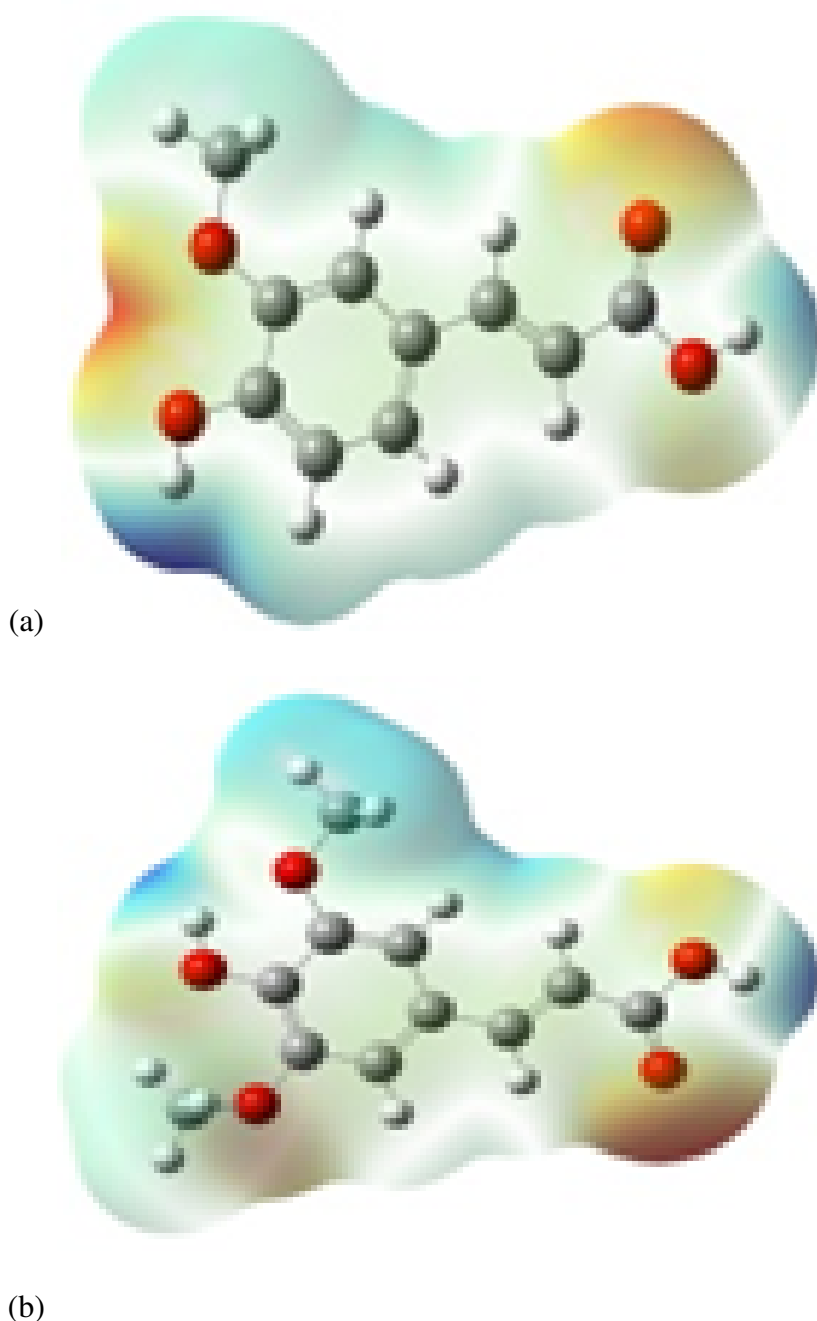
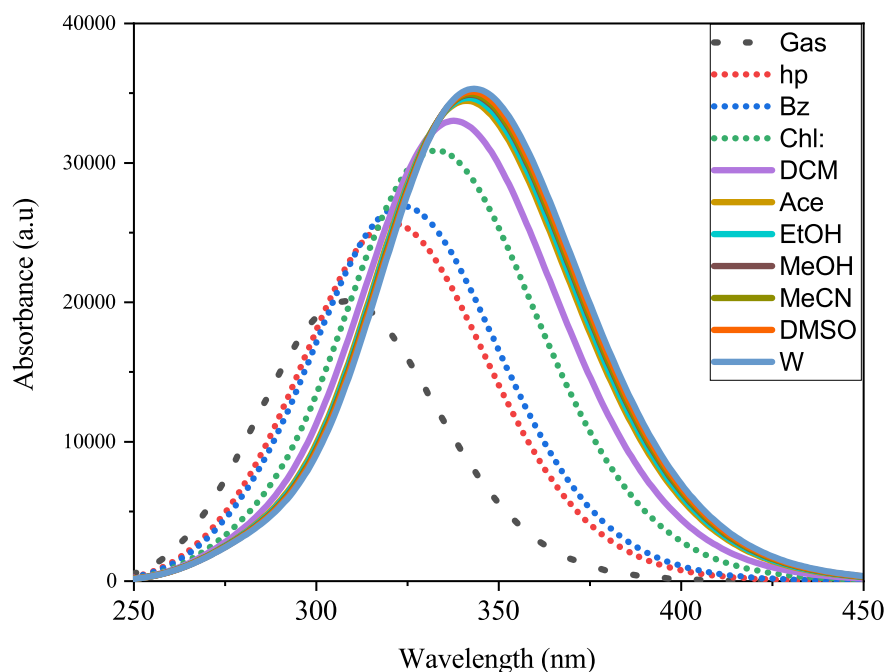
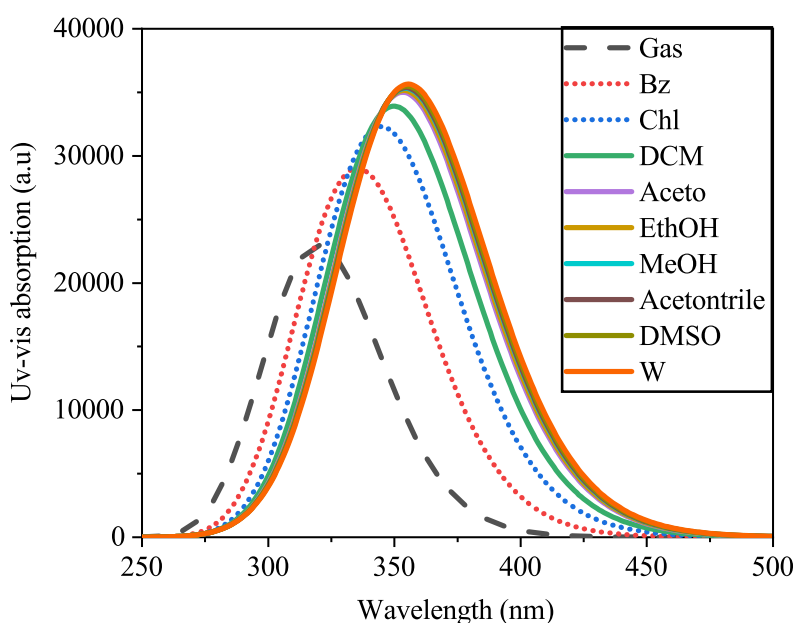


Figure 4.25: Total density matrix with electrostatic potential map (TDM-ESP) of ferulic acid (a) and sinapic acid (b) via DFT (B3LYP)/6-311++G (d, p).

solvation, the peak shifts slightly and broadens, indicating that solvent interactions affect the electronic transitions and, possibly, the excited-state relaxation. This shift is more pronounced in polar solvents, highlighting the solvent-dependent behavior of FA in terms of its emission properties. Similarly, for SA (Fig.4.27 (b)), the emission spectra show a peak at approximately 420 nm in the gas phase, which also shifts and broadens in different solvents. The observed a shift to longer wavelengths in polar solvents, suggesting the influence of solvation on the excited-state properties of SA, similar to the behavior observed in FA. These results align with experimental data, including those by (Sherefedin et al., 2023), confirming that solvent polarity significantly influences the fluorescence emission spectra of FA and SA.



(a)



(b)

Figure 4.26: Absorption spectra of ferulic acid (a) and sinapic acid (b) in gas and various solvents, computed using TD-DFT/B3LYP with the 6-311++G (d, p) basis set.

#### 4.2.9 Fourier Transform Infrared Spectra

FTIR spectrophotometer is a versatile analytical technique widely used to identify functional groups and investigate molecular structures (Dutta, 2017). Fig. 4.28 shows the FTIR spectra of FA and SA in the gas phase. For FA ( Fig. 4.28(a)), prominent peaks include a band at approximately  $3310\text{ cm}^{-1}$ , which corresponds to the O-H stretching vibration and is indicative of the presence of hydroxyl groups in the molecule. Additionally, a strong C=O

Table 4.20: Wavelengths ( $\lambda$ ), excitation energies (E, eV), and oscillator strengths (f, nm) of FA and SA in various solvent polarity.

Drug		Non-polar			Polar				
		Bz	Chl	DCM	Ace	EtoH	MeOH	DMSO	W
FA	E	3.0919	2.9983	2.9472	2.9106	2.9055	2.8993	2.8934	2.8880
	$\lambda$	401.00	413.52	420.68	425.97	426.73	427.63	428.51	429.31
	f	0.2381	0.3123	0.3580	0.3930	0.3982	0.4040	0.4101	0.4161
SA	E	3.6921	3.5897	3.5372	3.5016	3.4966	3.4909	3.4853	3.4801
	$\lambda$	335.81	345.39	350.52	354.08	354.59	355.17	355.73	356.26
	f	0.7055	0.7834	0.8226	0.8493	0.853	0.8572	0.8613	0.8651

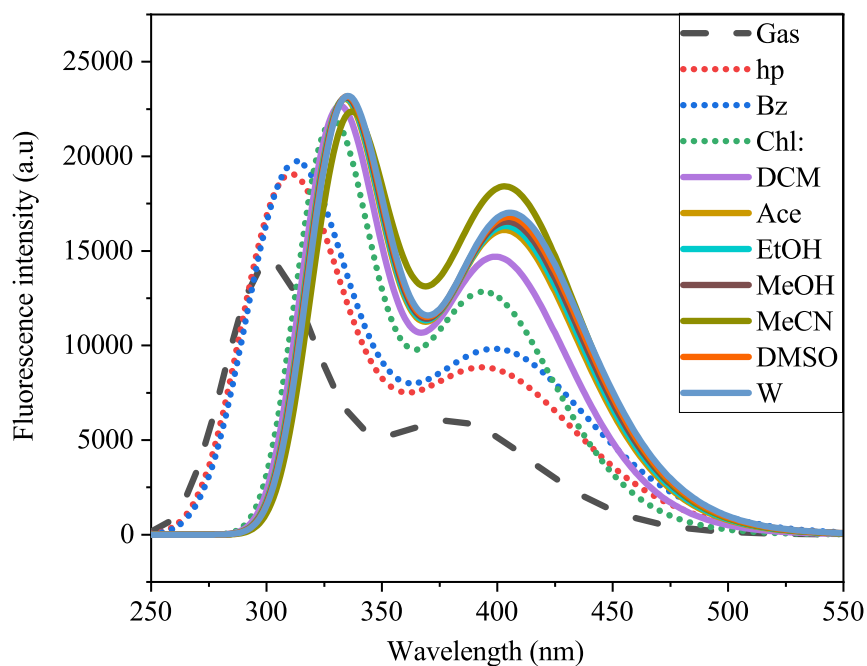
stretch is observed at approximately  $1650 \text{ cm}^{-1}$ , which is characteristic of the carboxyl group. Similarly, for SA ( Fig. 4.28 (b)), the O-H stretch appears at approximately  $3325 \text{ cm}^{-1}$ , and the C=O stretch is noted near  $1660 \text{ cm}^{-1}$ . These spectral features show the presence of similar functional groups in both acids, which are crucial for their interactions with other compounds in various environments. The observed peak positions in the gas phase closely match the experimental FTIR data reported by (Sherefedin et al., 2024), validating the accuracy of the computational FTIR predictions.

Figures 4.29(a) and (b) display the FTIR spectra of FA and SA in the water phase, respectively. The presence of water molecules has a pronounced effect on the functional groups of both acids. In this phase, both FA and SA exhibit broader O–H stretching bands, which indicates strong hydrogen bonding between the hydroxyl groups of the acids and the surrounding water molecules. This broadening is particularly prominent for FA, where the O-H stretching band appears more extensive, at approximately  $3400 \text{ cm}^{-1}$ . Additionally, the C=O stretching frequency slightly shifted to lower frequencies in water, implying a change in the conformation of the carboxyl group due to solvation effects. The water-phase spectra of FA and SA were significantly different from their gas-phase counterparts, indicating that hydration affects their molecular vibrations (Sharp et al., 2001).

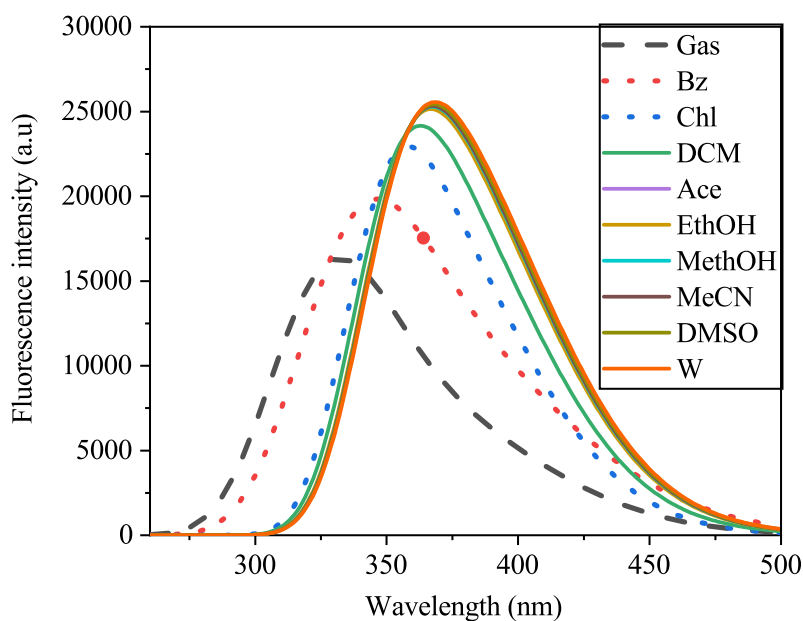
## 4.3 Molecular Docking Analysis

### 4.3.1 Ligand-Protein Interaction

The ligand-protein interaction examines the binding and interaction between ligands and proteins, which is critical for understanding biological processes and drug design. This analysis helps identify key binding sites, affinities, and the mechanism of action between the ligand and the protein target (Roche et al., 2015). Table 4.21 presents the binding affinities and root mean square deviation (RMSD) values for FA and SA with anticancer proteins (3ml8,5ekn, 6yky). Both compounds show moderate to strong binding affinities, ranging from  $-5.7$  to  $-6.8 \text{ kcal/mol}$ . Notably, FA demonstrates the highest binding affinity with protein 6yky ( $-6.4 \text{ kcal/mol}$ ), while SA exhibits the strongest affinity with protein



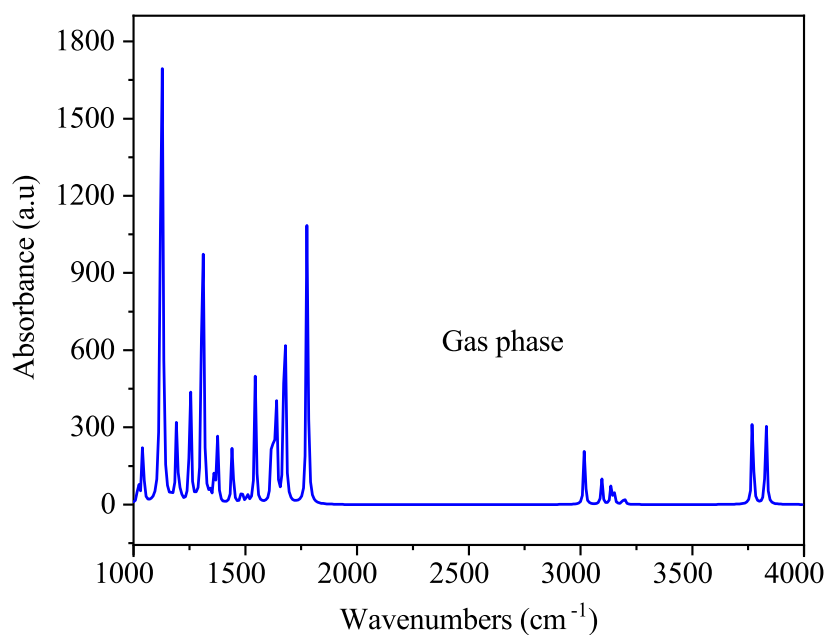
(a)



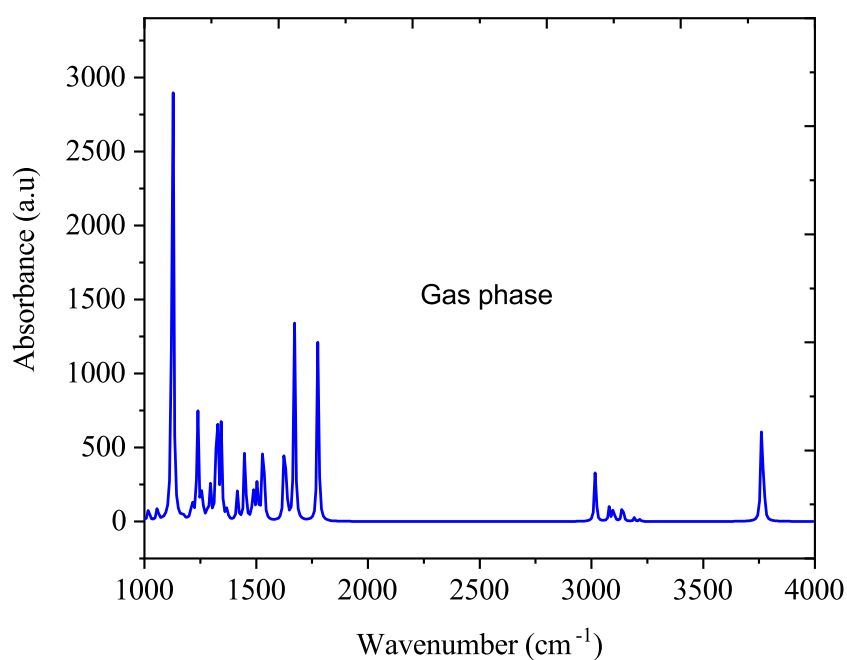
(b)

Figure 4.27: Emission spectra of ferulic acid (a) and sinapic acid (b) in the gas phase and solvents, computed using TD-DFT (B3LYP)/6-311++G (d, p).

3ml8 (-6.8 kcal/mol). These findings suggest that FA and SA can form stable complexes with their respective target proteins, a crucial feature for their potential therapeutic activity. Previous research aligns with the current results, demonstrating that ferulic acid inhibits EGFR, leading to reduced colorectal cancer cell proliferation Roy et al. (2016). Additionally, sinapic acid's interactions with DMT1 and Bcl-2 support its cytotoxic activity by potentially disrupting iron transport and promoting apoptosis. These findings confirm the anticancer



(a)

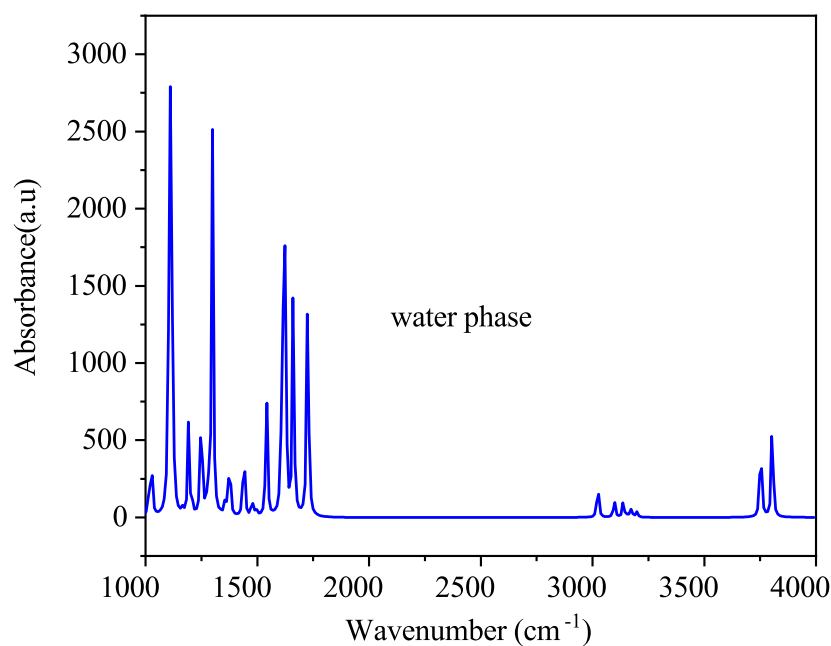


(b)

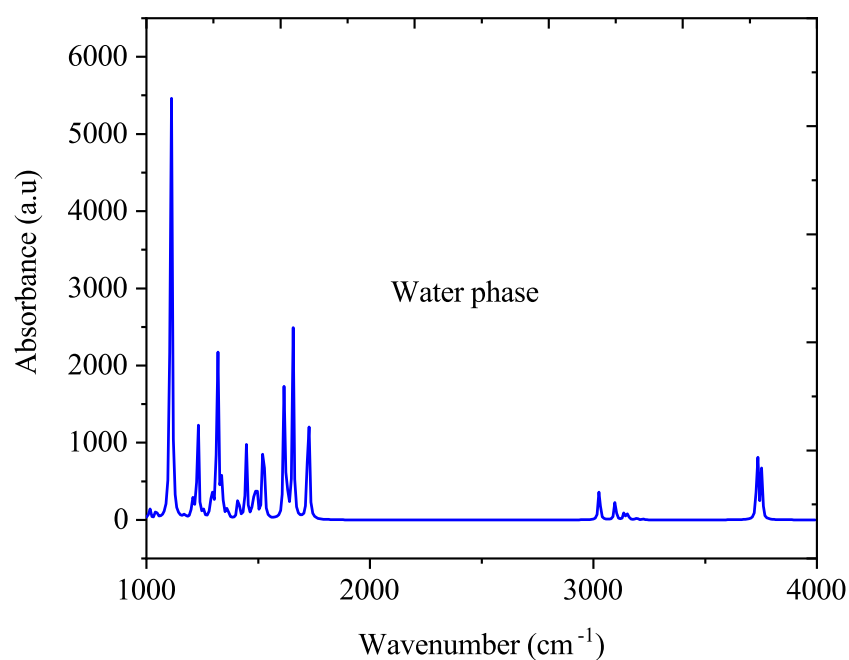
Figure 4.28: FTIR absorption spectra of ferulic acid (a) and sinapic acid (b) in gas phase, computed using TD-DFT (B3LYP)/6-311++G (d, p).

potential of both compounds Nurdiansyah et al. (2023). The current findings align with those of caffeic and p-coumaric acids, binding to the same proteins (3M18, 5EKN, and 6YKY) Sherefedin et al. (2025).

The RMSD values offer important insights into the stability and conformation of the



(a)



(b)

Figure 4.29: FTIR absorption spectra of ferulic acid (a) and sinapic acid (b) in water, computed using TD-DFT (B3LYP)/6-311++G (d, p).

docked complexes. In protein-ligand docking, an RMSD value below 2.5 Å is typically considered acceptable, as it indicates that the predicted ligand binding pose closely resembles the experimental or reference structure (Abdelilah et al., 2024). Lower RMSD values generally reflect higher accuracy in modeling the ligand-protein interaction. According to

Table 4.21: Binding affinity and RMSD (bounds) for FA and SA with potential anticancer proteins.

Ligand	Protein	Binding affinity	RMSD L.b	RMSD U.b
FA	3ml8	-5.7	1.173	2.67
	5ekn	-5.7	0.93	2.406
	6yky	-6.4	1.292	2.126
SA	3ml8	-6.8	0.337	3.162
	5ekn	-6.1	0.184	3.178
	6yky	-6.5	0.274	3.076

Table 4.21, the RMSD values for FA range from 0.93 to 1.292 Å, while for SA, they range from 0.184 to 0.337 Å, suggesting both compounds maintain stable binding poses. The lower RMSD value of 0.337 Å for SA with protein 3ml8 indicates a particularly strong and stable binding interaction.

### 4.3.2 Binding Mode

Binding mode refers to the specific orientation and conformation a ligand adopts when interacting with its target protein. This mode describes how the ligand fits into the protein's binding site, including its spatial arrangement and the specific interactions (e.g., hydrogen bonds, hydrophobic interactions, van der Waals forces) that stabilize the complex (Gohlke et al., 2000). Table 4.22 provides the interaction modes between the ligands (FA, SA) and specific amino acids in the PI3K protein complex (PDB code: 3M18). Table 4.22 lists both hydrogen bond interactions and hydrophobic interactions between the ligands and key amino acids, such as VAL882, ASP964, TYR867, and ILE879, among others. For both ligands, conventional hydrogen bonds are formed with amino acids like VAL882 and ASP964, with bond distances ranging between 2.07 to 3.32 Å, indicating strong and stable interactions.

Table 4.22: Ferulic acid and sinapic acid interaction modes with amino acids in protein complexes.

Docking	Amino acid	Distance	Category	Type
FA+P13k(3m18)	VAL882	2.12619	Hydrogen Bond	Conventional Hydrogen Bond
	ASP964	2.38797	Hydrogen Bond	Conventional Hydrogen Bond
	TYR867	3.10019	Hydrogen Bond	Pi-Donor Hydrogen Bond
	ILE879	3.76457	Hydrophobic	Pi-Sigma
	LEU838	5.11622	Hydrophobic	Alkyl
	CYS869	4.24125	Hydrophobic	Alkyl
	ILE879	3.9086	Hydrophobic	Alkyl
	TYR867	5.03402	Hydrophobic	Pi-Alkyl
SA+P13k(3m18)	ILE963	4.59543	Hydrophobic	Pi-Alkyl
	LYS833	2.62895	Hydrogen Bond	Conventional Hydrogen Bond
	LYS833	3.05469	Hydrogen Bond	Conventional Hydrogen Bond
	VAL882	2.07757	Hydrogen Bond	Conventional Hydrogen Bond
	ASP964	2.60467	Hydrogen Bond	Conventional Hydrogen Bond
	GLU880	2.46714	Hydrogen Bond	Conventional Hydrogen Bond
	ASP836	2.4838	Hydrogen Bond	Conventional Hydrogen Bond
	ASP841	3.31664	Hydrogen Bond	Carbon Hydrogen Bond
	ILE879	3.93583	Hydrophobic	Pi-Sigma
	LEU838	5.23062	Hydrophobic	Alkyl
	ILE879	4.03712	Hydrophobic	Alkyl
	ILE831	4.30576	Hydrophobic	Alkyl
	TYR867	5.28923	Hydrophobic	Pi-Alkyl
ILE963	4.53953	Hydrophobic	Pi-Alkyl	

Figures 4.30 (a) and (b) and Fig.4.31 (a) and (b) for FA and SA show (3D) and two-dimensional (2D) representations of the nonbonding interactions between each ligand and the P13K protein, respectively. In Fig 4.30 and Fig. 4.31, hydrogen bonds are depicted with dashed lines, while hydrophobic interactions are shown by solid lines or spatial proximity. The 3D structures help in understanding the exact spatial arrangement and the effectiveness of these interactions in stabilizing the ligand-protein complex, while the 2D maps simplify the visualization of the key residues involved in the interactions. These detailed representations further confirm the bond distances and types listed in the Table 4.21, offering insights into how both ligands interact with the P13K protein and suggesting potential structural or therapeutic implications for targeting P13K with these compounds.

### 4.3.3 Multiligand-Protein Interactions

Multiligand-protein interactions refer to the binding of multiple ligands to a protein, influencing its function and stability (Fu et al., 2018). Table 4.23 displays the binding affinities of FA+CF, SA+CF, FA+CF+AMX, and SA+CF+AM docked with anticancer proteins (3ML8, 5EKN, and 6YKY). For 3ML8, the addition of AMX enhances the binding affinity, with FA+AMX showing -8.1 kcal/mol compared to -7.4 kcal/mol for FA+CF. Similarly, SA+AMX has a slightly higher affinity of -8.1 kcal/mol compared to SA+CF (-7.8 kcal/mol), suggesting that AMX promotes stronger interactions. For 5EKN, both FA+CF and SA+CF show

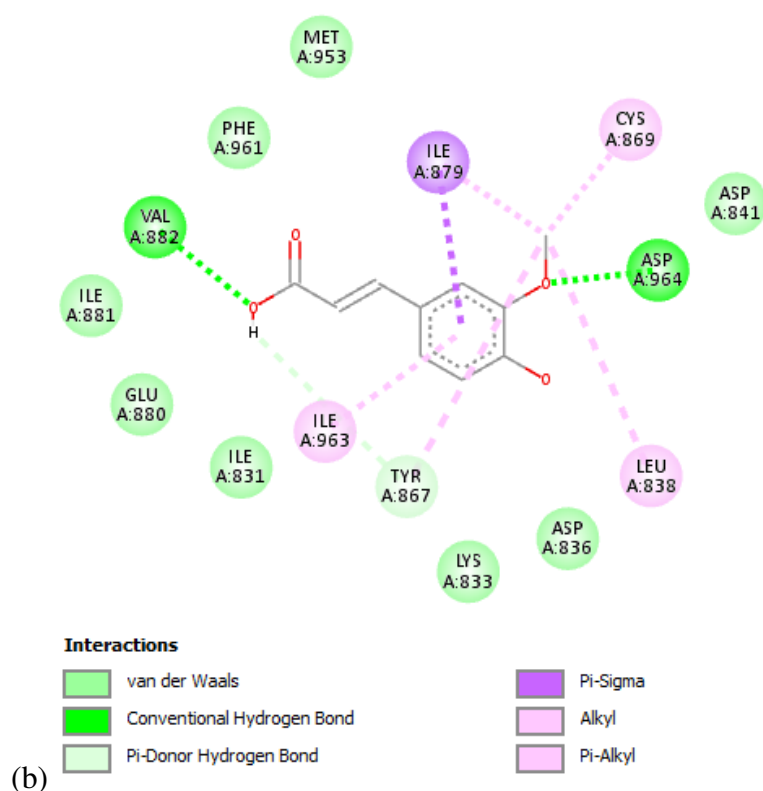
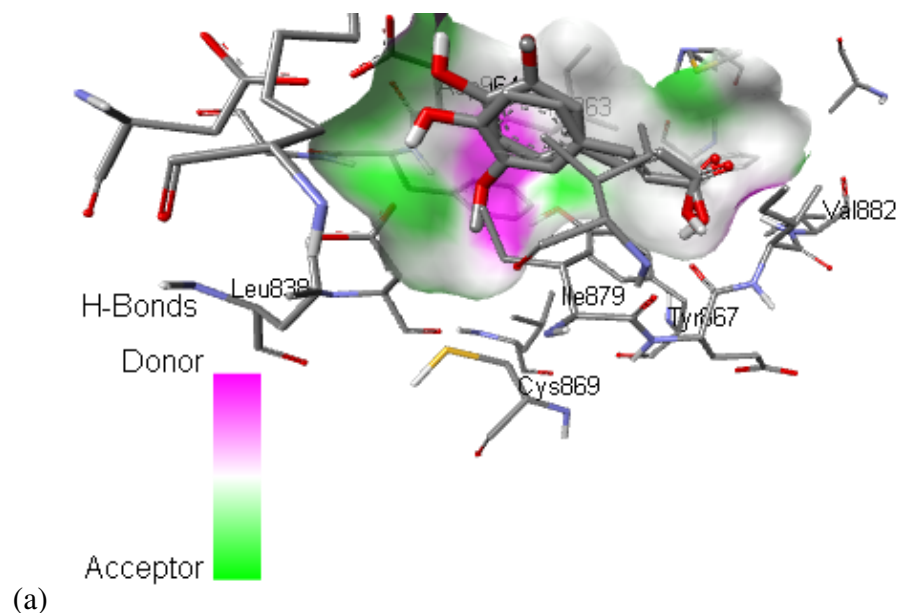


Figure 4.30: 3D (a) and 2D (b) representations of nonbonding interactions between ferulic acid and 3m18 protein.

weaker binding (-5.7 kcal/mol), indicating less favorable interactions, while 6YKY shows moderate binding with affinities of -7.0 kcal/mol and -6.5 kcal/mol for FA+CF and SA+CF, respectively. The three-ligand complexes (FA+CF+AMX, SA+CF+AMX) maintain stable binding for 3ML8 and 6YKY, with values of -8.1 kcal/mol and -8.0 kcal/mol, respectively.

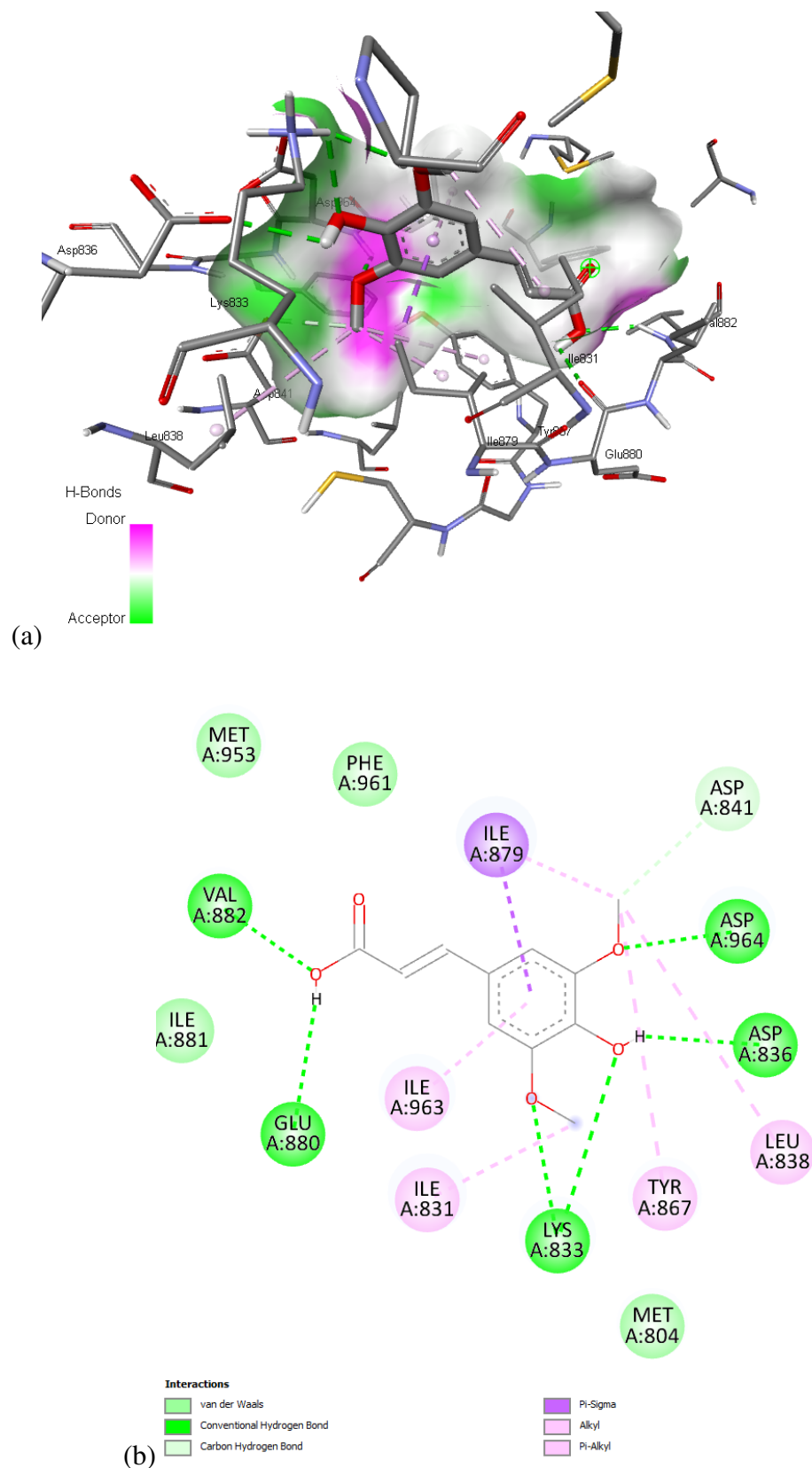


Figure 4.31: 3D (a) and 2D (b) representations of nonbonding interactions between sinapic acid and 3m18 protein.

The addition of AMX does not significantly change the binding for 3ML8 but helps maintain strong interaction, while the impact for 5EKN is less pronounced.

Comparing the two-ligand and three-ligand results with single-ligand docking (Table 4.21), combining ligands enhances binding for 3ML8, with FA+AMX showing -8.1 kcal/mol compared to -5.7 kcal/mol for single-ligand FA. Similarly, SA+AMX has a higher affinity of -8.1 kcal/mol compared to the single-ligand SA (-6.8 kcal/mol). For 5EKN and 6YKY, single-ligand affinities are similar to or slightly better than those of the two-ligand complexes, suggesting these proteins do not benefit as much from additional ligands. The RMSD values for the complexes show that while two- and three-ligand combinations exhibit stronger binding, their stability varies across proteins. Overall, the results highlight that combining ligands significantly enhances binding for 3ML8, but for 5EKN and 6YKY, the effect is less substantial.

Table 4.23: Predicted binding affinities of ligands docked with selected anticancer proteins.

2 Ligands	Protein	affinity	2 Ligands	Protein	affinity	3 Ligands	Protein	affinity
FA+CF	3ml8	-7.4	FA+AMX	3ml8	-8.1	FA+CF+AMX	3ml8	-8.1
	5ekn	-5.7		5ekn	-7.4		5ekn	-7.4
	6yky	-7.0		6yky	-8.0		6yky	-8.0
SA+CF	3ml8	-7.8	SA+AMX	3ml8	-8.1	SA+CF+AMX	3ml8	-8.0
	5ekn	-5.7		5ekn	-7.8		5ekn	-7.4
	6yky	-6.5		6yky	-8.0		6yky	-8.0

---

## CONCLUSIONS AND RECOMMENDATIONS

---

### 5.1 Conclusions

This study investigated the solvatochromic effects and photophysical properties, thermodynamic properties, and binding interactions of ferulic acid and sinapic acid with caffeine via experimental, DFT, and molecular docking approaches. The experimental results demonstrated that both FA and SA exhibited higher dipole moments in their excited states than in their ground state, indicating an increase in polarity upon excitation. This suggested significant electronic reorganization, which enhanced their reactivity and interactions with other molecules. photophysical properties studies revealed that solvent polarity and concentration influenced the UV–visible absorption and emission spectra, with redshifts observed owing to changes in electronic transitions. As the concentration increased, the quantum yield and radiative decay rates decreased, whereas the nonradiative decay rates and fluorescence lifetimes increased. Additionally, optical properties such as oscillator strength, absorption cross-sections, molar extinction coefficients, Einstein coefficients, and transition dipole moments are affected by solvent–FA or SA interactions. This occurs because solvent molecules can alter the electronic environment of the solute, modifying its energy levels, molecular dipole moments, and transition probabilities, which in turn affects the interaction strength and optical properties of the system. Both compounds formed ground-state complexes with caffeine, causing fluorescence quenching and UV–Vis absorption, and the FTIR spectra confirmed conformational changes upon caffeine binding. Van't Hoff analysis indicated that the binding process was spontaneous and was driven by Van der Waals forces and hydrogen bonding for SA and electrostatic interactions for FA.

DFT and TDDFT calculations provided deeper insights into the thermodynamic and photophysical properties of FA and SA. The study revealed that temperature and solvent polarity influenced the structure, dipole moments, HOMO–LUMO energy gaps, reactivity, vibrational frequencies, and thermodynamic properties of FA and SA. The computationally calculated dipole moments for both the ground and excited states of FA and SA were greater than the experimental values, likely due to idealized assumptions in the model that did not account for solvent interactions or molecular packing effects. A decrease in the HOMO–LUMO energy gap was observed in polar solvents, suggesting increased reactivity

106 and reduced kinetic stability. Furthermore, the UV–vis absorption and emission spectra of FA redshifted with increasing solvent polarity, indicating alterations in the electronic transitions and molecular behavior. These computational results aligned with the experimental findings, reinforcing the critical role of solvent interactions in modulating the photophysical properties of both FA and SA.

Molecular docking studies further supported the experimental and DFT/TDDFT results, revealing stable complexes between FA, SA, and caffeine, with SA exhibiting the highest binding affinity for protein 3ml8. The stability of these complexes was confirmed through RMSD values and interaction analysis, which revealed hydrogen bonds and hydrophobic interactions between the compounds and caffeine. These interactions suggested that caffeine enhanced the binding ability of FA and SA, potentially influencing their pharmacokinetics and therapeutic efficacy. The docking studies also supported the role of FA-CF and SA-CF interactions in modulating their anticancer properties, reinforcing their potential as leads in drug development. In general, this study provides essential insights into the solvatochromic and photophysical properties of ferulic acid and sinapic acid and their molecular interactions with caffeine, offering valuable guidance for designing more effective drug delivery systems and enhancing the therapeutic potential of these compounds in pharmaceutical applications.

## 5.2 Future Research and Recommendations

Future research should use both computational and experimental methods to better understand these compounds and their interactions. Techniques such as molecular dynamics simulations, Hirshfeld surface analysis, and structure–activity relationship (SAR) analysis can help improve the effectiveness of these compounds in binding to anticancer targets. These methods provide valuable insights into molecular interactions, stability, and drug properties, which can aid in designing more effective treatments.

Additionally, *in vitro* studies should test the anticancer effects of these compounds, focusing on their mechanisms of action and interactions with caffeine and other therapeutic agents. Exploring combination therapies and conducting long-term molecular dynamics simulations will help determine the stability and behavior of these compounds in drug-protein interactions. This approach will support the development of improved anticancer treatments and enhance their potential for clinical applications.

---

## List of publication

---

### A. Articles Included in the Dissertation

- Paper I: **Sherefedin, U.**, Belay, A., Kebede, A., Asemare, S., Woldegiorges, K., Kumela, A. G., & Gudishe, K. (2023). Determination of the ground and excited state dipole moments of ferulic and sinapic acids by solvatochromic effects and density function theory method. **AIP Advances (IF = 1.67)**.
- Paper II: **Sherefedin, U.**, Belay, A., Gudishe, K., Kebede, A., Kumela, A. G., & Asemare, S. (2024). Photophysical Properties of Sinapic Acid and Ferulic Acid and Their Binding Mechanism with Caffeine. **Journal of Fluorescence (IF= 2.9)**.
- Paper III: **Sherefedin, U.**, Belay, A., Gudishe, K., Kebede, A., Kumela, A. G., Wakjira, T. L., ... & Gurumurthi, T. (2024). Effects of Temperature and Solvent Polarity on the Thermodynamic and Photophysical Properties of Ferulic Acid Using Density Functional Theory (DFT). **Journal of Molecular Liquids (IF=6.0)**.
- Paper IV: **Sherefedin, U.**, Belay, A., Gudishe, K., Kebede, A., Kumela, A. G., Wakjira, T. L., ... & Gelanu, D. (2024). Investigating the effects of solvent polarity and temperature on the molecular, photophysical, and thermodynamic properties of sinapic acid using DFT and TDDFT. **RSC advances (IF= 3.9)**.
- Paper V: **Sherefedin, U.**, Belay, A., Gudishe, K., Kebede, A., Kumela, A. G., Feyisa, T., ... & Fekadu, S. (2025). Physicochemical properties and drug likeness of hydroxycinnamic acids and their molecular docking with caffeine and amoxicillin: Potential anticancer drugs. **Results in Chemistry (IF=2.3)**.

### B. Articles Not Included the Dissertation

- Paper I: **Sherefedin, U.**, Belay, A., Gudishe, K., Kebede, A., Kumela, A. G., Wakjira, T. L., ... Gizew, K. S. (2024). DFT and molecular docking analyses of the effects of solvent polarity and temperature on the structural, electronic, and thermodynamic properties of p-coumaric acid: Insights for anti-cancer applications. **Results in Physics (IF= 4.4)**.
- Paper II: Asemare, S., Belay, A., Kebede, A., & **Sherefedin, U.** (2024). Ground and excited state dipole moments of metformin hydrochloride using solvatochromic effects

and density functional theory. **Journal of Fluorescence (IF = 2.9)**.

- Paper III: Kumela, A. G., Gemta, A. B., Hordofa, A. K., Birhanu, R., Mekonnen, H. D., **Sherefedin, U.**, & Weldegiorgis, K. (2023). A review on hybridization of plasmonic and photonic crystal biosensors for effective cancer cell diagnosis. **Nanoscale Advances (IF = 4.2)**.
- Paper IV: Kumela, A. G., Gemta, A. B., Hordofa, A. K., Dagnaw, H., **Sherefedin, U.**, & Tadesse, M. (2023). Quantum machine learning assisted lung cancer telemedicine. **AIP Advances (IF = 1.67)**.
- Paper V: Feyisa, T., Belay, A., Tolessa, F., Mathewos, G., Haji, J., & **Sherefedin, U.** (2024). High temperature dependent absorber-emitter pair nanostructure metamaterial matched with low band-gap PV cell for solar thermo photovoltaic application. **Indian Journal of Physics (IF = 1.6)**.
- Paper VI: Dangish, M., Gemta, A. B., Kumela, A. G., **Sherefedin, U.**, & Birhanu, R. (2025). Synchronization of chaotic optomechanical system with plasmonic cavity for secured quantum communication. **AIP Advances (IF= 1.4)**, 15(1).
- Paper VII: Wakjira, T. L., Gemta, A. B., Tadele, K., Kassahun, G. B., **Sherefedin, U.**, Gurumurthi, T., & Feyisa, T. (2024). Molecular structures and adsorption of dyes on bismuth oxychloride surfaces using density functional theory and Monte Carlo dynamic simulation. **Results in Physics (IF=4.4)**.
- Paper VIII: Asemare, S., Belay, A., Kebede, A., **Sherefedin, U.**, Gurumurthi, T., Feyisa, T. (2025). Photophysical Properties, Fluorescence Quenching of Metformin Hydrochloride by Caffeine, and its Docking with the AMP-activated protein kinase receptor. **Journal of Fluorescence (IF= 2.6)**.

## D. Articles under Review

- Paper I: Near Infrared Thermal Emitter Based on Nano Scale Grating Metamaterial for Thermo Photovoltaic Power Generation **Accepted in Physica Scripta (IF= 2.6)**.
- Paper II: Investigation on the Effect of Solvent Polarity and Temperature on Vibrational Spectra, Photophysical Properties, Optical and Thermodynamic Behaviours of Benzofuran-1 Using Density Functional Theory (DFT) and Time Dependent-DFT approach submitted to Journal of Solution Chemistry
- Paper III: Synthesis of Silver Nanoparticle from Neem (*Azadirachta Indica*) Leaf Extract for Antimicrobial Activity Against Tomato Leaf Pathogens submitted to **Journal of plasmonic**.

- Paper IV: DFT Investigation of Pyrazole: Effect of Temperature and Solvent Polarity on Thermodynamic, Molecular, and Photophysical Properties submitted to **Results in Physics**.
- Paper V: Integration of Optical Biosensors, Machine Learning, and Quantum Information Processing for Cancer Telemedicine: A Review<sup>†</sup> Submitted to **Lab on a Chip**.

## D. Articles under Preparation

- Paper I: Investigating the Effect of Solvent polarity on the Thermodynamic and Photophysical Properties of Metronidazole: A DFT and Molecular Docking Analysis for Antibacterial Applications
- Paper II: Hydrocinamic Acid and Its Role in Medical Applications: A Comprehensive Review
- Paper III: Investigating Temperature and Solvent polarity effect on the Thermodynamic and Photophysical Properties of Tinidazole : A DFT, Molecular Docking and Moleculaire dDynamic Simulations Analysis for Antibacterial Applications

---

## Conferences, Editorial Activities , and Certificates

---

### A. Conferences

The results of this study were shared at various national conferences. Valuable feedback and recommendations from these presentations were integrated into the documents. The conferences attended are as listed below.

- Determination of the ground and excited state dipole moments of ferulic and sinapic acids by solvatochromic effects and density function theory methods was presented at the 18th Annual National Conference of the Ethiopian Physical Society (EPS) held at Addis Ababa University on February 17-18, 2024.
- Effects of temperature and solvent polarity on the thermodynamic and photophysical properties of ferulic acid using Density Functional Theory (DFT) were presented at the 6th Annual National Conference of Jinka University on May 10-11, 2024.

### B. Editorial Activities

- 2024–present: Reviewer for Physica Scripta, published by the Institute of Physics (IOP) Publishing (Reviewed two papers).
- 2024–present: Reviewer for Public Library of Science (PLOS) (Reviewed 8 papers).
- 2024–present: Reviewer for The Journal of Optics, published by the Institute of Physics (IOP) Publishing (Reviewed two papers).
- 2025–present: Reviewer for the European Journal of Chemistry, published by Atlanta Publishing House LLC (Reviewed one paper).
- 2025–present: Reviewer for the Current Journal of Applied Science and Technology (Reviewed one paper).

### C. Certificates

- Certificate of IOP peer review excellence
- Certificate of Research excellence Open data: a practical primer

- Certificate of participation from Wolkite University for attending the 15th Ethiopian Physical Society (EPS) Annual Conference. Date: February 26-27, 2021.
- Certificate of participation from Addis Ababa University for presenting a paper at the 18 th Annual Conference of the Ethiopian Physical Society. Date: March 27, 2024.
- Certificate of participation from Jinka University for presenting a paper at the 6th National Research Conference. Date: May 11, 2024

---

## Bibliography

---

- Abdelilah, T., Oussama, C., Abdellah, E. A., Youssef, E. O., Mohammed, B., kamal, M., and Abdelkrim, O. (2024). Computational integration of trpv4 antagonists: 3d qsar, molecular docking, molecular dynamics simulations, adme/tox, and retrosynthesis studies. *ChemistrySelect*, 9(42):e202404026.
- Abebe, B. G. (2011). *Spectrophotometric Investigation of Major Bioactive Compounds of Coffee Beans*. PhD thesis, Addis Ababa University.
- Abraha, A., Gholap, A., and Belay, A. (2016a). Investigation of self-association, optical transition probability and hetero-association with chlorogenic acid of nicotinamide using uv-vis spectroscopy. *International Journal of Physical Sciences*, 11(21):269–278.
- Abraha, A., Gholap, A., and Belay, A. (2016b). Study self-association, optical transition properties and thermodynamic properties of neomycin sulfate using uv-visible spectroscopy. *Int. J. Biophys*, 6:16–20.
- Abraha, G. A. and Belay, G. A. (2023). Binding of caffeine with nicotinamide: A study by means of fluorescence quenching and uv-vis spectroscopic techniques. *The South African-Scottish snowflake*, 16(1):111–124.
- Acheson, K. J., Gremaud, G., Meirim, I., Montigon, F., Krebs, Y., Fay, L. B., Gay, L.-J., Schneiter, P., Schindler, C., and Tappy, L. (2004). Metabolic effects of caffeine in humans: lipid oxidation or futile cycling? *The American journal of clinical nutrition*, 79(1):40–46.
- Addison, K. (2015). *The photophysics of fluorescent protein chromophores*. PhD thesis, University of East Anglia.
- Adeyi, O. E., Somade, O. T., Ajayi, B. O., James, A. S., Adeboye, T. R., Olufemi, D. A., Oyinlola, E. V., Sanyaolu, E. T., and Mufutau, I. O. (2023). The anti-inflammatory effect of ferulic acid is via the modulation of nf $\kappa$ b-tnf- $\alpha$ -il-6 and stat1-pias1 signaling pathways in 2-methoxyethanol-induced testicular inflammation in rats. *Phytomedicine Plus*, 3(3):100464.
- Alberty, R. A. (1969). Standard gibbs free energy, enthalpy, and entropy changes as a function of ph and pmg for several reactions involving adenosine phosphates. *Journal of biological chemistry*, 244(12):3290–3302.

- Aravindhan, R., Hu, J., and Momeen, M. U. (2023). Role of the solvent polarity on the optical and electronic characteristics of 1-iodoadamantane. *RSC advances*, 13(42):29489–29495.
- Arbogast, J. W. and Foote, C. S. (1991). Photophysical properties of c70. *Journal of the American Chemical Society*, 113(23):8886–8889.
- Baer, R. and Kronik, L. (2018). Time-dependent generalized kohn–sham theory. *The European Physical Journal B*, 91:1–9.
- Baerends, E., Ricciardi, G., Rosa, A., and Van Gisbergen, S. (2002). A dft/tddft interpretation of the ground and excited states of porphyrin and porphyrazine complexes. *Coordination chemistry reviews*, 230(1-2):5–27.
- Bakhshiev, N. G., Knyazhanskii, M. I., Minkin, V. I., Osipov, O. A., and Saidov, G. V. (1969). Experimental determination of the dipole moments of organic molecules in excited electronic states. *Russian Chemical Reviews*, 38(9):740.
- Bartolotti, L. J. (1982). Time-dependent kohn-sham density-functional theory. *Physical Review A*, 26(4):2243.
- Barzykin, A., Razumov, V., and Alfimov, M. (1991). Fluorescence concentration self-quenching dynamics in monodisperse micellar systems. *The Journal of Physical Chemistry*, 95(12):4814–4818.
- Becker, R. and Sauter, F. (1982). *Electromagnetic fields and interactions*, volume 1. Courier Corporation.
- Belay, A. (2010). Measurement of integrated absorption cross-section, oscillator strength and number density of caffeine in coffee beans by integrated absorption coefficient technique. *Food Chemistry*, 121(2):585–590.
- Belay, A. (2011). The semi classical approaches for the comparison of time dependent schrödinger equation with experimental quantities. *Lat. Am. J. Phys. Educ. Vol*, 5(4):726.
- Belay, A. (2012). Self-association, sodium ion complexation and optical transition probabilities of caffeic acid determined spectrophotometrically. *infection*, 1:3.
- Belay, A., Kim, H. K., and Hwang, Y.-H. (2016a). Binding of caffeine with caffeic acid and chlorogenic acid using fluorescence quenching, uv/vis and ftir spectroscopic techniques. *Luminescence*, 31(2):565–572.
- Belay, A., Libnedengel, E., Kim, H. K., and Hwang, Y.-H. (2016b). Effects of solvent polarity on the absorption and fluorescence spectra of chlorogenic acid and caffeic acid compounds: determination of the dipole moments. *Luminescence*, 31(1):118–126.

- Bi, S., Ding, L., Tian, Y., Song, D., Zhou, X., Liu, X., and Zhang, H. (2004). Investigation of the interaction between flavonoids and human serum albumin. *Journal of Molecular Structure*, 703(1-3):37–45.
- Bilot, v. L. and Kawski, A. (1962). Zur theorie des einflusses von lösungsmitteln auf die elektronenspektren der moleküle. *Zeitschrift für Naturforschung A*, 17(7):621–627.
- Bin Jordan, Y. A., Ansari, M. A., Raish, M., Alkharfy, K. M., Ahad, A., Al-Jenoobi, F. I., Haq, N., Khan, M. R., and Ahmad, A. (2020). Sinapic acid ameliorates oxidative stress, inflammation, and apoptosis in acute doxorubicin-induced cardiotoxicity via the nf- $\kappa$ b-mediated pathway. *BioMed research international*, 2020(1):3921796.
- Blinder, S. (2019). Introduction to the hartree-fock method. In *Mathematical Physics in Theoretical Chemistry*, pages 1–30. Elsevier.
- Bocko, M. F. and Onofrio, R. (1996). On the measurement of a weak classical force coupled to a harmonic oscillator: experimental progress. *Reviews of Modern Physics*, 68(3):755.
- Bolton, J. R. and Archer, M. D. (1991). Calculation of natural radiative lifetimes from the absorption and fluorescence properties of semiconductors and molecules. *The Journal of Physical Chemistry*, 95(22):8453–8461.
- Borges, A., Ferreira, C., Saavedra, M. J., and Simões, M. (2013). Antibacterial activity and mode of action of ferulic and gallic acids against pathogenic bacteria. *Microbial drug resistance*, 19(4):256–265.
- Burdan, F. (2015). Pharmacology of caffeine: the main active compound of coffee. In *Coffee in Health and Disease Prevention*, pages 823–829. Elsevier.
- Buterbaugh, J. S., Toscano, J. P., Weaver, W. L., Gord, J. R., Hadad, C. M., Gustafson, T. L., and Platz, M. S. (1997). Fluorescence lifetime measurements and spectral analysis of adamantyldiazirine. *Journal of the American Chemical Society*, 119(15):3580–3591.
- Callis, P. R. (2014). Binding phenomena and fluorescence quenching. i: Descriptive quantum principles of fluorescence quenching using a supermolecule approach. *Journal of Molecular Structure*, 1077:14–21.
- Campolongo, S., Siegumfeldt, H., Aabo, T., Cocolin, L., and Arneborg, N. (2014). The effects of extracellular ph and hydroxycinnamic acids influence the intracellular ph of *brettanomyces bruxellensis* dsm 7001. *LWT-Food Science and Technology*, 59(2):1088–1092.
- Carlström, S., Spanner, M., and Patchkovskii, S. (2022). General time-dependent configuration-interaction singles. i. molecular case. *Physical Review A*, 106(4):043104.

- Carrillo, J. A. and Benitez, J. (2000). Clinically significant pharmacokinetic interactions between dietary caffeine and medications. *Clinical pharmacokinetics*, 39:127–153.
- Chattaraj, P., Nath, S., and Maiti, B. (2003). Reactivity descriptors. *Computational medicinal chemistry for drug discovery*, 11:295.
- Chen, H., McMahon, J. M., Ratner, M. A., and Schatz, G. C. (2010). Classical electro-dynamics coupled to quantum mechanics for calculation of molecular optical properties: a rt-tddft/fdtd approach. *The Journal of Physical Chemistry C*, 114(34):14384–14392.
- Choudhary, A. S. and Sekar, N. (2015). Phenazine fused benzo coumarins with negative solvatochromism and positive solvatochromic emission-synthesis, photo physical properties, dft and tddft studies. *Journal of Fluorescence*, 25:675–684.
- Choudhary, V., Bhatt, A., Dash, D., and Sharma, N. (2019). Dft calculations on molecular structures, homo–lumo study, reactivity descriptors and spectral analyses of newly synthesized diorganotin (iv) 2-chloridophenylacetohydroxamate complexes. *Journal of computational chemistry*, 40(27):2354–2363.
- Cohen, M. H., Ganduglia-Pirovano, M. V., and Kudrnovský, J. (1995). Reactivity kernels, the normal modes of chemical reactivity, and the hardness and softness spectra. *The Journal of chemical physics*, 103(9):3543–3551.
- Cooper, A. (2005). Heat capacity effects in protein folding and ligand binding: a re-evaluation of the role of water in biomolecular thermodynamics. *Biophysical chemistry*, 115(2-3):89–97.
- Dallakyan, S. and Olson, A. J. (2015). Small-molecule library screening by docking with pyrX. *Chemical biology: methods and protocols*, pages 243–250.
- de Carvalho, A. C. C., da Silva Paganini, W., de Almeida Piai, K., and Bocchiglieri, M. M. (2024). The presence of pharmaceuticals and caffeine in water, as well as the methods used to eliminate them. *Current Opinion in Environmental Science & Health*, page 100550.
- Demasa, J. and Crosby, G. (1968). The measurement of photoluminescence quantum yields. 1 a review<sup>2</sup>. *J. Chem. Phys*, 48:4726.
- dePaula, J. and Farah, A. (2019). Caffeine consumption through coffee: Content in the beverage, metabolism, health benefits and risks. *Beverages*, 5(2):37.
- Di Giacomo, S., Percaccio, E., Gullì, M., Romano, A., Vitalone, A., Mazzanti, G., Gaetani, S., and Di Sotto, A. (2022). Recent advances in the neuroprotective properties of ferulic acid in alzheimer’s disease: A narrative review. *Nutrients*, 14(18):3709.
- Dong, X. and Huang, R. (2022). Ferulic acid: An extraordinarily neuroprotective phenolic acid with anti-depressive properties. *Phytomedicine*, 105:154355.

- Douglas, P., Burrows, H. D., and Evans, R. C. (2013). Foundations of photochemistry: a background on the interaction between light and molecules. In *Applied photochemistry*, pages 1–88. Springer.
- Dovesi, R., Orlando, R., Roetti, C., Pisani, C., and Saunders, V. (2000). The periodic hartree-fock method and its implementation in the crystal code. *Computer Simulation of Materials at Atomic Level*, pages 63–88.
- Durand, P. and Malrieu, J.-P. (1987). Effective hamiltonians and pseudo-operators as tools for rigorous modelling. *Advances in Chemical Physics: Ab Initio Methods in Quantum Chemistry Part I*, 67:321–412.
- Dutta, A. (2017). Fourier transform infrared spectroscopy. *Spectroscopic methods for nanomaterials characterization*, pages 73–93.
- Dutta, A., Tiainen, V., Qureshi, H. A., Duarte, L., and Toppari, J. J. (2022). Modeling optical constants from the absorption of organic thin films using a modified lorentz oscillator model. *Optical materials express*, 12(7):2855–2869.
- Echenique, P. and Alonso, J. L. (2008). Efficient model chemistries for peptides. i. general framework and a study of the heterolevel approximation in rhf and mp2 with pople split-valence basis sets. *Journal of computational chemistry*, 29(9):1408–1422.
- Eichinger, M., Tavan, P., Hutter, J., and Parrinello, M. (1999). A hybrid method for solutes in complex solvents: Density functional theory combined with empirical force fields. *The Journal of chemical physics*, 110(21):10452–10467.
- El-Seedi, H. R., El-Said, A. M., Khalifa, S. A., Goransson, U., Bohlin, L., Borg-Karlson, A.-K., and Verpoorte, R. (2012). Biosynthesis, natural sources, dietary intake, pharmacokinetic properties, and biological activities of hydroxycinnamic acids. *Journal of agricultural and food chemistry*, 60(44):10877–10895.
- El-Seedi, H. R., Taher, E. A., Sheikh, B. Y., Anjum, S., Saeed, A., AlAjmi, M. F., Moustafa, M. S., Al-Mousawi, S. M., Farag, M. A., Hegazy, M.-E. F., et al. (2018). Hydroxycinnamic acids: Natural sources, biosynthesis, possible biological activities, and roles in islamic medicine. *Studies in natural products chemistry*, 55:269–292.
- Elliott, P., Burke, K., and Furche, F. (2007). Excited states from time-dependent density functional theory. *arXiv preprint cond-mat/0703590*.
- Fahmy, H. M., Kandel, H. M., Al-Shamiri, H. A., Negm, N. A., Elwahy, A. H., and Abou Kana, M. T. (2018). Spectroscopic study of solvent polarity on the optical and photo-physical properties of novel 9, 10-bis (coumarinyl) anthracene. *Journal of fluorescence*, 28:1421–1430.

- Fatima, S., Mansha, A., and Asim, S. (2022). Computational studies followed by effect of solvent polarity and salts on homo–lumo gap of 7-hydroxy coumarine notabally reflected by absorption and emission spectra. *Journal of Fluorescence*, 32(6):2351–2362.
- Ferreira, L. G., Dos Santos, R. N., Oliva, G., and Andricopulo, A. D. (2015). Molecular docking and structure-based drug design strategies. *Molecules*, 20(7):13384–13421.
- Forsman, E. N. and Clark, K. (1973). Measurement of the oscillator strength of the o i (s 1- p o 1) transition at 1217.6 Å. *Physical Review A*, 7(4):1203.
- Förster, H. (2004). Uv/vis spectroscopy. *Characterization I: -/-*, pages 337–426.
- Frankel, T. (1974). Maxwell’s equations. *The American Mathematical Monthly*, 81(4):343–349.
- Frisch, A. et al. (2009). gaussian 09w reference. *Wallingford, USA*, 25p, 470.
- Fu, Y., Zhao, J., and Chen, Z. (2018). Insights into the molecular mechanisms of protein-ligand interactions by molecular docking and molecular dynamics simulation: a case of oligopeptide binding protein. *Computational and mathematical methods in medicine*, 2018(1):3502514.
- Gao, J., Yu, H., Guo, W., Kong, Y., Gu, L., Li, Q., Yang, S., Zhang, Y., and Wang, Y. (2018). The anticancer effects of ferulic acid is associated with induction of cell cycle arrest and autophagy in cervical cancer cells. *Cancer Cell International*, 18:1–9.
- Gehlen, M. H. (2020). The centenary of the stern-volmer equation of fluorescence quenching: From the single line plot to the sv quenching map. *Journal of Photochemistry and Photobiology C: Photochemistry Reviews*, 42:100338.
- Ghosh, A. K., Ghosh, C., and Gupta, A. (2013). A simple approach to detect caffeine in tea beverages. *Journal of agricultural and food chemistry*, 61(16):3814–3820.
- Gill, P. M. and von Rague Schleyer, P. (1994). Density functional theory (dft), hartree-fock (hf), and the self-consistent field. *J. Chem. Phys*, 100:5066–5075.
- Gohlke, H., Hendlich, M., and Klebe, G. (2000). Predicting binding modes, binding affinities and hot spots’ for protein-ligand complexes using a knowledge-based scoring function. *Perspectives in Drug Discovery and Design*, 20:115–144.
- Gohlke, H. and Klebe, G. (2002). Approaches to the description and prediction of the binding affinity of small-molecule ligands to macromolecular receptors. *Angewandte Chemie International Edition*, 41(15):2644–2676.
- Goodman, L. (1961). n→π transitions in the azines. *Journal of Molecular Spectroscopy*, 6:109–137.

- Gorbatshevich, S. K. and Smirnova, O. Y. (2004). Solvatochromic and thermochromic shifts of electronic spectra of polar solute molecules in a mixture of polar and nonpolar solvent; the role of solvent–solvent interactions. *The Journal of chemical physics*, 120(3):1369–1374.
- Grabowski, J. and Gantt, E. (1978). Photophysical properties of phycobiliproteins from phycobilisomes: fluorescence lifetimes, quantum yields, and polarization spectra. *Photochemistry and photobiology*, 28(1):39–45.
- Grabowski, Z. R., Rotkiewicz, K., and Rettig, W. (2003). Structural changes accompanying intramolecular electron transfer: focus on twisted intramolecular charge-transfer states and structures. *Chemical reviews*, 103(10):3899–4032.
- Grechko, M. and Zanni, M. T. (2012). Quantification of transition dipole strengths using 1d and 2d spectroscopy for the identification of molecular structures via exciton delocalization: application to  $\alpha$ -helices. *The Journal of chemical physics*, 137(18).
- Guedes, I. A., de Magalhães, C. S., and Dardenne, L. E. (2014). Receptor–ligand molecular docking. *Biophysical reviews*, 6:75–87.
- Gurbuzer, A. (2021). Investigation of in vitro antimicrobial activities of some hydroxybenzoic and hydroxycinnamic acids commonly found in medicinal and aromatic plants. *International Journal of Plant Based Pharmaceuticals*, 1(1):42–47.
- Hădărugă, N.-G. and Hădărugă, D.-I. (2023). Hydroxycinnamic acids. In *Handbook of Food Bioactive Ingredients: Properties and Applications*, pages 59–109. Springer.
- Han, J. (2021). Chemcraft: a ludic approach to educational game design. In *extended abstracts of the 2021 CHI conference on human factors in computing systems*, pages 1–5.
- Hu, Y.-J., Liu, Y., Zhang, L.-X., Zhao, R.-M., and Qu, S.-S. (2005). Studies of interaction between colchicine and bovine serum albumin by fluorescence quenching method. *Journal of Molecular Structure*, 750(1-3):174–178.
- Hua, X., Chen, X., and Goddard, W. (1997). Generalized generalized gradient approximation: An improved density-functional theory for accurate orbital eigenvalues. *Physical Review B*, 55(24):16103.
- Iqbal, M., Raish, M., Ahmad, A., Ali, E. A., Bin Jordan, Y. A., Ansari, M. A., Shahid, M., Ahad, A., Alkharfy, K. M., and Al-Jenoobi, F. I. (2022). Cytochrome p450 3a2 and pgp-mdr1-mediated pharmacokinetic interaction of sinapic acid with ibuprofen in rats: Potential food/herb–drug interaction. *Processes*, 10(6):1066.
- Isbell, J. J. and Brodbelt, J. S. (1996). Effects of functional group interactions on the gas-phase methylation and dissociation of acids and esters. *Journal of the American Society for Mass Spectrometry*, 7(6):565–572.

- Jabed, M. A., Zhao, J., Kilin, D., and Yu, T. (2021). Understanding of light absorption properties of the n-doped graphene oxide quantum dot with td-dft. *The Journal of Physical Chemistry C*, 125(27):14979–14990.
- Jaggi, N. and Vij, D. (2006). Fourier transform infrared spectroscopy. In *Handbook of Applied Solid State Spectroscopy*, pages 411–450. Springer.
- Jalaludeen, A. M. and Pari, L. (2011). Studies on the antioxidant and free radical-scavenging effect of sinapic acid: An in vivo and in vitro model. *Journal of Pharmaceutical Sciences and Research*, 3(9):1447.
- Janani, S., Rajagopal, H., Muthu, S., Aayisha, S., and Raja, M. (2021). Molecular structure, spectroscopic (ft-ir, ft-raman, nmr), homo-lumo, chemical reactivity, aim, elf, lol and molecular docking studies on 1-benzyl-4-(n-boc-amino) piperidine. *Journal of Molecular Structure*, 1230:129657.
- Johnson, G. (1980). Effect of concentration on the fluorescence spectra and lifetimes of pyrene in polystyrene films. *Macromolecules*, 13(4):839–844.
- Kable, S. (2019). Basic principles of fluorescence. In *Fundamentals of Fluorescence Imaging*, pages 1–34. Jenny Stanford Publishing.
- Kapusta, K., Voronkov, E., Okovytyy, S., Korobov, V., and Leszczynski, J. (2018). Reconstruction of sto-3g family basis set for the accurate calculation of magnetic properties. *Russian Journal of Physical Chemistry A*, 92:2827–2834.
- Kawski, A., Bojarski, P., and Kukliński, B. (2002). Excitation wavelength dependence of acrylodan fluorescence spectra in some polar solvents. *Zeitschrift Für Naturforschung A*, 57(9-10):94–97.
- Khan, M. F., Rashid, R. B., Rahman, M. M., Al Faruk, M., Rahman, M. M., and Rashid, M. A. (2017). Effects of solvent polarity on solvation free energy, dipole moment, polarizability, hyperpolarizability and molecular reactivity of aspirin. *Int. J. Pharm. Pharm. Sci*, 9(2):217–221.
- Khan, S. A., Khan, S. B., Khan, L. U., Farooq, A., Akhtar, K., and Asiri, A. M. (2018). Fourier transform infrared spectroscopy: fundamentals and application in functional groups and nanomaterials characterization. *Handbook of materials characterization*, pages 317–344.
- Kohn, W., Becke, A. D., and Parr, R. G. (1996). Density functional theory of electronic structure. *The journal of physical chemistry*, 100(31):12974–12980.
- Komorowski, L. (1987). Electronegativity and hardness in the chemical approximation. *Chemical physics*, 114(1):55–71.

- Kootstra, F. a., De Boeij, P., and Snijders, J. (2000). Application of time-dependent density-functional theory to the dielectric function of various nonmetallic crystals. *Physical Review B*, 62(11):7071.
- Krishna Sri, P. and Padmavathy, S. (2018). A short review on the effect of functional group in methylxanthine (caffeine) class of drugs. *Biochem Pharmacol (Los Angel)*, 7(257):2167–0501.
- Kristyan, S. (2008). Properties of the multi-electron densities “between” the hohenberg–kohn theorems and variational principle. *Journal of Molecular Structure: THEOCHEM*, 858(1-3):1–11.
- Krystkowiak, E., Dobek, K., and Maciejewski, A. (2006). Origin of the strong effect of protic solvents on the emission spectra, quantum yield of fluorescence and fluorescence lifetime of 4-aminophthalimide: Role of hydrogen bonds in deactivation of s1-4-aminophthalimide. *Journal of Photochemistry and Photobiology A: Chemistry*, 184(3):250–264.
- Kumar, V., Teotia, J., and Yadav, A. K. (2022). Vibrational (ft-raman and ftir) spectroscopic study, molecular structure, thermodynamic properties and non-linear optical properties of benzyl-3-oxopyperazine-1-carboxylate by density functional theory. *Materials Today: Proceedings*, 62:7137–7141.
- Kunstatter, G., Das, S., Kunstatter, G., and Das, S. (2020). The schrödinger equation. *A First Course on Symmetry, Special Relativity and Quantum Mechanics: The Foundations of Physics*, pages 213–252.
- Lakowicz, J. R. and Lakowicz, J. R. (1983). Quenching of fluorescence. *Principles of fluorescence spectroscopy*, pages 257–301.
- Lalasangi, D., Hanagodimath, S., Khanadal, T., Padmashali, B., and Jadhav, M. S. (2024). Solvent effects on the absorption and emission spectra of the [5-amino-1-bromoindolizin-3-yl](4-bromophenyl) methanone molecule. *Journal of Fluorescence*, pages 1–9.
- Langer, U., Pauly, D., and Repin, S. (2019). *Maxwell's equations*, volume 24. Volume.
- Li, S., Huang, K., Zhong, M., Guo, J., Wang, W.-z., and Zhu, R. (2010). Comparative studies on the interaction of caffeic acid, chlorogenic acid and ferulic acid with bovine serum albumin. *Spectrochimica Acta Part A: Molecular and Biomolecular Spectroscopy*, 77(3):680–686.
- Li, W., Li, N., Tang, Y., Li, B., Liu, L., Zhang, X., Fu, H., and Duan, J.-a. (2012). Biological activity evaluation and structure–activity relationships analysis of ferulic acid and caffeic acid derivatives for anticancer. *Bioorganic & Medicinal Chemistry Letters*, 22(19):6085–6088.

- Li, Y., Liu, C., Zhang, Y., Mi, S., and Wang, N. (2011). Pharmacokinetics of ferulic acid and potential interactions with honghua and clopidogrel in rats. *Journal of ethnopharmacology*, 137(1):562–567.
- Lima, E. C., Gomes, A. A., and Tran, H. N. (2020). Comparison of the nonlinear and linear forms of the van't hof equation for calculation of adsorption thermodynamic parameters ( $s^\circ$  and  $h^\circ$ ). *Journal of Molecular Liquids*, 311:113315.
- Limbu, S., Ojha, T., Ghimire, R. R., and Rai, K. B. (2024). An investigation of vibrational analysis, thermodynamics properties and electronic properties of formaldehyde and its stretch by substituent acetone, acetyl chloride and methyl acetate using first principles analysis. *BIBECHANA*, 21(1):23–36.
- Lin, F.-H., Lin, J.-Y., Gupta, R. D., Tournas, J. A., Burch, J. A., Selim, M. A., Monteiro-Riviere, N. A., Grichnik, J. M., Zielinski, J., and Pinnell, S. R. (2005). Ferulic acid stabilizes a solution of vitamins c and e and doubles its photoprotection of skin. *Journal of Investigative Dermatology*, 125(4):826–832.
- Lippert, E. (1955). Dipolmoment und elektronenstruktur von angeregten molekülen. *Zeitschrift für Naturforschung A*, 10(7):541–545.
- Liu, J., Guo, Z., Sun, J., and Liang, W. (2010). Theoretical studies on electronic spectroscopy and dynamics with the real-time time-dependent density functional theory. *Frontiers of Chemistry in China*, 5:11–28.
- Liu, Q., Qiu, L., Wang, Y., Lv, G., Liu, G., Wang, S., and Lin, J. (2016). Solvent effect on molecular structure, ir spectra, thermodynamic properties and chemical stability of zoledronic acid: Dft study. *Journal of molecular modeling*, 22:1–11.
- Lorigooini, Z., Jamshidi-kia, F., and Hosseini, Z. (2020). Analysis of aromatic acids (phenolic acids and hydroxycinnamic acids). In *Recent Advances in Natural Products Analysis*, pages 199–219. Elsevier.
- Lu, W., Wang, C., Schmidt, M., Bytautas, L., Ho, K., and Ruedenberg, K. (2004). Molecule intrinsic minimal basis sets. i. exact resolution of ab initio optimized molecular orbitals in terms of deformed atomic minimal-basis orbitals. *The Journal of chemical physics*, 120(6):2629–2637.
- Mabesoone, M. F., Palmans, A. R., and Meijer, E. (2020). Solute–solvent interactions in modern physical organic chemistry: Supramolecular polymers as a muse. *Journal of the American Chemical Society*, 142(47):19781–19798.
- Magalhaes, A. L. (2014). Gaussian-type orbitals versus slater-type orbitals: a comparison. *Journal of Chemical Education*, 91(12):2124–2127.

- Maity, D. K. (2002). Sigma bonded radical cation complexes: a theoretical study. *The Journal of Physical Chemistry A*, 106(23):5716–5721.
- Majumdar, D., Samanta, P. N., Roszak, S., and Leszczynski, J. (2021). Slater-type orbitals. In *Basis Sets in Computational Chemistry*, pages 17–40. Springer.
- Mandal, D., Sarmah, J. K., and Gupta, J. (2024). Advanced nano-enhanced therapies: The role of phenolic acid-infused (syringic acid, sinapic acid, and o-coumaric acid) guar-gum nanoformulation in antimicrobial and anti-inflammatory wound care.
- Mannekutla, J., Mulimani, B., and Inamdar, S. (2008). Solvent effect on absorption and fluorescence spectra of coumarin laser dyes: evaluation of ground and excited state dipole moments. *Spectrochimica Acta Part A: Molecular and Biomolecular Spectroscopy*, 69(2):419–426.
- Mataga, N., Kaifu, Y., and Koizumi, M. (1956). Solvent effects upon fluorescence spectra and the dipole moments of excited molecules. *Bulletin of the Chemical Society of Japan*, 29(4):465–470.
- Matos, M. S., Hofkens, J., and Gehlen, M. H. (2008). Static and dynamic bimolecular fluorescence quenching of porphyrin dendrimers in solution. *Journal of Fluorescence*, 18:821–826.
- Matsuzaki, Y., Uchikoga, N., Ohue, M., and Akiyama, Y. (2017). Rigid-docking approaches to explore protein–protein interaction space. *Network Biology*, pages 33–55.
- Mayerhöfer, T. G., Pahlow, S., and Popp, J. (2020). The bouguer-beer-lambert law: Shining light on the obscure. *ChemPhysChem*, 21(18):2029–2046.
- Mazziotti, D. A. (2012). Two-electron reduced density matrix as the basic variable in many-electron quantum chemistry and physics. *Chemical reviews*, 112(1):244–262.
- Melavanki, R., Muddapur, G., Srinivasa, H., Honnanagoudar, S., and Patil, N. (2021). Solvation, rotational dynamics, photophysical properties study of aromatic asymmetric di-ketones: An experimental and theoretical approach. *Journal of Molecular Liquids*, 337:116456.
- Melavanki, R. M., Patil, H., Umopathy, S., and Kadadevarmath, J. (2012). Solvatochromic effect on the photophysical properties of two coumarins. *Journal of fluorescence*, 22:137–144.
- Melhuish, W. H. (1961). Quantum efficiencies of fluorescence of organic substances: effect of solvent and concentration of the fluorescent solute. *The Journal of Physical Chemistry*, 65(2):229–235.

- Mendelsohn, L. D. (2004). Chemdraw 8 ultra, windows and macintosh versions. *Journal of chemical information and computer sciences*, 44(6):2225–2226.
- Miar, M., Shiroudi, A., Pourshamsian, K., Olliaey, A. R., and Hatamjafari, F. (2021). Theoretical investigations on the homo–lumo gap and global reactivity descriptor studies, natural bond orbital, and nucleus-independent chemical shifts analyses of 3-phenylbenzo [d] thiazole-2 (3 h)-imine and its para-substituted derivatives: Solvent and substituent effects. *Journal of Chemical Research*, 45(1-2):147–158.
- Mihaiescu, T., Turti, S., Souca, M., Muresan, R., Achim, L., Prifti, E., Papuc, I., Munteanu, C., and Marza, S. M. (2024). Caffeine and taurine from energy drinks—a review. *Cosmetics*, 11(1):12.
- Mosapour Kotena, Z., Razi, M., and Ahmadi, S. (2021). Evaluation of hydrogen bonds formation in the selected rare sugars based on 6-31g\* and 6-311++ g (d, p) basis sets. *Journal of Molecular Modeling*, 27:1–10.
- Mota, F. L., Carneiro, A. P., Queimada, A. J., Pinho, S. P., and Macedo, E. A. (2009). Temperature and solvent effects in the solubility of some pharmaceutical compounds: Measurements and modeling. *European Journal of Pharmaceutical Sciences*, 37(3-4):499–507.
- Nagy, B. and Jensen, F. (2017). Basis sets in quantum chemistry. *Reviews in computational chemistry*, 30:93–149.
- Neese, F. (2009). Prediction of molecular properties and molecular spectroscopy with density functional theory: From fundamental theory to exchange-coupling. *Coordination Chemistry Reviews*, 253(5-6):526–563.
- Nicholls, R. (1977). Transition probability data for molecules of astrophysical interest. *In: Annual review of astronomy and astrophysics. Volume 15. (A78-16576 04-90) Palo Alto, Calif., Annual Reviews, Inc., 1977, p. 197-234.*, 15:197–234.
- Nile, S. H., Ko, E. Y., Kim, D. H., and Keum, Y.-S. (2016). Screening of ferulic acid related compounds as inhibitors of xanthine oxidase and cyclooxygenase-2 with anti-inflammatory activity. *Revista Brasileira de Farmacognosia*, 26(1):50–55.
- Nurdiansyah, R., Putra, A. B. N., Nadhifah, A., Chriscensia, E., Kusumo, U. K. G., Yosiano, S. A., Musung, A. B., Wenas, S. A., Makalew, S., Lovina, P., et al. (2023). Cytotoxic activity of indonesian pogonatum neesii dozy from cibodas botanical garden: In silico molecular docking and in vitro evaluation. *Pharmaceutical Sciences*, 29(4):448–458.
- Ojha, H., Mishra, K., Hassan, M. I., and Chaudhury, N. K. (2012). Spectroscopic and isothermal titration calorimetry studies of binding interaction of ferulic acid with bovine serum albumin. *Thermochimica Acta*, 548:56–64.

- Othman, A. M., Abdel-Rahman, N., Denewer, M., and Eissa, L. A. (2023). Sinapic acid and 3, 3-diindolylmethane potentiate cyclophosphamide antitumor activity through induction of apoptosis and inhibition of metastasis. *International Immunopharmacology*, 118:110074.
- Pacchioni, G. (2013). Electronic interactions and charge transfers of metal atoms and clusters on oxide surfaces. *Physical Chemistry Chemical Physics*, 15(6):1737–1757.
- Panyam, J. and Patil, Y. (2008). Distribution: movement of drugs through the body. *ADME and Biopharmaceutical Properties*, page 323.
- Papagiouvannis, G., Theodosis-Nobelos, P., and Rezza, E. A. (2024). Trolox, ferulic, sinapic, and cinnamic acid derivatives of proline and gaba with antioxidant and/or anti-inflammatory properties. *Molecules*, 29(16):3763.
- Pariser, R. and Parr, R. G. (1953). A semi-empirical theory of the electronic spectra and electronic structure of complex unsaturated molecules. i. *The Journal of Chemical Physics*, 21(3):466–471.
- Parker, E. (2000). *Newton, Maxwell, and magnetospheric physics*, volume 118. AGU Washington, DC.
- Pathak, A. K., Mukherjee, T., and Maity, D. K. (2005).  $\sigma/\sigma^*$  and  $\pi/\pi^*$  two-center three-electron bonding in complexes formed between charged thiocyanate and x radicals (x= cl, br, i and scn). *Journal of Molecular Structure: THEOCHEM*, 755(1-3):241–245.
- Patsidis, A. C. and Psarras, G. C. (2024). Basic principles of dielectrics. *High Temperature Polymer Dielectrics: Fundamentals and Applications in Power Equipment*, pages 21–55.
- Paul, S. P. M., Praveena, G., Beula, R. J., Haris, M., Abiram, A., et al. (2022). Theoretical investigation on the interaction between metformin and ferulic acid-a dft approach. *Journal of the Indian Chemical Society*, 99(3):100368.
- Pawar, S. S. and Rohane, S. H. (2021). Review on discovery studio: An important tool for molecular docking.
- Pearson, R. G. (1992). The electronic chemical potential and chemical hardness. *Journal of Molecular Structure: THEOCHEM*, 255:261–270.
- Perez, N. (2024a). Basic quantum mechanics. In *Materials Science: Theory and Engineering*, pages 101–138. Springer.
- Perez, N. (2024b). Thermodynamics of phase change. In *Materials Science: Theory and Engineering*, pages 303–377. Springer.
- Pérez, P., Domingo, L. R., Aizman, A., and Contreras, R. (2007). The electrophilicity index in organic chemistry. In *Theoretical and computational chemistry*, volume 19, pages 139–201. Elsevier.

- Pernas, P. and Cantelar, E. (2005). Emission and absorption cross-section calculation of rare earth doped materials for applications to integrated optic devices. *Physica Scripta*, 2005(T118):93.
- Pilli, S. R., Banerjee, T., and Mohanty, K. (2015). Homo–lumo energy interactions between endocrine disrupting chemicals and ionic liquids using the density functional theory: Evaluation and comparison. *Journal of Molecular Liquids*, 207:112–124.
- Pluta, T. and Skrzyński, G. (2021). Time-dependent dft calculations of the dipole moment and polarizability for excited states. In *Advances in Quantum Chemistry*, volume 83, pages 305–327. Elsevier.
- Politzer, P. and Murray, J. S. (2021). Molecular electrostatic potentials: significance and applications. *Chemical reactivity in confined systems: theory, modelling and applications*, pages 113–134.
- Povrozin, Y. and Barbieri, B. (2016). Fluorescence spectroscopy. *Handbook of Measurement in Science and Engineering*, 3:2475–2498.
- Prachalith, N., Vibha, K., Suresh Kumar, H., Thipperudrappa, J., and Khadke, U. (2024). Solvatochromism, preferential solvation and excited state dipole moments of flufenamic acid in different solvent polarities. *International Journal of Modern Physics B*, page 2550104.
- Precupas, A., Sandu, R., Leonties, A. R., Anghel, D.-F., and Popa, V. T. (2017). Complex interaction of caffeic acid with bovine serum albumin: calorimetric, spectroscopic and molecular docking evidence. *New Journal of Chemistry*, 41(24):15003–15015.
- Rauf, M., Hisaindee, S., Graham, J., and Al-Zamly, A. (2015). Effect of various solvents on the absorption spectra of dithizone and dft calculations. *Journal of Molecular Liquids*, 211:332–337.
- Ravi, M., Soujanya, T., Samanta, A., and Radhakrishnan, T. (1995). Excited-state dipole moments of some coumarin dyes from a solvatochromic method using the solvent polarity parameter, ent. *Journal of the Chemical Society, Faraday Transactions*, 91(17):2739–2742.
- Reddy, V. S., Shiva, S., Manikantan, S., and Ramakrishna, S. (2024). Pharmacology of caffeine and its effects on the human body. *European Journal of Medicinal Chemistry Reports*, page 100138.
- Reichardt, C. (1979). Empirical parameters of solvent polarity as linear free-energy relationships. *Angewandte chemie internationale edition in English*, 18(2):98–110.
- Reichardt, C. (1994). Solvatochromic dyes as solvent polarity indicators. *Chemical reviews*, 94(8):2319–2358.

- Renk, K. F. and Renk, K. F. (2012). Basis of the theory of the laser: The einstein coefficients. *Basics of Laser Physics: For Students of Science and Engineering*, pages 83–93.
- Roberts, A. (2021). Caffeine: an evaluation of the safety database. In *Nutraceuticals*, pages 501–518. Elsevier.
- Roche, D. B., Brackenridge, D. A., and McGuffin, L. J. (2015). Proteins and their interacting partners: An introduction to protein–ligand binding site prediction methods. *International journal of molecular sciences*, 16(12):29829–29842.
- Ross, P. D. and Subramanian, S. (1981). Thermodynamics of protein association reactions: forces contributing to stability. *Biochemistry*, 20(11):3096–3102.
- Roy, N., Narayanankutty, A., Nazeem, P., Valsalan, R., Babu, T., and Mathew, D. (2016). Plant phenolics ferulic acid and p-coumaric acid inhibit colorectal cancer cell proliferation through egfr down-regulation. *Asian Pacific Journal of Cancer Prevention*, 17(8):4019–4023.
- Sadigh, M. K., Zakerhamidi, M., Ahmadian, S. S., Johari-Ahar, M., and Haghghi, L. Z. (2016). Environment and solute-solvent interaction effects on photo-physical behaviors of folic acid and folinic acid drugs. *Journal of Molecular Structure*, 1125:177–185.
- Sahni, V., Bohnen, K.-P., and Harbola, M. K. (1988). Analysis of the local-density approximation of density-functional theory. *Physical Review A*, 37(6):1895.
- Sahni, V. and Sahni, V. (2004). The hohenberg-kohn theorems and kohn-sham density functional theory. *Quantal Density Functional Theory*, pages 99–123.
- Sahu, M. K., Nayak, A. K., Hailemeskel, B., and Eyupoglu, O. E. (2024). Exploring recent updates on molecular docking: Types, method, application, limitation & future prospects. *International Journal of Pharmaceutical Research and Allied Sciences*, 13(2-2024):24–40.
- Salam, A. (2011). Molecular quantum electrodynamics of radiation-induced intermolecular forces. In *Advances in Quantum Chemistry*, volume 62, pages 1–34. Elsevier.
- Salam, A. (2015). Quantum electrodynamics effects in atoms and molecules. *Wiley Interdisciplinary Reviews: Computational Molecular Science*, 5(2):178–201.
- Saraiva, S. M., Jacinto, T. A., Gonçalves, A. C., Gaspar, D., and Silva, L. R. (2023). Overview of caffeine effects on human health and emerging delivery strategies. *Pharmaceuticals*, 16(8):1067.
- Sarangi, R., Vidal, M. L., Coriani, S., and Krylov, A. I. (2020). On the basis set selection for calculations of core-level states: Different strategies to balance cost and accuracy. *Molecular Physics*, 118(19-20):e1769872.

- Sarkar, R., Boggio-Pasqua, M., Loos, P.-F., and Jacquemin, D. (2021). Benchmarking td-dft and wave function methods for oscillator strengths and excited-state dipole moments. *Journal of Chemical Theory and Computation*, 17(2):1117–1132.
- Schwab, A. J. (2012). *Field Theory Concepts: Electromagnetic Fields. Maxwell's Equations Grad, Curl, Div. Etc. Finite-Element Method. Finite-Difference Method. Charge Simulation Method. Monte Carlo Method.* Springer Science & Business Media.
- Shahid, M., Raish, M., Ahmad, A., Bin Jordan, Y. A., Ansari, M. A., Ahad, A., Alkharfy, K. M., Alaofi, A. L., and Al-Jenoobi, F. I. (2022). Sinapic acid ameliorates acetic acid-induced ulcerative colitis in rats by suppressing inflammation, oxidative stress, and apoptosis. *Molecules*, 27(13):4139.
- Sharp, K. A., Madan, B., Manas, E., and Vanderkooi, J. M. (2001). Water structure changes induced by hydrophobic and polar solutes revealed by simulations and infrared spectroscopy. *The Journal of Chemical Physics*, 114(4):1791–1796.
- Sherefedin, U., Belay, A., Gudishe, K., Kebede, A., Kumela, A. G., and Asemare, S. (2024). Photophysical properties of sinapic acid and ferulic acid and their binding mechanism with caffeine. *Journal of Fluorescence*, pages 1–15.
- Sherefedin, U., Belay, A., Gudishe, K., Kebede, A., Kumela, A. G., Feyisa, T., Mahamud, J. H., and Fekadu, S. (2025). Physicochemical properties and drug likeness of hydroxycinnamic acids and their molecular docking with caffeine and amoxicillin: Potential anticancer drugs. *Results in Chemistry*, page 101996.
- Sherefedin, U., Belay, A., Kebede, A., Asemare, S., Woldegiorges, K., Kumela, A. G., and Gudishe, K. (2023). Determination of the ground and excited state dipole moments of ferulic and sinapic acids by solvatochromic effects and density function theory method. *AIP Advances*, 13(10).
- Shirai, K., Matsuoka, M., and Fukunishi, K. (1999). Fluorescence quenching by intermolecular  $\pi$ - $\pi$  interactions of 2, 5-bis (n, n-dialkylamino)-3, 6-dicyanopyrazines. *Dyes and pigments*, 42(1):95–101.
- Shivaleela, B., Shivraj, G., and Hanagodimath, S. (2023). Estimation of dipole moments by solvatochromic shift method, spectroscopic analysis of uv-visible, homo-lumo, esp map, mulliken atomic charges, nbo and nlo properties of benzofuran derivative. *Results in Chemistry*, 6:101046.
- Shivaleela, B., Shivraj, G., Mayadevi, K., Mahantesh, B., and Hanagodimath, S. (2022). Effect of solvent on fluorescence and absorption spectra of fluorescent coumarin derivative: Estimation of ground and excited state dipole moments. *Materials Today: Proceedings*, 68:564–572.

- Sıdır, İ., Sıdır, Y. G., Berber, H., and Türkoğlu, G. (2016). Specific and non-specific interaction effect on the solvatochromism of some symmetric (2-hydroxybenzilydeamino) phenoxy schiff base derivatives. *Journal of Molecular Liquids*, 215:691–703.
- Singh, D. P., Inamdar, S. R., and Kumar, S. (2021). Fluorescence spectrometry. *Modern Techniques of Spectroscopy: Basics, Instrumentation, and Applications*, pages 431–468.
- Smyk, B. (2003). Fluorescence study of sinapic acid interaction with bovine serum albumin and egg albumin. *Journal of Fluorescence*, 13:349–356.
- Srivastava, A., Khan, M. S., et al. (2020). Density functional theory calculations for electronic, optoelectronic and thermodynamic properties of dibenzothiophene metal complexes. *Materials Research Express*, 7(1):016311.
- Strickler, S. and Berg, R. A. (1962). Relationship between absorption intensity and fluorescence lifetime of molecules. *The Journal of chemical physics*, 37(4):814–822.
- Suppan, P. (1983). Excited-state dipole moments from absorption/fluorescence solvatochromic ratios. *Chemical Physics Letters*, 94(3):272–275.
- Suresh, C. H., Remya, G. S., and Anjalikrishna, P. K. (2022). Molecular electrostatic potential analysis: A powerful tool to interpret and predict chemical reactivity. *Wiley Interdisciplinary Reviews: Computational Molecular Science*, 12(5):e1601.
- Szekeres, Z., Bogar, F., and Ladik, J. (2005). B3lyp, blyp and pbe dft band structures of the nucleotide base stacks. *International journal of quantum chemistry*, 102(4):422–426.
- Tamaki, T. (1982). Solvent effects on the fluorescence quantum yields and lifetimes of 1-and 2-acetyl-or benzoylanthracenes. *Bulletin of the Chemical Society of Japan*, 55(6):1756–1760.
- Tamayose, C., Torres, P., Roque, N., and Ferreira, M. (2019). Hiv-1 reverse transcriptase inhibitory activity of flavones and chlorogenic acid derivatives from moquiniastrium floribundum (asteraceae). *South African journal of botany*, 123:142–146.
- Taneja, L., Sharma, A., and Singh, R. (1995). Study of photophysical properties of coumarins: substituent and concentration dependence. *Journal of luminescence*, 63(4):203–214.
- Taştemur, Ş., Hacısüleyman, L., Karataş, Ö., Yulak, F., and Ataseven, H. (2023). Anticancer activity of sinapic acid by inducing apoptosis in ht-29 human colon cancer cell line. *Canadian Journal of Physiology and Pharmacology*, 101(7):361–368.
- Thakkar, A., Wang, J., and Prabhu, S. (2014). Novel combinations of nano-formulated ferulic acid and aspirin show high potential for chemoprevention of pancreatic cancer. *Cancer Research*, 74(19\_Supplement):2155–2155.

- Thanikachalam, V., Arunpandiyam, A., Jayabharathi, J., and Ramanathan, P. (2014). Photophysical properties of the intramolecular excited charge-transfer states of  $\pi$ -expanded styryl phenanthrimidazoles—effect of solvent polarity. *RSC advances*, 4(13):6790–6806.
- Thomasson, B. (2016). High accuracy relative luminescence quantum yield measurements of upconverting nanoparticles.
- Tiwari, S., Mishra, P., and Suhai, S. (2008). Solvent effect of aqueous media on properties of glycine: significance of specific and bulk solvent effects, and geometry optimization in aqueous media. *International Journal of Quantum Chemistry*, 108(5):1004–1016.
- Trott, O. and Olson, A. J. (2010). Autodock vina: improving the speed and accuracy of docking with a new scoring function, efficient optimization, and multithreading. *Journal of computational chemistry*, 31(2):455–461.
- Tsaparlis, G. (1997). Atomic orbitals, molecular orbitals and related concepts: Conceptual difficulties among chemistry students. *Research in Science Education*, 27:271–287.
- Tsuneda, T. and Tsuneda, T. (2014). Hartree–fock method. *Density Functional Theory in Quantum Chemistry*, pages 35–63.
- Umar, Y. and Abdalla, S. (2017). Dft study of the molecular structure, conformational preference, homo, lumo, and vibrational analysis of 2-, and 3-furoyl chloride. *Journal of Solution Chemistry*, 46:741–758.
- Van Oss, C., Good, R., and Chaudhury, M. (1986). The role of van der waals forces and hydrogen bonds in “hydrophobic interactions” between biopolymers and low energy surfaces. *Journal of colloid and Interface Science*, 111(2):378–390.
- Van Speybroeck, V., Gani, R., and Meier, R. J. (2010). The calculation of thermodynamic properties of molecules. *Chemical Society Reviews*, 39(5):1764–1779.
- Vanzo, D., Topham, B. J., and Soos, Z. G. (2015). Dipole-field sums, lorentz factors, and dielectric properties of organic molecular films modeled as crystalline arrays of polarizable points. *Advanced Functional Materials*, 25(13):2004–2012.
- Venkatesh, G., Sixto-López, Y., Vennila, P., Siva, V., and Sumathi, P. (2024). Synthesis, solvent effects, chemical reactivity, molecular docking and molecular dynamic studies of triazole derivative. *Journal of Molecular Structure*, 1303:137561.
- Vinholes, J., Silva, B. M., and Silva, L. R. (2015). Hydroxycinnamic acids (hcas): Structure, biological properties and health effects. *Advances in Medicine and Biology*, 88(8):1–33.
- Viola, G., Facciolo, L., Canton, M., Vedaldi, D., Dall’Acqua, F., Aloisi, G. G., Amelia, M., Barbafina, A., Elisei, F., and Latterini, L. (2004). Photophysical and phototoxic

- properties of the antibacterial fluoroquinolones levofloxacin and moxifloxacin. *Chemistry & biodiversity*, 1(5):782–801.
- Vollmer, F. and Rettig, W. (1996). Fluorescence loss mechanism due to large-amplitude motions in derivatives of 2, 2'-bipyridyl exhibiting excited-state intramolecular proton transfer and perspectives of luminescence solar concentrators. *Journal of Photochemistry and Photobiology A: Chemistry*, 95(2):143–155.
- Wang, Q., Tang, Y., Yang, Y., Lei, L., Lei, X., Zhao, J., Zhang, Y., Li, L., Wang, Q., and Ming, J. (2022). The interaction mechanisms, and structural changes of the interaction between zein and ferulic acid under different pH conditions. *Food Hydrocolloids*, 124:107251.
- Wang, X., Zhang, S., Zhao, H., Wang, Q., Zhang, Y., Xu, H., Xia, X., and Han, S. (2021). Spectroscopic investigation into the binding of ferulic acid with sodium deoxycholate: Hydrophobic force versus hydrogen bonding. *Langmuir*, 37(4):1420–1428.
- Wiberg, K. B. (2004). Basis set effects on calculated geometries: 6-311++ g\*\* vs. aug-cc-pvdz. *Journal of computational chemistry*, 25(11):1342–1346.
- Woldegiorges, K., Belay, A., and Kebede, A. (2022). Photophysical properties of levofloxacin and norfloxacin drugs and their fluorescence quenching mechanism with caffeine. *Spectroscopy Letters*, 55(8):500–513.
- Woldegiorges, K., Belay, A., Kebede, A., and Abebe, T. (2021). Estimating the ground and excited state dipole moments of levofloxacin and norfloxacin drugs using solvatochromic effects and computational work. *Journal of Spectroscopy*, 2021(1):7214182.
- Wu, Q., Jiang, F., Li, C., Hu, Y., and Liu, Y. (2011). Interaction of caffeine with bovine serum albumin: determination of binding constants and the binding site by spectroscopic methods. *Chinese Journal of Chemistry*, 29(3):433–440.
- Wu, Y. and Zhu, W. (2013). Organic sensitizers from d- $\pi$ -a to d-a- $\pi$ -a: effect of the internal electron-withdrawing units on molecular absorption, energy levels and photovoltaic performances. *Chemical Society Reviews*, 42(5):2039–2058.
- Yang, J., Chen, J., Hao, Y., and Liu, Y. (2021). Identification of the DPPH radical scavenging reaction adducts of ferulic acid and sinapic acid and their structure-antioxidant activity relationship. *Lwt*, 146:111411.
- Yang, Y.-h. and Zhang, D.-h. (1995). Concentration effect on the fluorescence spectra of humic substances. *Communications in soil science and plant analysis*, 26(15-16):2333–2349.
- Yin, C.-l., Lu, R.-g., Zhu, J.-f., Huang, H.-m., Liu, X., Li, Q.-f., Mo, Y.-y., Zhu, H.-j., Chin, B., Wu, J.-x., et al. (2019). The study of neuroprotective effect of ferulic acid based on cell metabolomics. *European journal of pharmacology*, 864:172694.

- Yoon, M.-C., Choi, Y. S., and Kim, S. K. (1999). The oh production from the  $\pi-\pi^*$  transition of acetylacetone. *Chemical physics letters*, 300(1-2):207–212.
- Zare, K., Eidi, A., Roghani, M., and Rohani, A. H. (2015). The neuroprotective potential of sinapic acid in the 6-hydroxydopamine-induced hemi-parkinsonian rat. *Metabolic Brain Disease*, 30:205–213.
- Zargar, S., Alamery, S., Bakheit, A. H., and Wani, T. A. (2020). Poziotinib and bovine serum albumin binding characterization and influence of quercetin, rutin, naringenin and sinapic acid on their binding interaction. *Spectrochimica Acta Part A: Molecular and Biomolecular Spectroscopy*, 235:118335.
- Zel'Dovich, Y. B. (1975). Interaction of free electrons with electromagnetic radiation. *Soviet Physics Uspekhi*, 18(2):79.
- Zhan, C.-G., Nichols, J. A., and Dixon, D. A. (2003). Ionization potential, electron affinity, electronegativity, hardness, and electron excitation energy: molecular properties from density functional theory orbital energies. *The Journal of Physical Chemistry A*, 107(20):4184–4195.
- Zhao, G.-J. and Han, K.-L. (2012). Hydrogen bonding in the electronic excited state. *Accounts of chemical research*, 45(3):404–413.
- Zheng, M., Liu, Y., Zhang, G., Yang, Z., Xu, W., and Chen, Q. (2024). The antioxidant properties, metabolism, application and mechanism of ferulic acid in medicine, food, cosmetics, livestock and poultry. *Antioxidants*, 13(7):853.